Imperial College of Science, Technology and Medicine

Royal School of Mines

Department of Earth Science and Engineering

An Investigation into Gas Emission and Outburst Control in Thick Seam Coal Mining

by

Guangyao Si

A thesis submitted for the degree of
Doctor of Philosophy of Imperial College London
September 2015

Abstract

Nowadays, coal mining is extending to deeper and deeper levels, facing ever increasing coal seam gas contents, much higher gas emissions and outburst risks. Capturing coal seam gas before it migrates into atmosphere has been seen as an effective approach to simultaneously improve mining safety, reduce greenhouse gas emissions, and produce clean energy.

Thick seams account for a considerable share of global coal reserve. The application of longwall top coal caving (LTCC) method to extract thick seams generally yields a much higher productivity and is more efficient in comparison to a mechanised single-slice longwall panel. However, the greater productivity achieved by LTCC may further exacerbate the gas emission problems often faced in longwall mining. Geomechanical response of the strata and associated gas emission patterns around thick seam layouts are significantly different from coal mining under thinner multi-seam mining conditions, which is not well understood.

This thesis focuses on establishing an understanding of the stresses, pressure regimes, and gas emission patterns around advancing LTCC faces. During the PhD research, gas pressure and gas concentration were measured in a large number of boreholes in and around an advancing LTCC face at a coal mine. These data are complemented with ventilation and seismic monitoring programmes at the same LTCC district. An integrated analysis of the monitoring data has been carried out and conceptual models for gas emission and drainage for LTCC faces have been developed. These were later used as the basis for numerical modelling research.

A two-way sequential coupling of a geomechanical simulator with a reservoir simulator has been achieved, whereby mining induced stresses and pressures are linked by two coupling parameters: permeability and pore pressure. By applying this approach, gas emission during coal extraction at a LTCC panel in the study coal mine has been successfully modelled and history matched with field data. Recognising that coal and gas outbursts are the most serious and violent gas emissions in both thick and thin seam mining, the application of the coupled modelling approach has been further extended to model two common types of outbursts experienced in an outburst-prone coalfield.

Gas drainage before mining is a standard gas emission control technique, however, its application is largely limited to high permeability coal seams and roof/floor source seams undermined/overmined by single level longwall mining. The feasibility of utilising mining induced permeability enhancement zones to drain gas at thick and tight seams mined by multi-level LTCC method was studied via field trials and numerical models. Building upon the gas emission model developed earlier, a parametric study was carried out to assess different borehole layouts in order to optimise gas drainage designs.

It is believed that the findings of this research and gas drainage methods developed for thick seam mining will create a safer underground environment for miners at high productivity LTCC panels.

DEDICATED TO MY PARENTS

Affirmation

The work submitted in this thesis is my own, and has not been submitted previously for any other degree. The following publications and presentations have resulted from this work:

Si, G., Jamnikar, S., Lazar, J., Shi, J. Q., Durucan, S., Korre, A., Zavšek, S., 2015, Monitoring and modelling of gas dynamics in multi-level longwall top coal caving of ultra-thick coal seams, part I: Borehole measurements and a conceptual model for gas emission zones. International Journal of Coal Geology, 144, 98-110. doi:10.1016/j.coal.2015.04.008.

Si, G., Shi, J. Q., Durucan, S., Korre, A., Lazar, J., Jamnikar, S., Zavšek, S., 2015, Monitoring and modelling of gas dynamics in multi-level longwall top coal caving of ultra-thick coal seams, Part II: Numerical modelling. International Journal of Coal Geology, 144, 58-70. doi:10.1016/j.coal.2015.04.009.

Si, G., Durucan, S., Jamnikar, S., Lazar, J., Abraham, K., Korre, A., Shi, J. Q., Zavšek, S., Mutke, G., Lurka, A., 2015, Seismic monitoring and analysis of excessive gas emissions in heterogeneous coal seams. International Journal of Coal Geology, 149, 41-54. doi:10.1016/j.coal.2015.06.016.

Si, G., Shi, J. Q., Durucan, S., 2013, Micro-seismic monitoring for uncontrolled gas emissions in underground coal mining. In: The 30th International Pittsburgh Coal Conference, 15th-18th September 2013, Beijing, China, 1516-1537.

Copyright Declaration

Acknowledgements

I would like to express my most sincere gratitude to my supervisor, Professor Sevket Durucan for his invaluable advice and endless encouragement over the years. I also thank him for being patient in guiding and supporting my work, which stimulates me to learn critical thinking and academic writing.

I am extremely grateful to Dr Ji-Quan Shi, with whom I could discuss all kinds of technical and scientific issues, and sometimes even complaints. Many thanks also go to Professor Anna Korre, who has provided indispensable advice to help me to improve my English and explore the diversity of life. It was a great fortune for me to benefit from their mentorship during my PhD period. I would also like to thank the Imperial College London, which has provided the scholarships for me to conduct my research at a world-class university.

Thanks all to the senior members of the Minerals, Energy and Environmental Engineering Research Group at Imperial College London, who have always been there to help through these years: Dr Zhenggang Nie, Dr Amer Syed, Dr Rajesh Govindan, Dr Masoud Babaei, and Dr Dong Chen. I would like to thank all my peers, Dr Julio Castro Molinare, Dr Indranil Pan, Saba Manzoor, Jorge de La Torre Guzman, Tareq Al-Ansari, and Nondas Andrianopoulos. The time we spent together I shall never forget.

I also extend my thanks to Jerneja Lazar, Sergej Jamnikar, and Dr Simon Zavšek, from Coal Mine Velenje in Slovenia, who undertook most of the arduous underground measurements and provided essential field data for this research. Dr Grzegorz Mutke and Dr Adam Lurka from Central Mining Institute of Poland are thanked for providing the microseismic data. Thanks also go to Kerstin Abraham, from KUTEC of Germany, who provided the time-lapse seismic tomography data.

Last but not least, I wish to thank my family and friends. Without their support, love and trust, this research would have not been possible. I am particularly indebted to my parents for everything they have done in last 25 years.

Table of Contents

List of Figures

List of Tables

Nomenclature

Alphabet

Symbol	Description	Units
A	cross sectional area for fluid flow	m^2
A_f	surface area of the fault	m^2
a	half length of a crack	m
b_j	reciprocal of Langmuir pressure of j component	Pa^{-1}
C	permeability compressibility factor for intact coal	MPa^{-1}
C_c	cleat compressibility	MPa^{-1}
C_f	permeability compressibility factor for fractured coal	MPa^{-1}
C_g	gas concentration	fractional
CP	coal production per day	t/day
c	Cohesion	Pa
$\mathbf{D}$	matrix of ray path	m
D	fractal dimension	dimensionless
D_c	diffusion coefficient	m^2/s
D_f	average fault slip	m
DC	degassing coefficient for roof or floor strata	fraction
E	Young’s modulus	Pa
E_c	potential energy released from tensile failure	J
E_f	potential energy released from shear failure	J
E_r	radiated seismic energy	J
G	shear modulus	Pa
GC	as content in the floor and roof coals	m^3/t
g	gravitational acceleration	m/s^2
h	burial depth from the surface	m
I_1	first stress invariant	Pa
K	bulk modulus	Pa
K_0	initial bulk modulus for goaf material	Pa
k	absolute permeability	m^2
k_c	corrected permeability due to Klinkenberg effect	m^2
k_i	permeability in i direction for intact coal/rock	m^2
k_f	permeability in i direction for fractured coal/rock	m^2
k_{rg}	relative permeability to gas	fraction
k_{rw}	relative permeability to water	fraction
k_∞	permeability at high pressure	m^2

k_0	initial permeability	m^2
$\hat{k}$	permeability tensor indicating anisotropic permeability	m^2
L_x	size of a coal element along the x-axis	m
m	mass for each elected coal element(s)	kg
N	number of boxes in box counting method	dimensionless
n	number of gas component in a gas mixture	dimensionless
n_t	time index depending on coal rank and degree of cleating	dimensionless
P	gas pressure of the natural fracture system	Pa
P_i	gas partial pressure for component *i*	Pa
P_{cavity}	mean gas pressure in the connected void space	
P_{coal}	pore pressure of a solid coal element before being ejected	
P_L	Langmuir pressure	Pa
P_{sc}	standard pressure	Pa
p	size of boxes in box counting method	m
Q	total amount of gas emission per tonne of mined coal into a seam being-mined	m^3/t
Q_m	volume of gas release from the coal seam being-mined with respect to per tonne extraction	m^3/t
Q_x	mass flow rate along *x* direction	m^3/s
q	gas emission rate related to coal production	m^3/t
R	distance between seismic source and receiver	m
r	radial distance from the centre of a particle	m
$\boldsymbol{S}$	slowness matrix	s/m
S	slippage factor	dimensionless
S_{ij}	deviatoric stress	Pa
$\boldsymbol{T}$	travel time matrix	s
T_0	tensile cut-off	Pa
TA	thickness of the gassy strata in roof and floor	m
TM	thickness of the coal seam being-mined	m
t	time of gas molecule diffusion	s
t_0	time constant which is defined as the time taken for 63.2% of the total methane to be released from coal	s
V	volume of adsorbed gas per unit weight coal	m^3/kg
$V(t)$	volume of gas emissions at time t	m^3
V_i	volume of component *i* adsorbed per unit weight of coal	m^3/kg
V_L	Langmuir volume per unit weight of coal	m^3/kg
V_{Li}	Langmuir volume for component *i* per unit weight of coal	m^3/kg
$V_{\max}$	maximum volume of gas to be released from coal	m^3
V_{gas}	volume of released gas during coal and gas outbrust	m^3
V_{void}	cavity volume and the volume of developed roadway	m^3
v_p	P-wave velocity	m/s
v_s	S-wave velocity	m/s

Greek symbol

Symbol	Description	Units
α	Biot coefficient	fraction
δ_{ij}	Kronecker delta	dimensionless
ε	elastic strain	dimensionless
ε^p	plastic strain	dimensionless

ε_V	volumetric strain	dimensionless
θ	internal friction angle	degree
λ	plastic multiplier	dimensionless
μ	fluid viscosity	Pa·s
ρ	mean density of rock layers	kg/m^3
ρ_c	coal density	kg/m^3
ρ_f	fluid density	kg/m^3
σ	total stress	Pa
σ_e	effective stress	Pa
σ_n	normal stress	Pa
σ_t	tensile stress	Pa
σ_f	final stress after faulting	Pa
$\Delta\sigma_j$	stress change in *j* direction	MPa
$\Delta\sigma_f$	stress drop during faulting	Pa
τ	shear stress	Pa
τ_s	sorption-kinetic characteristic	s
υ	Poisson's ratio	dimensionless
ϕ	porosity of the porous media	fraction

Subscript and superscript

0	initial value;
i,*j*,and *k*	x,y,and z directions in a three dimensional Cartesian coordinate system;
w and *g*	represent water and gas respectively;
f and *t*	represent floor and roof coal seams respectively;
n	index for excavation step;

Acronyms and Abbreviations

AFC	Armoured Face Conveyor
ANN	Artificial Neural Network
ART	Algebraic Reconstruction Techniques
ASTM	American Society for Testing and Material
CDMI	Carbon Dioxide and Methane Index
CFD	Computational Fluid Dynamics
GHG	Greenhouse Gas
GIG	Central Mining Institute
K-UTEC	K-UTEC Salt Technologies (Germany)
LTCC	Longwall Top Coal Caving
MRDE	Mining Research and Development Establishment
PCG	Pingmei Shenma Energy and Chemical Group
SIRT	Simultaneous Iterative Reconstruction Techniques
SOS	Seismic Observation System

Chapter 1 Introduction and Objectives

1.1 Motivation

‘Coal provides around 30.1% of global primary energy needs, generates over 40% of the world's electricity and is used in the production of 70% of the world's steel (World Coal Association, 2015).’ There is no doubt that coal will still play an important role in the foreseeable future, particularly in emerging economies such as China and India. Unfortunately, the history of coal mining is written by not only black coal but also red blood. After two hundred years of struggle with harsh and extreme underground conditions, modern mining techniques have significantly improved mining safety, however, underground coal mining accidents still claim thousands of lives every year.

Coal mine gas emissions (consisting of mainly methane and carbon dioxide), which occur along with coal extraction activities, have long been recognised as the main threat to mining safety. More specifically, methane is an explosive gas when its concentration ranges from 5 to 15% in air, and carbon dioxide can have major detrimental physiological effects on human metabolism at a concentration above 2% in air. Generally, in order to maintain the concentrations of these harmful gases below a safety threshold, ventilation systems are essential for coal mines.

In recent years, with the depletion of shallow coal resources, coal mining is extending to deeper and deeper levels, facing ever increasing coal seam gas contents and much higher gas emission rates at production districts. This situation, unfortunately, cannot be simply addressed by a ventilation system, or at least on its own. It is even worse that the increase of gas content with burial depth coincides with an increase of in-situ stress conditions and decreasing permeability. This combination makes today's coal mining more susceptible to a mining hazards such as outbursts or uncontrolled gas emissions. An outburst is recognised as a spontaneous and instant ejection of rock/coal and gas from a solid coal face into mine openings. The dynamic ejection of rock/coal can destroy equipment at mine openings and even cause fatalities. Furthermore, excessive gas emissions within a short time period can significantly increase gas concentrations in the ventilation air and result in secondary disasters such as methane explosions, dust explosions, and fire. Table 1.1 summaries a number of large-scale gas-related coal mine disasters which occurred in several major coal production countries since the 1990's (Mining accident, 2015).

Table 1.1: Major gas-related coal mine accidents which occurred in recent years.

Country	Year	Mine	Fatalities	Country	Year	Mine	Fatalities
Canada	1992	Westray mine	26	United States	2006	Sago mine	12
Turkey	1992	TCC Kozlu mine	263	China	2007	Xinyao coal mine	105
South Africa	1993	Middelbult coal mine	53	China	2007	Tunlan coal mine	78
China	2000	Muchonggou mine	159	Russia	2007	Yubileinaya mine	39
China	2002	Chengzihe	124	Russia	2007	Ulyanovskaya mine	108
China	2004	Daping mine	148	China	2009	Xinxing mine	108
China	2004	Chenjiashan mine	166	China	2009	Xinhua No.4 mine	54
China	2005	Dongfeng mine	171	Turkey	2009	Bursa province	19
China	2005	Sunjiawan mine	214	China	2010	Pingyu coal mine	37
China	2005	Shenlong Mine	83	Russia	2010	Raspadskaya	66
China	2005	Xishui colliery	72	Turkey	2010	Zonguldak province	30
China	2005	Liuguantun colliery	103	China	2012	Xiaojiawan mine	45
China	2006	Linjiazhuang Mine	57	China	2013	Machang coal mine	25
China	2006	Nanshan colliery	24	China	2013	Babao coal mine	53
Poland	2006	Halemba mine	21	China	2013	Taozigou coal mine	28

In addition, the release of coal mine gas into the atmosphere can exacerbate global climate change. Methane accounts for 16% of all global greenhouse gas (GHG) emissions, and emissions from coal mines represent 8% of global anthropogenic methane emissions (IEA, 2009). According to recent estimates, worldwide methane emissions from coal mines have reached and exceeded 390 MMt CO_2 equivalents (Figure 1.1), with approximately two-thirds of this methane being emitted in the ventilation air, the rest being captured via the methane drainage systems employed and only partly utilised.

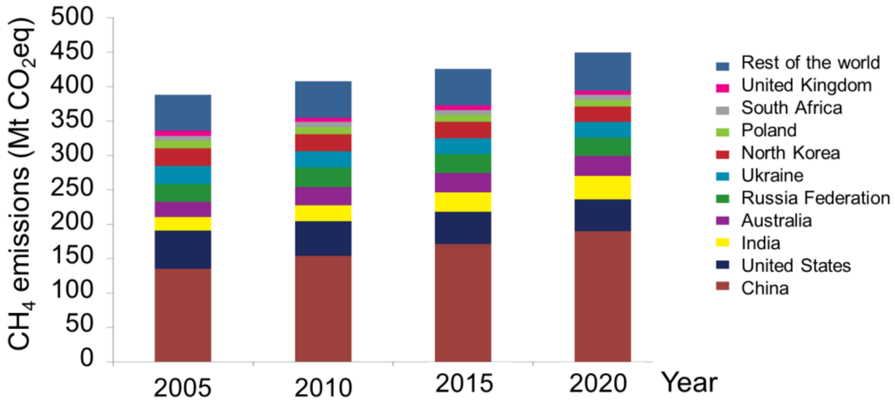

Figure 1.1: Global methane emissions from coal mines (IEA, 2009).

However, there is the bright side to the presence of natural gas in coal: methane is a clean energy source to alleviate current global energy demands. Over the last 30 years coalbed methane developments have flourished in North America where, today, gas extracted from coal makes up around 5% of US domestic gas consumption (U.S. Energy Information Administration, 2014). Therefore, capturing/collecting coal mine methane before it migrates into atmosphere has been seen as an effective approach to simultaneously improve mining safety, reduce GHG emissions, and produce clean energy.

1.1.1 Gas Emissions in Thick Seam Mining

The thickness of coal seams varies significantly from region to region. Multi-layer thin seams each measuring less than 3.5 metres are commonly seen in almost every coal producing country. To extract thin seams, longwall mining has been developed in Germany, the UK, and the US, and then being widely accepted all over the world. As the mining of thin seams with the application of longwall layouts thrived, the knowledge on gas emission patterns around traditional longwall faces has become well-established.

Thick seams (thickness > 3.5 - 4.0 m) also account for a considerable share of coal reserves in many coal production countries, e.g., China, Australia, India, Turkey, South Africa, former Yugoslavia, and Spain (Ghose, 1984). It is estimated that around 45% of total coal reserves are categorised as thick seams in China. In India, this number is reported to be over 60% (Singh, 2011). The measured and indicated thick seam resources in Australia amount to 6.5 and 17.6 billion tonnes, respectively (Hebblewhite, 2005).

After years of perfection, the longwall top coal caving (LTCC) mining method has emerged as the most effective approach to extract thick seams. Being able to recover a coal seam as much as 20 m thick by operating only one longwall face, a LTCC face generally yields a much higher productivity and is more efficient in comparison to a traditional longwall face. However, the greater productivity achieved by LTCC mining may further exacerbate the gas emission problems often faced in longwall mining.

Although there has been widespread applications of LTCC in thick seam mining, fundamental investigations regarding gas emissions around LTCC faces during the extraction of thick seams are relatively limited. It is expected that mining thick seams may result in a distinctly different stress pattern and strata behaviour, which can consequently affect gas flow patterns around mine openings. The face advance rate and coal productivity of a LTCC panel may be seriously constrained by high gas emissions in some gassy mines. Gas emission control during the recovering of thick gassy seams presents a new challenge for today's mining industry.

1.1.2 In-situ Measurement and Monitoring of Gas Emissions

Stress distributions, pressure regimes, and gas emissions around an operating coal face are three factors interacting with each other, which are best evaluated using in-situ measurements. Borehole measurements and ventilation environment monitoring are standard techniques used to understand the responses of strata and gas dynamic behaviour around mining activities. Coal seam responses to face advance including stress, pressure, and permeability changes can be directly or indirectly measured via underground boreholes. The amount of gas emissions induced by coal extraction can be recorded by sensors installed in return airways.

In recent years, the application of geophysical techniques, such as seismic tomography and microseismic monitoring, in underground coal mining has received increasing attention (Lu *et al.*, 2013, 2014; Cai *et al.*, 2014). Attempts to use these techniques to provide early warning for mining hazards (catastrophic roof failure, rock burst, and outburst) have been made by many researchers (McKavanagh and Enever, 1978; Styles *et al.*, 1988; Fujii *et al.*, 1997; Li *et al.* 2007; Kabiesz and Makówka, 2009; Lu *et al.*, 2013; Cai *et al.* 2014). These techniques are demonstrated to be able to image geological structures, interpret stress redistributions, and even analyse fracture source mechanisms.

Field measurement results provided by some standard and some novel techniques are essential to study the mechanism of gas release and migration around coal faces. However, these techniques have so far been conducted in thin seams with longwall layouts and, in most cases, on their own. An integrated analysis of different measurement data has rarely been achieved, and even less practised in the case of thick seam mining.

In addition, although geophysical techniques are promising, they are still immature in field applications, particularly regarding the early detection of uncontrolled gas emissions. Geophysical data obtained from the field needs further analysis and interpretation using other monitoring data which may support these analyses.

1.1.3 Numerical Modelling of Gas Emissions around Coal Faces

In addition to field measurements and monitoring, numerical modelling is a tool to explore stress, pressure, and permeability distributions around operating coal faces. Geomechanical simulators can realistically reproduce stress responses and strata behaviour to coal extraction and estimate the size of mining disturbed zones. It is essential to achieve coupled geomechanical and fluid flow modelling in order to simulate gas flow induced by mining activities within these zones. By this approach, the amount of gas being released during mining can be predicted and the corresponding gas control techniques can be assessed and optimised.

However, previous coupling approaches in coal mine gas emission modelling have mainly used one-way coupling (Esterhuizen and Karacan, 2005; Whittles *et al.*, 2006; Karacan *et al.*, 2007b), ignoring the impact of pore pressure changes on permeability. This may lead to errors in the simulation of gas flow around coal faces. Furthermore, the modelling approach to simulate progressive longwall face advance and associated gas flow in detail has rarely been attempted, nor implemented for LTCC panels. As another application of coupled geomechanical and fluid flow modelling, current outburst modelling practice is mostly limited to a small number of theoretical studies (Choi *et al.*, 2004a, 2004b; Xu *et al.*, 2006; Xue *et al.*, 2011).

1.1.4 Gas Drainage in Thick and Low Permeability Coal Seams

In terms of gas control techniques in thick seam mining, in-seam borehole pre-drainage is widely accepted as a standard methodology, not only to reduce gas content of mined seams for mining safety, but also capture gas for utilisation. There is one main limitation about this technique: it can only be applied in coal seams with relatively high permeability ($\geq 1\times10^{-15}$ m^2). In low permeability coal seams, gas drainage performance is low and stimulation techniques are normally required to enhance gas recovery.

The idea of taking the advantage of mining-enhanced permeability zones to improve gas drainage performance in thick seam mining sounds practical and feasible, however, this requires more fundamental studies to guide field practice. The relationship between gas drainage performance and face advance in thick seam mining is yet unclear and extremely rare in thick and low permeability coal seams.

1.2 Research Objectives and Methodologies

It can be concluded that gas emission problems experienced in mining of thick seams are challenging and yet to be explored well. Knowledge gaps in terms of gas emission modelling and prediction, early detection of outburst and the development of gas drainage methods for thick and low permeability seams need to be investigated thorough integrated field measurements and data analysis.

Therefore, the main objective of this PhD research was to improve the understanding of gas emission patterns around LTCC faces used in thick seam coal mining. This was achieved through:

- an integrated analysis of field measurement data from various sources such as, borehole gas pressure and concentration and ventilation measurements;
- field implementation and analysis of seismic monitoring;
- a two-way coupled geomechanical and fluid flow modelling approach to simulate gas emissions and coal/gas outbursts at outburst prone seams; and

- the implementation of the models developed to assess and optimise gas drainage performance of underground boreholes that are stimulated by mining activities.

In doing so, the author has worked closely with industrial partners over his PhD period. The two European Commission funded research projects (CoGasOut and GHG2E) by provided extensive field data collected by the industrial partners of these projects. Thus, the first phase of this research involved intensive analysis and interpretation of field data. At a study coal mine, gas pressure and gas concentration were measured with a large number of boreholes in and around an advancing LTCC face. These data were complemented with ventilation and seismic monitoring data around LTCC districts. At the end of the first phase, a conceptual model describing stress, pressure, and gas emission patterns around LTCC faces was developed.

Building upon the knowledge gained during this first phase, the second phase of research focused on developing a two-way sequential coupling of geomechanical and fluid flow simulators and applying this methodology to model gas emissions around LTCC faces. Field measurement data from the study mine provided input for the development of numerical models and, in return, numerical models provided an insight into stress and pressure distributions and gas migration pathways around LTCC faces. Later, the coupling approach was further modified to model two different types of coal and gas outbursts at development headings in an outburst-prone coal field in China.

The third phase of this research investigated the impact of mining activities on the performance of gas drainage with different types of borehole layouts. Gas drainage data from field trials were analysed and borehole layouts and settings from these trials were then used as the reference for further numerical modelling studies. A number of drainage scenarios with various borehole parameters (length, inclination, azimuth, and spacing) were assessed to optimise gas drainage performance.

1.3 Thesis Structure

The main structure of this thesis and inter-relationship between the chapters are depicted in Figure 1.2. Chapter 2 reviews the fundamentals of coal science, including coal structure, gas storage and transport mechanisms in coal, rock mechanics, and permeability behaviour. Chapter 3 presents an extensive literature review on geomechanics and gas emissions around mechanised single-slice longwall faces in thin seam mining as well as LTCC faces in thick seam mining. Knowledge gaps, which are to be addressed in the main body of this thesis, are also identified.

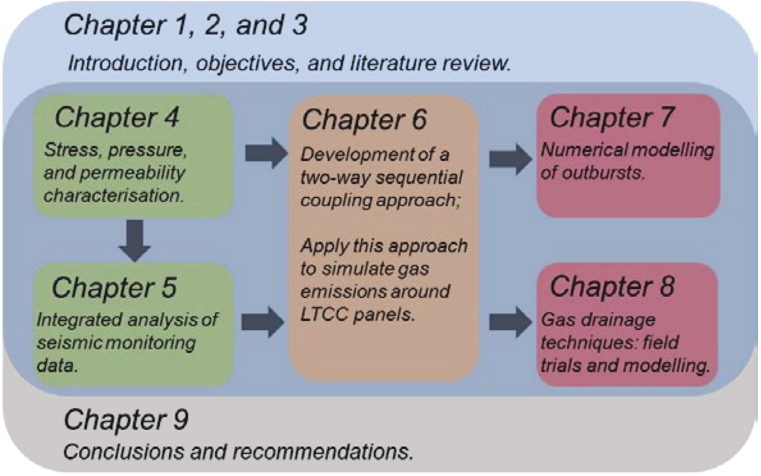

Figure 1.2: Thesis structure and inter-relationships between individual chapters.

Chapters 4 and 5 form the analysis and interpretation of the field measurement and monitoring data and provide inputs for the modelling study in Chapter 6. Using various field measurement techniques, Chapter 4 focuses on building up a preliminary understanding of stress changes, pressure regimes, and permeability responses around an advancing LTCC face. An integrated analysis of all measurement data has been achieved and a conceptual model for gas emissions in LTCC has been developed. Following Chapter 4, Chapter 5 aims at further improving the understanding of the stresses and gas dynamic around LTCC faces using geophysical techniques (time-lapse seismic tomography and microseismic monitoring). The feasibility of using these techniques for the early detection of gas outbursts is also explored.

In Chapter 6, a two-way sequential coupling approach for geomechanical and fluid flow simulators is proposed and a field-scale model based on a typical LTCC panel at the study mine is developed. Around three months of face advance and associated gas emissions are simulated and matched with field data. Chapter 7 further applies the two-way coupling approach to modelling coal and gas outbursts.

With the established understanding of coal seam behaviour and gas dynamics around LTCC faces, Chapter 8 focuses on the effects of face movement on gas drainage performance with different types of boreholes layouts. Gas production stimulated by face approach is studied via field trials and numerical models. A parametric study regarding borehole layouts is also conducted to optimise gas drainage designs.

Finally, Chapter 9 draws the main conclusions and accomplishments from the research presented and makes recommendations for future research.

Chapter 2 Coal as a Reservoir Rock

The maturation process of coal driven by temperature and pressure over long geologic time involves physical as well as chemical reactions changing the molecular structure of coal. Associated with these reactions, coal seam gases, such as methane, are evolved in large volumes. Meanwhile, micropores develop to store a considerable amount of gas per unit coal, which characterise coal seams as both source and storage reservoirs. This chapter reviews the fundamentals of coal structure, gas storage and transport mechanisms in coal, rock mechanics, and permeability behaviour.

2.1 Coal Structure

2.1.1 Pore Structure

The internal structure of coal is dominated by its dual-porosity characteristics, which can be generalised as micropores and macropores. Micropores, which are essential for gas storage, refer to the capillaries and cavities of molecular dimensions, which mainly exist in the coal matrix (Rogers *et al.*, 2007). The macropores consist of mutually orthogonal or near orthogonal fractures called cleats. As shown in Figure 2.1, there are two kinds of cleats, perpendicular or near perpendicular to bedding planes: face cleats and butt cleats, which are known as primary fractures and secondary fractures in coal, respectively. Face cleats are continuous throughout coal seams, whereas butt cleats are discontinuous and terminated by face cleats at intersections. Since the matrix is normally low permeability or impermeable, the cleat system is the critical factor determining the permeability of coal seams as it provides main paths for gas migration.

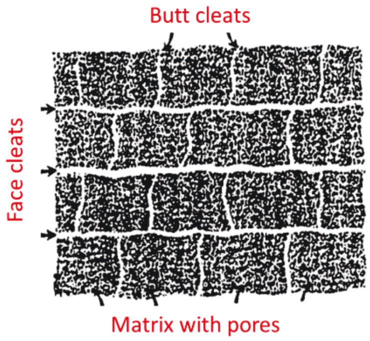

Figure 2.1: Schematic of the plan view of coal dual-porosity structure (after Shi and Durucan, 2005).

Two models have been widely accepted to describe the dual-porosity structure of coal: (1) the rectangular parallelepiped model (King *et al.*, 1986), which is very similar to the classical W&R model (Warren and Root, 1963) originally developed for naturally fractured petroleum reservoirs and (2) the bundled matchstick model (Seidle *et al.*, 1992). Figure 2.2 (a) presents the rectangular parallelepipeds model. Although this model properly defines the idealised coal structure of matrix, cleats, and bedding planes, due to the high in-situ vertical stress caused by overburden weight, bedding planes seldom play a role in fluid transportation. Therefore, as also confirmed by laboratory resulte (Harpalani and Chen, 1995, 1997), a bundled matchstick geometry proposed by Seidle *et al.* (1992) is believed to be more suitable for respresenting fluid flow in coal seams (Figure 2.2 (b)).

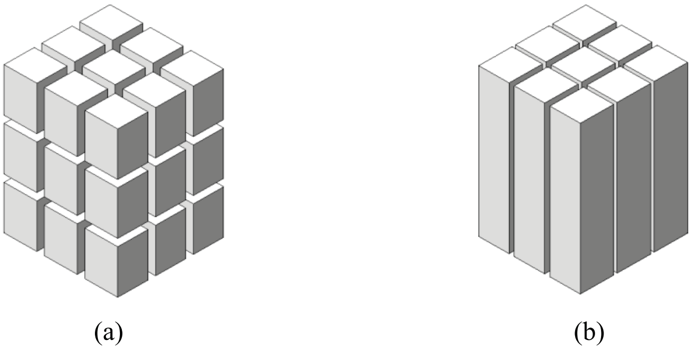
(a) (b)

Figure 2.2: (a) The rectangular parallelepiped model (after King *et al.*, 1986); and (b) the bundled matchstick model (after Seidle *et al.*, 1992).

2.1.2 Coal Rank

Coal rank is used to characterise different coal types in terms of chemical and physical properties after maturation. Coal rank classification proposed by the American Society for Testing and Material (ASTM) is shown in Figure 2.3. Various measures are used to establish rank. For higher coal ranks, measures such as the values of Vitrinite Reflectance, Volatile Matter, and Fixed Carbon content are normally used. Whereas calorific value and moisture content are more suitable in distinguishing lower rank coals.

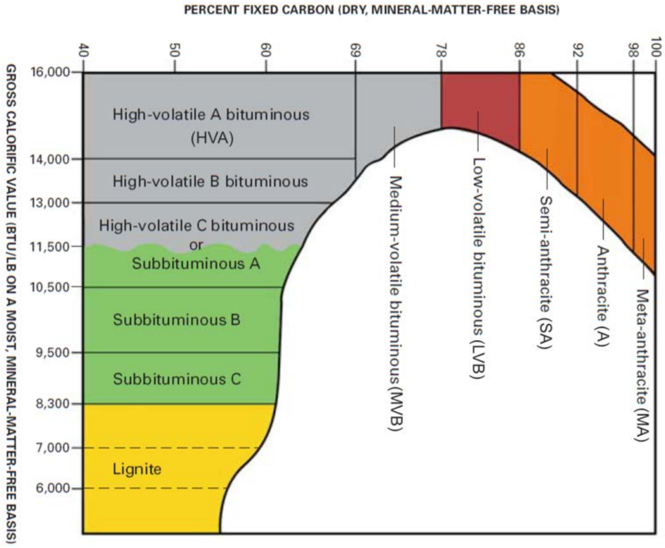

Figure 2.3: Classification of coal rank suggested by the American Society for Testing and Materials (after Schweinfurth and Finkelman, 2003).

Physical properties such as mechanical strength, density, and porosity normally vary with rank and most of these properties peak as minimum values when the percentage of fixed carbon ranges from 70% to 90% (see Figures 2.4 and 2.5). Lignite and subbituminous coals possess relatively high compressive strengths. The compressive strength of coal decreases as the Fixed Carbon percentage increases, reaches minimum at mid-volatile bituminous (MVB) rank, and later rebound in low-volatile bituminous (LVB) and anthracite (A) classes (Jones *et al.*, 1988). Porosity has also been found to decline with increasing rank, being the lowest at mid-volatile bituminous coal, and increase again in the anthracite range (King and Wilkins, 1944). The density of coal shows a similar trend with the variation of rank, which bottoms in the upper bituminous ranks.

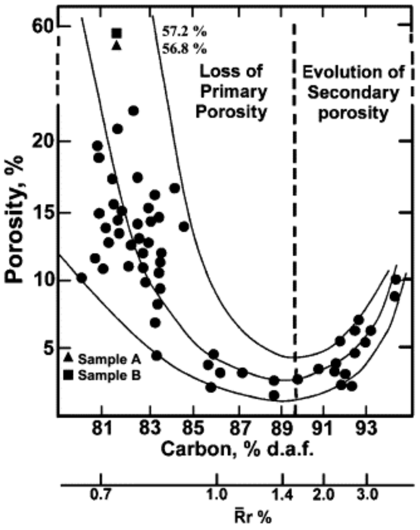

Figure 2.4: Relationship between coal porosity and coal rank (extracted from Rodrigues and Lemos de Sousa, 2002).

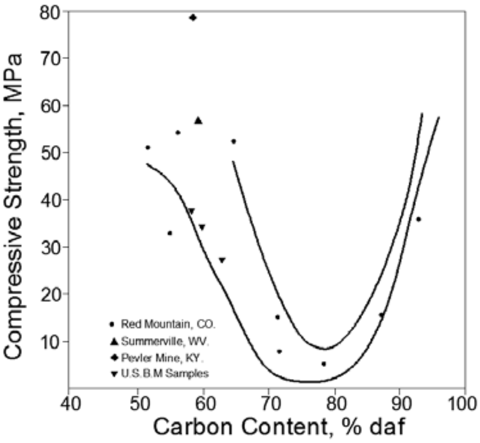

Figure 2.5: Relationship between coal's unconfined compressive strength with rank (after Jones *et al.*, 1988).

Note that the brittleness of coal increases throughout coal rank, and fractures are hard to develop in lignite due to its ductility (Das *et al.*, 1991). The most well-developed cleat system is reported to be in high-volatile A bituminous and low-volatile bituminous coals, and this can be partly attributed to brittleness increase with rank.

Methane generation is relatively mild in the lower ranks of coal and accelerates in mid-volatile bituminous coal (Das *et al.*, 1991). It is estimated that about ten times more methane than that retained may have been generated during coalification. Most of this methane escaped to the atmosphere in the early stages due to the incomplete sealing of the cap rock. Ground water movement over long geological time could also have dissolved and removed a large portion of gas (Hedberg, 1980). In addition, deep coal deposits may be uplifted by tectonic activities and lose the methane produced earlier (Patching, 1970).

2.1.3 Gas Retention in Coal

Compared with conventional gas reservoirs, the storage mechanism of methane in coal seams is significantly different. Rather than in a free state compressed in pores, gas in coal seams is primarily adsorbed on the internal surfaces of pores and micro-fractures. The percentage of adsorbed methane can be as high as 98% and the other 2% is retained as free gas (Gray, 1987). It is estimated that the micropores account for 95% percentage of the total internal coal surfaces (Thimons and Kissell, 1973). Thus, a remarkable volume of gas is stored on the surfaces of coal micropores in an adsorbed state. Macropores are expected to be statured with formation water. Figure 2.6 shows a schematic of gas molecules inside a coal pore.

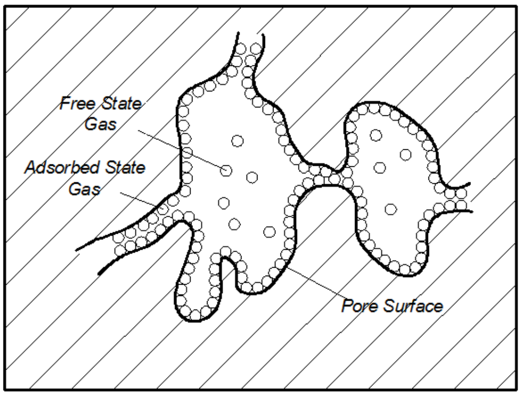

Figure 2.6: Schematics of gas molecules inside a coal pore (after Durucan, 1981).

The primary mechanism of gas sorption in coal is a reversible process controlled by weak physical forces. Sorption isotherms, which describe the relationship of gas pressure and adsorbed/desorbed gas volume under a constant temperature, are widely used to represent the adsorptive properties of coal. Due to its close fit for the sorption data for various coals and its appealing simplicity, the Langmuir isotherm (Langmuir, 1918) has gained the widest application. The Langmuir isotherm is given as follows:

$$V = \frac{V_L P}{P_L + P} \qquad 2.1$$

where, V (m^3/kg) is the volume of adsorbed gas per unit weight of coal; V_L (m^3/kg) is the Langmuir volume, representing the maximum volume of gas that can be adsorbed at gas pressure P (Pa) per unit weight of coal; P_L (Pa) is the Langmuir pressure, corresponding to the pressure at which half of the Langmuir volume has been adsorbed.

In addition to pressure, the sorption capacity of coal is determined by certain other factors. With the increase of reservoir temperature, moisture, or coal ash content, the sorption capacity of coal decreases substantially (Barker Read and Radchenko, 1989; Mavor *et al.*, 1990). On the other hand, increase of coal rank can favour sorption capacity (Kim, 1977).

In coal mining activities, it is not unusual to encounter coal seams which hold more than one type of gas, such as a mixture of CO_2 and CH_4. In this case, the Langmuir isotherm has to be extended to take into account of the adsorption of gas mixture. The extended Langmuir isotherm is presented in Equation 2.2 (Harpalani and Pariti, 1993).

$$V_i = \frac{V_{Li} b_i P_i}{1 + \sum_{j=1}^{n} b_j P_j} \tag{2.2}$$

where, V_i (m^3/kg) is the gas volume of gas component i adsorbed per unit weight of coal at partial pressure P_i (Pa); V_{Li} (m^3/kg) is the Langmuir volume for component i per unit weight of coal; n is the total number of gas components in the mixture; b_j (Pa^{-1}) is the reciprocal of the Langmuir pressure of gas component j.

Note that coal matrix shows preferential adsorption to different gases. Compared with CH_4, CO_2 has a stronger affinity for the pore surface of coal, and N_2 is less readily adsorbed by the pore surface. The selective adsorption of CO_2 in coal was also reported to be affected by moisture and coal composition (Clarkson and Bustin, 2000).

2.2 Gas Flow in Coal Seams

Gas migration in coal can be represented as a two-stage process. The first stage is diffusional flow in the matrix and the second stage is Darcy flow in cleats and fractures. In fact, before gas diffuses from the matrix to cleats, gas desorption from the pore surfaces takes place. However, this process is usually considered along with the diffusion stage as it is much faster than the diffusion process (Smith and Williams, 1984). A schematic describing the whole process of gas migration is shown in Figure 2.7.

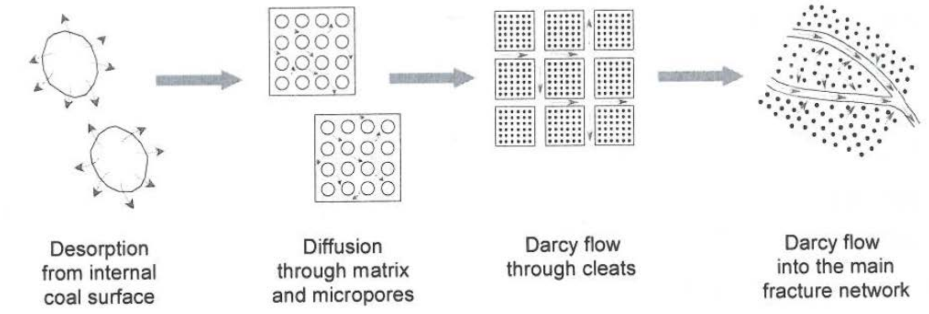

Figure 2.7: Schematic of gas transport processes in coal seams (after Ahsan, 2006).

2.2.1 Diffusional Flow

As gas is originally adsorbed on the surface of micropores in low permeability matrix, the migration of gas in coal mining is not simply driven by pressure gradient created by ventilation. Due to mining disturbance or other degasification activities, pore pressure in cleats and micropores can decrease substantially, especially around mine openings. According to the Langmuir isotherm, together with the decreasing of pore pressure, gas desorbs from the micropore surfaces. Consequently, a concentration gradient is established between the coal matrix and cleats. Since the mean free path of gas molecules is larger than the diameter of micropores, this is a diffusional process which follows the Fick's law (Harpalani and Chen, 1997). Using Fick's second law, spherically symmetric gas diffusion in coal matrix can be described as (Crank, 1975):

$$\frac{\partial C_g}{\partial t} = -\frac{D_c}{r^2}\frac{\partial}{\partial r}\left[r^2\frac{\partial C_g}{\partial r}\right] \qquad 2.3$$

where, C_g (fraction) is the gas concentration, D_c (m^2/s) is the diffusion coefficient, t (s) is the time of gas molecule diffusion, and r (m) is the radial distance from the centre of a particle.

2.2.2 Darcy Flow

Following diffusion, when desorbed gas reaches the cleat system, gas migration starts to be dominated by the permeability of cleats and fractures. The driving force for this flow regime is pressure gradient, and in this case Darcy's law can be applied. For incompressible laminar flow through homogenous porous media along *x* direction, Darcy's law can be simplified as:

$$Q_x = -\frac{kA}{\mu}\left(\frac{\partial P}{\partial x} - \rho_f g_x\right) \qquad 2.4$$

where, Q_x (m^3/s) is the mass flow rate along *x* direction, k (m^2) is the absolute permeability, A (m^2) is the cross sectional area, μ (Pa·s) is the fluid viscosity, ρ_f (kg/m^3) is the fluid density, g_x (m/s^2) is the gravitational acceleration component in x direction, and P (Pa) is the pressure at cleats/fractures.

Gas slippage may be important in narrow passages, especially under low pressure conditions. This phenomenon, known as the Klinkenberg effect, can increase effective permeability of gas linearly with the reciprocal pressure.

$$k_c = k_\infty\left(1 + \frac{S}{P}\right) \qquad 2.5$$

where, k_c (m^2) is the corrected permeability due to Klinkenberg effect, k_∞ (m^2) is the permeability at high pressure, S (dimensionless) is the slippage factor.

Using Darcy's law, the general time-dependent equation for a perfect gas flowing through a porous media can be described as (Ediz, 1991):

$$\frac{\partial P}{\partial t} = \frac{1}{2\mu\phi}\nabla \cdot (\hat{k}\nabla P^2) \qquad 2.6$$

where, $\hat{k}$ (m^2) is a tensor indicating anisotropic permeability, and ϕ (fraction) is the porosity of the porous media.

2.2.3 Sorption Kinetics

Sorption time indirectly provides a hint about the magnitude of diffusion coefficient. Airey (1968) conducted an experimental and theoretical investigation on gas emissions from broken coal. He measured the rate of methane released at different pressures, and proposed an empirical equation for the volume of gas emissions ($V(t)$, m^3) in terms of time:

$$V(t) = V_{\max} \left\{ 1 - \exp\left[-(\frac{t}{t_0})^{n_t} \right] \right\} \qquad 2.7$$

where, t_0 (s) is a time constant which is defined as the time taken for 63.2% of the total methane to be released from coal, $V_{\max}$ (m^3) is the maximum volume of gas to be released from coal, and n_t (dimensionless) is a time index depending on coal rank and degree of cleating.

Sorption-kinetic characteristic τ_S (s) has been suggested as a reliable parameter to assess gas desorption behaviour and quantify the risk of outbursts in the disturbed areas of a coal seam. The value of τ_S is largely dependent on the degree of geological disturbance, i.e. the amount and distribution of the macropores and fractures in test samples (Barker Read and Radchenko, 1989). Ettinger *et al.* (1986) proposed Equation 2.8 to estimate τ_S as:

$$\tau_S = 60 \left\{ 1 - \exp\left[-(\frac{t_0}{60}) \right]^{-n_t} \right\}^{-2} \qquad 2.8$$

where, t_0 and n_t are the same as that defined in Equation 2.7.

2.3 Stress, Strain and Failure

Coal as a rock material follows the fundamentals of rock mechanics. The in-suit stress conditions on coal are determined by burial depth, geology, and tectonic history. As a nine-component tensor, stress at one point can be expressed in the form of maximum (σ_1, Pa), intermediate (σ_2, Pa), and minimum (σ_3, Pa) principal stresses. For shallow coal seams where the burial depth is less than 500 m, the maximum principal stress is normally the vertical stress (σ_V, Pa) and a result of gravitational force induced by the overlying rock layers, which can be determined as (Harrison and Hudson, 2000):

$$\sigma_1 = \sigma_V = \rho g h \qquad 2.9$$

where, ρ (kg/m^3) is the mean density of rock layers, g (m/s^2) is the gravitational acceleration, and h (m) is the burial depth from the surface.

The horizontal stresses, which include intermediate stress σ_2 (σ_H, Pa) and minimum stress σ_3 (σ_h, Pa), are induced by the confining force to constrain the tendency of rock body to expand by the effect of vertical compressing force. This is referred to as the Poisson effect and the two horizontal stresses are seen as a function of the vertical stress and Poisson's ratio (υ, dimensionless).

$$\sigma_{2,3} = \sigma_{H,h} = \sigma_V \frac{\upsilon}{1-\upsilon} = \rho g h \frac{\upsilon}{1-\upsilon} \qquad 2.10$$

Stress regimes at deep coal seams are rather complex and cannot be simply estimated by burial depth. The maximum principal stress may be no longer in the vertical direction but in the horizontal direction since tectonic stresses, which are generally horizontal and uniform over large areas, start to play a dominant role. In this case, in-situ stress measurements are necessary to provide sufficient information to guide the design of underground workings.

The existence of fluid within coal pore-structures acts isotropically as a normal stress. Based on Terzaghi's theory (Equation 2.11), effective stress (σ_e, Pa) imposed on coal structure can be described as the difference between the total stress (σ, Pa) and pore pressure (P, Pa). In Equation 2.11, α (fraction) is the Biot coefficient and normally taken as unit for rock (Jaeger *et al.*, 2007).

$$\sigma_e = \sigma - \alpha P \qquad 2.11$$

Strain is a measure of rock deformation to stress changes. It can be divided into elastic strain and plastic strain depending on whether rock will return to its initial shape after applied stress is removed. Figure 2.8 depicts the complete stress-strain curve under triaxial compression. The Young's modulus is defined to describe the ability of rock to resist stress changes in elastic deformation. For triaxial conditions, the increase of confining stress can significantly increase the peak strength of a specimen and shift the post-failure behaviour of the specimen from brittle to ductile (Harrison and Hudson, 2000).

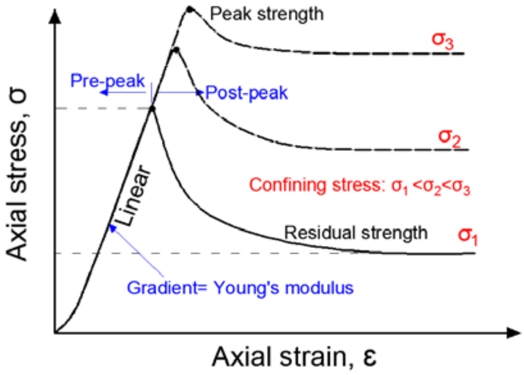

Figure 2.8: Complete stress-strain curves during tri-axial compression tests (after Harrison and Hudson, 2000).

A classical form of a stress-strain relationship can be found in Equation 2.12, where ε_{ij} (dimensionless) is the elastic strain, E (Pa) is the Young's modulus, G (Pa) is the shear modulus, I_1 ($I_1 = \sigma_1 + \sigma_2 + \sigma_3$, Pa) is the first invariant of stress tensor, and δ_{ij} is the Kronecker delta.

$$\varepsilon_{ij} = \frac{\sigma_{ij}}{2G} - \frac{\upsilon}{E} I_1 \delta_{ij} \qquad 2.12$$

Rock failure is an inevitable part of coal mining activities, which suggests the degrading of the capability of rock to withstand loading. Unlike in most of the civil engineering practices, which aim at avoiding failure as much as possible, mining engineering requires accommodating and making the best use of failed (fractured) rock. As rock has natural flaws, with a lot of defects called micro-cracks, failure can occur under both compression and tension, being represented by extending and coalescing micro-cracks into macroscopic fractures.

The Mohr-Coulomb failure criterion, which is defined by a group of shear failure envelopes, has been widely used to analyse whether shear failure on a plane is to be initiated by comparing shear stress (τ, Pa) with normal stress (σ_n, Pa) acting on it, as described in Equation 2.13:

$$|\tau| = c + \sigma_n \tan\theta \qquad 2.13$$

where, c (Pa) is the cohesion indicating the shear strength of rock when the normal stress is zero and θ is the internal friction angle (Jaeger *et al.*, 2007).

Since Mohr-Coulomb failure criterion is developed for shear failure induced by compression, a tensile cut-off (T_0, Pa) is introduced to quantify whether applied tensile stress can cause failure. In order to generate a tensile failure, the applied tensile stress (σ_t, Pa) needs to be:

$$\left|\sigma_t\right| > T_0 \tag{2.14}$$

After the yielding point, elastic strain is almost negligible compared with plastic strain, which can be estimated by Levy-Mises equations:

$$\frac{d\varepsilon_{ij}^{p}}{S_{ij}} = d\lambda \tag{2.15}$$

where, ε_{ij}^{p} (dimensionless) is the plastic strain, S_{ij} (Pa) is the deviatoric stress and $S_{ij} = \sigma_{ij} - \frac{I_1}{3}$, and λ is a scalar plastic multiplier determined from the yield criteria by ensuring the stress-state lies on the yield surface during plastic flow (Khan, 1995).

2.4 Coal Permeability

Permeability is the measure describing the ability for fluid to flow through porous media, and it is probably the most important parameter that needs to be considered for gas flow in coal seams. In-situ permeability is influenced by a variety of factors, including the characteristics of cleats, water saturation, and in-situ stress conditions. Furthermore, mining induced stress changes and fractures may significantly alter initial permeability fields. Therefore, it is difficult to determine the initial permeability from laboratory experiments without reproducing the in-situ stress conditions and considering the size effect of test samples. In reservoir engineering, in-situ permeability is normally estimated by history matching well production data and performing pressure transient tests such as slug test, injection falloff test, and pressure build-up test.

2.4.1 Absolute Permeability and Relative Permeability

The absolute permeability of coal is reported to have considerable diversity in various coal basins throughout the world. But, in general, as the in-situ stress increases with depth, deeper coal seams tend to have lower permeability values. More than one order of magnitude reduction (from 10^{-13} to 10^{-14} m^2) in permeability was observed when the depth of coal seams varied from 30 m to 300 m at San Juan Basin in the US (McKee *et al.*, 1988). As Darcy flow takes place in coal cleats, the absolute permeability of fluid passing through a serious of parallel cleats can be related to the cleat aperture and spacing using a cubic law as described by Snow (1968). Since cleats are expected to be initially occupied by water, gas transport in coal involves two-phase flow. The presence of water can significantly hinder gas transport. The effective permeability for gas (k_g, m^2) increases rapidly with the reducing of water saturation, which is normally described by gas-water relative permeability curves (see Figure 2.9 for example).

$$k_g = k \cdot k_{rg} \tag{2.16}$$

Effective permeability for water (k_w, m^2):

$$k_w = k \cdot k_{rw} = k \cdot (1 - k_{rg}) \tag{2.17}$$

where, k (m^2) is the absolute permeability, k_{rg} (fraction) is the relative permeability to gas, and k_{rw} (fraction) is the relative permeability to water.

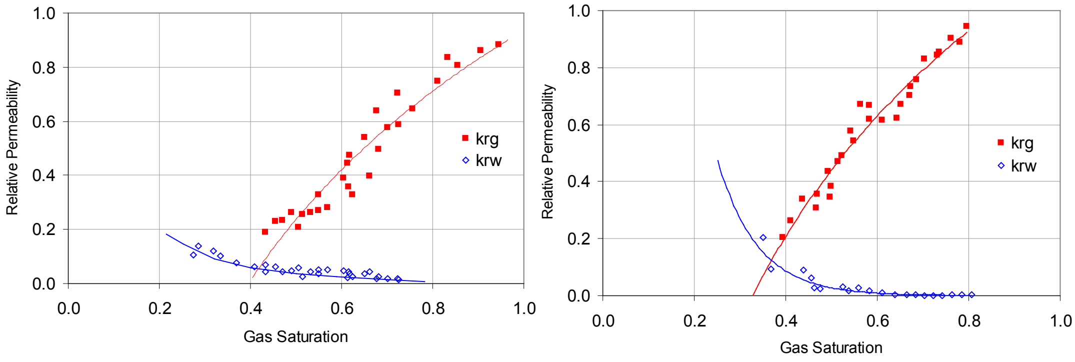

(a) Schwalbach coal sample from Germany (b) Warndt-Luisenthal coal sample from Germany

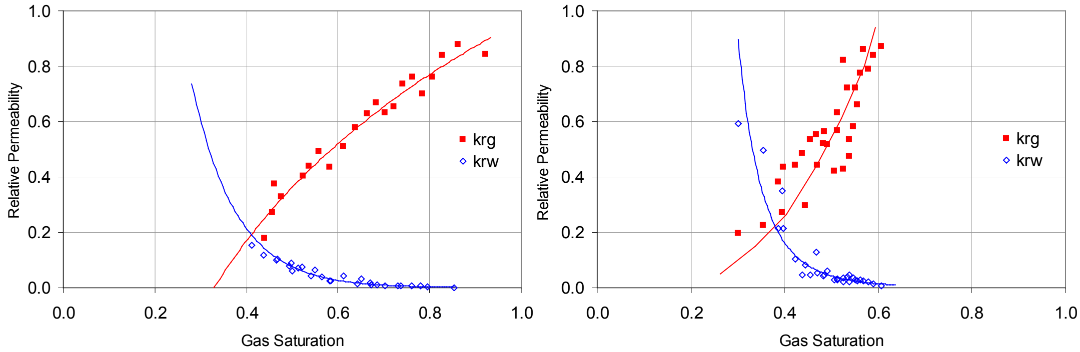

(c) Dora coal sample from France (d) Tupton coal sample from the UK

Figure 2.9: Examples of relative permeability curves for selected Europen coals (after Ahsan, 2006 and Durucan *et al.*, 2014).

Due to the friable and brittle nature of coals, the measurement of coal relative permeability is more challenging compared with reservoir rocks such as sandstone. Most of the early work to determine the gas-water permeability behaviour is given by Reznik *et al.* (1974). Later, Gash (1991) conducted both steady state and unsteady state experiments to measure relative permeability curves in coal under the context of coalbed methane production. Using the unsteady state method, Ahsan (2006) measured gas-water relative permeability curves for seven European coals of different ranks. He noticed that the shapes of relative permeability curves vary considerably for different rank coals (Figure 2.9).

2.4.2 Stress Dependent Permeability

Numerous investigators have shown the effects of stress on the permeability of coal measure rocks and coals (Patching, 1965; Mordecai, 1971; Somerton *et al*., 1975; Durucan, 1981). The earliest study into the effects of confining stress on coal permeability was carried out by Patching (1965). More than three orders of magnitude decrease in permeability was observed by him when confining pressure was raised from 0.07 to 20.7 MPa. Mordecai conducted an extensive research on stress dependent permeability of carboniferous strata rocks for the first time from the viewpoint of mining engineering. He suggested that the application of confining stress first closed up permeable channels and, as confining stress increased, permeability decreased gradually (Mordecai, 1971). However, he also found that a sufficiently high deviatoric stress could result in the opening up of fractures and contribute to the propagation of flow channels which would significantly increase the permeability of coal measure rocks.

An in-depth investigation on stress dependent permeability of different ranks of coal was presented by Durucan (1981). He proposed the following empirical stress-permeability relationship after extensive laboratory tests on different coals:

$$k = (1.12 - 0.03\sigma_3) \cdot k_0 e^{-(1.12-0.03\sigma_3)C\sigma_3} \qquad 2.18$$

where, k (m^2) is the permeability at the confining stress σ_3 (MPa), k_0 (m^2) is the initial permeability, and C (MPa^{-1}) is the permeability compressibility factor depending on coal rank. The permeability compressibility factor C for a number of

UK coals has been reported to be in the range of 0.38 to 0.73, which is believed to correlate with coal Volatile Matter content as shown in Figure 2.10 (Durucan, 1981).

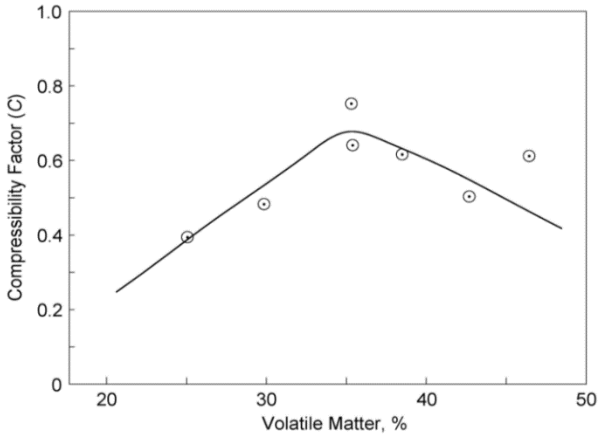

Figure 2.10: Compressibility factor plotted against percentage volatiles for UK coals (after Durucan, 1981).

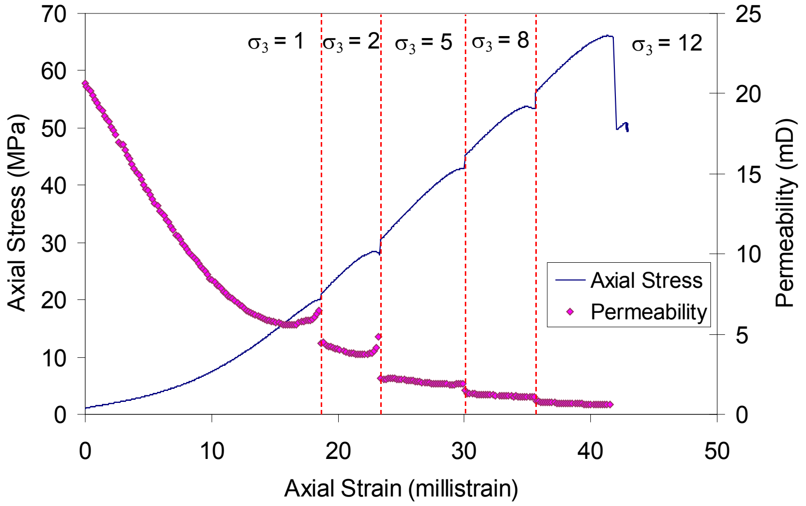

(a) Tupton coal sample

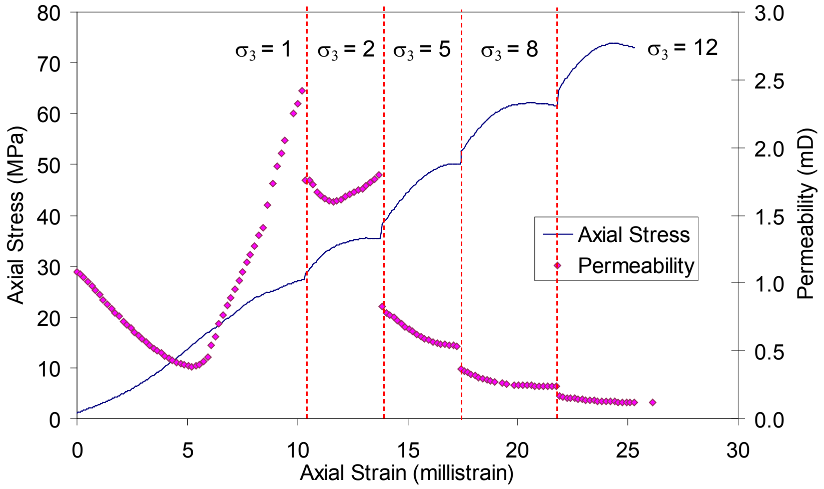

(b) Schwalbach coal sample

Figure 2.11: Stress and permeability *versus* axial strain (after Ahsan, 2006).

Based on the assumption of bundled matchsticks geometry for coal structure, the mathematical derivation of stress-dependent permeability in cleats was given by Seidle *et al.* (1992):

$$k = k_0 e^{-3C_c \Delta\sigma} \quad 2.19$$

where, k_0 (m^2) is the initial permeability, C_c (MPa^{-1}) is the cleat compressibility and $\Delta\sigma$ (MPa) is the stress change in the direction perpendicular to *k*.

Ahsan (2006) conducted multistage triaxial tests to further investigate permeability response of different coal samples to stress under different confining stresses. An exponential reduction in permeability was observed as the confining stress increased if the sample remained intact (Figure 2.11 a). On the other hand, a sharp increase in permeability was observed once failure was initiated in a tested coal sample (Figure 2.11 b).

2.5 Summary

The maturation process of coal over long geologic times can evolve large volumes of gas as well as micropores for gas storage. Gas storage in coal is controlled by the sorption mechanism, which enables a considerable amount of gas to be retained in coal seams provided by the well-developed pore structure. Gas flow in coal can be divided into two stages: diffusional flow and Darcy flow. The former controls gas migration from matrix to cleats while the latter dominates gas flow in cleats and fractures.

Like any other type of rock, coal follows the fundamentals of rock mechanics. Elastic strain and plastic strain are used to define recoverable and unrecoverable deformation of coal to stress changes, respectively. Three types of fractures induced by different failure mechanisms are introduced. The most common shear failure criterion and tensile failure criterion are also presented. Stress changes of samples under loading can be reflected by P-wave and S-wave velocity changes. The failure process of coal is reported to be associated with detectable geophysical signals such as microseismic emissions.

Permeability is recognised as the key parameter that controls gas transport in coal seams. The permeability of porous media is believed to be highly stress-dependent.

An exponential relationship between permeability and stress changes has been constantly observed by laboratory experiments as well being observed in the field.

The fundamental characteristics of coal introduced in this chapter will be helpful to understand the mechanism of gas release and migration induced by mining activities. Next chapter will expand the literature review into the engineering application of longwall mining, LTCC, and associated gas emission phenomena.

Chapter 3 Previous Research on Gas Emissions in Longwall Coal Mining

3.1 Introduction

The basic principles of longwall coal mining operations, including longwall top coal caving, are introduced at the beginning of this chapter. Previous investigations into geomechanics and gas dynamics around mechanised single-slice longwall panels are reviewed. In comparison, literature on gas emissions in longwall top coal caving (LTCC) panels is relatively rare. Next, coal and gas outburst as a special case of excessive gas emissions is introduced, followed by the review of gas emission control techniques. Knowledge gaps in these subjects are also identified.

3.2 Longwall Coal Mining Layouts

Longwall mining gained wide application all over the world due to its advantages of high productivity and high resource recovery. Conventional mechanised longwall mining operations progressively extract a panel of coal in a single slice with the thickness of up to 4.0 - 4.5 m. A longwall panel, which is typically 250~400 m wide and 2~3 km long, is normally outlined by pre-developed gateroads or entries (Figure 3.1). The height of a longwall panel is mostly restricted by the thickness of a coal seam.

Coal is cut by a shearer under hydraulic shields, which also ensure the safety of miners at a working face. Coal extraction process is continuous and affects an extensive area around the mined coal seam. After the removal of coal, roof strata are allowed to collapse into the void known as 'goaf' or 'gob' behind the shields. With the subsidence of overlying strata, the collapsed roof will be gradually re-compacted.

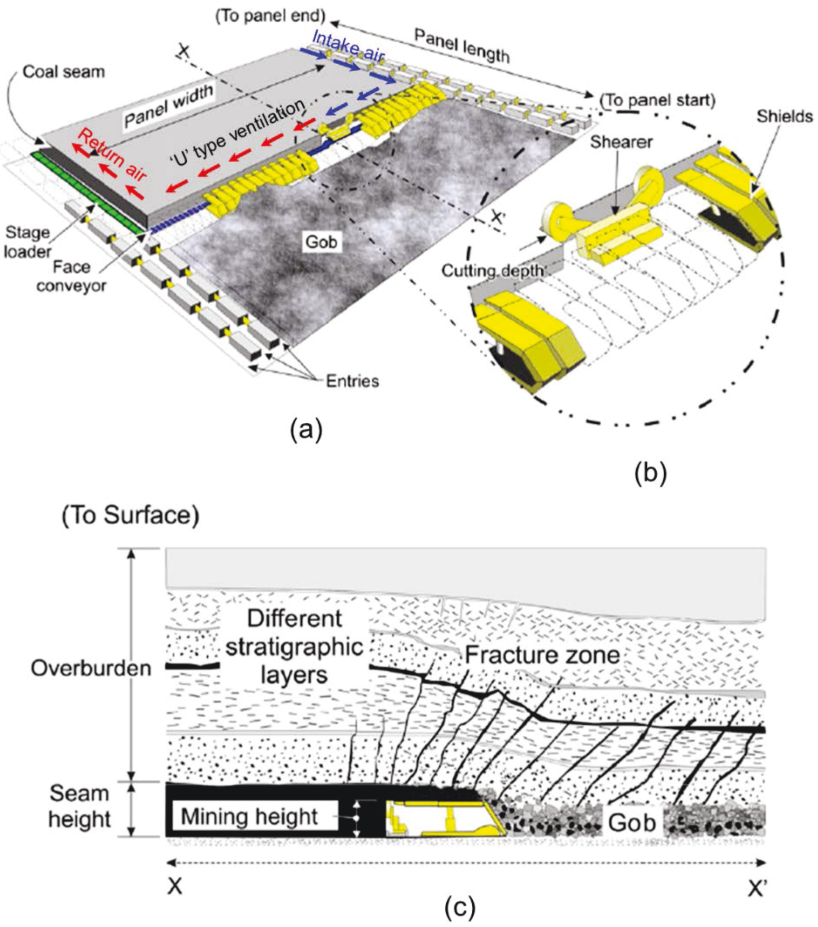

Figure 3.1: (a) Schematic of a mechanised single-slice longwall panel; (b) a detailed view of shearer and cutting depth while mining coal; (c) a vertical cross-section along the X-X' profile in (a) (after Karacan, 2008).

In underground coal mining, a ventilation system supplies the essential fresh air to miners and dilutes coal dust, as well as harmful gas emissions such as methane and carbon dioxide. As shown in Figure 3.1 (a), the 'U' type ventilation is one of the most common ventilation systems used in a longwall mining layout, and other ventilation systems such as 'Y' or 'W' may also be applied. Driven by negative pressure, fresh air in the 'U' type ventilation travels up from the intake gateroad, across the face, and then down to the return gateroad.

3.2.1 Longwall Top Coal Caving

Being developed to exploit relatively thinner seams separated by coal measure rocks, longwall mining cannot easily recover thick seams (~> 4.5 m) without a modification. A simpler approach, referred to as multi-level or sublevel mining, provides an option to extract thick seams without improving coal production. This approach divides an entire coal deposit into several levels with an appropriate thickness that mechanised single-slice longwall mining can be adopted to. Roof control is sometimes problematic in the mining of lower levels since they are operated just under the previously mined goaf.

As a derivative to mechanised single-slice longwall panel (referred to as conventional mechanised longwall panel in this thesis), longwall top coal caving (LTCC) has been developed to extract thick seams of up to 20 m in a much more productive and efficient manner. The most distinct difference between conventional mechanised longwall mining and LTCC is that a caving stage of top coal is performed apart from the normal coal cutting process. As shown in Figure 3.2, the whole height of the extracted coal can be divided into the lower part and the upper part. In a mechanised LTCC panel, the lower section of the coal seam is cut by a shearer supported by the hydraulic shields, while the upper section of the mined seam is allowed to cave by gravity and be collected at the face. Therefore, a LTCC panel generally yields a much higher productivity and is more efficient in comparison to a mechanised single-slice longwall panel. However, the greater productivity achieved by LTCC mining may further exacerbate the gas emission problems often faced in longwall mining, and thus poses a serious challenge for underground gas emission control.

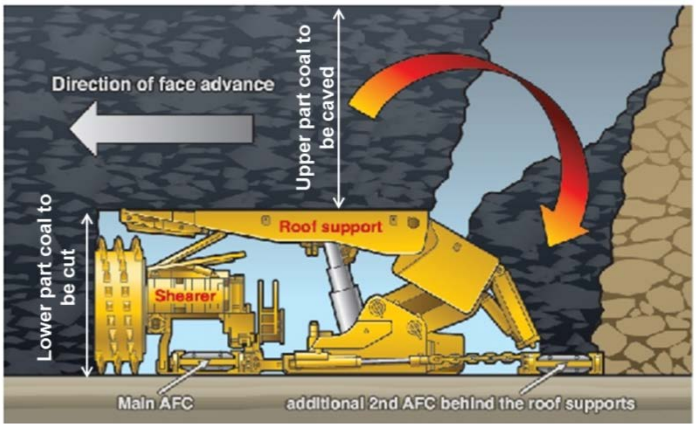

Figure 3.2: Schematic of longwall top coal caving with two AFCs (after Mining.com, 2014).

The application of LTCC may be slightly different depending on the how the caved top coal is collected. The normal practice in China and Australia is that the caving process occurs at the back of shields, which requires an additional armoured face conveyor (AFC) at the rear of shields (Figure 3.2). This may also need a special design of shields to protect both the front and rear conveyors.

A key debate about the feasibility of LTCC is the recovery ratio of top coal, which is highly dependent on the strength of coal and the flow pattern of coal particles. Small fragments with low friction between each other are desirable to maintain an efficient coal flow. Since strong coal is difficult to fracture into small fragments and large coal blocks will not favour LTCC production, LTCC is preferred to be applied in the mining of low strength and brittle coals. In addition, to increase the fragmentation of coal ahead of a LTCC face and improve the recovery ratio of top coal, techniques such as pre-blasting, hydraulic fracturing, and vibration are frequently used (Unver and Yasitli, 2006; Xie and Zhao, 2009).

3.3 Geomechanics and Gas Flow in Conventional Mechanised Longwall Faces

3.3.1 Gas Release Mechanism During Longwall Coal Extraction

As discussed in Section 2.1.3, since coal serves as a source and storage rock for gas, its extraction process is inevitably associated with gas release and migration. Being extensively fractured and exposed to ventilation pressure, coal extracted by a shearer loses a high proportion of its in-situ gas in a relatively short time, which can be a direct source of longwall gas emission.

Furthermore, coal extraction at a longwall face can disturb surrounding coal seams and stimulate gas desorption. A longwall at near atmospheric pressure can be viewed as a ‘horizontal well’. Significant pressure drawdown can be expected around the low pressure sink created by the face, the gateroads and parts of the goaf area. Driven by the declining pore pressure, the originally adsorbed gas starts to desorb from the surrounding coal seams and migrate towards the low pressure sink. This gas migration provides the remaining share of total gas emissions at a longwall face.

The progressive advance of a longwall face and the response of surrounding strata to mining disturbances are a continuous and dynamic process. This suggests that, with the advance of a longwall face, the pressure sink and mining disturbed zone moves and extends simultaneously with the face. Consequently, gas will be continuously emitted from newly disturbed coal along with face the advance. Therefore, the amount of gas that is released during longwall mining is highly dependent on coal production rate and how much surrounding coal is being disturbed.

3.3.2 Stress Distribution around Conventional Mechanised Longwall Faces

Stress regimes around a longwall coal face evolve with progressive face advance. During the process of coal extraction, the initial stress equilibrium breaks down and readjusts to establish a new equilibrium, which has zones with both increased and reduced stress regimes. The increased stress zone, also referred to as the abutment stress zone, normally occurs ahead of a face-line and its magnitude is related to mining height and in-situ stress conditions (Whittaker, 1974). A vertical stress profile along the direction of face advance at the mining horizon is plotted in Figure 3.3, where the stress distribution around a face is depicted.

In response to coal extraction, three distinct zones in the overlying strata can be identified according to the degree of rock deformation and fracturing, namely the caved zone, the fractured zone and the continuous deformation zone (Peng and Chiang, 1984; Hasenfus *et al*., 1988; Whittaker and Reddish, 1989; Yavuz, 2004). After coal extraction, the overlying roof layers break into irregular shapes and various sizes, fall down, and backfill the space created by previous mining. This highly fractured zone is called the caved zone. Above the caved zone is the fractured zone which is defined by rock blocks, vertical fractures and horizontal fractures caused by bedding layer separations. From the top of the fractured zone to the surface is called the continuous deformation zone, in which major fractures hardly propagate. In addition, the stress state of the underlying strata is also affected, though to a lesser degree and extent, by longwall mining.

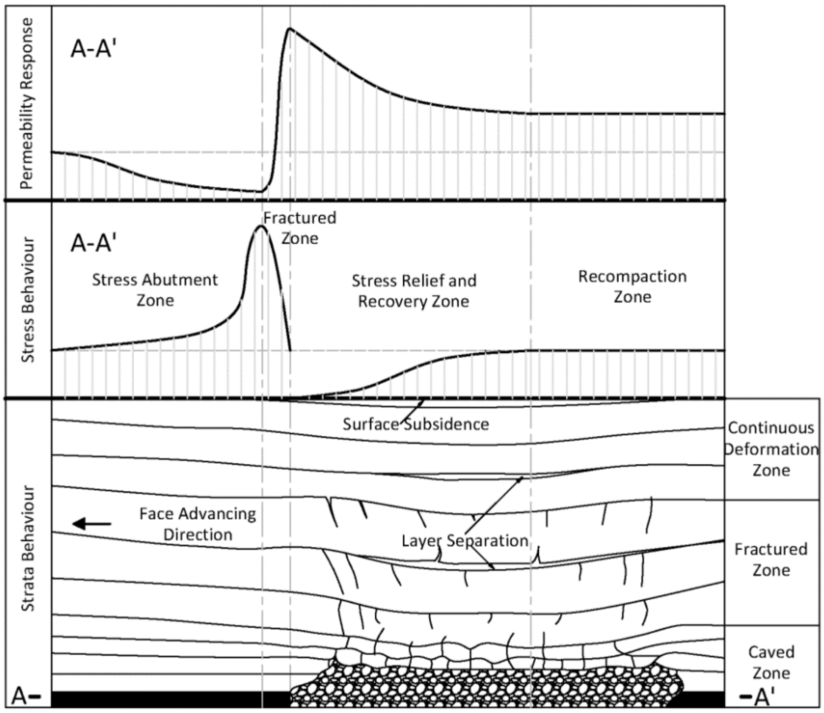

Figure 3.3: Longitudinal section of an advancing longwall coal face: strata stress and permeability behaviour around longwall workings (complied after Whittaker, 1974 and McPherson, 1975).

Through field drilling tests, Palchik (2002; 2003) concluded that the height of the caved zone might reach 4.1~11.25 times the height of extracted coal; and the fractured zone might vary greatly from 19 to 92 times the thickness of the mined seams. The development of the fractured zone is highly dependent on the properties of overlying strata. Kelly *et al.* (2002) conducted an assessment to study the longwall stress and near-face fractures in Australian coal mines using integrated tools, which include microseismic monitoring, numerical stress and deformation modelling, and underground piezometer and extensometer monitoring. They suggested that the complex strata stresses induced by mining required a multi-path programme to gain as much information as possible from different approaches. Unfortunately, integrating various measurement sources to achieve a comprehensive understanding about mining problems has been rarely attempted.

3.3.3 Permeability Distribution around Conventional Mechanised Longwall Faces

Recognising the impact of stress on coal permeability, McPherson (1975) was one of the early researchers who considered dynamic changes in permeability of worked seam in responses to longwall coal extraction (Figure 3.3). As shown in Figure 3.3, the coal in the front abutment zone is tri-axially compressed. Although micro-fractures can be generated in this zone, permeability may not experience an increase as the high confining stress. In the fractured zone, the vertical stress reaches a peak, whereas the horizontal stress presents a dramatic reduction as the confinement on the coal is removed due to production at coal faces. Thus, this high deviatoric stress opens the micro-fractures and contributes to the enhancement of permeability. The stress in the stress relief zone is relatively complex and low in magnitude, fractures are well propagated and connected, and the adjacent rocks are much more stable than the previous two zones. All of these factors considerably further increase permeability in the stress relief zone. In the recompaction zone, stress starts to recover to in-situ stress gradually, and the permeability of fractured rocks starts to decrease but still higher than the in-situ value.

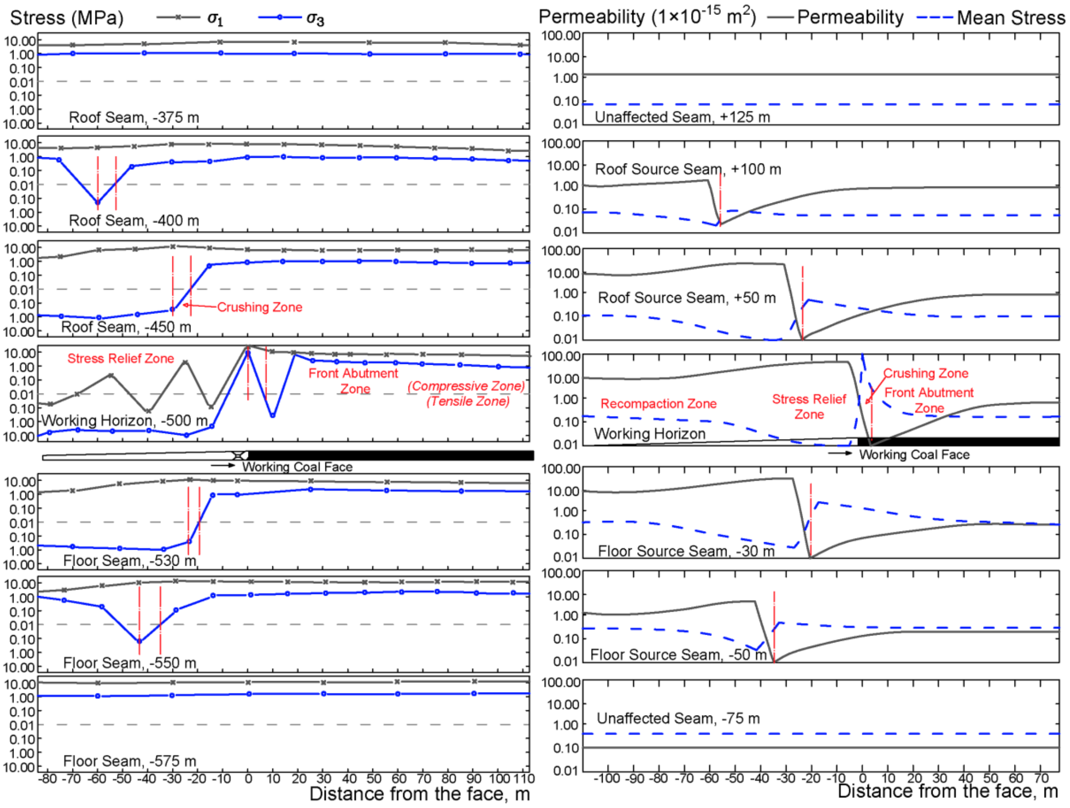

(a) (b)

Figure 3.4: (a) Numerically simulated maximum and minimum principal stresses, and (b) mean stress and permeability profiles around a 500m deep longwall face (after Durucan, 1981).

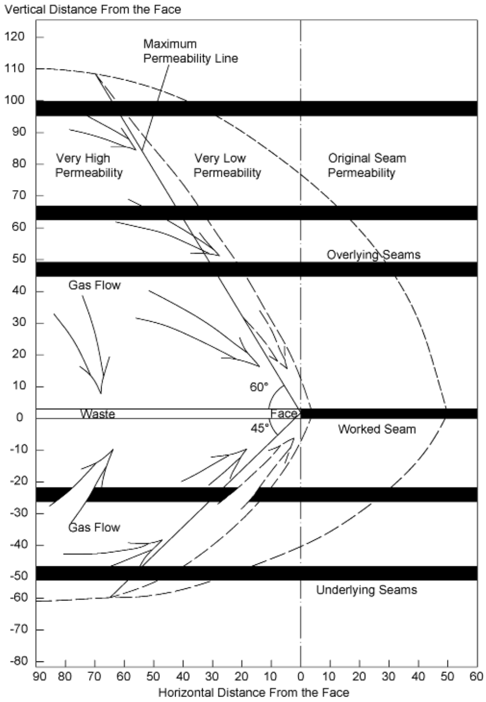

Figure 3.5: Different permeability zones and suggested flow paths of methane around an advancing longwall face (after Durucan, 1981).

Later, based on his laboratory investigations into stress-permeability relationship of coals and numerical modelling of stresses around working longwall faces, Durucan (1981) derived models for permeability distribution and associated gas flow around an advancing longwall coal face (see Figure 3.4). He suggested that coal seams within 100 m above and 50 m below the coal seam being-mined are the main gas sources after stress relief and permeability increase. Based on these observations, Durucan (1981) proposed a gas emission zone and flow paths for gas migration as illustrated in Figure 3.5 above.

3.3.4 Theory of Gas Emission around Conventional Mechanised Longwall Faces

The early approaches to predicting gas emissions around working longwall panels in Europe were mostly empirical and adopted the same basic principle of *degree of gas emission* function (Curl, 1978). Research carried out by the Mining Research and Development Establishment (MRDE) in the UK during the 1970's and 80's developed a methane prediction method which was unique in Europe, such that time dependent behaviour of gas emission was introduced to the predictions. The method is based on Airey's theory of gas emission from broken coal, which was later extended to include fractured or fragmented coal seams around a working longwall face (Airey 1968; 1971). The rate of gas release from the coal blocks was assumed be determined entirely by the emission characteristics of the broken coal, represented by a variable time constant t_1 (s) defined as a function of distance from the face (Airey, 1971) as,

$$t_1 = t_o \exp\left(\frac{x}{x_o}\right), \; x \geq 0 \tag{3.1}$$

where x (m) represents the distance ahead of the position of the maximum stress (front abutment), x_o (m) is a distance constant and t_o (s) is the minimum time constant in hours, which occurs at and behind the front abutment position. Therefore, smaller the value of t_1, larger the gas emission rate from the relatively smaller blocks of coal nearer to the working coal face. From a subsequent theoretical work in rock mechanics, Airey used the ratio of principal stresses σ_1/σ_3 as a criterion for coal failure around a longwall face and assumed that surfaces of equal σ_1/σ_3 would be coincident with the surfaces of equal t_1 (MRDE, 1980), thus providing the theoretical basis to his *degree of gas emission* surfaces. Using analytical solutions for the stresses around a coal face given by Berry and Sales (1967), Airey then computed the distribution of time constants around a coal face, and hence the degree of gas emission from sources seams in the roof and floor as a function of distance from the face line. As well as accounting for the emission from the roof and floor source seams, Airey proposed gas emission curves for the seam being mined, based on the weekly advance rate, and the coal being transported out of the district on the conveyor in order to calculate the total gas volume entering the longwall district.

These methods were progressively fine-tuned using extensive field observations. Airey's theory and the accuracy of his degree of gas emission curves were validated through field measurements of gas quantities and residual gas contents of coal seams at a large number of UK collieries. Based on these validation studies carried out over a period several years the gas emission curves were modified to eliminate the observed over- and underestimates and produced the *British Coal Firedamp Prediction Method* as it is known today.

Later, another function (Equation 3.2) to link gas emissions with coal production in high productive longwall faces was proposed by Lunarzewski (1998). Where q (m^3/t) is the gas emission rate, CP (t/day) is the coal production per day, and a and b are empirical coefficients related to coal production levels and the number of working days per week.

$$q = a\sqrt{CP} + b \qquad 3.2$$

By considering gassy coal seams in both floor and roof, total amount of gas emission per tonne of mined coal into a seam being-mined (Q, m^3/t) can be estimated by (Lunarzewski, 1998):

$$Q = Q_m + \sum \frac{GC_f \times DC_f \times TA_f}{TM} + \sum \frac{GC_r \times DC_r \times TA_r}{TM} \qquad 3.3$$

where, Q_m (m^3/t) is the volume of gas release from the coal seam being-mined with respect to per tonne extraction, GC (m^3/t) is the gas content in the floor (f) and roof (r) coals, DC (fraction) is the degassing coefficient for (f) and (r), TA (m) is the thickness of the gassy strata in (f) and (r), and TM (m) is the thickness of the coal seam being-mined.

Karacan and Goodman (2011) developed a probabilistic approach to define gas emission zones in specific sites. Gas flow percentage, gas content, and displacement as a function of distance from a mined seam were determined by deriving bivariate normal distributions from a series of borehole experiments.

An interesting attempt at using an artificial neural network (ANN)-based methodology to predict gas emissions in ventilation airflow from longwall faces was achieved by Karacan (2008). By establishing a database including ventilation emission data, coalbed properties, geographical information, and longwall operation parameters in a wide range of coal mines in the US, ANN models gave high accuracy in predicting gas emissions in the ventilation systems of US longwall faces. Later, by employing this ANN model together with other statistical and mathematical predication approaches (Karacan, 2009a, b, c), a software suite (Methane Control and Prediction) was developed to predict gas emissions from longwall faces (Dougherty and Karacan, 2011). However, these methodologies cannot reflect the actual physics involved in the gas emission process and require a database pool for model training.

3.3.5 Modelling of Longwall Geomechanics and Associated Gas Emissions

Researchers at Nottingham University have contributed greatly to the early-stage development of gas flow modelling around longwall faces (Keen, 1977; O'Shaughnessy, 1980; Ediz, 1991). Keen (1977) was the first to develop transient solutions for methane flow in longwall mining using the finite difference method. Later, O'Shaughnessy (1980) used finite element method instead to investigate gas flow around a longwall workings. Their models were only suitable for single-porosity media and the time-dependent gas transport from micropores to macropores was not considered. Ediz (1991) further developed a finite element approach, which could account for the time-dependent behaviour of desorption and diffusion for methane flow simulation in longwall faces. However, in most of these early studies, the mechanical impact of coal extraction on gas flow was neglected or over simplified.

It is widely recognised that coupled simulation is necessary in order to capture the interactive physics between mining geomechanics and gas flow (Ren and Edwards, 2000; Esterhuizen and Karacan, 2005; Whittles *et al.* 2006; Guo et al., 2012). Four types of coupling methods are available and listed according to the level of coupling tightness as follows: pseudo coupling, one-way coupling, two-way coupling, and full coupling. In pseudo coupling, geomechanical responses have been incorporated into a fluid simulator through empirical relationships, analytical functions or simple lookup tables (Beattie *et al.*, 1991). One-way coupling only transfers coupling information from one simulator to another and no feedback is considered (Minkoff *et al.*, 1999). Two-way coupling is an upgraded version of one-way coupling, whereby geomechanical equations and fluid flow equations are solved separately and sequentially in different simulators. Solutions are iteratively exchanged between different simulators in two-way coupling (Longuemare *et al.*, 2002; Tran *et al.*, 2005; Gu and Chalaturnyk, 2010). Full coupling, which has internal consistency for solving geomechanical and flow equations simultaneously, may provide the most accurate solutions, but it is also the most complex method and requires the largest computational time (Osorio *et al.*, 1998; Chin *et al.*, 2000). Since one-way and two-way coupling can benefit from the latest developments in both geomechanical simulators and fluid simulators, they have gained the most popularity in solving problems that require coupled modelling.

Ren and Edwards (2000) developed a pseudo coupling approach by using Computational Fluid Dynamics (CFD) to model three-dimensional methane flow. In their model, permeability was used as the linkage between mining stress and gas flow. Permeability values ranging from 10^{-14} to 10^{-8} m^2 were assigned to different regions in the flow model based on well-established knowledge on mining stress distributions and permeability responses to stress changes (Figure 3.6).

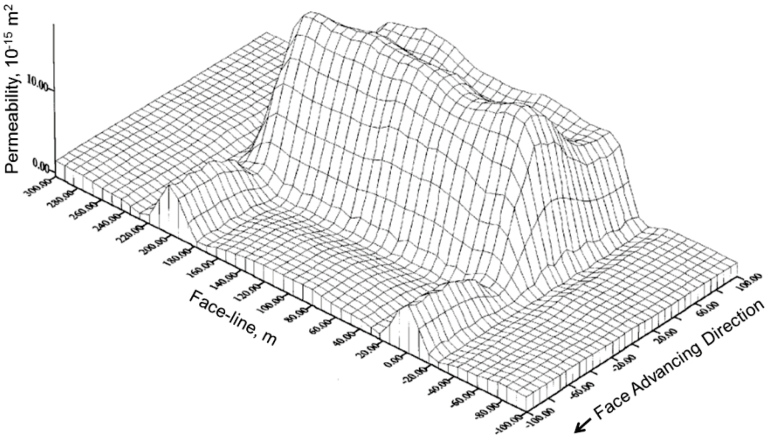

Figure 3.6: Three-dimensional view of permeability variations at the level above a working face (after Ren and Edwards, 2000).

Whittles *et al.* (2006) presented a methodology to derive permeability changes in coal measure rocks from the results of geomechanical modelling of a longwall face for fluid flow simulation. A 3D model was first developed in $FLAC^{3D}$ to identify the positions of three cross-sections with different degrees of compaction. Then three 2D models corresponding to the identified positions were developed in the fluid module of $FLAC^{2D}$ to characterise the likely gas sources and gas flow paths into the longwall face. The input permeability for the 2D models was inferred from the stress conditions obtained from geomechanical modelling. Note that only a steady coal face at a certain position was modelled, and stress and permeability updating with respect to dynamic face advance was not considered.

A one-way coupling approach was developed by Esterhuizen and Karacan (2005) to investigate gas migration from surrounding rocks towards longwall faces. In their models, a geomechanical simulator was used to simulate the continuous advance of a longwall face and provide dynamic permeabilities for the gas emission modelling in a reservoir simulator. The advance of a longwall face was modelled as a moving boundary problem and restart models were run sequentially representing different mining steps and corresponding strata responses.

Guo *et al.* (2012) presented a comprehensive study regarding stress changes, fractures, and gas flow patterns in the mining of multi-seams separated by coal measure rocks. To understand the effect of mining on surrounding rock and gas flow, displacements at overburden strata, stress and pressure changes were monitored at a study panel in Huainan Coal Mine Group, China. Numerical modelling was conducted with an in-house code to obtain a full-scale understanding about the mining-induced stress changes and corresponding permeability responses. Permeability distribution was later used as the input for gas migration modelling in a CFD code. From this one-way coupling approach, the authors found that there is a three-dimensional annular-shaped overlying zone along the perimeter of the longwall panel (Figure 3.7:), which can be used to maximise gas drainage performance.

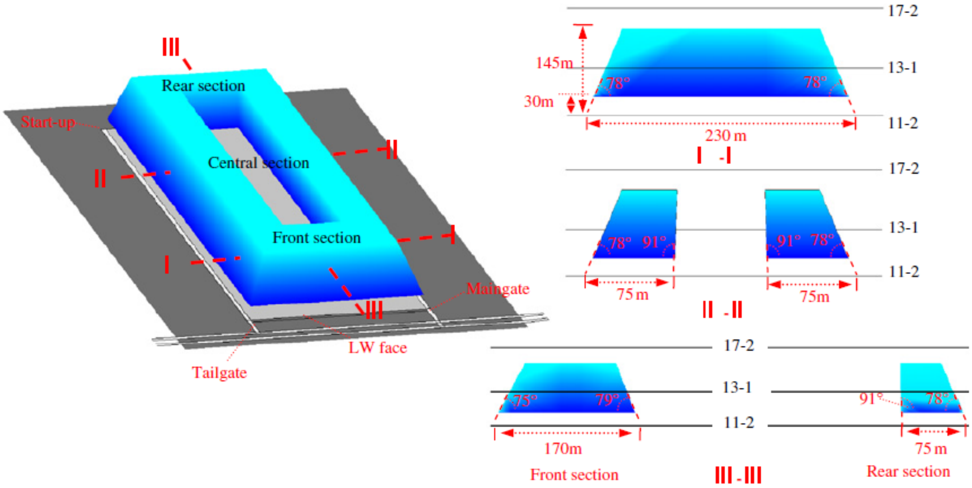

Figure 3.7: Three-dimensional zone of optimum gas drainage in the overburden strata of a conventional mechanised longwall panel (after Guo *et al.*, 2012).

Although significant improvements have been made in modelling gas flow around longwall coal faces by applying a one-way coupled approach, this coupling methodology does not provide feedback from the output of the flow simulator back to the geomechanical simulator to update the pore pressure distribution for computing the changes in the effective stresses. On the other hand, experience in coalbed methane industry suggests that two-way coupled modelling between geomechanics and fluid flow can improve the model predictions significantly (Shi and Durucan, 2005; Connell, 2009; Gu and Chalaturnyk, 2010). It is believed that, in the case of coal mine methane flow predictions, this missing link may incorrectly estimate the dynamic permeability, especially where significant changes in the pore pressure are expected in the fractured zone around a producing longwall face.

3.4 Previous Research into Longwall Top Coal Caving in Thick Seam Mining

Although extensive research has been carried out on gas emissions from longwall panels operated in relatively thin coal seams, only a relatively few studies have been reported on multi-level or LTCC operations. The gas emission hazards, together with spontaneous combustion and top-coal recovery, are referred to as the top three challenges that impede LTCC production (Wang *et al.*, 2014).

The distinctly different mining layouts and processes of LTCC generate different responses of strata stresses and gas dynamics in thick seams. Abutment stress ahead of a LTCC face is reported to be able to cover a larger area with a higher peak than conventional mechanised longwall faces (Xie *et al*., 2011). This means that LTCC mining disturbance can propagate into a larger area with acute permeability changes. Given that an LTCC face is normally operated under mostly or completely coal surroundings, a larger mining disturbance area may result in more coal contributing to gas emissions at the face. In addition, the increased coal production brings about the issue of heightened gas emissions released by extracting or caving coal at a LTCC face. Therefore, LTCC is expected to further exacerbate the gas emission problems often faced in longwall mining.

Cheng *et al.* (2003) reported that, compared with the conventional mechanised longwall mining, using LTCC had significantly increased gas emission rate in Yangquan Coal Group in China. They believed that over 90% of gas emissions were from the overlying adjacent strata. They also introduced the method of developing high-level strike or mid-level drainage roadways above or below the panels to reduce LTCC gas emissions. Later, the application of this method at a LTCC panel with increased width was reported by Xu *et al.* (2007). Although this method was reported to be able to maintain gas emissions below the statutory limits, the development of extra roadways in rock would significantly increase production costs.

Yasitli and Unver (2005) developed an approach to numerically reproduce the process of LTCC. The finite difference code FLAC^{3D} was applied into simulate LTCC operation at the Ömerler underground coal mine in Turkey. They suggested that uniformly fractured top coal could decrease dilution and increase recovery ratio. Later, they applied this modelling approach to study the strata movement induced by LTCC in thick seam coal mining (Unver and Yasitli, 2006). In addition, pre-fracture blasting as a method to generate uniform fractures was numerically assessed in their studies.

Through numerical and experimental studies, Xie *et al.* (2006) found that there was a stress shell arching between the virgin coal ahead of the face and goaf rubbles behind the face. This stress shell acted as a primary support, bearing and diverting the loads of the overlying strata. The authors also stated that since LTCC faces operated under the protection of this stress shell, stress loads on the shields of LTCC faces were generally lower than conventional mechanised longwall faces, which was also consistent with their field observations.

Xie and Zhao (2009) applied the discrete element method to model the caving process of LTCC. In order to improve the recovery rate, a novel technique was introduced, whereby vibration devices on the beams of shields were employed. The performance of this technique was numerically assessed by a 2D model. It has been found that the employment of vibration devices can effectively break the arching structure which is formed in LTCC and generate a uniform size of fractured top coal.

Based on the analysis of in-situ geological, geometrical and geotechnical conditions, Alehossein and Poulsen (2010) proposed a yield and cavability criterion to assess the productivity of a LTCC face. Similarly, a cavability assessment system was developed by Vakili and Hebblewhite (2010), and major parameters that can affect the cavability of a LTCC were also discussed.

In particular, the top coal caving process at Coal Mine Velenje was analysed by Likar *et al*. (2006) through laboratory physical, analytical and numerical models. A 3D numerical model was developed based on the actual geological condition at the mine. It was found that, if the height of extracted coal by a shearer is 4 m, the height of caving coal can range from 6 to 8 m. Through compression tests on crushed clay and coal, Jeromel *et al*. (2010) suggested that the mixture of clay and coal material at goaf could reach 98% of its maximum deformation immediately after reloading. Stress distribution around a LTCC face was simulated using the geomechanical code FLAC^{3D}, and have shown that the results compared reasonably well with stress monitoring data from the face (Jeromel *et al*., 2010). More recently, dynamic stress response of the coal seam to coal production at different levels of the coal seam was monitored and compared with the numerical modelling results (Likar *et al*., 2012).

Compared with conventional mechanised longwall mining, the fracturing and de-stressing of the floor coal during the extraction of a multi-level LTCC face may be more critical in evaluating its gas emission behaviour. Therefore, the stress and gas pressure regimes resulting from previous coal extraction in the upper levels of a multi-level LTCC operation need to be understood well. Furthermore, potential cavities and coal left in the upper levels of a multi-level operation may act as an additional gas emission source during top coal caving stage of a LTCC face.

3.5 Uncontrolled Gas Emissions/Gas Outbursts

3.5.1 Definition and Background

Gas outbursts, which are also referred to as uncontrolled gas emissions, pose a serious threat to the safety of underground coal mining throughout the world. As the understanding of the structural conditions and mechanisms leading to gas outbursts improve, more effective preventative measures are being developed and implemented. However, gas outbursts in coal mining still occur in both thin and thick seam mining.

Since the first documented coal and gas outburst occurred in the Issac Colliery in France (1843), as many as 30,000 outbursts have occurred in the world coal mining industry (Lama and Bodziony, 1998). An outburst can be defined as spontaneous and violent ejection of gas from a solid coal surface. Depending on the seam gas composition, the ejected gas can sometimes be a mixture of methane and carbon dioxide, and normally one component predominates (Beamish and Crosdale, 1998). For some powerful outbursts, the ejection of gas is normally accompanied by a considerable volume of failed coal. During the process of an outburst, a sudden state change of the rock-coal-gas system from static to dynamic occurs along with the release of a significant volume of gas over the duration (Choi and Wold, 2004b). It has been reported that the ejected coal and released gas can be as much as several hundred tonnes and thousand cubic meters in some catastrophic outbursts (Lama and Bodziony, 1998).

Farmer and Pooley (1967) suggested that outbursts only occur in districts subject to severe tectonic movement, hence their association in many places with depositional structures such as folds, faults, rolls and slips and in particular with rapid fluctuations in the seam thickness. Hargraves and Upfold (1985) have also concluded that microstructurally altered coal will lead to higher outburst tendency. Thresholds of 9 m^3/tonne for CH_4 and 6 m^3/tonne for CO_2 have been used in the Sydney Basin, Australia, to indicate outburst prone conditions (Beamish and Crosdale, 1998). In China, 10 m^3/tonne methane is used as the outburst threshold and the gas contents in the mines experiencing outbursts are higher than 10 m^3/ton, and generally range from 15 to 25 m^3/tonne coal (Cao *et al.*, 2001).

It is suggested that outburst-prone coal exhibits low permeability. Lama and Bodziony (1998) found that coal seams with in situ permeability >5 mD are not liable to outburst. Other studies (Hargraves, 1993; Shepherd, 1995) have concluded that stress is an additional contributing factor to outbursts. Kidybinski (1980) took into consideration the gas content and flow, stress, and coal failure to explain his theory of gas outbursts. Williams and Weissmann (1995) referred to the outbursts frequently encountered Australian conditions and stated that ‘‘the most important parameter is gas desorption rate, in conjunction with the gas pressure gradient ahead of the face”.

Over last 150 years of research on outbursts, two main theories, the gas pocket theory and the dynamic theory, have been proposed and evolved based on countless field observations and gradually established knowledge (Shepherd *et al.*, 1981; Singh, 1984; Lu *et al.*, 2011). As suggested by Choi and Wold (2001), the initiation of an outburst may be either dominated by geological factors or mining induced factors. In the gas pocket theory, outbursts are assumed to be dominated by geological structures. These geological structures are denoted by a large amount of soft or crushed coal, sometimes even coal powder, with high gas content enclosed by less fractured and low permeability coal. When mine openings advance close enough to this type of geological structure, this is considered to be a potential risk of outburst. An outburst induced by a gas pocket in Pingdingshan Coal field, China, is illustrated in Figure 3.8. A more detailed explanation on such structures will be presented in Chapter 7.

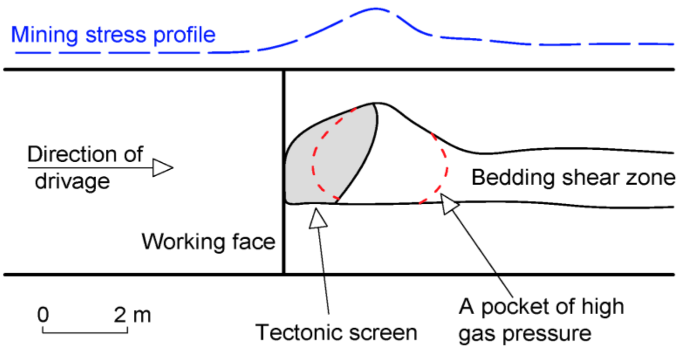

Figure 3.8: Illustration of an outburst induced by the gas pocket structure in Pingdingshan Coal field, China (after Li, 2001).

Compared with the gas pocket theory, mining effects overtake the importance of geological structures in the dynamic theory. The importance of mining-induced fractures adjacent to advancing faces has been emphasised: gas originally adsorbed in either solid or crushed coal can be rapidly released during mining-induced intensive failure. For example, as documented in the UK, the difficulties in fracturing relatively less permeable or impermeable floor strata might result in gas accumulation beneath the mining level and subsequent rapid release after fractures reoccurred at these strata (Shepherd *et al.*, 1981).

3.5.2 Modelling of Gas Outbursts

Due to the difficulties in accessing first-hand field data of the initiation and development of an outburst, replicating the evolution of an outburst numerically may be the best approach to understand this violent mining hazard. Paterson (1986) first developed an outburst model to explain field observations associated with outbursts in which gas flow, stress, and failure in coal seams were simulated. His modelling results suggested that an outburst is the structural failure of coal triggered by gas pressure gradients. To prevent outbursts, gas pressure gradient in advance of mine openings should be maintained below a certain threshold by degasification techniques.

On the basis of a series of research projects investigating gas outbursts carried out by CSIRO in Australia, coupled geomechanical-fluid models with the ability of modelling dual-porosity coal and multi-component gas flow have been developed to study outburst initiation (Choi and Wold, 2001). Stress-dependent permeability, large strain deformation, and gas and water two-phase flow in coal can also be considered by that model. Later on, in their upgraded models, the post-initiation of outbursts, including coal fragmentation and particle flow was incorporated (Choi and Wold, 2004a, b). The importance of coal strength was emphasised: the increase of coal strength can reduce the size of fragments that will be ejected and an outburst can be subdued if the coal strength is high enough.

Xu *et al.* (2006) developed a coupled gas flow and solid deformation numerical model to simulate the evolution of fractures in coal during an outburst. Four stages of an outburst are characterised in their models, which are stress concentration, coal/rock fracturing and splitting, crack propagation, and the ejection of coal (see Figure 3.9). The authors believed that in-situ stress, gas pressure, and the properties of coal and rock are the primary factors that contribute to the occurrence of coal and gas outbursts.

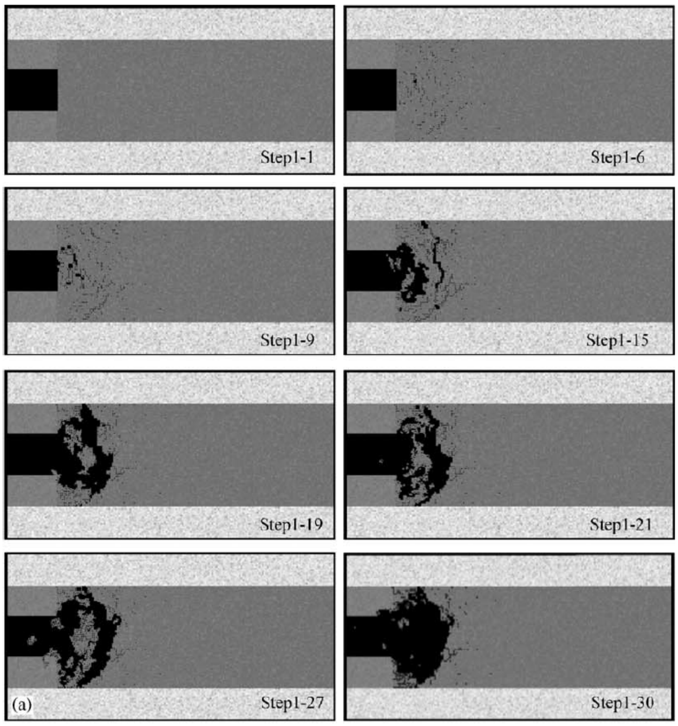

Figure 3.9: Simulation results of an instantaneous coal and gas outburst induced by the creation of a mine opening (after Xu *et al.*, 2006).

Using an integrated field, laboratory and numerical modelling approach, Wold *et al.* (2008) described the potential of applying stochastic coal strength and permeability data into outburst risk assessments. Reservoir heterogeneities including permeability, stress, and coal strength were repeatedly measured from both field and laboratory to obtain sufficient data for statistical descriptions of these properties. These statistical descriptions were formulated to generate realisations for outburst risk analysis and assessment. This provides a new approach for outburst risk assessment, but also requires abundant field work to generate reliable and robust statistical distributions.

By linking and sequentially executing a geomechanical stress analysis code FLAC^{3D} and a reservoir simulator COMET3, Xue *et al.* (2011) developed a coupling approach to model the initiation of an outburst. A simple two dimensional roadway development model was used to test the capability of the coupling approach. Since the FLAC^{3D} code is based on continuum media, coal fracturing and fragmentation was not considered in the model.

The abovementioned outburst modelling techniques have set very good examples of numerically reproducing the process of an outburst, including its initiation and post-initiation. However, most of these investigations focused on the development of modelling techniques, and only a few of them applied outburst modelling to actual geological settings and explained outburst cases that took place. Although the gas pocket theory and dynamic theory have been widely documented in most coal producing countries (Farmer and Pooley, 1967; Shepherd *et al.*, 1981; Singh, 1984; Guan *et al.*, 2009), outburst models tailored to reproduce these two most common outburst patterns are surprisingly rare.

In addition, stress evolution induced by mining activities, such as face advance or roadway development, as the trigger of an outburst was not simulated or over-simplified in previous studies. Furthermore, the criterion of quantifying an outburst element has not been clearly defined in these studies.

3.6 Gas Emission Control Techniques

3.6.1 Stress Relief Mining

One of the precautions used in outburst protection is “Stress Relief Mining” or “Protective Mining”. This method emphasises utilising redistributed stress and fracture fields induced by mining. A less gassy seam referred to as the “Protection Seam” is mined super or sub adjacent to a gassy coal seam called the “Protected Seam”. The principal aim of protective mining is to release the gas trapped at high pressure protected seams by reducing the stress distributed on them. As the protection seam is mined, open fractures and enhanced permeability allow gas to be released from the protected seam (Figure 3.10).

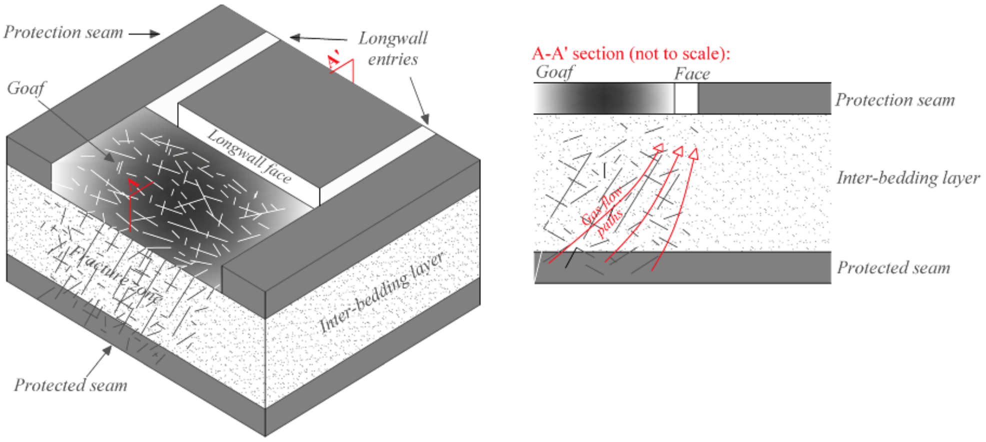

Figure 3.10: Schematic of protective mining applied in multi-seams.

Ideally, gas emissions from protected seams can be diluted and transported by the ventilation system in the protection seam. However, in order to capture and utilise coal seam gas, gas drainage in conjunction with stress relief mining may be a better solution. Boreholes can be drilled into the de-stressed areas with enhanced permeability and desorbed gas, where gas drainage performance can be maximised.

3.6.2 Gas Drainage through Underground Boreholes

Gas drainage through underground boreholes is an essential part to tackle high gas emissions from coal seams disturbed by mining when ventilation cannot maintain gas levels within statutory limits. Two types of underground boreholes, horizontal boreholes and inclined boreholes are normally used to capture as much gas as possible before it migrates into ventilation airways. In the mining of thin seams, horizontal boreholes are normally known as inseam boreholes to capture gas emissions from the seams being-mined and inclined boreholes, also referred to as cross-measure boreholes, are used to capture gas emissions from adjacent seams (Figure 3.11). Since thick seams are the main subject of this thesis, the terminology ‘horizontal’ and ‘inclined’ are used instead of ‘inseam’ and ‘cross-measure’ in order to avoid confusion.

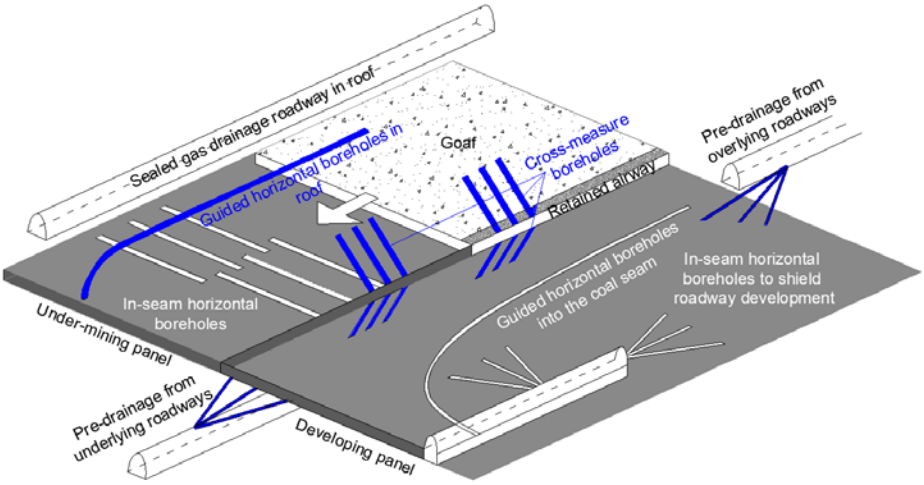

Figure 3.11: Various gas drainage techniques used for the extraction of coal seam gas.

Horizontal boreholes drilled into the intact coal of mined seams are normally used to reduce in-situ gas content prior to mining activities. The applicability of this method, however, is highly dependent on the natural permeability of coal seams. Measures such as hydraulic fracturing or blasting can be used to increase in-situ coal permeability (Lu *et al.*, 2011), but with largely increased working load and cost. Note that horizontal boreholes may also be stimulated by the approaching longwall faces but for a relatively short period before they are intercepted. Although this period of gas drainage during mining is short, it is important for low permeability seams as well as in the cases that pre-mining drainage has limited duration (Karacan *et al.*, 2007a).

Inclined boreholes have a big advantage over horizontal boreholes as they can produce for a longer period and utilise mining-induced permeability enhancement zones without being intercepted. Same as in stress relief mining, adjacent coal seams are expected to experience significant increase in permeability, which can stimulate gas drainage performance in inclined boreholes.

Although utilising mining-induced permeability enhancement zones to increase gas drainage performance has been practised in many coal mines, their application was mostly based on engineering experience. Furthermore, in thick or ultra-thick seam mining, this technique has seldom been trialled.

3.6.3 Numerical Modelling of Gas Drainage Techniques

Borehole gas drainage as the most cost-effective approach to control underground gas emissions has been an important area of research for decades. As this technique shares many common features with reservoir engineering in the coalbed methane industry, literature from this industry can also be referred to and learnt from. The transient behaviour of water and gas flow through dual-porosity coal seams into a vertical well was mathematically and numerically described by King *et al.* (1986). Remner *et al.* (1986) conducted a parametric study to investigate the effects of coal seam properties on gas drainage efficiency. Parameters including absolute permeability, sorption time, relative permeability curves, and well spacing were numerically assessed. Later, a numerical approach to simulate gas drainage from coal seams was proposed by Spencer *et al.* (1987) in which the dual-porosity characteristic of coal, gas desorption process, and pressure dependent porosity and permeability were considered. Ertekin *et al.* (1988) investigated the production performance of horizontal drainage wells for the degasification of coal seams by developing a two-phase coal seam degasification model. Although the primary motivation of these investigations were recovering and utilising methane from coal seams, and not the safety considerations, experience from these studies can be transferred to mining engineering.

The most significant difference between gas drainage in coal mining and reservoir engineering is the presence of dramatic stress changes induced by mining activities. Stress changes and associated fracturing of coal and the coal measure rocks may largely alter in-situ permeability, which may consequently have a significant impact on gas drainage performance. On the basis of established coupling approaches of geomechanics and fluid flow simulators, drainage functions can be simply modified and added in. Ren and Edwards (2002) incorporated their pseudo coupling approach with vertical well modelling to help the design of gas recovery wells in the goaf area of a longwall face. By coupling a geomechanical simulator and a reservoir simulator, Karacan *et al.* (2007b) assessed the performance of goaf wells in the Pittsburgh coal field and the impact of completion practices on optimising goaf gas production. Gas drainage performance from inseam horizontal boreholes with different borehole patterns, borehole lengths, and leading times were also evaluated by the same coupling approach (Karacan *et al*., 2007a). A screenshot of the model developed by Karacan *et al.* (2007a) is shown in Figure 3.12.

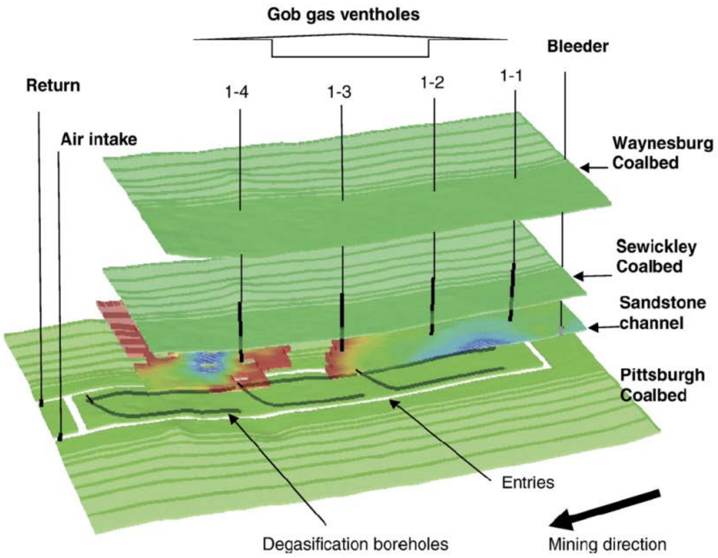

Figure 3.12: Gas drainage modelling with horizontal boreholes and goaf wells (after Karacan *et al*., 2007a).

Compared with horizontal boreholes and goaf wells, investigations regarding inclined boreholes are relatively limited. Whittles *et al.* (2007) developed a numerical model to predict the stability of gas drainage boreholes during the extraction of a longwall panel. The model was used to optimise roadway support systems and spacing between boreholes to achieve effective drainage. No gas flow modelling was carried out in that model.

In conclusion, it is clear from the literature that there is scope for further research on the performance of in-seam (both horizontal and floor) drainage boreholes placed in the zone affected by face advance during mining, particularly with respect to their application in the mining of thick and low permeability coal seams.

3.7 Summary

Continuous longwall extraction results in dynamic stress changes around underground openings. Recognising that coal seams are both the source and storage reservoirs for gases, the extraction of coal is inevitably associated with considerable gas emissions, and a potential hazard for mining operations. The migration of gases in the strata is driven by the pressure gradient created between the coal seams and near atmospheric pressure ventilation air stream, and largely dependent on permeability distribution around mine openings. Being sensitive to stress changes, permeability of coal and coal measure rocks near mine openings also change as mining progresses. A comprehensive understanding about stress changes, pressure regimes, and permeability responses around mine openings is necessary for the control of gas emissions induced by mining activities.

In thin seam mining, mining geomechanics and gas flow around mechanised conventional longwall panels are well understood after years of investigation. Hypotheses on stress and permeability redistributions around progressively advancing longwall faces are proposed and verified by extensive field observations. On the other hand, knowledge on stress, gas pressure and flow patterns around LTCC panels is relatively poor.

The phenomenon of uncontrolled gas emissions (or outbursts) as one of the most destructive mining hazards also requires research in thick and ultra-thick seam coal mining. An outburst is believed to be induced by the combined effect of mining stresses, coal/rock failure, and gas pressure gradient under certain geological conditions. A number of theories have been proposed to describe the mechanism of outburst occurrences and, among them, the gas pocket theory and the dynamic theory are the most accepted. The former emphasises the importance of geological structures while the latter places more weight on mining process as the precursor for an outbursts. Stress relief mining and gas drainage methods are normally applied in order to reduce in-situ gas content and the risk of outbursts. However, the use of geophysical techniques to help predict or warn against gas outbursts is yet to be explored.

One of the main objectives of this PhD research is to establish a thorough understanding of changes in stress, pressure regimes, and gas emission patterns around advancing LTCC faces. To achieve this, a suite of field measurements were carried out to capture geomechanical as well as fluid responses of a seam mined by LTCC at a coal mine. The next chapter will present a detailed description of these field measurements and data analysis at the study mine.

Chapter 4 Characterisation of Gas Dynamics around Longwall Top Coal Caving Panels

4.1 Introduction

This chapter describes field research carried out in order to establish a preliminary understanding of gas dynamics around an advancing LTCC face. A number of underground boreholes have been drilled and instrumented to monitor gas pressure and gas composition changes with respect to LTCC face advance at Coal Mine Velenje, the case study coal mine used in this research. Ventilation environment monitoring was also conducted to identify gas emission patterns induced by the LTCC production at the same panels. An integrated analysis of all the monitoring results has been carried out and a conceptual model for gas emission around multi-level LTCC panels has been developed. The data and experience gained through these analyses will be utilised in the numerical modelling work described in Chapter 6. Note that the teams at Coal Mine Velenje and Imperial College worked closely to design these experiments, which were performed by the mine. The author was mostly involved in the data analysis and interpretation of the results.

4.2 An Introduction to Coal Mine Velenje, Slovenia

4.2.1 Geology and Coal Lithotypes

Coal Mine Velenje, which is located in the North of Slovenia, has over one hundred forty years of mining history. The coal basin lies in a synclinal valley, which extends between the Šoštanj and Smrekovec faults (Figure 4.1). The Pliocene coal seam is overlain by a layer of clay and sand, which are followed by several younger rock layers. The sequence was caused by the subsidence of the area between faults and the simultaneous backfilling of continuous alluvial deposits (sand, silt, and marl). Figure 4.1 presents the main geological structure of the coal seam and surrounding rocks.

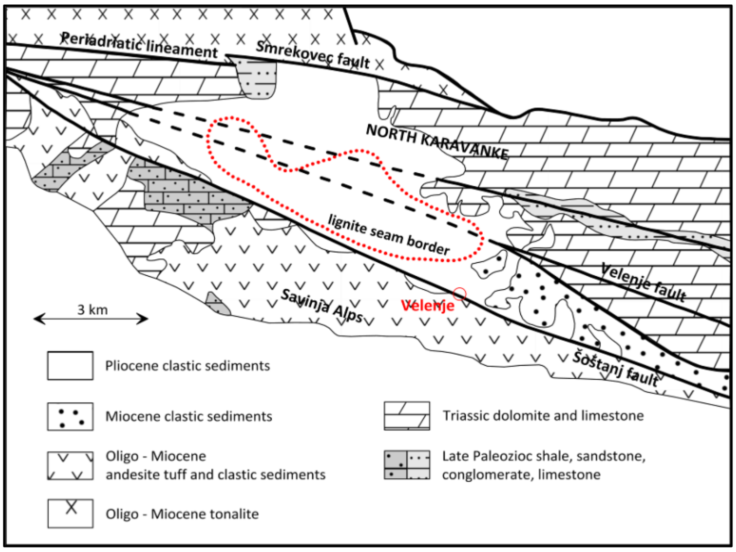

Figure 4.1: A plan view of the main geological structures of Velenje basin (after Brezigar, 1985/86).

Coal Mine Velenje currently mines a lens-shaped deposit, which is 165 m thick at the centre and pinches out towards the margins (Figure 4.2) (Markič and Sachsenhofer, 2010). The coal seam extends to a length of 8.3 km in the WNW-ESE direction and has a width between 1.5 and 2.5 km. The bedding planes are nearly horizontal or slightly inclined. Approximately four million tonnes of coal are currently produced per year from LTCC panels capable of yielding on average 8,000 tonnes of coal per day per panel.

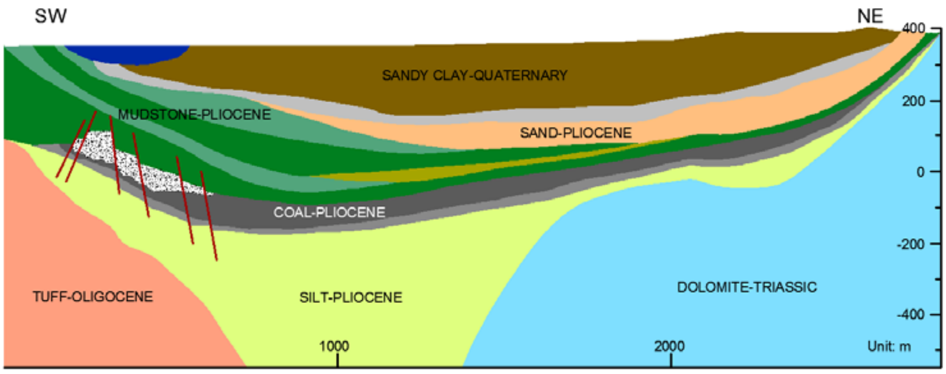

Figure 4.2: Schematic SW–NE trending geological cross-section of the Velenje coalfield (after Markič and Sachsenhofer, 2010).

(a) Detrite (D) fine lignite typically crushed and cracked due to drying

(b) Xylo-detrite (xD) composed of xylitic pieces smaller than the half of the core diameter

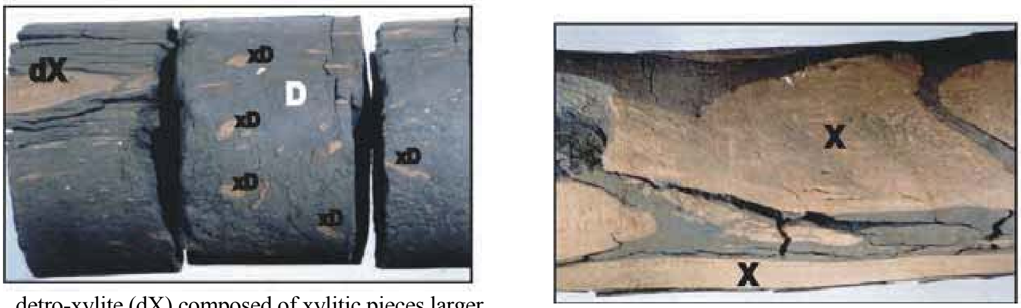

(c) detro-xylite (dX) composed of xylitic pieces larger than the half of the core diameter within the fine detrital matrix

(d) Xylite (X) as xylitic pieces larger than the core diameter

Figure 4.3: Lithotype components of the Velenje lignite as visible in horizontally drilled borehole cores (after Markič and Sachsenhofer, 2010).

The Velenje coal is a type of lignite, with varying abundance in xylite, fusinite, and mineral matter. Its matrix is fine-detrital, dark brownish in colour. Petrographic heterogeneity is further shown by different sizes, shapes, and orientations of xylitic fragments and by different degrees of gelification, which affects more severely the fine-detrital matrix. Figure 4.3 shows the lithotype components of the Velenje lignite as observed in borehole cores. The macerals and/or microlithotypes of the Velenje lignite are typical for the soft brown coals or lignites (Markič and Sachsenhofer, 2010).

Core samples taken from exploration boreholes suggested that the percentage of xylite and detrite might vary a lot even within a single borehole. It is worth noting that, depending on the ratio of xylite to detrite and the shape and spatial distribution of xylitic components, the Velenje lignite possesses different rock mechanical and reservoir properties with respect to gas content, sorption characteristics, permeability etc. This suggests that the coal deposit at Coal Mine Velenje is highly heterogeneous.

In terms of geomechanical strength, detrite is easily fractured once it loses moisture, and its unconfined compressive strength may range from 6 to 9 MPa. On the contrary, the xylite component in Velenje lignite shows a strong wooden structure and its unconfined compressive strength can be as much as twice of that for detrite. It may be expected that fracturing is more likely to be initiated preferentially and more intensively in a detrite-rich area than a xylite-rich area. Furthermore, it has also been established that the P-wave velocities measured in xylitic samples were up to 1.5 times that of detritic samples (Figure 4.4).

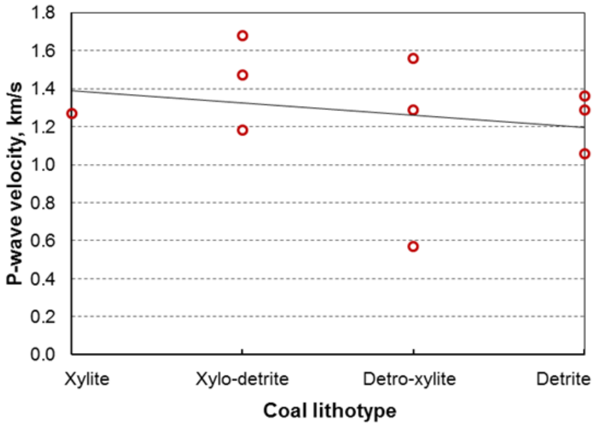

Figure 4.4: P-wave velocity for different coal lithotype at Coal Mine Velenje (lab measurement results provided to Coal Mine Velenje by the Graz University of Technology).

4.2.2 Velenje Mining Method

The so called “Velnje Mining Method” practised at Coal Mine Velenje in Slovenia is a combination of multi-level mining and longwall top coal caving, as illustrated in Figure 4.5. From the top to the bottom, the entire coal deposit is divided into a series of mining levels ranging from 10 to 20 m thick, mined in time-sequence with at least six months between the mining of each underlying longwall panel. At each level, the lower part of the seam (3 - 4 metres high) is cut by a shearer under the hydraulic supports while the upper section (7 - 17 metres) is allowed to cave.

Unlike most LTCC applications where the caved top coal is loaded from behind the hydraulic supports, the top coal is caved and recovered in front of the supports at Coal Mine Velenje. This is achieved by the use of shield supports with an extending canopy which allows up to 4 m face advance, through several cuts at the face, before the extending arm is collapsed and the top coal is caved. The caved coal is then cleared and transported by further cuts and advance of the longwall face. If the top coal to be caved is more than 10 m thick, or if the coal at the face is unstable, the length of face advance before top coal caving is less than 4 m. Through the implementation and continuous improvement of the technique at Coal Mine Velenje over the last several decades, the Velenje Mining Method has now been recognised worldwide as a standard mining method suitable for the exploitation of thick/ultra-thick coal seams (Unver and Yasitli, 2006). A more detailed account of the Velenje Mining Method can be found in Likar *et al*. (2012).

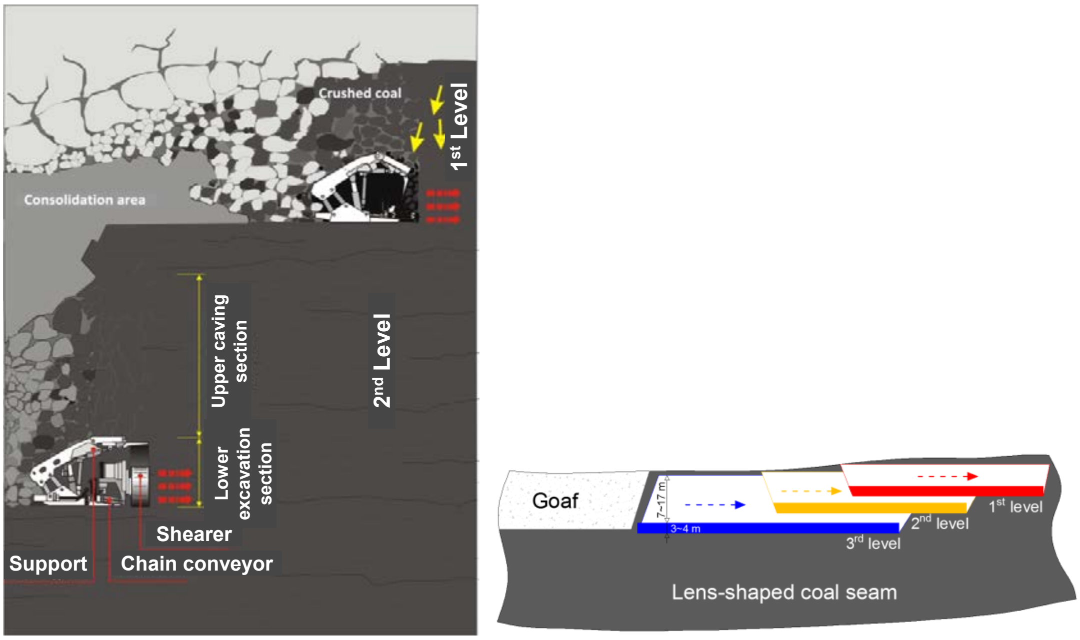

(a) (b)

Figure 4.5:(a) Schematic of the multi-level longwall top coal caving mining method implemented at the ultra-thick coal deposit of Coal Mine Velenje (after Jeromel *et al*., 2010), the yellow arrows indicate top coal caving direction; (b) schematic of the multi-level longwall layout.

Longwall and shaft monitoring data from the Velenje mine suggests that the coal mine emits 20 to 30 million m^3 methane and a similar volume of CO_2 to the atmosphere in its ventilation air each year. Due to the difficult mining conditions experienced and the application of novel thick seam mining methods it has so far not been possible to implement a gas drainage system at the mine.

4.2.3 Seam Gas Composition

Seam gas at Velenje is a mixture of CO_2 and CH_4. As reported by the mine, the gas mixture in coal varies from 98% CO_2 - 2% CH_4 to 0% CO_2 - 100% CH_4 throughout the mine. The distribution, composition and the origin of mine gases at Velenje Basin have been studied extensively and reported in detail by Lazar *et al.* (2014), however, CH_4 and/or CO_2 sorption characteristics, in situ gas pressure and content, and permeability of the Velenje coals have not been well established until very recently.

Previous laboratory studies carried out on samples of different lithotypes of lignite from Velenje report significant differences in some reservoir properties of different lithotypes, especially in porosity and pore surface area. For example, pore surface area of homogenous fine detrital lignite was measured as > 180 m^2/g, whereas that of xylite was “only” 35 m^2/g (Zapušek and Hoćevar 1998), indicating that detrite can adsorb much more gas than xylite.

The predominant component in underground gas emissions at Coal Mine Velenje is CO_2, rather than CH_4. CO_2 released from coal during mining depends on petrological characteristics of coal and production method/type at different levels and stages of mining. Likar (1995) quotes a CO_2 specific emission rate of 26 m^3/tonne of coal mined for Velenje. As normal practice, the mine measures gas composition in development headings as well as the coal seam using samples taken from 3m long boreholes during roadway and face development and monitors CO_2 and CH_4 content in the sample (%), Carbon Isotope (δ^{13} C) in CH_4 and CO_2. The gas composition in the lignite is used to calculate the so called Carbon Dioxide and Methane Index (CDMI), which is:

$$CDMI = \frac{CO_2}{CO_2 + CH_4} \times 100\% \qquad 4.1$$

Therefore, the higher the CDMI, the higher the CO_2 content of the coal seam in that region. As shown in Figure 4.6, the CDMI for coal varies throughout the deposit depending on seam height, geology, lithology, floor strata, and tectonic influences. Here, light blue shaded areas represent areas with lower CH_4 content (or higher CO_2 content) in coal.

Langmuir isotherms measured at Imperial College showed that, at a pore pressure of 2 MPa (Figure 4.7), around three times more CO_2 can be adsorbed by Velenje lignite compared to CH_4. The corresponding Langmuir parameters for the tested coal sample shown in Figure 4.7 are listed in Table 4.1.

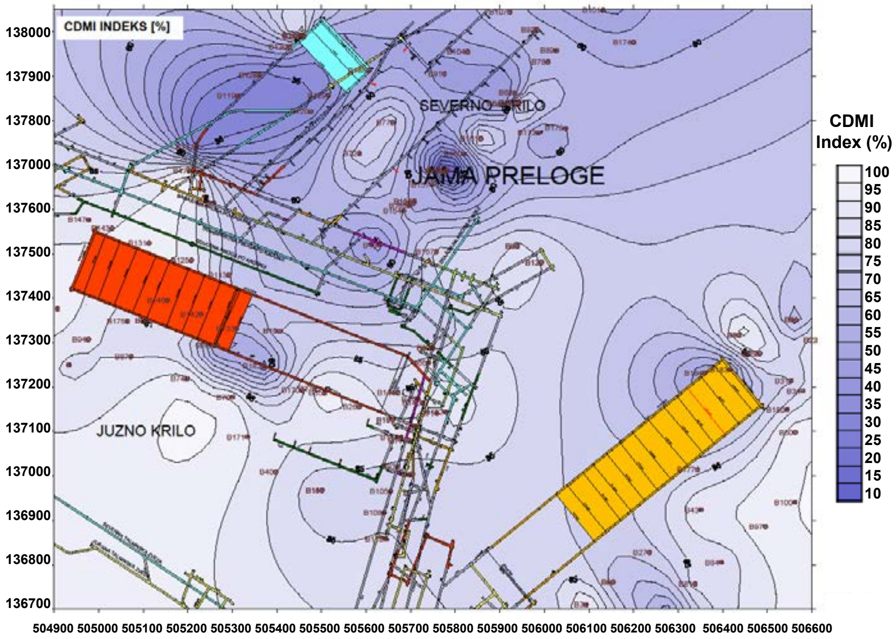

Figure 4.6: The CDMI index for the two longwall districts at Coal Mine Velenje (Courtesy of Coal Mine Velenje researchers).

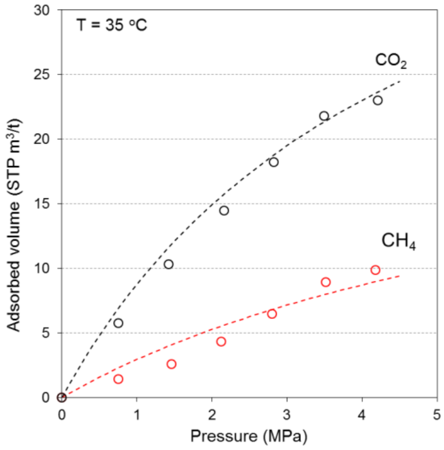

Figure 4.7: Pure gas adsorption isotherms for Velenje lignite.

Table 4.1: Langmuir parameters for pure gas adsorption on Velenje lignite

Gas	Langmuir parameters	
	Pressure (MPa)	Volume (m^3/t)
Methane	7.5	25
Carbon dioxide	4.7	50

Here, V_L is the Langmuir Volume, which represents the maximum volume of gas that can be adsorbed by a given coal at reference temperature and P_L is the Langmuir Pressure, corresponding to the pressure at which 50% of the gas represented by the Langmuir Volume is adsorbed.

4.3 In-situ Gas Pressure and Composition Monitoring and Analysis

In-seam boreholes were used as the most effective and direct method to investigate the changing pressure regimes at longwall panels throughout this study. In order to capture the impact of multi-level longwall top coal caving mining on gas pressure behaviour, a large number of boreholes were drilled in to panels operated at different mining levels within the coal seam. In addition, gas sampling boreholes were drilled adjacent to the pressure monitoring boreholes in order to analyse the composition of seam gas in the same location.

The gas pressure and composition monitoring is carried out in two stages: a) initial borehole stabilisation and b) impact of face dynamics. The first stage measurements were designed to establish the initial conditions at the study panel, which is independent of the face movement and normally involves a long period of pressure/gas composition stabilisation. The second stage covers the period of face advance towards the monitoring boreholes, so that the dynamic effects of face advance on gas pressure and composition can be investigated.

The boreholes used to measure gas pressure and composition changes were designed and implemented by the engineers at Coal Mine Velenje. A detailed description of the designs of these boreholes can be found in Appendix 1.

4.3.1 Gas Dynamics Monitoring around Longwall Panel K.-50/C

The LTCC panel K.-50/C was the first field site used for integrated analysis of the effect of face advance on gas dynamics around the mining panels. As depicted in Figure 4.8, the LTCC panel K.-50/C was unique that it is partly overlain by an intact clay roof and partly by the goaf created by the previous level of coal extraction.

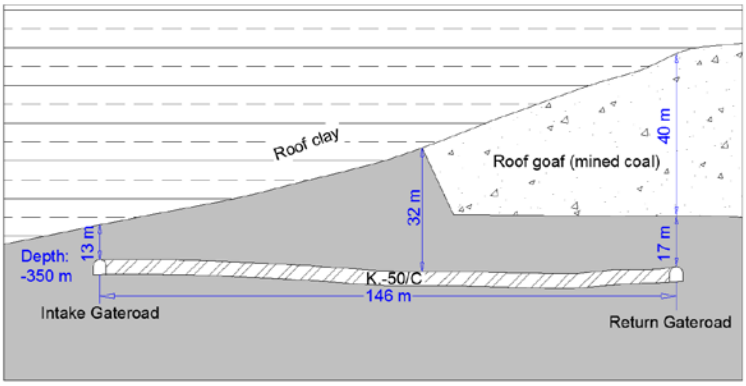

Figure 4.8: A cross-section of K.-50/C LTCC panel at Coal Mine Velenje.

Coal excavation at panel K.-50/C started in November 2010 and ended in October 2011. The average daily face advance and coal production were 2.9 m and 7,930 tonnes respectively.

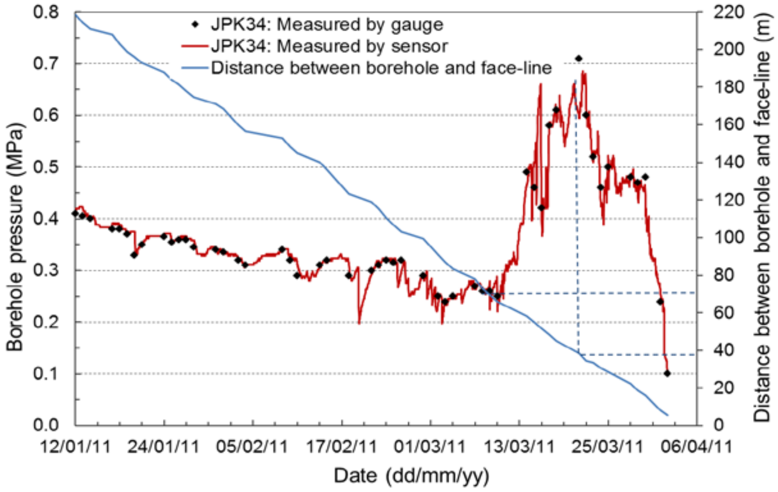

Figure 4.9: Gas pressure response to longwall face advance at panel K.-50/C.

Figure 4.9 presents the seam gas pressure response to longwall face advance in borehole JPK34, which was 25 m long, drilled into panel K.-50/C at +2^o from the horizontal. As this borehole was drilled long after the district development and start of longwall production, it only recorded the gradual pressure decline period and failed to establish the in-situ seam gas pressure in this panel. The pressure monitoring data show that, as the face approaches the borehole location, the seam gas pressure is reduced by nearly 0.15 MPa until the face is approximately 70 m from the borehole. From then on, the seam gas pressure shows a significant increase until the face is 40 m away from the borehole, which is followed by a rapid pressure decline due to extensive fracturing ahead of the coal face.

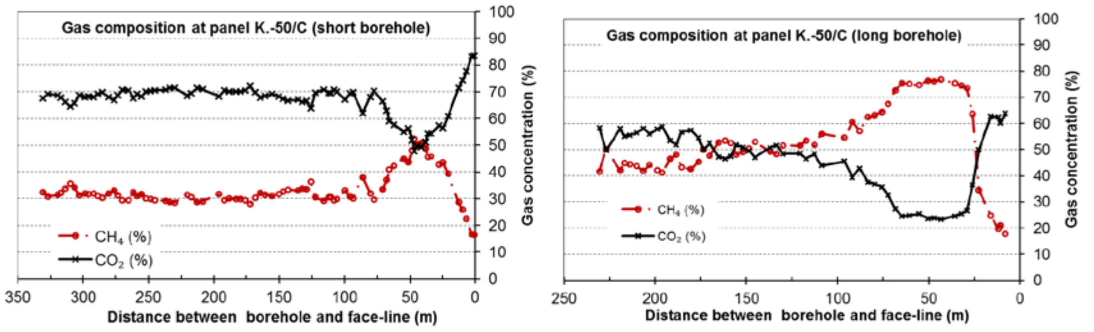

(a) Short borehole V2 (at 0^o to the horizontal plane) (b) Long borehole JPK 33 (at +30^o to the horizontal plane)

Figure 4.10: Seam gas composition changes in monitoring boreholes as the longwall face K.-50/C approaches. Both boreholes were drilled and monitored during December 2010 – April 2011 in parallel with borehole JPK34.

As illustrated in Figure 4.10, in-seam gas composition in the boreholes remained largely unchanged until the face was around 100 to 70 m from the boreholes. After that, the gas mixture became increasingly enriched in CH_4 until the face was approximately 40 m from the boreholes, at which point this trend was reversed and CO_2 concentration started to increase.

4.3.2 Monitoring and Analysis of Gas Pressure Dynamics at Different Mining Levels

Following on from the first stage in-seam gas pressure and concentration measurements at panel K.-50/C a systematic monitoring of gas dynamics around working LTCC panels was carried out over the next three years period. Table 4.2 summaries the gas pressure monitoring results from six roof boreholes drilled into LTCC panels in five different mining levels of the coal seam at Coal Mine Velenje (see Figure 4.11). Unfortunately, the mine did not have any longwall panels operating in third or fourth levels during the research period. Longwall panels K.-65/A, K.-65/B, K.-65/C, and K.-65/E were neighbouring panels operated at same elevation but with different previous mining histories and original coal thickness above. The longwall K.-5/A was operated at a higher elevation but excavated the lowermost section of the coal seam in the same area of the coalfield).

Table 4.2: In-situ gas pressure data for different mining levels.

Mining level	Borehole	LTCC panel	Height of previously mined coal above the panel (m)	Time to pressure stabilisation (day)	Stabilised pressure (MPa)
First	JPK 69	K.-65/E	0	129	~2.00* (1.70)
Second	JPK 74	K.-65/C	20	84	1.03
Fifth	JPK 65	K.-65/B	75	76	0.55
Sixth	JPK 47	K.-65/A	90	84	0.70
Seventh	JPK 39	K.-5/A	75	80	0.68
Seventh	JPK 40†	K.-5/A	75	-	0.80

*After borehole completion, pressure build-up in borehole JPK 69 took more than four months before being affected by the consolidation of the roof/goaf in the recently completed LTCC panel close to the borehole. Later on, the borehole pressure stabilised at 1.70 MPa. As a result, the initial gas pressure stabilisation was not fully achieved in this borehole.

† While all other boreholes were drilled in-seam at the mining level borehole JPK 40 was drilled at +60° in to the roof (goaf) area of LTCC panel K.-5/A.

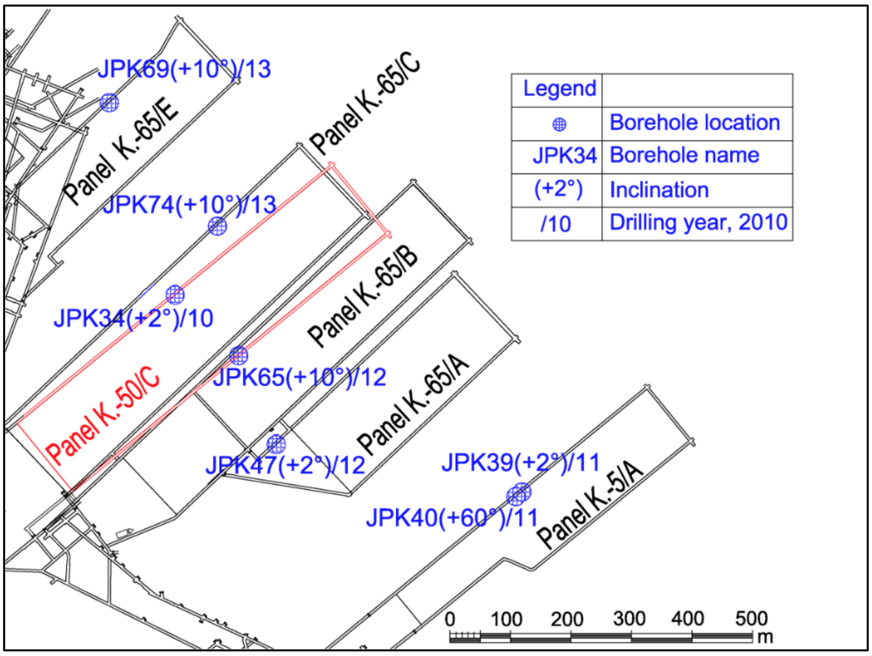

Figure 4.11: Mining layout illustrating the LTCC panels used for monitoring gas pressure and concentration during coal production at different mining levels in Coal Mine Velenje (after Si *et al*., 2015a).

In-seam gas pressure measurements have shown that the gas pressures in the first mining level were the highest, at over 2 MPa (Figure 4.12). From then on, and due to over-mining, seam gas pressure dropped significantly when coal extraction moved down to the lower levels (Table 4.2). Progressive reduction in gas pressure with depth of mining also resulted in reduced rates of gas emission in lower mining levels.

Figure 4.13 presents the measured seam gas pressure data against distance from the face line in borehole JPK 69 as the LTCC face approaches the monitoring site. Note that only the pressure gauge readings were available during 12 April 2013 to 29 October 2013, after which the data communication cables were extended to the panel and real-time data collected. During mining, the seam gas pressure was largely stable until the face moved within approximately 53 m of the borehole. After that point, the pressure readings were erratic and, once the distance to the face line reached 40 m, a dramatic pressure reduction was observed.

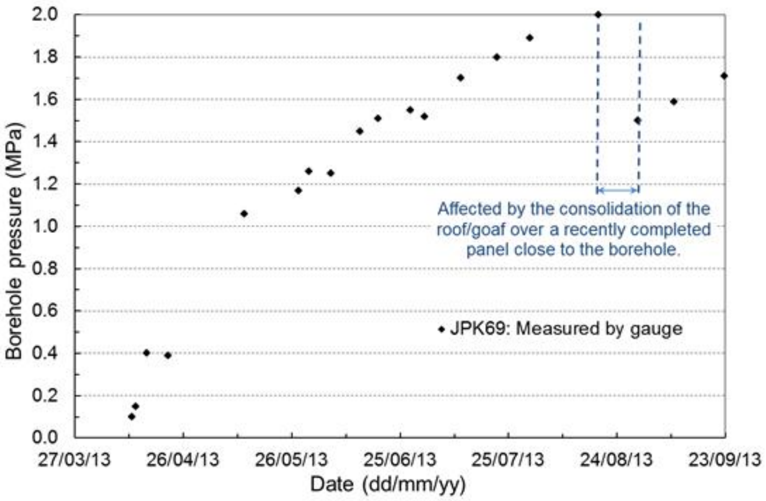

Figure 4.12: Gas pressure build-up at the first mining level borehole JPK69 at panel K.-65/E.

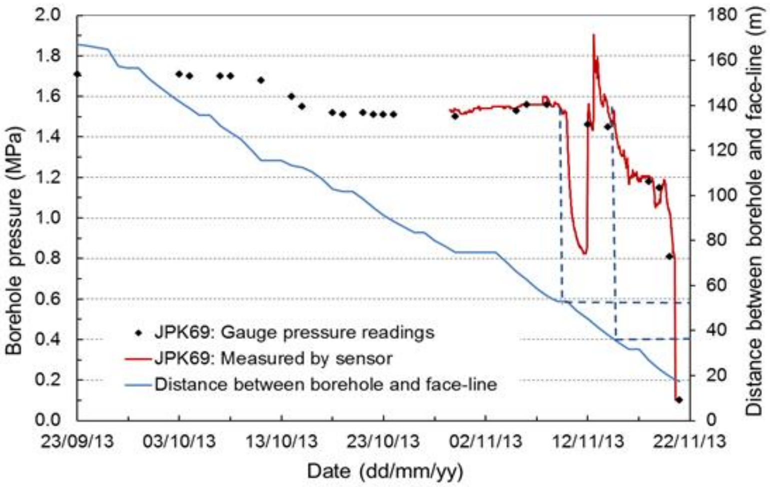

Figure 4.13: The effect of face advance on gas pressure at the first mining level (panel K.-65/E**)**.

Daily average gas pressures recorded at three in-seam boreholes (JPK39, JPK47, and JPK65) which were located at lower level mining panels are plotted against distance to the face-line position in Figure 4.14. As can be seen, seam gas pressure responses to face advance varied from borehole to borehole but with a general reduction trend as the face approached the boreholes.

For borehole JPK39, gas pressure started to decrease when the face was 200 m away from the borehole, and it declined gradually to atmospheric pressure when the distance reduced to 70 m. A nearly 0.2 MPa reduction in pressure was observed in borehole JPK47 when the face advanced from 200 m to 100 m away from the borehole. Then a dramatic pressure drop from 0.5 MPa to atmospheric pressure was observed when the face was 100 m away from the borehole.

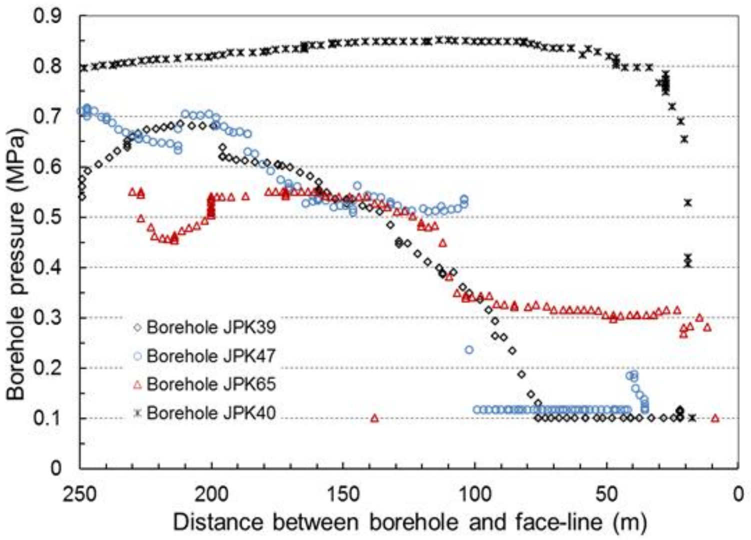

Figure 4.14: The effect of face advance on in-seam gas pressure in lower mining levels.

A period of pressure drop and re-stabilisation was occasionally observed in boreholes JPK65 and JPK47. A notable pressure drop was first recorded in JPK 65 when the face was around 100 m away. After that, the pressure stabilised at 0.3 MPa and dropped to atmospheric pressure when the face reached a point less than 10 m away from the borehole.

In addition to the three in-seam boreholes referred to above, a +60˚ inclined borehole JPK 40, located at K.-5/A panel, was drilled into the mined out roof (goaf) area of the panel to improve the understanding of gas pressure regimes at previous mined levels and its responses to face advance. The measured gas pressure in the goaf was surprisingly high (over 0.8 MPa) and increased slightly until the face was within approximately 40 m away from the borehole. After that, gas pressure dropped sharply as the face approached the borehole. Atmospheric pressure was recorded when the face was 17.3 m away from the borehole.

Figure 4.15 shows the gas composition monitored in a 25 m long borehole drilled into a first level panel (K.-65/E) against the distance between the borehole and the face-line. The ratio of CH_4 to CO_2 was maintained around 7:3 until the face was approximately 55 m away from the borehole. A slight increase of CH_4 concentration was recorded when the face was 49 m from the borehole. As the face approached closer, CO_2 concentration increased dramatically and became the dominant component.

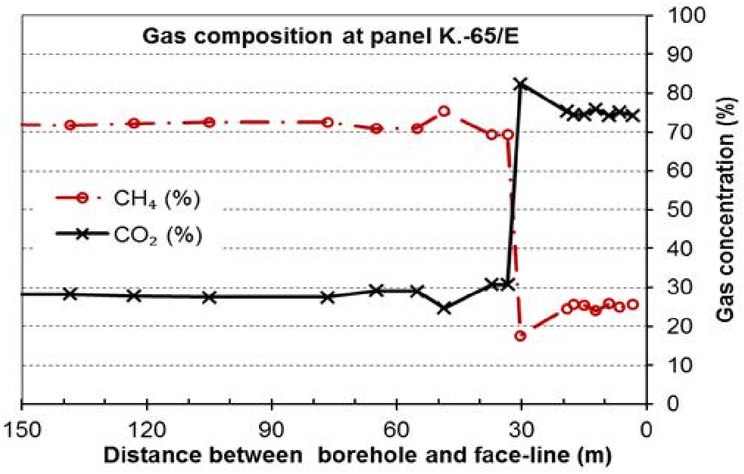

Figure 4.15: Seam gas composition changes in the gas concentration monitoring borehole JPK 70 as the first mining level longwall face K.-65/E approaches the borehole, which was drilled at +10° to the horizontal and monitored from 3 October 2013 to 4 December 2013.

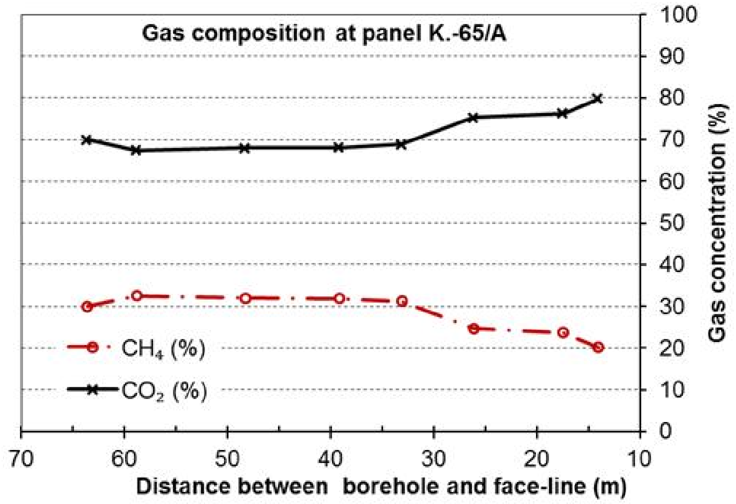

Figure 4.16: Seam gas composition changes in the 25 m long gas concentration monitoring borehole JPK 52 as the sixth mining level longwall face K.-65/A approaches the borehole, which was drilled at +10° to the horizontal and monitored from 4 June 2012 to 5 July 2012.

As illustrated in Figure 4.16, the gas composition behaviour at a lower level panel (K.-65/A) is significantly different to that observed in a first mining level panel. Here, CO_2 was recorded as the primary gas component. The share of CO_2 increased slightly when the face approached to less than 40 m away from the borehole.

4.4 Ventilation Environment Monitoring at Longwall Panel K.-50/C

Besides borehole gas dynamics measurements, mine environmental monitoring at return gateroads, which records gas concentration and ventilation quantity, is performed as normal practice at the mine. A representative period of face advance and gas data for the LTCC panel K.-50/C have been selected and plotted in Figure 4.17, in which an episode of increased gas emission was recorded as well as gas emissions during a two-week holiday period. CO_2 concentration in the emitted gas and daily face advance rate are also cross-plotted in this figure.

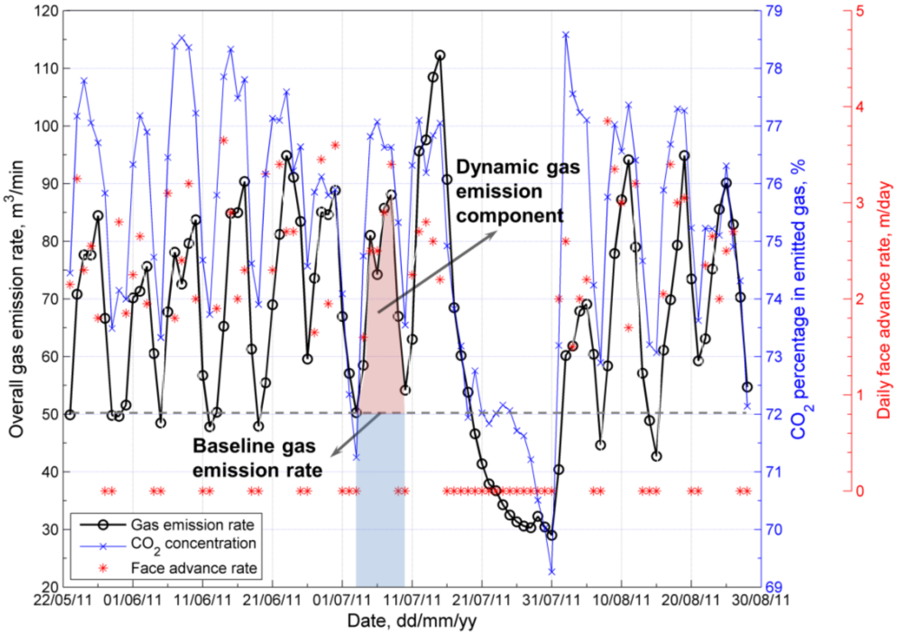

Figure 4.17: Emitted gas flow rate, CO_2 concentration in the emitted gas, and daily face advance rate at K.-50/C (from 23rd May to 28th August 2011).

Figure 4.17 suggests that gas emission pattern follows the coal production schedule at the mine closely, significantly reduced in the absence of mining activities at weekends. Furthermore, it is clear that, larger the daily face advance rate, the higher the gas emission. The peak rates of gas emissions were normally observed on Thursdays or Fridays. A marked increase (by over 20%) in gas emission rate was observed at around 14-15 July 2011 and production at the face was interrupted. The subsequent sharp reduction in gas emission was due to a two-week summer holiday at the mine. The gas flow rate recovered to its normal levels with the resumption of coal production.

Note that gas flow rates during weekends were almost identical, which have stabilised at around 50 m^3/min. This amount of gas, which provides a 'baseline' for gas emissions in this panel, is not a direct result of coal production activities, but due to gas migration around the coal face. Therefore, the total gas emission at this LTCC panel can be represented by two components: 1) the baseline gas emission, representing the period when no coal is produced, which is around 50 m^3/min and 2) the dynamic emission, representing the period during coal extraction, which is normally 30 to 40 m^3/min higher than the baseline emission and directly caused by the coal production at the K.-50/C panel.

As can be seen in Figure 4.17, CO_2 accounts for 70 - 80% of the total gas emitted during coal production. An interesting observation is that CO_2 concentration in the emitted gas followed the same trend as the gas flow rate, which increased during production days and decreased at weekends. This correlation will be further discussed by the modelling results in Section 6.5.4. In addition, the ratio of CO_2 to CH_4 in the emitted gas was almost consistent with the gas sorption capacity of CO_2 and CH_4 indicated by the Langmuir isotherms measured as well as the final gas compositions measured from boreholes.

4.5 Discussions

4.5.1 Pressure Relief and Gas Composition Changes as a Result of Multi-Level Longwall Top Coal Caving Extraction

The effect of coal extraction in the upper mining levels of an ultra-thick seam LTCC on the gas pressure regimes of the lower mining levels can be clearly seen in Table 4.2. It is clear that a pressure relief zone is established in the floor coal during multi-level mining.

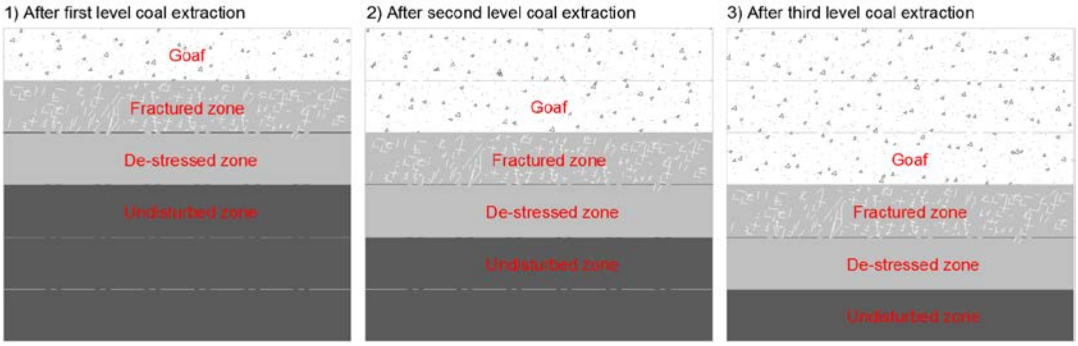

Figure 4.18: A conceptual illustration of pressure relief zones induced by multi-level LTCC mining (not to scale).

As illustrated in Figure 4.18, after coal extraction in the first mining level, a fractured and a de-stressed zone with reduced gas pressure occur at lower mining levels. The fractured zone may have a uniform and largely reduced pressure due to the creation of high permeability fractures. While the enhanced permeability induced by stress relief in the de-stressed zone is most likely to result in a reduced gas pressure gradient in the region. Coal extraction in the second mining level can turn the previously de-stressed zone into a new fractured zone and, compared with the previous fractured zone, a further gas pressure reduction can be expected in there. In addition, the original undisturbed zone may be affected by the second level coal extraction and start releasing its gas. After that, coal extraction in the third mining level may cause the previous de-stressed zone and undisturbed zone to be replaced by a new fractured zone and a de-stressed zone. This process would continue as mining extends to the lowermost levels of the coal seam.

The reduction of gas pressure in the lower mining levels also results in an upwards migration of gas and gases emitted from the lower levels of unmined coal would be accumulated in the goaf area. This goaf gas may be a potential source of gas emission during the mining of the next level.

Borehole gas concentration data suggest that the initial free gas at the first level panels is predominantly CH_4. After pressure relief induced by mining in the upper levels, CO_2 becomes the primary gas component of the free gas in lower level panels. This is consistent with the knowledge that coal has a higher adsorption affinity to CO_2 than CH_4, and CO_2 is much more strongly held in the coal matrix than CH_4 and will not be released unless the seam gas pressure is reduced significantly.

In addition, the long period of pressure build-up observed at the first mining level borehole JPK69 in LTCC panel K.-65/E, Figure 4.12 suggests that the in-situ permeability of Velenje lignite is extremely low and unfavourable for the pre-drainage of in-seam gas. However, pressure and stress relief caused by mining in the upper levels may help gas drainage from the roof (goaf) areas and the fractured floor coal in lower levels.

4.5.2 A Conceptual Model for Gas Emissions in Multi-Level Longwall Top Coal Caving Mining of Ultra-Thick Coal Seams

Based on the analysis of the borehole gas pressure and composition data presented above, a conceptual model has been developed to describe the response of the ultra-thick seam to multi-level LTCC mining at Coal Mine Velenje. Since the first mining level panels may have a distinct gas pressure and composition behaviour as compared to the lower level panels, LTCC faces operated at the first and second mining levels are presented in Figure 4.19 (a) and (b), where the second mining level is used to generalise the gas pressure regime experienced in lower mining levels. Given the relatively low gas pressure and CO_2 dominated initial gas composition at LTCC panel K.-50/C, the borehole gas pressure and concentration data from this panel were attributed to lower mining level panels.

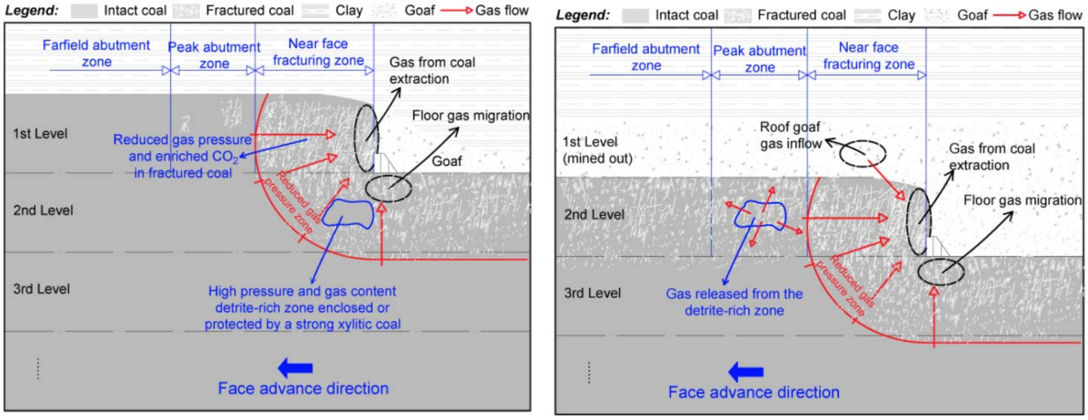

(a) (b)

Figure 4.19: A conceptual model for gas emission zones of a LTCC panel in the (a) first mining level and (b) the second and lower mining levels at Coal Mine Velenje.

As depicted in these two figures, the region of a LTCC panel ahead of the advancing face may be divided into three zones, characterised by distinctive gas pressure and composition behaviour that reflects the response of the panel to LTCC mining at a progressively reduced distance to the face:

- Farfield abutment zone

  The farfield abutment zone in the first mining level is believed to be over 50 m away from the face line. The most common observation made in this zone is the stabilised gas pressure and steady gas composition throughout the production period. The increase in the mining abutment stress is not large enough to cause a notable change in either gas pressure or composition. It can be concluded that, for intact coal, gas composition in the released free gas is around 70% CH_4 and 30% CO_2, and the in-situ gas pressure is at least 2.00 MPa.

  In the case of lower mining levels, this zone extends from 70 to 200 m from the face line. The initial low gas pressure and CO_2-dominated gas composition suggest that these levels have already been largely disturbed by previous mining and the coal seam may not be intact anymore. A minor mining disturbance may rearrange pressure regimes around the LTCC panels. Different degrees of fracturing may result in the difference in the timing and extent of pressure drop in the seam as observed across the lower mining level boreholes (see Figure 4.14).

It is worth noting that the coal extraction of an upper level may not completely fracture the next lower level, and certain intact areas with high strength xylite may exist. Moreover, pressure communication between the fractured and unfractured areas is expected to be minimum due to the very low permeability of intact xylite. This may result in a considerable volume of high pressure gas retained by a detrite rich zone enclosed or protected by a xylite-rich zone as illustrated in Figure 4.19 (a). In this case, the gas content of this heterogeneous zone is expected to be same as the in-situ conditions with primary CO_2 and secondary CH_4.

As it will be further discussed in Chapter 5, time-lapse (repeat) seismic tomography surveys were carried out over a fixed 100 m long section of panel K.-50/C as the face advanced towards this section. In addition, microseismic activities at this panel were monitored continuously. These measurements have identified a xylite-rich zone (matched by localised microseismic events, changes in P-wave velocities and gas pressure patterns) which formed a gas flow barrier ahead of the face. It is also in the mine’s records that this relatively large area of xylitic zone lead to an episode of sudden and excessive gas emission when the front abutment stresses were high enough to fracture this zone, which interrupted coal production (please see Figure 4.17 for the emission rate on 15 July 2011).

- Peak abutment zone

The peak abutment zone, which is around 40 to 50 m from the face line in the first mining level, is characterised by a dramatic gas pressure reduction as observed in borehole JPK69 (see Figure 4.13). Local fracturing of the coal seam is initiated due to the peak abutment stress effecting this zone. The sudden drop and rebound of gas pressure observed in JPK69 at around 50 m from the face line can be explained by the gas communication between the low and high pressure regimes around the borehole. The slight increase of CH_4 concentration (compensated by a similar decrease in the CO_2 level) observed in the same period may also confirm this conclusion (see Figure 4.15).

The peak abutment zone in the lower mining levels is developed around 40 to 70 m distance from the face line. Unless the coal seam is primarily xylite-rich, this zone is characterised by relatively low gas pressure and CO_2 dominated composition in the released gas. On the other hand, if the xylite-rich coal seam is not affected by over-mining, the increased abutment stresses may fracture the otherwise intact xylite-rich zones and increase the CH_4 concentration in the released gas (see Figures 4.9 and 4.10).

- Near face fracturing zone

  The near face fracturing zone extends up to 40 m from the face line and the in-seam gas pressure and composition regimes generally show a similar trend in both the first and lower mining levels. The seam gas pressure experiences a sharp drop and the emitted gas concentration is enriched in CO_2 in this zone. The rapid drop in seam gas pressure may be due to the combined effect of massive coal fracturing and the proximity of a pressure sink at the face. Note that higher CO_2 concentrations recorded against high gas emission rates in Figure 4.17 also confirm that CO_2 is released from the near face fracturing zone during production rather than at weekends and holiday periods when the face is idle and the emission rates are represented by the baseline rate. As suggested by the fast gas pressure decline in the roof (goaf) borehole JPK40 at LTCC panel K.-5/A (Figure 4.14), additional gas inflow from the roof area would also play a significant role in contributing to the overall gas emission in this zone.

The analysis of ventilation air gas concentrations and specific gas emission at LTCC panel K.-50/C also supports the above conceptualisation. Table 4.3 presents estimated in-situ gas contents for the Velenje coal at different gas pressures and mining levels based on the Langmuir parameters listed in Table 4.1. As the table illustrates, the estimated in-situ gas contents at various pressure regimes and gas compositions are all less than the actual specific gas emission recorded at K.-50/C. Given that the in-situ seam gas pressure of coal at panel K.-50/C is likely to be close to a second level panel (1.1 MPa), this suggests that a large share of gas emitted into the ventilation system in this panel was not from the mined coal, but from the roof area (goaf) and/or floor (lower level coal seam). In fact, on occasions where the roof coal is not completely caved and left behind the advancing supports, an inrush of a mixture of gas and coal dust into the working area from the roof has occasionally been observed by the production engineers at the mine.

Table 4.3: Comparison of estimated in-situ and/or residual gas contents per tonne of coal at different in-situ gas pressures (or mining levels) and the specific gas emission recorded at LTCC panel K.-50/C during the period of borehole observations.

P (MPa)	ϕ (%)	ρ (kg/m^3)	S_w (%)	R (CO$_2$:CH$_4$)	V_e (m^3/t)	V_a (m^3/t)	V_e/V_a (%)
0.7	10	1250	30	7:3	5.27	17.58	29.99
0.7	10	1250	30	8:2	5.67	17.58	32.27
1.1	10	1250	30	7:3	7.82	17.58	44.46
1.1	10	1250	30	8:2	8.39	17.58	47.74
2.0	10	1250	30	7:3	12.66	17.58	72.00
2.0	10	1250	30	8:2	13.52	17.58	76.91

*P is the initial gas pressure, ρ is coal density, S_w is water saturation, ϕ is porosity, R is the volume ratio of CO_2 to CH_4, V_e is the estimated in-situ gas content per tonne of coal, and V_a is the actual specific gas emission (total volume of emitted gas / total tonnage of produced coal) recorded at LTCC panel K.-50/C.

4.6 Conclusions

Gas pressure and gas composition changes induced by multi-level coal extraction in LTCC faces have been investigated through borehole measurements at different mining levels of an ultra-thick coal seam at Coal Mine Velenje. A conceptual model for gas emissions from multi-level mining layouts has been proposed based on extensive field measurements of gas pressure, gas composition, and ventilation environment. Three gas pressure zones, namely the farfield abutment, peak abutment and near face fracturing zones, ahead of an advancing LTCC have been characterised in the conceptual model.

The near face fracturing zone, which is ~40 m ahead of a LTCC face, is believed to play a significant role in contributing to the gas emissions at the face. It was also confirmed that the gas emission into the LTCC face is very sensitive to the rate of fracturing experienced due to stress relief and the size of fractured zone in the floor coal at multi-level mining layouts.

As also confirmed by the mine’s past experience, the first mining level is expected to experience the highest rate of gas emission both from the mined coal and the floor level due to high initial in-situ gas pressure. On the other hand, for LTCC panels operating at lower mining levels, gas inflow from both the floor coal and the roof goaf may form a considerable share of overall gas emissions. The concentration of

CO_2 in the gas emitted to the ventilation air is expected to increase progressively as the mining reaches lower level of the ultra-thick seam.

Although seam gas pressure may be relatively low when mining the lower level panels, xylite-rich zones trapping high pressure gas may still exist due to the heterogeneous lithological structure of Velenje lignite and uneven fracturing induced by coal extraction in the upper mining levels. Although xylite is not capable of storing large volumes of gas, it may enclose detrite, which is weak and gas-rich. Such structures of strong xylitic coal, enclosing pockets of weak detritic coal with high gas pressure and content, may increase the risk of coal and gas outbursts.

As briefly mentioned and illustrated in Figure 4.17, an episode of increased gas emissions was actually recorded at the K.-50/C LTCC panel during the research periods. Since this episode may share some common features with outbursts, analyses of the seismic monitoring data recorded during this period was also carried out to understand the nature of this excessive emission episode. A detailed discussion on these analyses will be presented in Chapter 5.

Chapter 5 Seismic Monitoring and Analysis of Gas Dynamics in Longwall Top Coal Caving Panels

5.1 Introduction and Background

Seismic velocity tomography is an established non-invasive technology used to investigate geological formations (Friedel *et al.*, 1992; Young and Maxwell, 1992; Friedel *et al.*, 1996). By transmission of acoustic waves through the rock, lithological parameters and structural information can be gained. With active seismic tomography, the transmitters and the receivers of the seismic waves are placed on different sides of a block of rock or coal in the field. The result of the measurement is the distribution of the seismic velocity in a plane and tomograms are created by mapping this velocity distribution. Active sources have also been implemented repeatedly to image individual pillars in underground mines (Watanabe and Sassa, 1996; Scott and Williams, 2004). Tunnels have also been imaged to determine stress distribution around an excavation, implementing both passive (Maxwell and Young, 1996) and active sources.

In the early days, seismic tomography measurements have been used in coal mines mainly to detect voids, to image structures and/or old workings well ahead of planned developments (Hanson *et al.*, 2002). This reduced the need to drill probe-holes. An earlier study was able to image velocity on a longwall panel and has shown that high velocity areas advanced with the longwall face (Kormendi *et al.*, 1986).

There are fewer large scale mine studies in the literature. Roof bolt mounted receivers have been used with a longwall shearer as the seismic source to image a section of a longwall panel mine in the western United States (Westman, 2001). This study has shown a correlation between averaged tomogram values and seismically active areas and demonstrated that the tomography system is capable of imaging heavy shield-leg loading and outburst-prone conditions prior to them disrupting the face operation. Recognising that outbursts are often associated with geological anomalies, active seismic tomography may be useful in detecting these anomalies and providing early warnings.

Underground coal extraction activities lead to continuous stress and pressure redistributions around mine openings. It has been well documented that dynamic failure of rocks is associated with detectable geophysical signals such as microseismic events (Cook, 1976; Sato and Fujii, 1988; Tang, 1997). The energy released in an outburst is from accumulated strain energy in the coal, roof or floor. Numerous factors have been stated to influence the occurrence of bumps, including properties of coal, geology (joints, folds, faults, etc.), mining induced stresses, strong sandstone beds in the roof, pillar size and shape, mining technique and mining rate (Westman, 2001). Therefore, microseismic monitoring has been suggested as a potential approach to provide early warning and even prediction for rock bursts and gas outbursts (Flores, 1998; Shepherd *et al*., 1981).

Microseismic monitoring first gained wide applications for rock burst prediction in hard rock mines. In a pioneering study of applying microseismic monitoring at gold mines in South Africa, Cook (1976) noted that mining-induced microseismic events tended to concentrate in the afternoon of a working day and on Thursday and Friday of a working week. Based on the observation of anomalous seismic behaviour, miners were successfully evacuated prior to a moderate rock burst at a zinc-mine in the US (Brady and Leighton, 1977). High-frequency seismic waveform was monitored prior to a rock burst event, which was believed to be a valid precursor (Archibald *et al.*, 1990).

In recent years, with the improvement of monitoring and interpretation techniques, microseismic monitoring has been accepted as a standard approach to understand and predict rock bursts in coal mines (Fujii *et al*., 1997; Kabiesz and Makówka, 2009; Lu *et al.*, 2013; Cai *et al.* 2014). Li *et al*. (2007) suggested that rock bursts might induce high gas emission in underground coal mining. In Laohuitai coal mine, China, a few incidences of unusual gas emissions were found to be correlated with rock bursts which occurred within 1,500 m of the face. Lu *et al*. (2014) reported that gas outbursts at Junde coal mine in China were induced by shock waves associated with rock bursts.

In terms of application of microseismic monitoring to gas outburst prediction, several case studies in the US, Canada, the UK, Poland and China can be found in literature (Leighton, 1984; Lu *et al.*, 2012; Styles *et al.*, 1988; Talebi *et al.*, 1995). The first effort to develop microseismic monitoring as a predictive tool for coal and gas outbursts was made by McKavanagh and Enever (1978). Anomalous microseismic activities suggesting irregular fracturing was occasionally recorded prior to the occurrence of outbursts in the collieries investigated. Rapid micro-fracturing was suggested by the seismic events prior to outbursts (Leighton, 1984). Styles *et al.* (1988) noted a strong correlation between coal extraction rate and the intensity of seismic events at Cynheidre Colliery in the UK. .

Seismo-acoustic activity and permeability of sandstone samples taken from the outburst prone Nowa Ruda mine subjected to triaxial stresses were measured in the laboratory by Majewska and Marcak (1989). The experiments have shown that fracture formation and propagation, accompanied by a significant increase in permeability, also increased seismo-acoustic emission as a result of fracturing. Furthermore, field monitoring of seismo-acoustic emissions in the former Thorez mine in Poland, which was classified as gas and rock outburst hazard mine, have confirmed that, with increased gas flow, the micro-seismological activity was also much higher than that observed when gas flow/emissions were much smaller (Majewska and Marcak, 1989). It has also been reported that P-wave velocity increases with increase in stress (Kowalczuk and Szwejkowski, 1975). Every seismic event is a source of discontinuous deformation and development of fractured zones in coal seam or rock mass, which are conducive to stronger gas flow. Therefore, the measurements of seismic wave velocities can be used to estimate gas emission hazards.

Although previous research has achieved some success in using microseismic monitoring to provide early warning for rock bursts, the relationship between microseismicity and gas outbursts is still poorly understood. In particular, the spatial evolution of microseismic events with respect to longwall face advance and its impact on gas emissions need to be investigated. Furthermore, active seismic tomography in conjunction with microseismic monitoring has rarely been applied together to investigate excessive gas emissions and gas outbursts.

Building upon the field monitoring results presented in Chapter 4, this chapter focuses on seismic monitoring data and their analyses and interpretation in terms of gas dynamics around the K.-50/C LTCC panel. The episodes of increased gas emissions at this panel will be explained using an integrated analysis of the borehole monitoring, seismic tomography, microseismicity and ventilation air gas concentration data. Finally, the microseismic monitoring data is used to propose a methodology for the early detection of the build-up of uncontrolled gas emissions and gas outbursts, which needs to be investigated further in the future.

5.2 The Field Monitoring Site at Coal Mine Velenje

In order to study microseismicity induced by LTCC method of coal extraction and explore the possibility of using microseismic monitoring to predict outbursts in thick seam mining, two LTCC panels (K.-130/A and K.-50/C) at Coal Mine Velenje were selected to set up a microseismic monitoring programme. Compared to the LTCC panel K.-130/A, the monitoring scheme at panel K.-50/C included a more comprehensive data collection programme, which included time-lapse seismic tomography, gas dynamics and ventilation environment monitoring as the LTCC face advanced towards the instrumented section of the panel. The deployment of a suite of monitoring techniques implemented at LTCC panel K.-50/C is depicted in Figure 5.1.

As presented in Figure 5.2, the longwall top coal caving panel K.-50/C, which was being developed for production at the start of the research described here, was selected as the test panel for the seismic monitoring campaigns. Panel K.-50/C lies at -350 m depth, overlain partly by a layer of clay and partly by a previously caved goaf. Coal excavation at panel K.-50/C started in November 2010 and ended in October 2011. In addition to seismic tomography and microseismic monitoring, ventilation air gas concentration, face advance rate and coal production were also recorded throughout the research period. The average weekly face advance rate and daily coal production were approximately 11 - 12 metres and 7,930 tonnes respectively. The study area for active seismic tomography is shaded in blue in Figure 5.1.

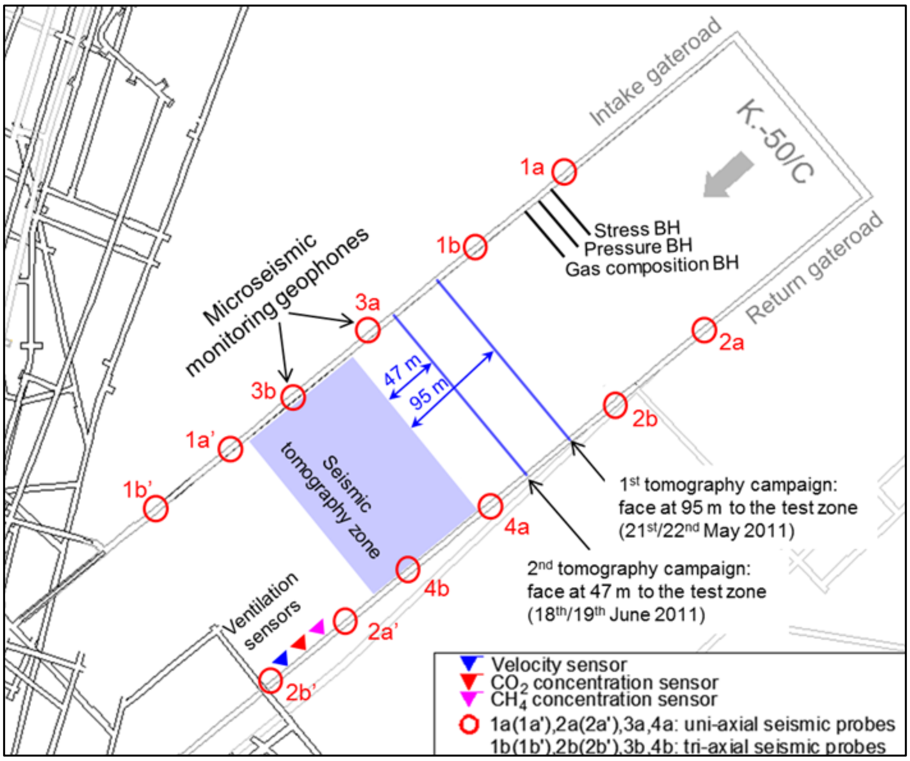

Figure 5.1: Seismic stations and the configuration of sensors used for microseismic monitoring and ventilation measurements at LTCC panel K.-50/C in Coal Mine Velenje (after Si *et al.*, 2015b).

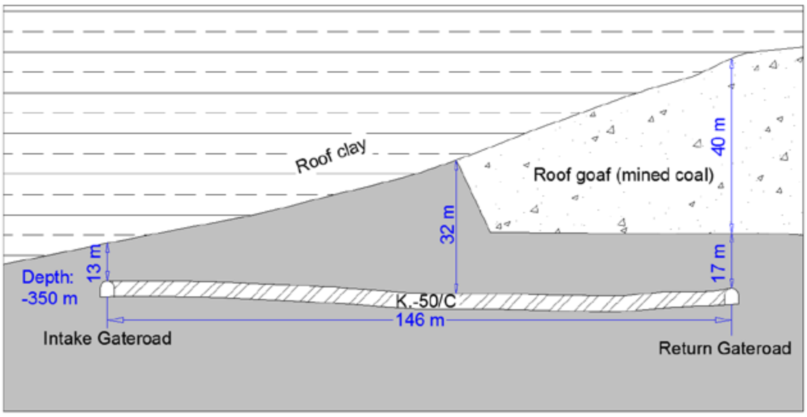

Figure 5.2: A cross-section of K.-50/C LTCC panel at Coal Mine Velenje.

Continuous monitoring of gas emissions as a result of coal production at K.-50/C LTCC face was performed with permanent gas composition (CH_4 and CO_2) and velocity sensors placed at the outby end of the return gateroad. All measurements were recorded in 10-second intervals to analyse and identify short-time gas build up and potential high gas emission episodes. This allowed for accurate analyses of the events leading to large volumes of gas emitted. The recorded gas emission data were sent to and stored at the surface information centre of Coal Mine Velenje via underground fibre optic cables.

Figure 5.3 shows the measured daily gas emission rate and coal production tonnage during the period from 23 May to 28 August 2011. The figure demonstrates that gas emission pattern follows closely the coal production schedule at the mine, reduced significantly in the absence of coal production at weekends or holidays. Peak emissions have normally been recorded on Thursdays or Fridays. A marked increase in the near steady gas emission rate recorded each week was observed on 15 July 2011, which interrupted coal production at the face. A closer review of gas emission rate during the week from 11 to 17 July 2011 (later presented in Figure 5.18) has shown that gas emission rate increased very rapidly (from 100 to 179 m^3/min) within two hours on 15th July, resulting in the abandonment of the production area as required by the mine. The subsequent sharp reduction was due to a two-week summer holiday at the mine management. The gas flow rate recovered to its normal levels with the resumption of coal production.

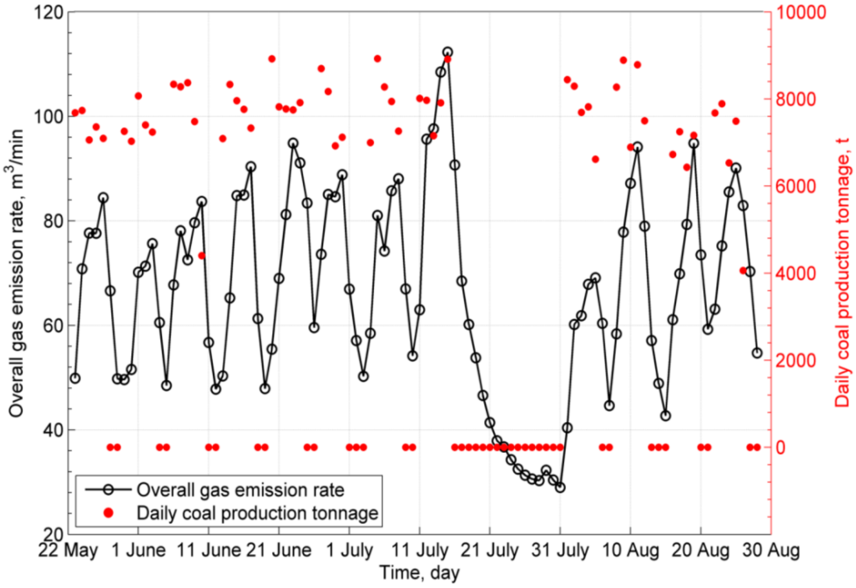

Figure 5.3: Gas flow rate and daily coal production tonnage from 23 May to 28 August 2011.

5.3 Time-lapse Seismic Tomography at Coal Mine Velenje

5.3.1 Overview

Underground coal extraction activities can significantly alter the in-situ stress field around mine openings. Mining-induced stresses may lead to fracture initiation, or the reactivation of pre-existing faults. It has been found that the variation of applied stress on rock mass can positively affect the P-wave velocity (Maxwell and Young, 1996). In addition, the creation of fractures during the process of rock failure can dramatically reduce the P-wave velocity perpendicular to the loading direction (Scott *et al.*, 1993). Therefore, seismic tomography allows for the inference of stress distribution and fractured areas through a velocity image (Westman *et al.*, 1996; Scott *et al.*, 1999; Westman, 2004).

Furthermore, seismic velocity is characterised by rockmass properties such that local variations in coal lithology would affect P-wave velocity as:

$$v_P = \sqrt{\frac{K + 4G/3}{\rho}} \tag{5.1}$$

where v_P (m/s) is the P-wave velocity, K (Pa) is bulk modulus, G (Pa) is the shear modulus, and ρ (kg/m^3) is the density of the rock.

Solving velocity tomograms is a classic problem of inversing travel time data. Assuming that n rays are recorded by a receiver, there is a vector of travel time $\boldsymbol{T}$ (n×1). By spatially discretising the study area into an m number of grids, the slowness vector $\boldsymbol{S}$ (m×1) for all grids has the following relationship with travel time $\boldsymbol{T}$:

$$\boldsymbol{T} = \boldsymbol{DS} \tag{5.2}$$

To solve ***S,***

$$\boldsymbol{S} = (\boldsymbol{D}^T\boldsymbol{D})^{-1}\boldsymbol{D}^T\boldsymbol{T} \tag{5.3}$$

where $\boldsymbol{D}$ (n×m) is the matrix of ray path and its data represent the distance of each ray at each grid to the receiver point. In order to effectively solve $\boldsymbol{S}$, iterative methods, such as Algebraic Reconstruction Techniques (ART), Simultaneous Iterative Reconstruction Technique (SIRT), conjugate gradient, and least squares method, can be used (Mendecki, 1997).

5.3.2 Field Implementation of Time-Lapse Seismic Tomography

In this research, time-lapse active seismic imaging was conducted at a 100 m-long section of K.-50/C LTCC panel to detect geological anomalies in this section. In addition, the idea of repeat/time-lapse seismic tomography was introduced to study the changes of seismic wave velocity as the face approaches to the tomography zone (Figure 5.1). It was believed that, within the tomography section, changes in stress and fracturing induced by mining can be inferred from repeat tomography campaigns.

Time-lapse seismic tomography measurements at Coal Mine Velenje were jointly conducted by K-UTEC Salt Technologies (Germany) and the mine staff. The seismic sources and receivers were placed along two gateroads. The horizontal distance between the two gateroads was 141 m. The boreholes required for the sources and receivers were planned and drilled in advance, before the installation of conveyors and other mining equipment in the main (intake) gateroad. In total, 40 receiver and 40 source boreholes, which were spaced regularly at ~2.5 m, were prepared in the intake and return gateroads, respectively. During the surveys, 120 receiver components located on 40 receiver points (each point equipped with x-, y- and z-three component) were used. X-component represents the P-wave velocity parallel to the gateroad, y-component represents the P-wave velocity perpendicular to the gateroad, and z-component represents vertical direction. For the generation of P-waves, explosive sources in small boreholes were used. The seismic wave recording equipment consisted of geophones, signal transceivers and system control/recording computer.

During the lifetime of longwall K.-50/C, two seismic tomography measurement campaigns were carried out successfully (face positions with respect to the tomography zone as indicated in Figure 5.1). The first (baseline) successful survey was carried out on the weekend of 21st/22nd May 2011. During this campaign the nearest receiver was 95 m away from the longwall face which was advancing towards the tomography zone. For the second measurement, carried out during 18th/19th June 2011, this distance was 47 m.

Note that two more campaigns had been planned, but unfortunately, they were not successful. The very first campaign failed on 7th May 2011 because the mine power supply system was unable to serve the test purpose and the mine had to prepare a battery pack as an alternative. The second failed campaign should have been conducted during the weekend of 25th/26th June 2011, when the face line was 32 m to the tomography study zone. However, during this period, the CH_4 and CO_2 concentrations in the mining district remained too high throughout the weekend and the test equipment had to be withdrawn from the mine due to safety requirements.

5.3.3 Analysis of Time-lapse Seismic Tomography Results

The seismic tomography data were processed by K-UTEC using the software GeoTomGC licensed by GeoTom, LLC of Apple Valley, Minnesota, which uses the SIRT method for performing the inversion required to solve Equation 5.3 for $\boldsymbol{S}$, and also offers good anisotropy analysis functions. The grid dimension measuring 5×5 m was used to discretise the study area. As in the case of microseismic monitoring, the vertical sample range of active seismic tomography was also highly constrained by the conditions in the workspace underground. Thus, in the inversion process, a 2D horizontal plane was simply assumed. P-wave velocities were calculated and gridded to produce velocity tomograms for each receiver component and every campaign. After finishing the processing of data from these two campaigns, the differences of the velocity images have also been computed and imaged.

Figure 5.4 to Figure 5.6 show the P-wave velocity tomograms of the 1st and 2nd campaign when the LTCC face was 95 m and 47 m away from the tomography zone respectively. For either the 1st or 2nd campaigns, the tomograms produced by the three components were reasonably consistent, reflecting the overall stress concentrations on both sides of the panel (NW under the solid roof coal and the SE under caved roof) with differences caused by lithology and anisotropy effects.

Note that a relatively high velocity zone was detected diagonally across at the centre of the study area by the 1st campaign. During the time of the first campaign, the 100 × 141 m tomography zone was relatively far from the face-line and almost unaffected by the mining-induced abutment stresses, which suggests that the P-wave velocity variations reflect the lithological conditions within the study zone. No notable faults were detected. As mentioned earlier in Section 4.2.1, the relatively high seismic velocity zone is believed to be a xylite-dominated zone. Naturally, even higher seismic velocities would have been expected if this zone contained pure xylite.

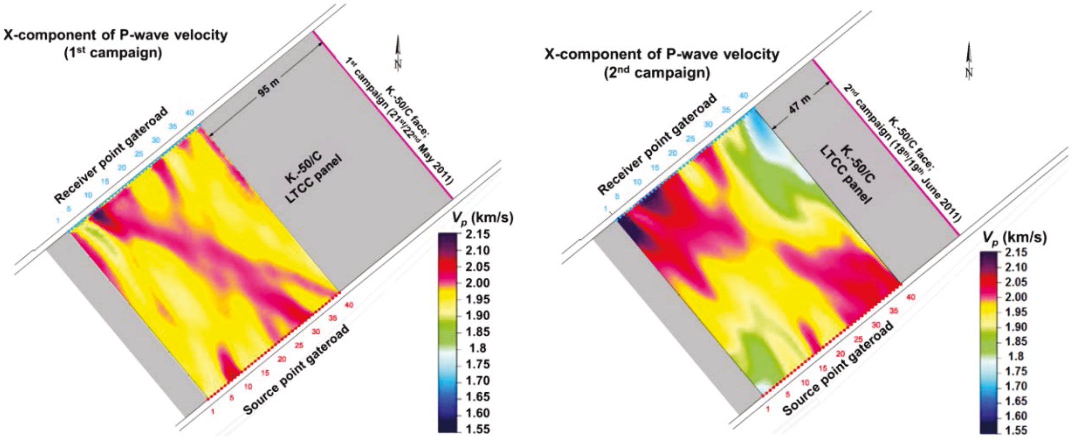

(a) (b)

Figure 5.4: LTCC face K.-50/C P-wave velocity tomograms in X-component for the (a) 1st tomography campaign during 21-22 May 2011 and (b) 2nd tomography campaign during 18-19 June 2011 (after Si *et al*., 2015b).

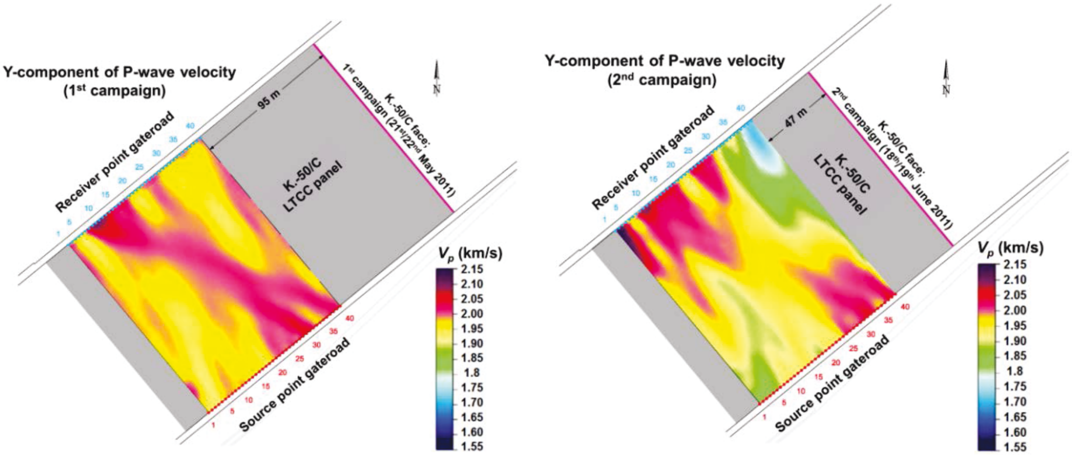

(a) (b)

Figure 5.5: LTCC face K.-50/C P-wave velocity tomograms in Y-component for the (a) 1st tomography campaign during 21-22 May 2011 and (b) 2nd tomography campaign during 18-19 June 2011 (after Si *et al*., 2015b).

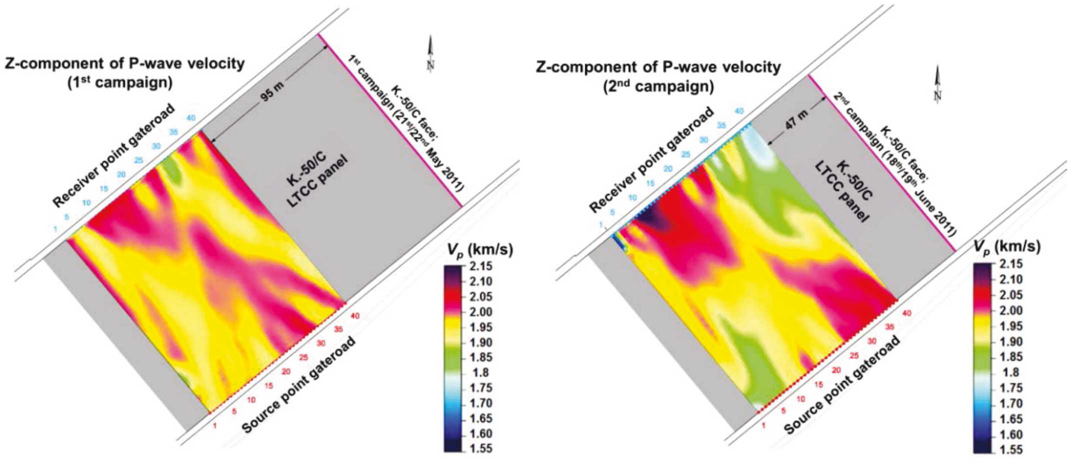

(a) (b)

Figure 5.6: LTCC face K.-50/C P-wave velocity tomograms in Z-component for the (a) 1st tomography campaign during 21-22 May 2011 and (b) 2nd tomography campaign during 18-19 June 2011 (after Si *et al*., 2015b).

As the face approached the tomography zone, a notable P-wave velocity change in all three components was observed between the 1st and the 2nd campaigns. Seismic velocity response to mining activities of the coal seam under the solid roof (NW) and the caved roof (SE) were also different as indicated by the 2nd campaign results. A more straightforward comparison can be seen in Figure 5.7, where the P-wave velocity difference (P_{n2} - P_{n1}) for the X- and Z- components between the 2nd and 1st campaigns is illustrated. On the solid roof side, the coal seam within approximately 70 m of the face-line experienced over ten percent velocity reduction by the time the 2nd tomography was run during 18th/19th June 2011. The P-wave velocity increased slightly or remained unchanged in the rest of the study area.

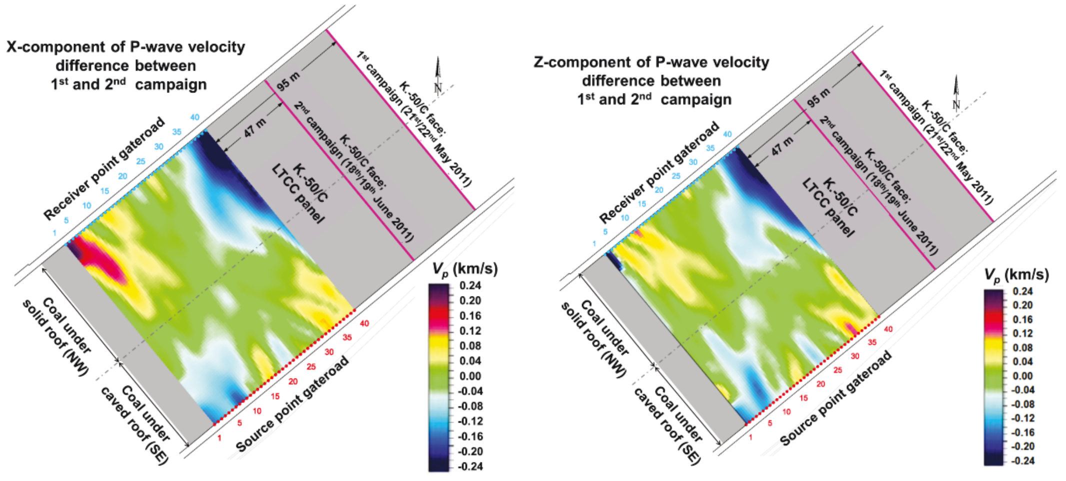

(a) (b)

Figure 5.7: P-wave velocity difference between the two seismic tomography campaigns in (a) X-component and (b) Z-component (after Si *et al*., 2015b).

In coal mining, it is well recorded and established through field measurements that extreme stress concentrations are experienced under solid coal pillars, whereas areas under caved waste are stress relieved. Therefore, it is expected that the NW half of longwall K.-50/C should experience higher levels of stress abutment and, as the face moves closer to the tomography zone, the stress abutment effects may be further amplified. On the other hand, by the very nature of LTCC method, there is always a slice of roof coal over the working face which later will be extracted by caving. Thus, in the case of K.-50/C, even the SE half of the longwall panel, which is under the caved roof should experience a kind of abutment loading, but this would be much gentler.

The tomograms shown in the above figures support these hypotheses. According to the borehole gas pressure and concentration measurements presented in Chapter 4, the coal seam from around 40 m to 70 m ahead of the face-line experiences peak abutment stresses and pre-failure cracks are initiated. With the longwall face 47 metres from the tomography zone, the area nearest to the face-line in the NW half of the panel has the lowest P-wave velocities, suggesting the fracturing of the coal under extreme abutment stresses. A medium-to-high velocity zone beyond this may indicate compacted coal under the initial stages of stress build up.

The SE half of the tomograms, on the other hand, suggest that the seam under a relatively thin slice of coal and caved roof only experiences a mild stress abutment, enough to compact the coal seam, but not fracture, leading to high P-wave velocities nearer the face, and lower P-wave velocities beyond this area due to a slight increase in the stress.

5.4 Microseismic Monitoring at Coal Mine Velenje

5.4.1 Overview

Both fracture initiation and fault reactivation involve the change of elastic energy in a rockmass, which are generally accompanied by the radiation of some energy in the form of seismic waves (Cook, 1964). Fracture initiation around mine openings is predominately caused by tensile failure (Cai, 1998). The potential energy (E_c, J) released from this type of failure is of low magnitude and can be described by (Griffith, 1921; Broek, 1986):

$$E_c = \frac{(1-\mu^2)\pi\sigma_n^2 a^2}{E} \tag{5.4}$$

where a (m) is the half length of the crack, E (Pa) is the Young's modulus, μ (dimensionless) is the Poisson's ratio, σ_n (Pa) is the normal stress acting on the crack.

Fault reactivation as a result of shear failure occurs some distance from the mining activities and the potential energy (E_f, J) released is associated with larger magnitude (Gibowicz and Kijko, 1994):

$$E_f = \frac{1}{2}\Delta\sigma_f D_f A_f + \sigma_f D_f A_f \tag{5.5}$$

where A_f (m^2) is the surface area of the fault, D_f (m) is the average fault slip, $\Delta\sigma_f$ (Pa) is the stress drop between the initial stress and the final stress σ_f (Pa) after faulting.

The measured seismic energy is a relatively small fraction of the total energy released (E_c or E_f). The energy released during failure can also be consumed in overcoming the cohesion of crack tips/faults or attenuated during wave transmission. In the absence of attenuation, the radiated seismic energy (E_r, J) can be computed based on the time-integrated values of P-wave and S-wave seismograms, $u_P(t)$ and $u_S(t)$ respectively (Shearer, 2009):

$$E_r = 4\pi\rho v_P R^2 \frac{<U_{Pm}^2>}{U_P^2}\int_{t_1}^{t_2}\left|u_P(t)\right|^2 dt + 4\pi\rho v_S R^2 \frac{<U_{Sm}>}{U_S}\int_{t_1}^{t_2}\left|u_S(t)\right|^2 dt \tag{5.6}$$

where R (m) is the distance between the source and receiver, ρ (kg/m^3) is the density of medium, v_P (m/s) and v_S (m/s) are P-wave and S-wave velocities of the medium, U_P^2 and U_S^2 are the radiation pattern terms, and $<U_{Pm}^2>$ and $<U_{Sm}^2>$ are the mean values for P-wave and S-wave. t_1 (s) and t_2 (s) are times bounding a group of P-wave and S-wave.

Microseismic monitoring does not only record the scale of energy released during fracturing or faulting, but also locate the hypocentre of a failure episode by assessing the P-wave and S-wave arrival times at geophones. Ideally, the geophones should be placed in a non-planar array, but this is sometime restricted by the engineering conditions, such as that in underground longwall panels where access to the coal seam is limited to the gateroads.

5.4.2 Field Implementation of Microseismic Monitoring

The underground microseismic monitoring campaign at Coal Mine Velenje was jointly conducted by the Department of Geology and Geophysics of Central Mining Institute (GIG) in Poland and the mine staff. GIG has designed a flameproof automated seismic observation system (SOS) for underground installation in coal mines (Mutke, 2013). An entire SOS includes a number of low frequency underground geophones combined with seismic signal transmitters in the form of current signals via transmission lines, and a surface DLM-SO Receiving Station which is connected with the Seismic Recording System (see Figure 5.8). The hardware allows for automatic triggering and recording of mining induced seismic events. The MULTILOK and SEISGRAM software, which are integrated into the SOS seismic system, enable data acquisition and data processing so as to provide information about source parameters and location of seismic events. The 32-channel SOS was designed as flame-proof equipment.

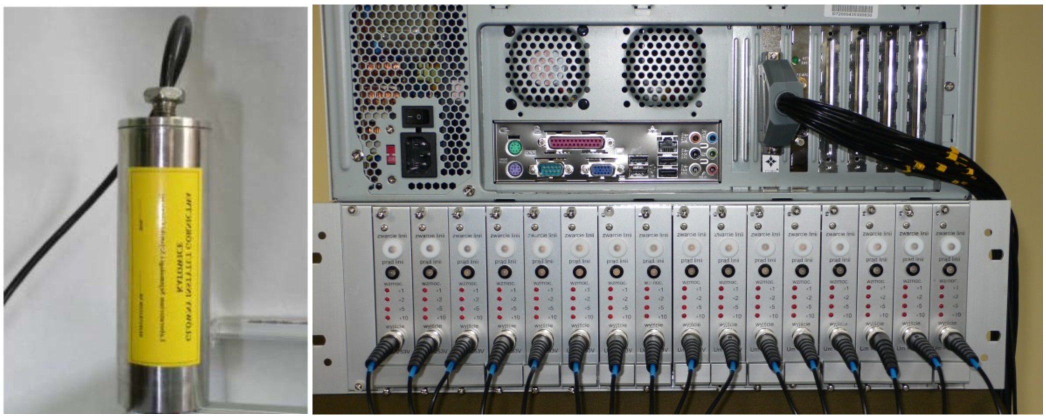

(a) (b)

Figure 5.8: Microseismic monitoring equipment: (a) the low frequency DLM-2001 geophone probe and (b) DLM-SO surface data receiver (after Si *et al*., 2015b).

Data sampling frequency was 500 Hz and the recordable frequency bandwidth of microseismic events was between 0.8 and 250 Hz. Since most of the microseismic hypocentres are relatively close to the geophones, the attenuation of microseismic events in Velenje coal was assumed to be less than 10%.

In total, eight probes (four uniaxial and four triaxial) were installed at the K.-50/C LTCC panel to record microseismicity induced by coal extraction from 27 April to 30 August 2011. Initially, the 8 probes were placed in pairs at locations 1a-2a, 3a-4a, 1b-2b, and 3b-4b as shown in Figure 5.1. Each pair of probes was placed parallel to the coal face. The spacing between each pair of probes was around 100 m in order to achieve the optimised coverage of the study area. To make best use of the probes, the probes initially located at 1a-2a (1b-2b) were later moved to 1a'-2a' (1b'-2b') after the passing of the face-line. Each probe was fixed into floor coal with a 1.5 m long anchor as depicted in Figure 5.9. Cement was used to ensure the coupling between probes and coal. Microseismic data recorded by the probes were sent to surface via the data transmission system as illustrated in Figure 5.10.

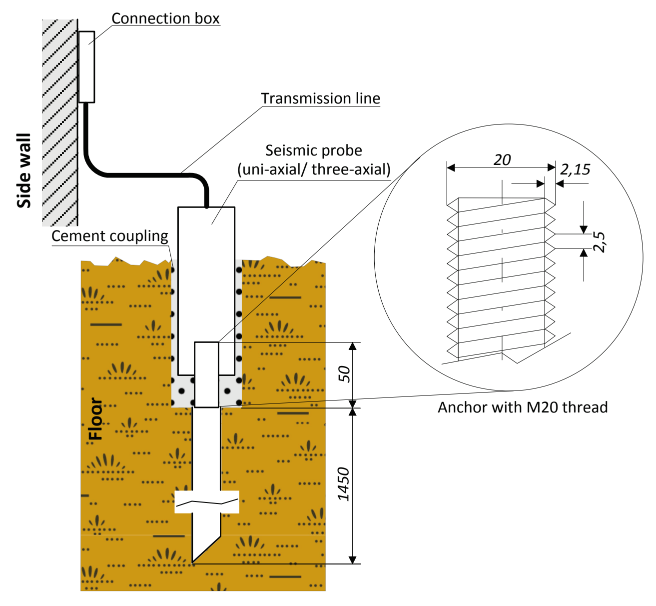

Figure 5.9: Schematic of geophone probe installation(after Si *et al.*, 2015b).

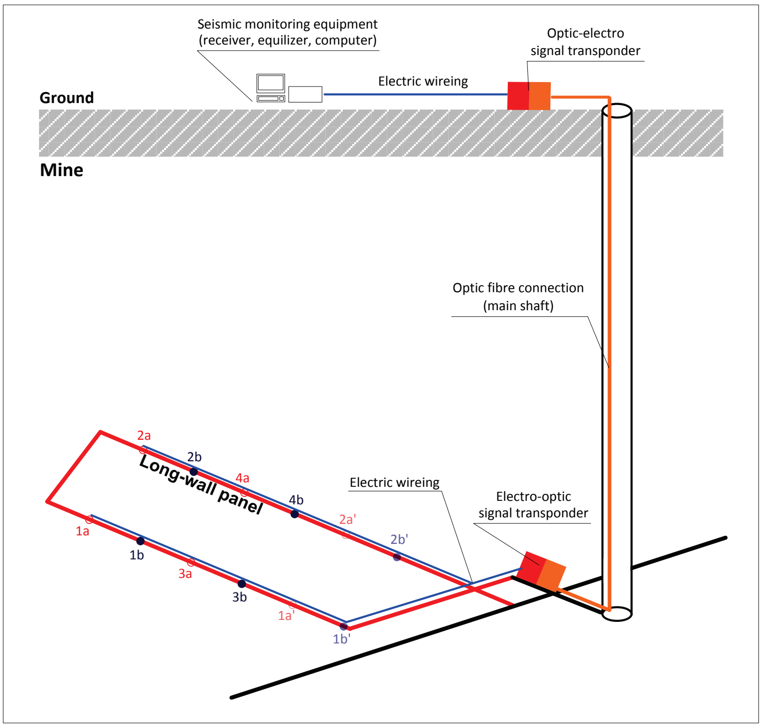

Figure 5.10: Schematic of the data transmission system (after Si *et al*., 2015b).

5.4.3 Preliminary Data Analysis Conducted by the Central Mining Institute

The recorded raw data was post-processed by the Central Mining Institute (GIG) using the MULTILOK software, which implements Equation 5.6 to calculate the seismic energy of mining-induced events, as well as determining the arrival time of longitudinal and transverse waves and the location of microseismic events. Furthermore, the MULTILOK software has built-in modules to convert energy into magnitude as well as calculating seismic source parameters based on Brune's model (1970; 1971).

Over 2,000 microseismic events were recorded as a direct result of coal extraction at the K.-50/C LTCC panel during the monitoring period between 27 April and 30 August 2011. Figure 5.11 illustrates the correlation of daily face advance, seismic activity and seismic energy at LTCC panel K-50/C. Over the same period, there also was a recorded episode of relatively high gas emission in the same longwall district (see Figure 5.3).

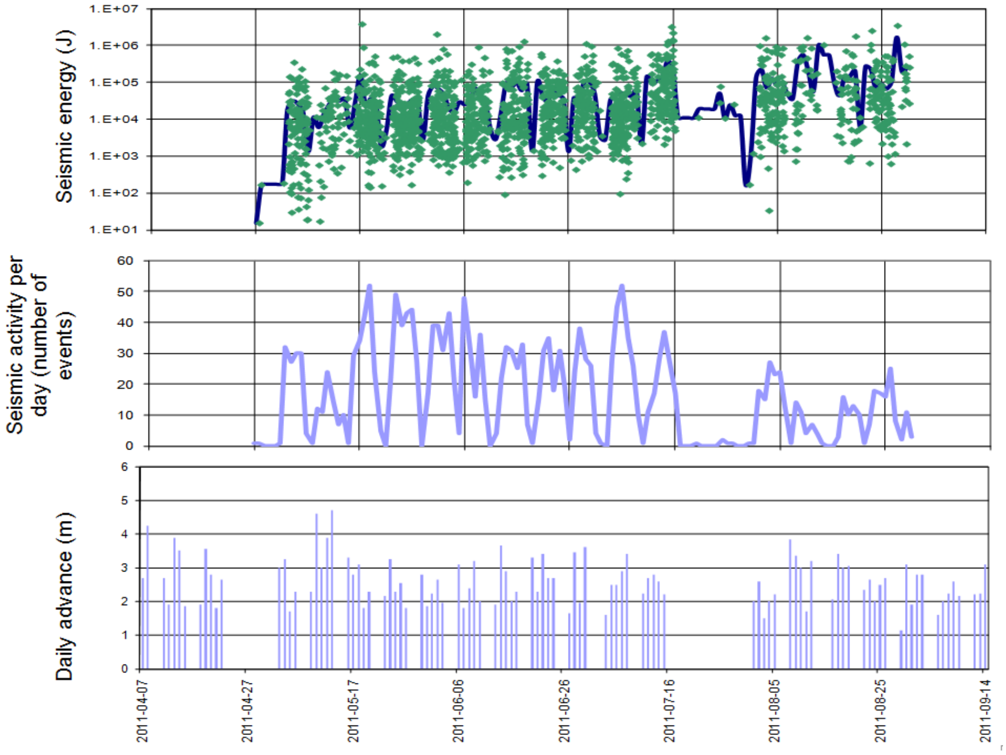

Figure 5.11: Daily seismic activity, seismic energy and face advance at LTCC panel K-50/C in Coal Mine Velenje during the monitoring period (Courtesy of GIG researchers).

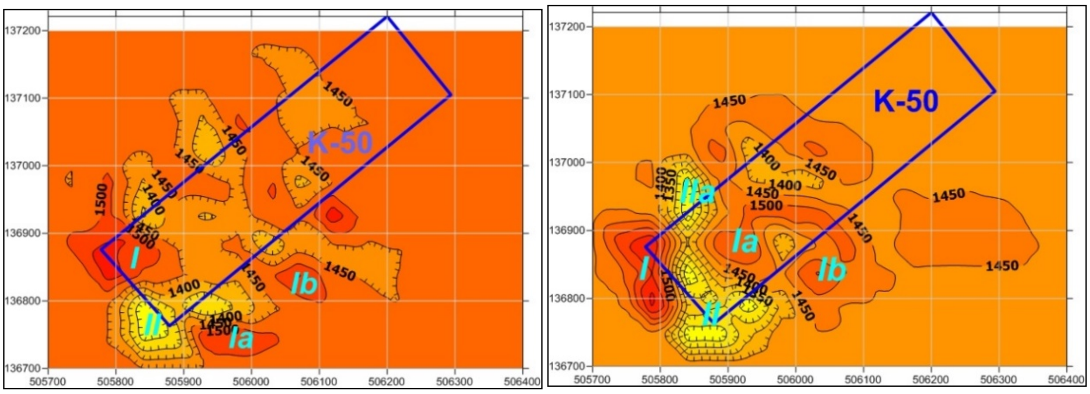

(a) 27 April to 22 May 2011

(b) 23 May to 19 June 2011

Figure 5.12: Bent-ray tomography P-wave velocity images (units m/s) obtained using seismic events recorded from (a) 27 April to 22 May 2011 and (b) 23 May to 19 June 2011 for K.-50/C LTCC panel in Coal Mine Velenje (Courtesy of GIG researchers).

Using microseismic data as the passive source P-wave velocity tomograms were constructed by GIG (see Figure 5.12). It was concluded that the high P-wave velocity zones correlate with the highest stress zones due to a combination of mining and local geological conditions. The zones of the lowest P-wave velocity may correlate with weaker or fractured coal seam and in these zones more intensive gas emission may be expected. However, these assumptions proposed in the preliminary analysis needed to be supported by further analysis of gas emission data at K.-50/C.

5.4.4 Analysis and Interpretation of the Processed Microseismic Data

Preliminary analysis of the processed microseismic data showed a strong link with the mining activity: there was little or no microseismicity at weekends or during the holidays when coal extraction was halted. Furthermore, during a production week, the intensity of seismic activities experienced was the lowest on Mondays (Figure 5.13). As shown in Figure 5.14, the seismic magnitude *M* (Gutenberg and Richter, 1956) of most of the mining-induced microseismic events fell in the range -1.5 to +1.0, which is consistent with that observed by Fujii and Ishijima (1991).

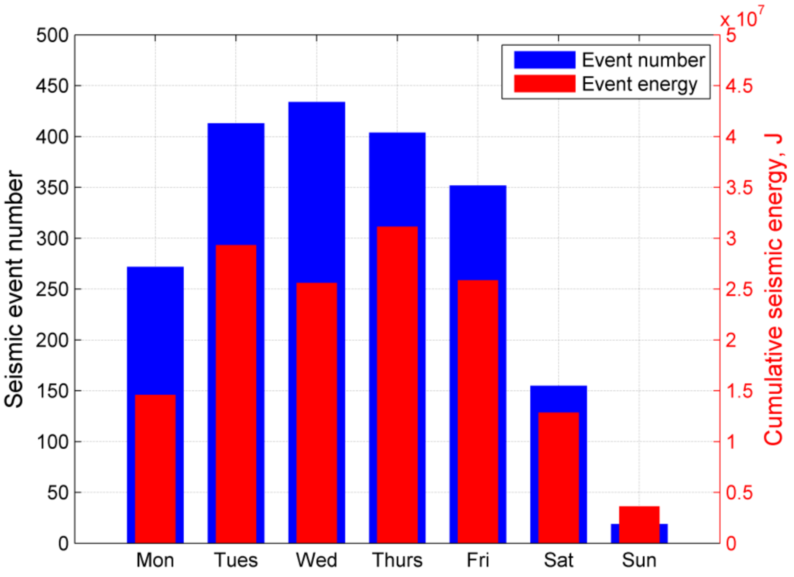

Figure 5.13: Weekly distribution of mining-induced seismic events from 2 May to 30 August 2011.

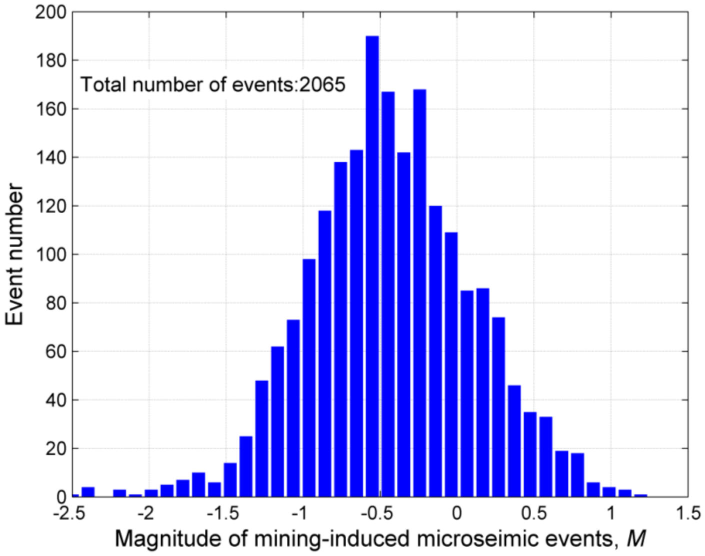

Figure 5.14: Richer-Gutenberg magnitude-frequency plot for mining-induced microseismic events.

The increase in seismic activity is interpreted as discontinuous deformation of the coal seam and surrounding rocks, thereby increasing their permeability and allowing more intensive migration of gases. The increase in seismic activity may be one of the precursors of increased gas emission which may support real-time risk assessment during mining.

In an effort to gain an understanding of the induced microseismicity due to mining activity, the microseismic data was plotted and analysed on a weekly basis. Figure 5.15 illustrates an example plot of the spatial distribution of microseismic events. In the figure, red circles denote the events recorded during the week 23 to 29 May 2011, with the size of the circles reflecting the energy intensity released.

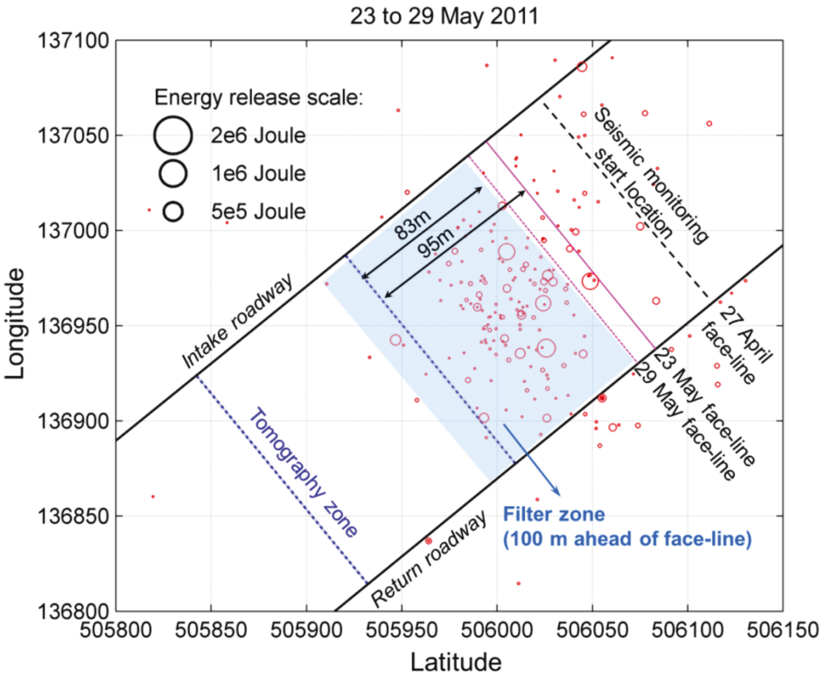

Figure 5.15: An example plot of the spatial distribution of microseismic events with respect to the face-line positions at K.-50/C LTCC panel.

Examination of the spatial distribution of the recorded microseismic events has shown that most of the microseismic activity occurred ahead of the advancing face. Similar observations have also been reported in coal mines in Australia and the US (Gale *et al.*, 2001; Iannacchione *et al.*, 2005). Considering that mining stress disturbance can reach as far as 100 m ahead of an advancing face, it was decided to track the face position at each week and focus on microseismic events which occur within a moving rectangular area up to 100 m ahead of the coal face (blue area laterally bounded by the two roadways in Figure 5.15) throughout the data analysis.

Microseismic events falling outside this range were considered to be not directly related to the mining activities at this face and were filtered.

The two repeat (or time-lapse) seismic tomography campaigns discussed before were also conducted in the area outlined by the two blue dotted lines and the roadways shown in Figure 5.15. As the LTCC face advanced over a period of several weeks, the seismic tomography and microseismic data analysis zones have overlapped, which will be discussed later in the Chapter.

Figure 5.16 shows the spatial distribution of the weekly microseismic events over a period of 12 weeks, during which the coal face advanced 139 m. It can be seen that the events predominantly occurred within 70 m of the advancing coal face and tended to concentrate in the central region of the face width. With the advance of the longwall face, the new microseismic events tended to cluster and form a cloud, and be localised at certain areas. As shown in Figure 5.16 (d), the start of microseismic event localisation is characterised by new events (red circles) with relatively low energy, occurring in a ‘virgin’ area and further away from the coal face. This is probably because the near face area was already highly fractured. As the face advanced further in the following weeks, new microseismic events with increased seismic energy occurred in the same area (Figures 5.16 e to i). By the time week 8 - 14 August 2011 is reached, a dense cloud of microseismic events was formed in this area, which was highly fractured and close to the face-line (Figure 5.16 j).

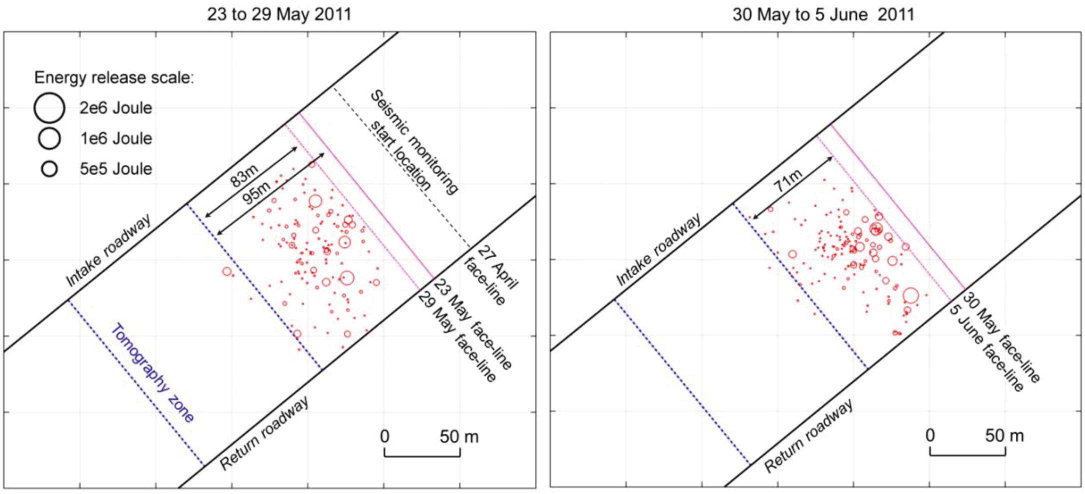

(a) Week 23 to 29 May 2011 (b) Week 30 May to 5 June 2011

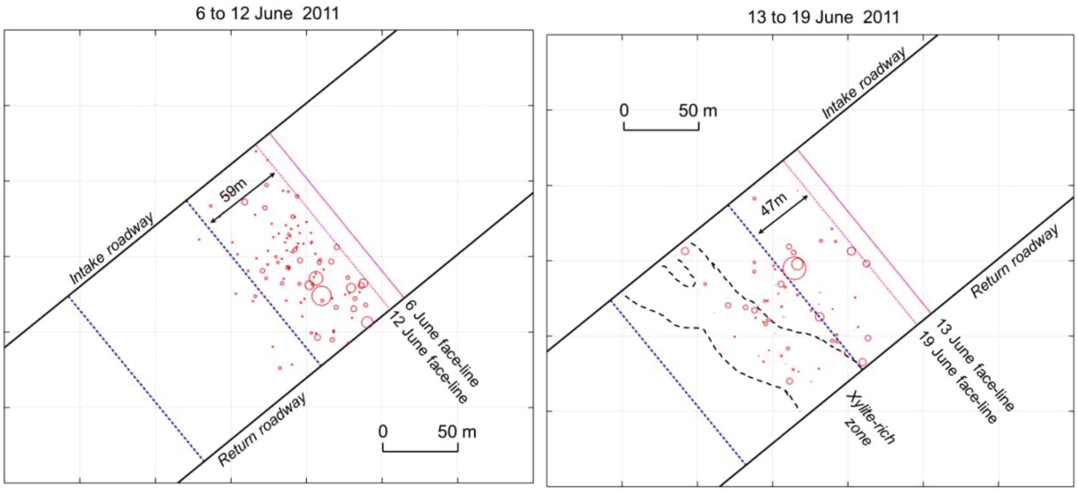

(c) Week 6 to 12 June 2011 (d) Week 13 to 19 June 2011

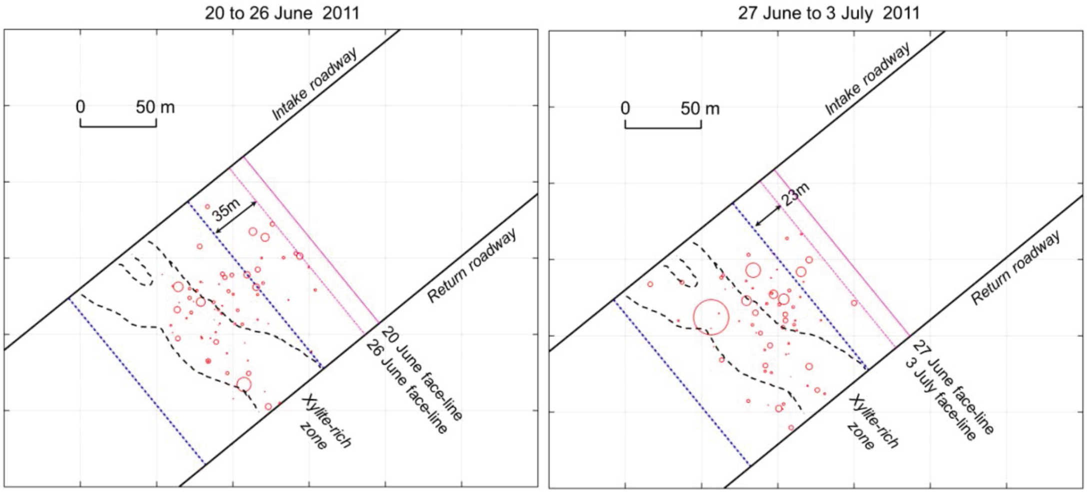

(e) Week 20 to 26 June 2011 (f) Week 27 June to 3 July 2011

Figure 5.16: Spatial evolution of microseismic events leading to an episode of increased gas emission at K.-50/C LTCC panel.

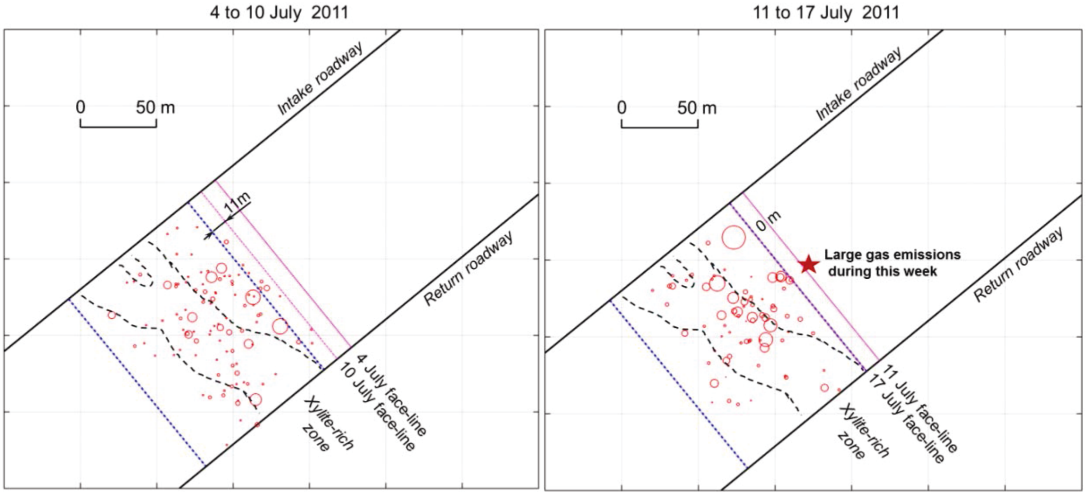

(g) Week 4 to 10 July 2011 (h) Week 11 to 17 July 2011

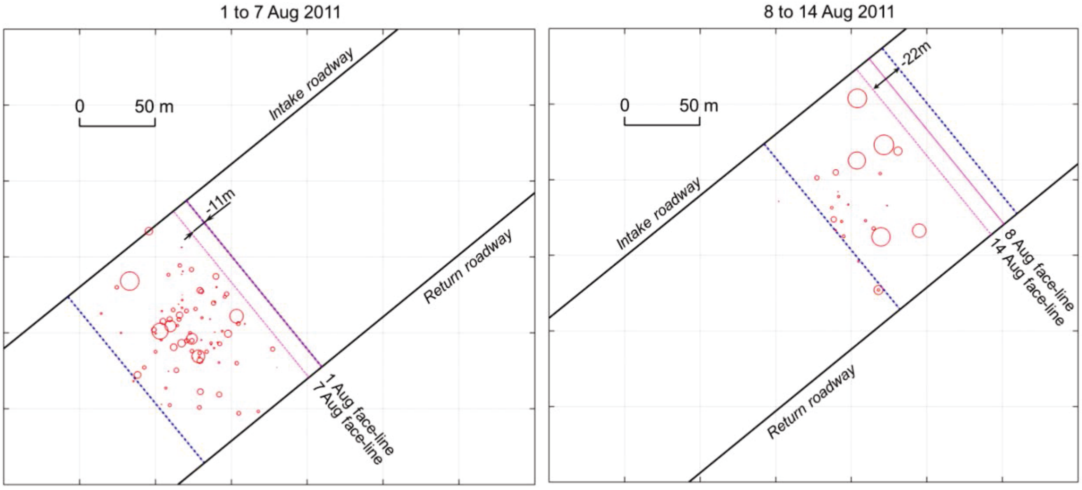

(i) Week 1 to 7 August 2011 (j) Week 8 to 14 August 2011

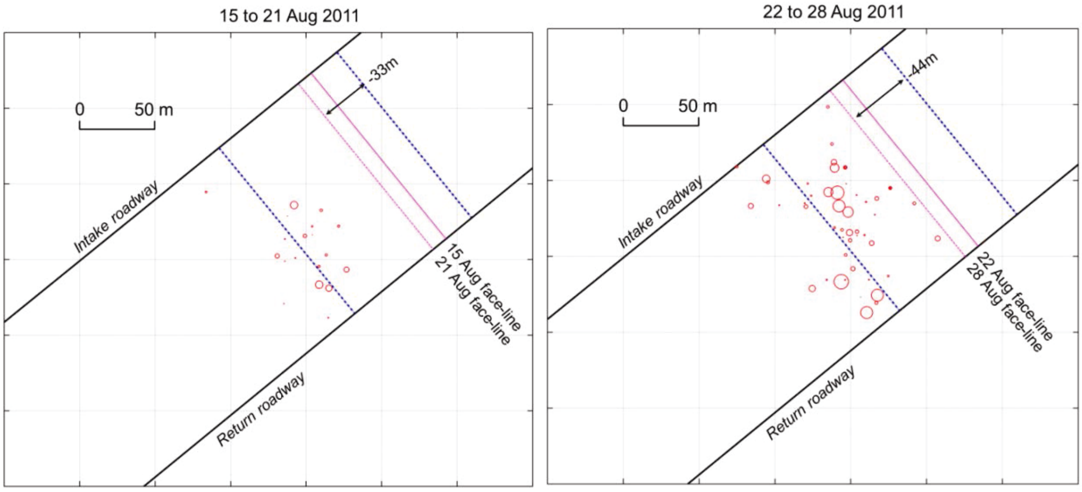

(k) Week 15 to 21 August 2011 (l) Week 22 to 28 August 2011

Figure 5.16: Spatial evolution of microseismic events leading to an episode of increased gas emission at K.-50/C LTCC panel (Continued).

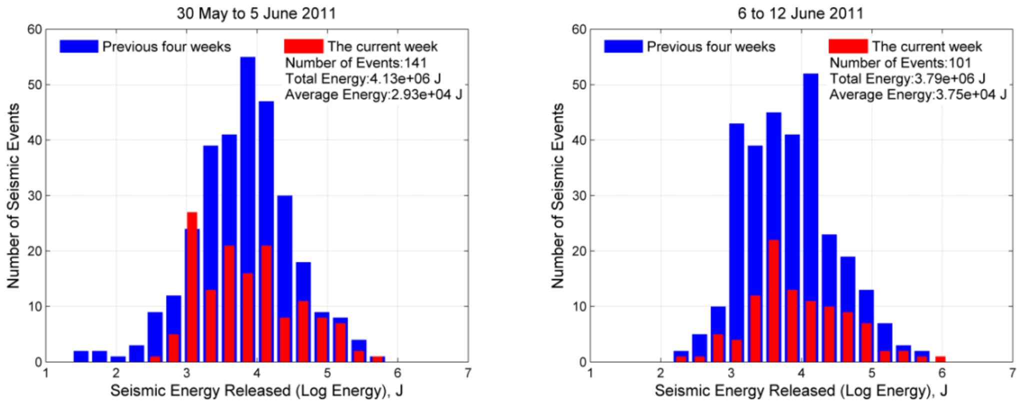

(a) Week 30 May to 5 June 2011 (b) Week 6 to 12 June 2011

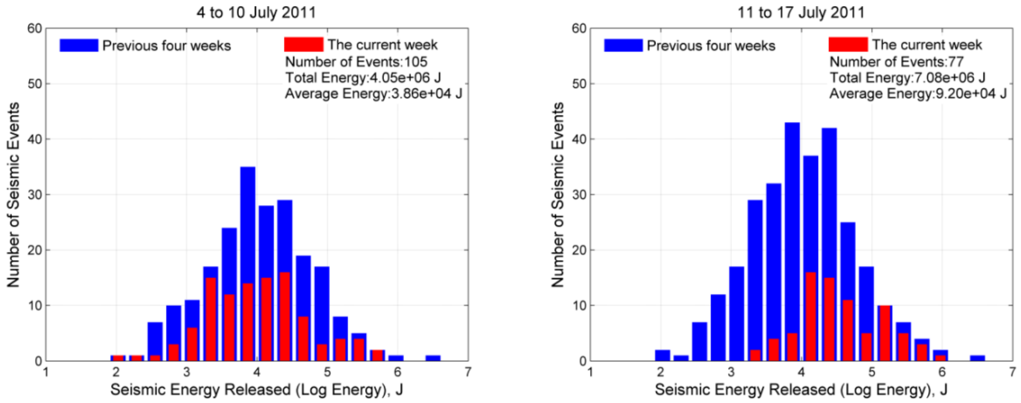

(c) Week 4 to 10 July 2011 (d) Week 11 to 17 July 2011

Figure 5.17: Analysis of seismic energy released in a production week and previous weeks.

In order to analyse the energy released by the microseismic events, histograms of the energy released per week have also been plotted (see Appendix 2). Four examples of the weekly microseismic energy histograms are shown in Figure 5.17. In this figure, red bars indicate the statistics of the new events which occurred during the reference week; while blue bars represent the events which occurred during the previous four production weeks. As can be seen, the energy released by different events varied significantly, spanning as much as four to five orders of magnitude. The distribution of microseismic events within a production week follows a Gaussian distribution. A notable shift of the red bars to the right (higher energy levels) was observed during the week of 11 to 17 July 2011 (Figure 5.17 d). Although the number of events recorded during this week was relatively smaller, the total energy released reached a maximum, coinciding with the unusually high gas emission episode which interrupted the coal production at the face on 15 July 2011.

5.4.5 Results and Discussions

5.4.5.1 Correlation Between Increased Gas Emissions and Microseismicity

Since the geophones placed in the gateroads at LTCC panel K. -50/C could not be spaced widely in the vertical plane, the hypocentres of detected events are not well constrained vertically, on the other hand, horizontally, a relatively high accuracy (within 5 to 10 m) is expected. Although microseismic monitoring did not provide sufficient data on the sources and migration of gases in the vertical plane, most detected events were assumed to occur within the coal seam and around the mining level, given the large thickness of each LTCC level, as well as the coal deposit itself. The spatial distributions of seismic events induced during the production weeks from 23 May to 12 June 2011 (Figures 5.16 a, b, and c) suggest that seismic events mostly occurred within 40 m of the face. The variation in the spatial distribution of the seismic events from 13 June 2011 onwards is believed to be caused by coal heterogeneity.

Figure 5.18 presents a cross-plot between the gas flow rate (at 30 minute intervals) and the cumulative seismic energy released during 11-17 July 2011 period. Although the mine normally works three shifts per day and each shift is 8 hours (06.00 to 14.00, 14.00 to 22.00 and 22.00 to 06.00) the production schedule at LTCC panel K. -50 C, had to be rescheduled as 2 shifts of production and 1 shift of pause cycles because of increased gas emissions experienced in the district. As shown in Figure 5.18, the gas emission peaks are normally reached during the night (or the second production shift). The most significant increase in gas emission was experienced during the early hours of 15th July 2011, which increased by 80% and peaked at 179 m^3/min within two hours. This also coincides with the heightened microseismic activity identified for the 11-17 July 2011 production period (Figures 5.16 h and 5.17 d). Figure 5.18 also confirms that there is a direct correlation between microseismicity and the gas emission rate, and that gas emission rate tends to reach a peak when seismic energy increases dramatically.

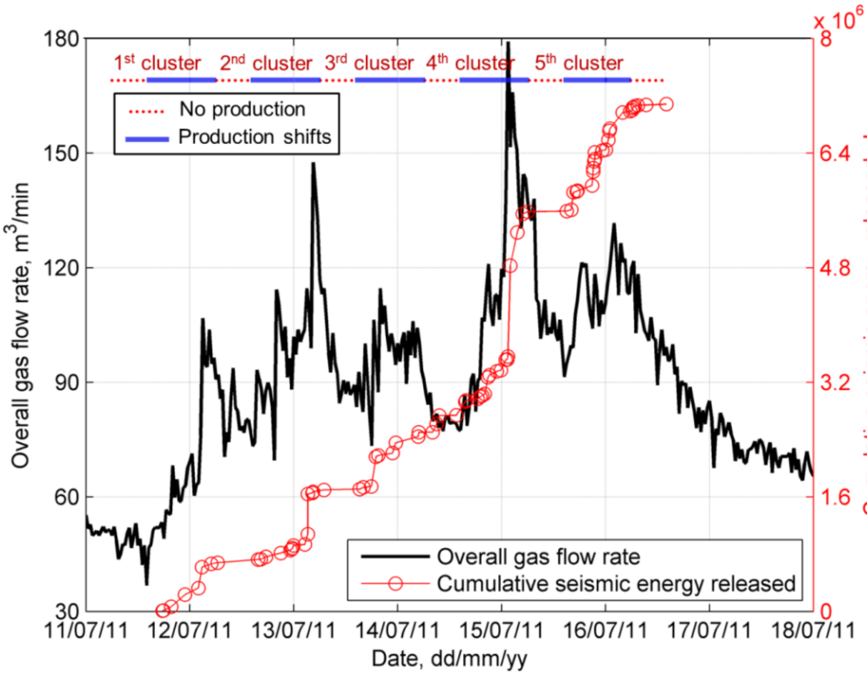

Figure 5.18: Microseismic activities and gas flow rate during the week of increased gas emissions (11 to 17 July 2011).

As mentioned earlier, a xylite-rich zone has a high mechanical strength and, if this zone creates a barrier in front of a low mechanical strength and high gas content detritic coal, this may result in gas build up and a sudden emissions of gas when the stress abutment exceeds the strength of the gas barrier as the face gets closer to this zone. It is believed that, as marked in Figures 5.16 and 5.19, a xylite-rich zone located ahead of the face-line has formed one such barrier, progressive fracturing and eventual failure of which eventually led to the increased gas emissions. This would also explain the significant increase in microseismic energy released during this week and its correlation with the high rate of gas emitted.

In view of reduced coal production schedule at LTCC panel K. -50/C, the microseismic events which occurred during this week were organised into five clusters to match the timing of production shifts at the same longwall district (Figures 5.18 and 5.19). The spatial distribution of each cluster of microseismic events is presented in Figure 5.19, which helps to identify the sources of gas emission peaks. As the figure illustrates, the majority of high energy (>10^4 Joule) microseismic events are located in an area between 30 to 50 metres ahead of the coal face, which also overlaps with the xylite-rich zone confirmed by the 1st seismic tomography data (Figures 5.4 to 5.6). This is reasonable as relatively stronger xylitic zone can, for some period of time, withstand the higher stress concentration experienced along the transition zone between solid coal roof (to the NW) and the partially mined out zone (to the SE) over this LTCC panel but, once it fails, more seismic energy will be emitted. At the time of highest gas emission recorded on 15 July 2011, the LTCC face had reached the edge of the tomography zone, bordering on the xylite-rich coal zone, causing extensive fracturing of the xylite-rich barrier and releasing the gas trapped in the detrite-rich coal behind.

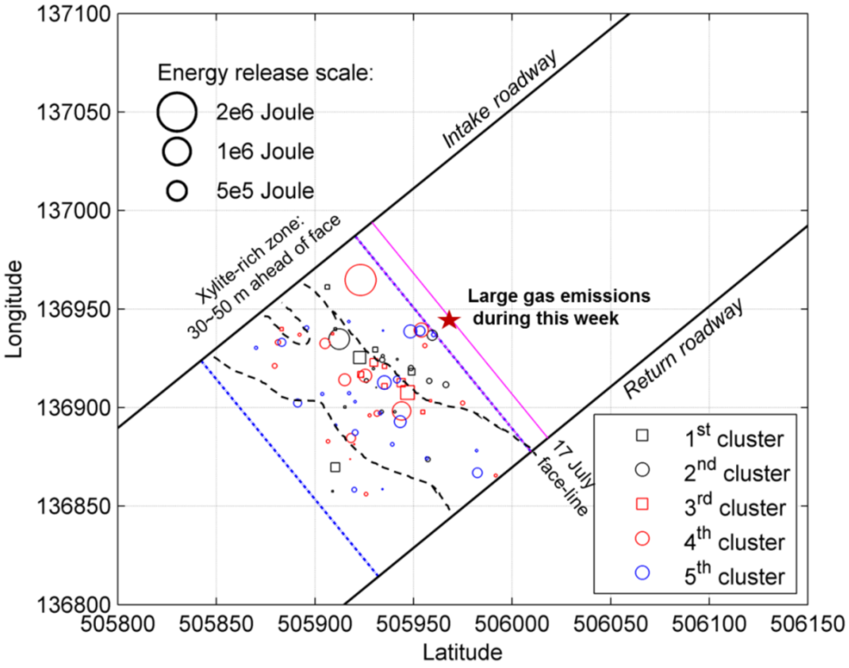

Figure 5.19: Spatial distribution of microseismic clusters observed during the week of increased gas emissions at K.-50/C LTCC panel (11 to 17 July 2011).

5.4.5.2 Fractal Dimension as an Indicator for Fracture Network Evolution

Fractal dimension is an effective measure to characterise the fracture patterns in rock failure process (Balankin, 1997; Poliakov *et al.*, 1994; Zhao *et al.*, 1993). During the analysis of the microseismic data, an attempt was made to compute the fractal dimension (D) of recorded weekly events in order to characterise the fracture network induced by mining. A box counting method was used (Barton and Larsen, 1985), whereby the study area ahead of the face-line (blue area referred to as the "Filter Zone" in Figure 5.15) was first discretised into 2D small boxes of $p \times p$ in length. A script written in MATLAB was then run to count the number of boxes (N) which contain at least one event. By varying the size of the box (p), N as a function of p can be obtained for the determination of fractal dimension D:

$$N \propto p^{-D} \qquad 5.7$$

By plotting log(N) against log(p), the slope of the straight-line section can be used to compute D as illustrated in Figure 5.20. Same box size range, log(p) from 0.8 to 2.0, was used to fit the straight lines for individual weeks. The lower boundary of the straight line fitting was selected based on Odling (1997), in which the cut-off point was suggested as 5% to 10 % of the study region size. The spatial distribution of microseismic events for each coal production week presented under Figure 5.16 is shown in Figure 5.21, which illustrates that the fractal dimension of the weekly seismic events displays a positive correlation with the measured gas flow rate. The calculation of fractal dimensions for the rest of production weeks can be found in Appendix 3.

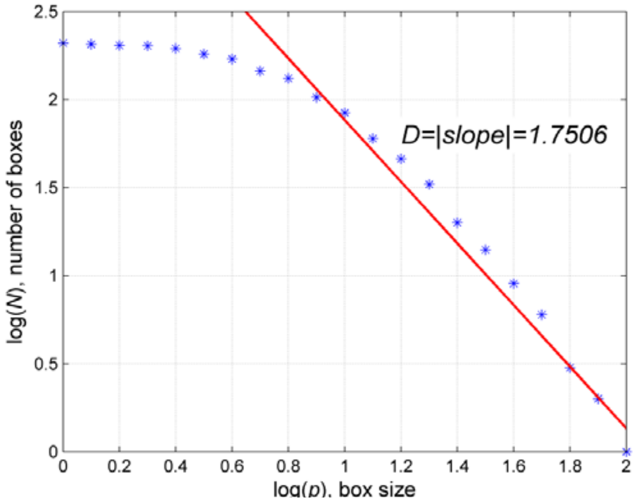

Figure 5.20: Calculation of fractal dimension by box counting (week 11 to 17 July 2011).

These preliminary analysis has shown that the fractal dimension increased steadily, from just below 1.60 to 1.75 over the 8 weeks period leading to the heightened flow rate. Following the two-week holiday period, the fractal dimension of the seismic events started to drop, after peaking as the production was resumed. It is clear that, during the two week holiday period, the gas emission was significantly reduced as no coal was produced, however, the microseismic activity continued with further fracturing of the xylite-rich zone and the re-settlement of the roof coal and the goaf.

Investigating rockbursts in mines, Lu *et al*. (2005) concluded that fractal dimension decreases as the degree of clustering of microseismicity increases, and this might be used as a possible precursor of a catastrophic failure in the roof or floor rock.

However, in the episode of increased gas emissions, an increase of fractal dimension, rather than a drop was observed. This may be attributed to different mechanisms between roof failure and gas outbursts. The former may be initiated by a massive linear failure at roof, while the latter requires an extensively fractured area to provide flow paths and gas sources.

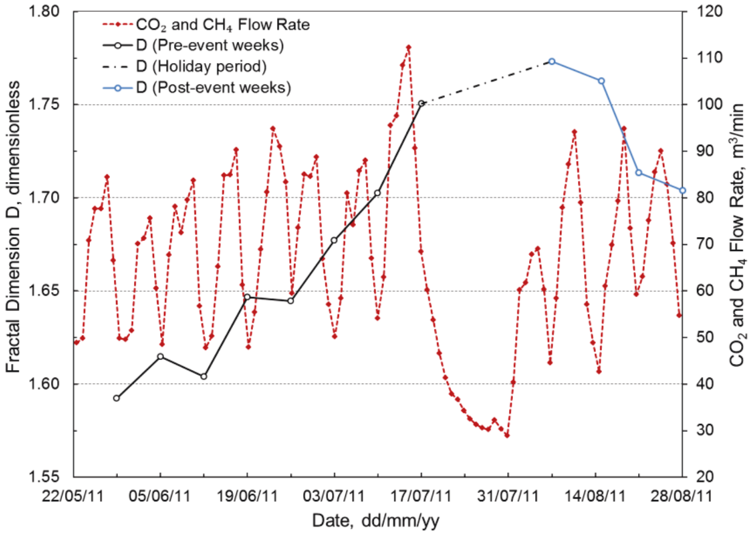

Figure 5.21: Evolution of fractal dimension against the flow rate of gas emitted during 23 May to 28 August 2011.

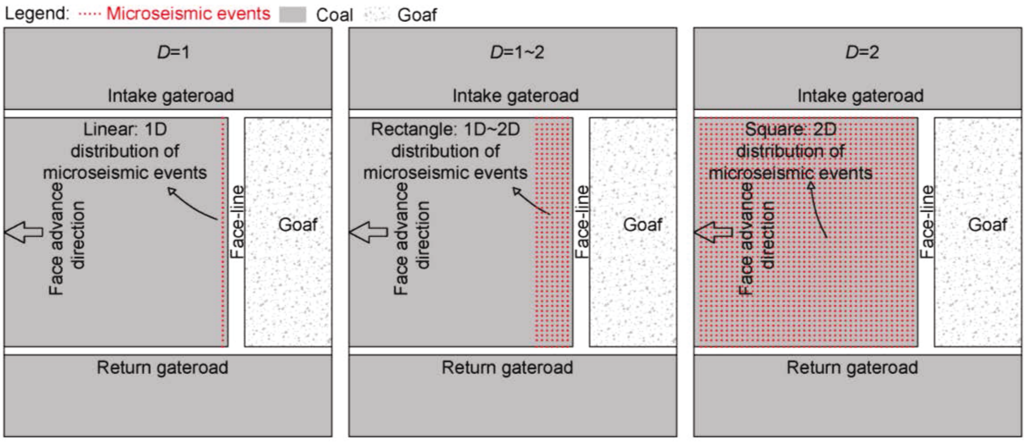

Figure 5.22: The relationship between fractal dimension and the idealised spatial distribution of microseismic events in a longwall panel.

As illustrated in Figure 5.22, given the distribution of mining abutment stresses, the most likely location of microseismic events are in a rectangular area ahead of the longwall face (*D*=1~2). The observed increase in the fractal dimension may suggest that the mining induced fractures evolve and form a two-dimensional network over a period of time and extend further away from the face. If, a flow barrier, such as the xylite-rich zone observed at LTCC face K.-50/C exists in this moving front ahead of the longwall face, progressive fracturing of this zone (represented by increasing *D*) would at some point form a flow conduit and lead to an excessive gas emission or a gas outburst.

5.5 Conclusions

A suite of monitoring techniques has been employed to investigate the dynamic response of the coal seam being mined to longwall face advance at Coal Mine Velenje in Slovenia. The data obtained from ventilation environment monitoring, time-lapse seismic tomography, and microseismic monitoring at LTCC panel K.-50/C were analysed and integrated. The following observations were made:

- The onset of microseismic events ahead of an advancing LTCC face tended to be localised over relatively stronger zones, such as the xylite-rich coal.
- A marked increase (by ~ 80% in two hours) in gas emission at the study LTCC face coincided with the period where there was heightened microseismic activity.
- Seismic tomography can accurately detect coal heterogeneity and reflect mining-induced stress changes around a longwall panel
- A detailed analysis of microseismic events which occurred during the week of excessive gas emissions suggests the spatial and temporal clustering of microseismic events at the heterogeneous zone indicated by seismic tomography.
- Although the number of seismic events recorded during the week when excessive gas emissions interrupted production was relatively smaller, the total energy released during this week reached a maximum, coinciding with the unusually high gas emission episode.
- Fractal dimension, estimated from the spatial density of the recorded microseismic events, displays a positive correlation with the measured gas flow rate.

As reported earlier in Chapter 4, a comprehensive borehole gas pressure and composition monitoring programme around production faces at Coal Mine Velenje has shown that, an extensively fractured “near face fracturing zone”, within ~40 m of the LTCC faces in the upper mining levels of the seam contributes significantly to the gas emissions in a longwall district. A conceptual gas emission model proposed at the end of Chapter 4 also suggested that, a relatively strong xylite- rich zone forming a barrier in front of a high gas content but relatively weaker detrite-rich zone may be the cause of increased gas emissions or gas outbursts at the mine. A detailed analysis of the spatial concentration of the microseismic events and gas emission rates described in this Chapter provides further evidence towards this conceptualisation.

The underground testing of active time-lapse seismic tomography have confirmed that geological anomalies, such as the xylite-rich zone at Coal Mine Velenje, as well as increased stress abutments can be detected by this technique. However, this technique requires significant underground activity and staff time, yet it is not effective in providing continuous remote monitoring data. On the other hand, long term real-time microseismic monitoring has the advantages of detecting high stress zones and fracturing of the coal around mine openings to provide early warning for the potential occurrence of high rates of gas emissions and perhaps even outbursts.

Although no coal or gas outbursts have been observed during the microseismic monitoring period at LTCC face K.-50/C, the strong correlation between the episode of excessive gas emission and the increased microseismic activity strengthens our confidence in using microseismic monitoring as a tool for the early detection of mining conditions which may lead to gas and/or coal outbursts and help take preventative measures. The proposed approach by using fractal dimension to characterise mining induced microseismic activity may provide a quantitative methodology to predict excessive gas emissions or gas/coal outbursts. However, this methodology needs to be further validated through long-term field measurements and in-depth analyses of monitored microseismic data.

As already discussed in Chapters 4 and 5, the analysis and interpretation of different sources of field data helped establish an understanding of gas dynamics around working LTCC panels. Nevertheless, field measurements can only reflect the underground conditions in an area where these measurements are taken. Numerical simulation of mining scenarios, on the other hand, can help further this knowledge and obtain an in-depth understanding of the global stress and pressure changes around LTCC faces. The following chapters will therefore focus on the development of numerical models for simulating mining activities and associated gas emissions around LTCC panels.

Chapter 6 Numerical Modelling of Gas Emissions around Longwall Top Coal Caving Panels

6.1 Introduction

This chapter focuses on numerical modelling of gas emission patterns around LTCC panels. Recognising that gas emissions into a LTCC face is a process involving interactive physics between geomechanics and fluid flow, a two-way coupling approach is proposed. Preliminary numerical tests are then performed to optimise computational time and simulation accuracy. After that, using the field data presented in Chapters 4 and 5 as the input, a field-scale model based on the K.-50/C LTCC panel at Coal Mine Velenje is developed. About three months of face advance and associated gas emissions are simulated and matched with field data. The modelling results provide a new insight into the gas emission patterns in advancing LTCC faces.

6.2 Methodological Development for Coupled Gas Emission Modelling

6.2.1 Two-way Coupling Model Workflow

Modelling of gas emissions in a longwall panel can be carried out through either one-way or two-way coupling of a geomechanical and flow simulator. With one-way coupling, mining induced dynamic stress changes are first solved using the geomechanical simulator assuming a constant pore pressure field in the model domain. The computed (effective) stress profiles, which evolve with the advance of the face, are used to estimate corresponding permeability changes in the mined coal seam and the surrounding strata. The prevailing permeabilities around the mining opening at each excavation step are then used in the flow simulator to obtain the pressure field and compute the gas emission rates. In this way, the impact of mining induced stress changes on gas flow around the mine openings and gas emission rates are accounted for. This coupling approach is justified since stress wave propagation is normally several orders of magnitude faster than pressure propagation (ITASCA, 2012), and thus stress equilibrium can be considered to be established almost instantly after each excavation step.

The main drawback of this simplified coupling approach is that there is no feedback from the output of the flow simulator back to the geomechanical simulator at the end of each excavation step to update the pore pressure distribution for computing the changes in the effective stresses in the next excavation step. This missing feedback is included in the two-way explicit sequential coupling workflow adopted in this work, as illustrated schematically in Figure 6.1.

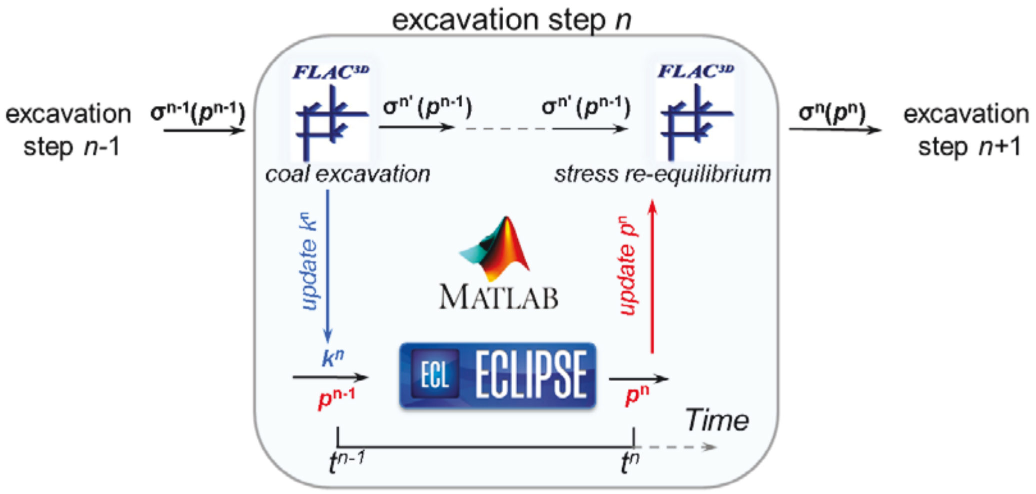

Figure 6.1: Model coupling workflow of FLAC^{3D} and ECLIPSE (modified after Rutqvist and Tsang, 2003).

The two-way coupling achieved in this research is between FLAC^{3D}, a widely used commercial software package for conducting advanced geomechanical analysis encountered in geotechnical engineering applications, and ECLIPSE 300 (Schlumberger, 2010), an industry standard compositional reservoir simulator which has a coalbed methane module. As shown in the workflow, pore pressure field ($p^{n\text{-}1}$) arrived at by the previous excavation step (n-1) by ECLIPSE 300 is passed on to

FLAC^{3D} to compute a provisional total stress ($\sigma^{n'}$) after coal extraction in the first instance of the current excavation step n, using the pore pressure field (p^{n-1}). Then, the permeability field k^n, which is computed based on the provisional total stress $\sigma^{n'}$ and pore pressure p^{n-1}, is sent to ECLIPSE 300 as the input to derive the pressure field (p^n) after coal extraction. The simulated fluid time from t^{n-1} to t^n represents the actual time spent in coal extraction activity at step n. The updated pore pressure field p^n is then fed back to FLAC^{3D} to re-equilibrate the disturbance caused by pressure change within step n. The final stress field σ^n at pore pressure p^n is then produced as the input for the next excavation step n+1. A special script was written in Matlab to facilitate seamless exchange of parameters between the two software packages. Since the permeability of coal is controlled by the effective stress, two-way coupling allows a more accurate representation of the dynamic permeability where significant changes in the pore pressure are expected, e.g. in the fractured zone around a longwall face.

6.2.2 Geomechanical and Gas Flow Modelling of Coal Excavation in a Longwall Top Coal Caving Panel

As with mechanised conventional longwall mining, face advance at a LTCC face in a given period of time (e.g. one weekday) is modelled as a single coal excavation step in FLAC^{3D}. Considering that the top coal is allowed to cave shortly after the coal underneath has been taken out by a shearer, the following procedure is adopted in the modelling of coal excavation/top coal caving and goaf recompaction: at each excavation step those elements in the grid representing the coal blocks to be extracted by shearer, and the associated top coal that is deemed to cave, are “removed” from the geomechanical model grid; these elements are “reinstated” at the next excavation step but assigned with the properties of a recompacted goaf material. Each excavation step in geomechanical modelling thus involves removing, simultaneously, of the elements to be mined/caved and reinstating the elements removed at the previous excavation step.

The elements used to represent reinstated goaf are simulated as totally elastic. Furthermore, to capture the behaviour of goaf recompaction, the elastic modulus of each goaf element is updated with the change of its volumetric strain after every excavation step. A simple reciprocal relationship between bulk (shear) modulus (K)

and volumetric strain (ε_V) of each goaf element is adopted to reproduce the strain-hardening behaviour of goaf as depicted by Equation 6.1:

$$K = \frac{K_0}{1-\varepsilon_V} \qquad 6.1$$

where K_0 is assumed to be one third of caved roof bulk modulus. The same principle also applies to the shear modulus. The elastic properties of the broken goaf material are based on observations that goaf material is highly compactable and its stiffness may increase during recompaction (Pappas and Mark, 1993). At each excavation step, the FLAC^{3D} model is solved to equilibrium to leave sufficient computational time-steps for the propagation of plastic zone and stress redistribution. Mohr-Coulomb failure criterion is used to evaluate failure of coal and coal measure rocks caused by coal excavation, and post-failure strength of the rocks is described using the strain-softening constitutive model.

In flow simulations using ECLIPSE, the low pressure sinks, namely the gateroads and the LTCC face, are modelled by placing a horizontal well with its pressure fixed at the ventilation pressure to the relevant elements (see Figure 6.9 c). Note that no ventilation air flow was simulated and thus the modelled gas flow in the gateroads and the face was the gas emitted from the coal seam alone. In order to keep up with the face advance, a group of horizontal wells is placed in advance at different face-line positions coinciding with the excavation steps. When the coal face moves to a new face-line position, the corresponding horizontal well at this position is set as ‘OPEN’, while the others remain ‘SHUT’. The gas produced from this well over one excavation step is then taken as the gas emission when the face-line reaches this position.

Since this model is designed to reproduce gas emissions during progressive face advance, the initial conditions representing the stress and pressure distributions before the first excavation step are almost impossible to be accurately assigned. Disturbances caused by roadway development or previous coal extraction outside the model domain are difficult to be evaluated. However, it can be assumed that progressive face advance normally results in a steady change of stress and pressure regimes around the LTCC panel. Although first several excavation steps in a simulation can hardly reflect reality, it may be useful in generating initial conditions for areas that are critical in the analysis of gas emissions. Therefore, a number of extra excavation steps are required to produce the relativistic initial conditions for a study area.

6.2.3 Stress Dependent Permeability

With the advance of coal face, it is expected that the coal seams and coal measure rocks around the coal face would undergo a cycle of ‘in-situ stress – stress abutment – failure and stress reduction – stress recovery’, as illustrated in Figure 6.2. Permeability of intact coal at *i* direction (k_i) has been shown to be highly stress dependent (Equation 6.2), through laboratory experiments and field measurements, decreasing exponentially with increasing stress or burial depth:

$$k_i = k_{i0} \cdot e^{-C\sum_{j=1}^{3}\Delta\sigma_j \cdot (1-\delta_{ij})} \tag{6.2}$$

where, k_{i0} (m^2) is the initial permeability for intact coal in i direction, C (MPa^{-1}) is the permeability compressibility factor for intact coal, $\Delta\sigma_j$ (MPa) is the stress change in j direction, and δ_{ij} is the Kronecker Delta.

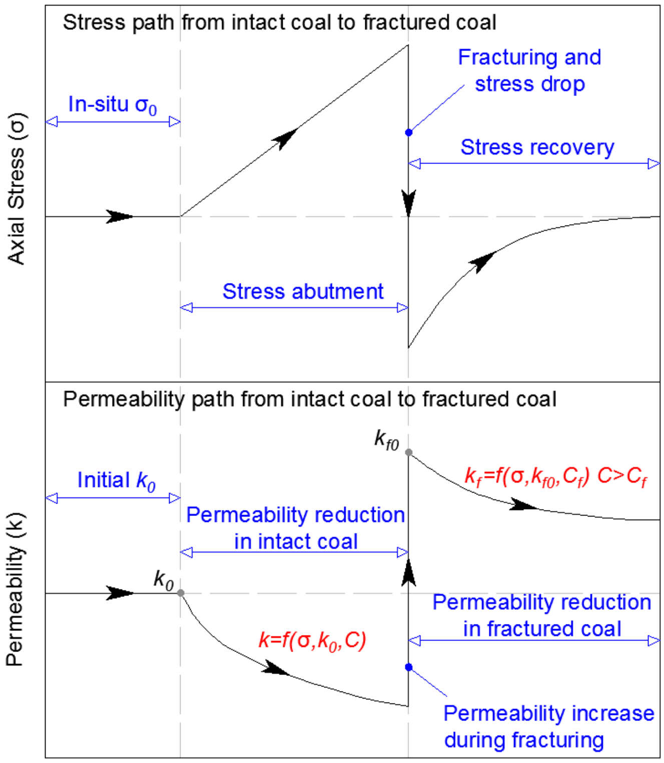

Figure 6.2: Conceptual stress and permeability paths from intact coal to fractured coal.

As mentioned in Section 2.4.2, the permeability compressibility factor C for a number of UK coals has been reported to be in the range of 0.38 to 0.73 and may be correlated with the fraction of volatile matter in coal as shown in Figure 2.10 (Durucan, 1981). Based upon the proximate analysis for the Velenje lignite samples, which yielded a volatile matter in the range from 34% to 47%, a permeability compressibility factor of 0.7 was used in this work.

The permeability of failed (fractured) coal is usually between one to two orders of magnitude higher than that of intact coal. Thus, it may be assumed that the permeability of coal within the stress abutment zone would experience a dramatic increase once it is failed and de-stressed (see Figure 6.2). It has also been shown that the post-failure permeability of coal tends to be less sensitive to stress than intact coal (Durucan *et al.*, 1993). In this work, in addition to Equation 6.2 for intact coal, a separate equation is employed to compute the permeability response of post-failure coals (Equation 6.3):

$$k_{if} = k_{if0} \cdot e^{-C_f \sum_{j=1}^{3} \Delta\sigma_j \cdot (1-\delta_{ij})} \tag{6.3}$$

where k_f (m^2) and C_f (MPa^{-1}) are the fractured coal permeability and compressibility respectively.

Velenje lignite disintegrates rapidly once it loses its moisture content in ambient conditions, therefore, it was not possible to determine its post-failure flow characteristics through long term stress-permeability experiments. In this study, the models were run using a range of k_{f0} (k_{f0} = 5k_0, 10k_0, and 20k_0) and C_f (C_f = 0.25, 0.45, and 0.65) values and the results compared with field observations.

The following assumptions were made when representing the permeability of mine openings and voids: elements representing the gateroads and the excavated (including both extracted and caved) coal in an excavation step were assigned with a permeability value of 1×10^{-11} m^2. It is rather difficult to accurately define the goaf permeability since the goaf is formed of a large number of disordered coal/rock fragments. For a detailed investigation on how to predict goaf porosity and permeability one can refer to Karacan (2010), whereby fractal scaling in porous media is integrated with the principles of fluid flow. Here, a relatively simplified assumption was made such that the goaf permeability also follows a stress dependent permeability relationship (Equation 6.3), but with a much higher initial permeability (1×10^{-13} m^2). Given the increasing stiffness of goaf material during gradual recompaction as explained in Equation 6.1, stress recovery as well as a reduction in goaf permeability can be expected, which is updated at every excavation step as shown in Figure 6.1. This simplified assumption is justified since the goaf area close to the face normally has low pressure and low gas content. Thus, compared with other gas emission sources, such as the solid coal face, gas emission from the goaf accounts for a relatively small portion of overall gas emission in a longwall district.

6.3 Preliminary Numerical Experiments

6.3.1 Grid Resolution along the Face Advance Direction

The first problem that needed to be addressed was the selection of grid size along the face advance direction. A high resolution grid cannot only represent the dynamic movement of face advance as detailed as possible, but also would not produce accurate prediction of stress and pressure distributions induced by mining. On the other hand, a refined grid will inevitably increase the computational time required for problem solving.

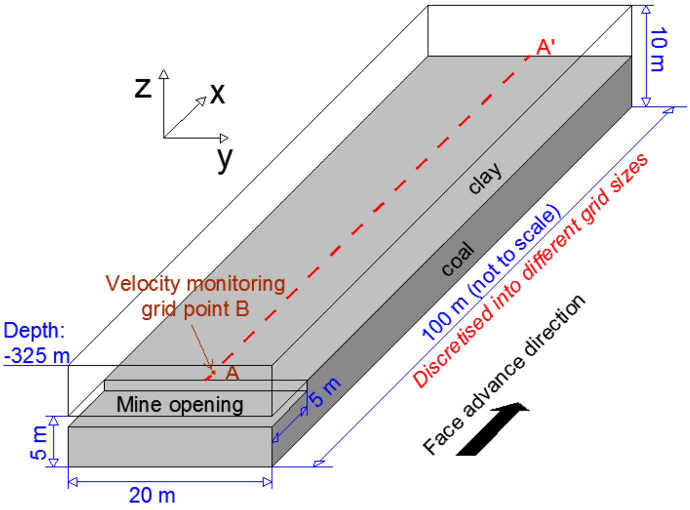

Figure 6.3: Schematic representation of the model geometry for the grid size assessment.

As shown in Figure 6.3, a simple model was developed to study the dependency of model results on grid size. A 5 m thick coal seam under 5 m thick clay roof was simulated. Vertical loading to reproduce the weight caused by a 325 m thick overburden was applied at the top of the model domain. The model domain was 100 m long along its x-axis, which was also assumed as the face advance direction. Seven scenarios with different grid sizes (0.50 m, 0.75 m, 1.00 m, 1.50 m, 2.50 m, and 5.00 m) along the x-axis were modelled. Model grid dimensions along y-axis and z-axis were set as uniform at 1 m for all the scenarios.

The initial stress equilibrium was established before any excavation was performed. The boundary conditions of the model were such that it was laterally confined and fixed at the base. Only an elastic model was used in this experiment and the mechanical properties used are listed in Table 6.1.

Table 6.1: Elastic properties used in the model.

Lithology	Bulk modulus (GPa)	Shear modulus (GPa)
Coal	0.90	0.19
Clay	1.10	0.24

After initial stress stabilisation, a mine opening which is 5 m long and 1 m high was created in the very front part of the model as shown in Figure 6.3. Then the model was run to reach a new equilibrium with a mechanical ratio as 1×10^{-5} (to be discussed in the next section). Horizontal stress (along the x-axis) and node vertical displacement profiles along Section A-A’ obtained for all seven scenarios are plotted in Figure 6.4. The computational steps required to reach equilibrium for different grid sizes are shown in Figure 6.5.

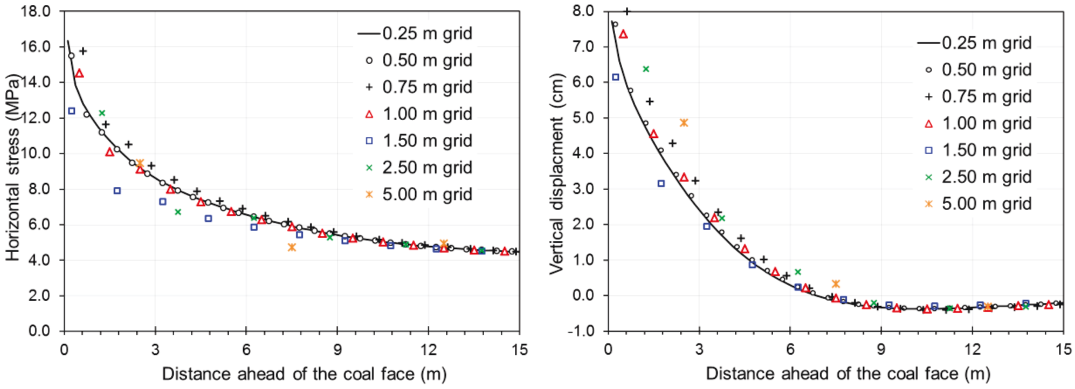

(a) (b)

Figure 6.4: (a) Horizontal stress and (b) vertical displacement profiles for different scenarios.

As indicated in Figure 6.4, notable difference in stress and displacement profiles can be observed by varying the grid sizes, especially close to the production face area. Using the 0.25 m grid scenario as the benchmark experiment, it was clear that scenarios with grid sizes lower than 1.0 m can overall capture the stress and displacement changes induced by mining. However, the number of computational steps used also increases dramatically for scenarios with smaller grid block sizes (Figure 6.5 a). As shown in the logarithm plot of cumulative error against grid block size (Figure 6.5 b), the order of convergence is close to unit. This suggests increasing grid block size by one order of magnitude can linearly amplify the error by the same magnitude.

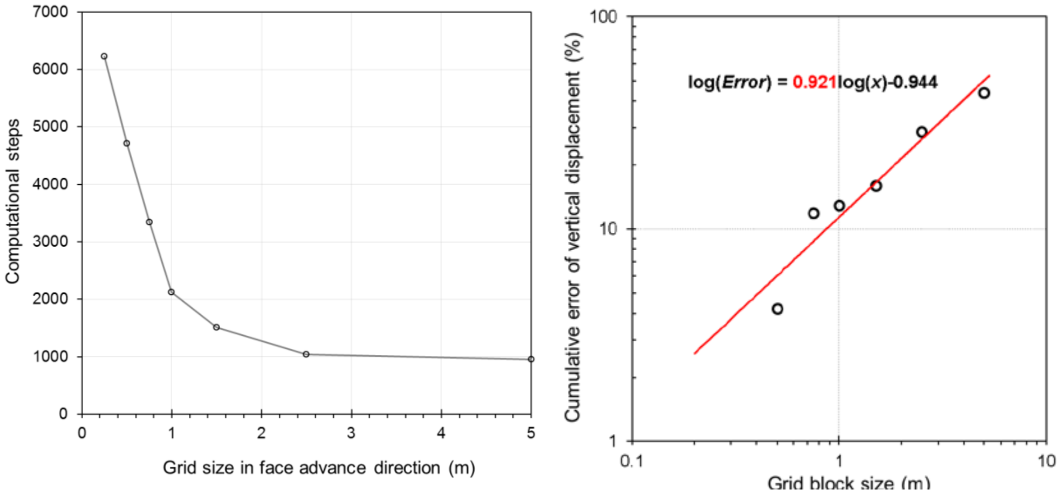

(a) (b)

Figure 6.5: (a) The number of computational steps versus grid block size (along the x-axis) required to reach equilibrium in the model; (b) Logarithm plot of cumulative error against grid block size.

6.3.2 Determination of Convergence Criteria

In FLAC^{3D}, mechanical ratio, which is the ratio of maximum unbalanced force to average applied grid force, is defined for users to adjust and decide the equilibrium states of models. FLAC^{3D} solves equations in an explicit and time-marching scheme, and the termination of each run is controlled by checking whether unbalanced forces on nodes approach zero. A model in equilibrium suggests that the maximum unbalanced force is small compared to the average applied grid force.

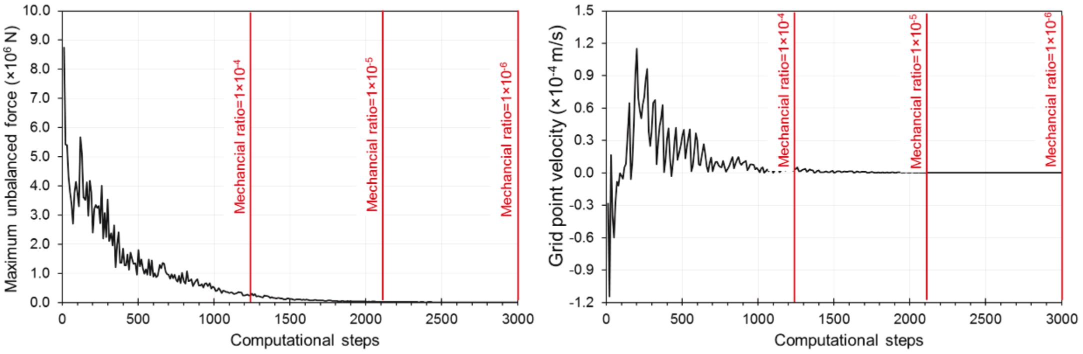

(a) (b)

Figure 6.6: (a) Maximum unbalanced force and (b) grid point velocity in model computational steps.

Take the 1 m grid scenario in the previous section as an example, the maximum unbalanced force and grid point velocity (at the monitoring point shown in Figure 6.3) were monitored throughout the computational steps (see Figure 6.6). The predefined mechanical ratio 1×10^{-5} was reached after 2,119 computational steps, when the maximum unbalanced force and grid point velocity converged to zero and reflected model equilibrium. A smaller mechanical ratio will result in a more stable equilibrium state but also require a longer run time.

6.3.3 The Effect of Face Advance Rate on Model Accuracy

For elastic material, final stress regimes are independent from loading paths. However, to consider plastic behaviour of rock/coal, different loading procedures may result in different stress responses. This may create errors in the modelling of longwall coal extraction since geomechanical response, particularly in the case of post-failure behaviour, may vary depending on the modelled coal extraction strategies.

As introduced in Section 3.2, longwall or LTCC advance recovers coal at the face slice by slice, and each slice has a thickness of 0.6~1.0 m in the horizontal plane. Ideally, to model the progressive coal extraction as realistically as possible, coal extracted at each excavation step should use the same geometry, removing the same volume of coal from the model as in actual coal production. However, for a longwall panel, which is at least several hundred metres long, this will result in a very large number of excavation steps and become impractical. Thus, to reduce the number of excavation steps, each simulated mining advance needs to cover a larger area than that achieved in one actual machine cut.

In order to establish the impact of modelled face advance rate at each time step on stress response, a simple numerical experiment was designed using the same model presented in Section 6.3.1. In this experiment, each grid block was assigned a uniform size of 1×1×1 m, and a 12 m long mine opening, instead of 5 m as in the previous section, was used. The clay layer was assumed to be elastic with the same properties listed in Table 6.1. Strain-softening model was assigned to the coal seam and its plastic properties used in the model are listed in Table 6.2. Residual strength was used once the inelastic strain exceeds 0.001.

Table 6.2: Plastic properties used in the model.

Lithology	Cohesion (MPa)	Friction angle (°)	Tensile strength (MPa)	Residual cohesion (MPa)
Coal	2.10	23	0.92	0.35

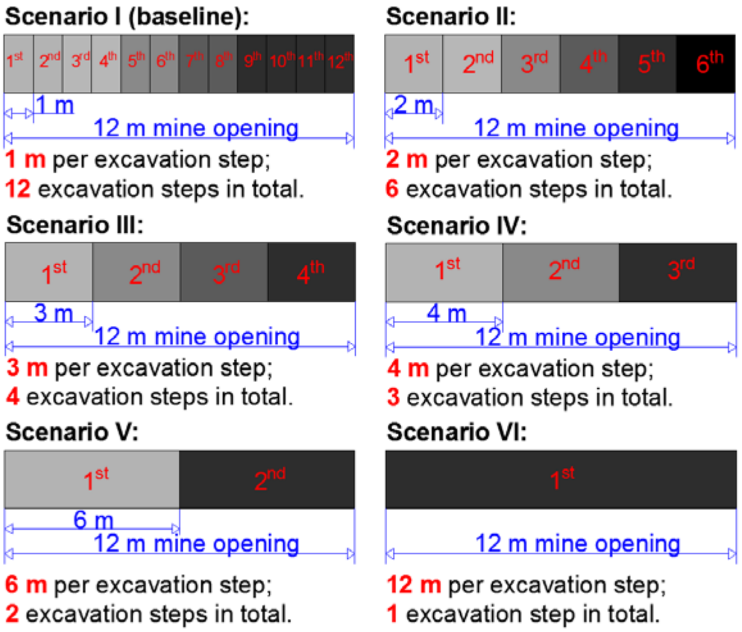

Figure 6.7: Illustration of different coal extraction strategies used in the numerical experiments.

As illustrated in Figure 6.7, the 12 m long mine opening was created by different extraction strategies implemented in the numerical experiments. For example, in the first scenario, each excavation step only represented 1 m coal extraction per face advance and, in total 12, excavation steps were performed sequentially to create the 12 m long mine opening. Five more scenarios with 2 m, 3 m, 4 m, 6 m, and 12 m face advance per excavation step were tested.

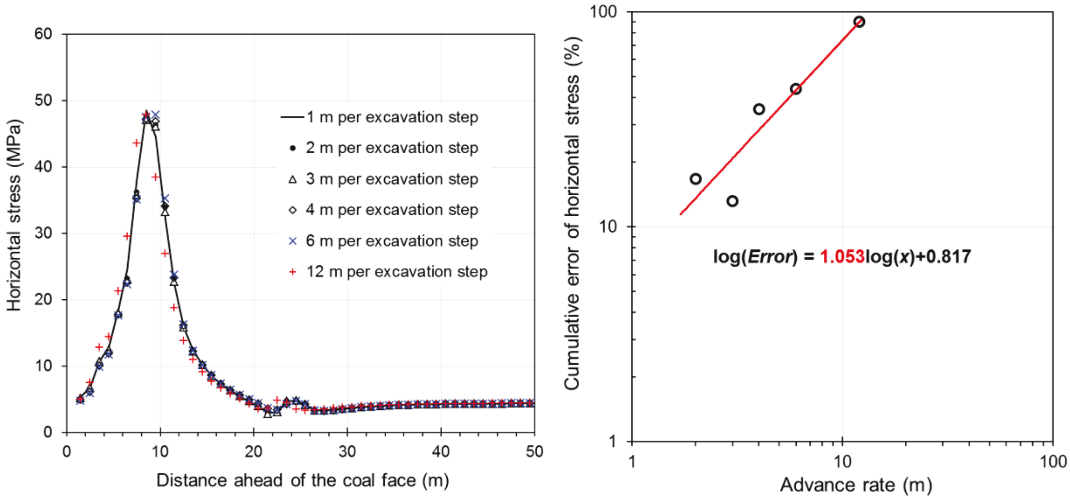

(a) (b)

Figure 6.8: Stress responses to different model excavation strategies: (a) Horizontal stress profiles; (b) Logarithm plot of cumulative error against advance rate.

Horizontal stress (along the x-axis) profiles along Section A-A' are plotted in Figure 6.8 (a). By taking the results of the first scenario as the baseline, cumulative errors are plotted against different advance rates in Figure 6.8 (b). The order of convergence between advance rate and cumulative error is close to unit. This suggests that increasing advance rate by one order of magnitude can linearly amplify the error by the same magnitude.

6.4 Field Scale Model Set-up for Coal Mine Velenje

A 200 m × 250 m × 170 m (length × width × height) model domain was constructed to simulate coal extraction at LTCC panel K.-50/C during the period from 09 May to 07 August 2011, which also represents the most comprehensive data monitoring period at the mine (Figure 6.9 a). The thickness of the coal to be extracted by the shearer and the caving top coal was assumed to be 5 m and 15 m, respectively. The width of the LTCC panel was set as 150 m including the intake and return gateroads. Three different structures, including coal, clay, and failed clay representing the goaf were used in the model domain. It was further assumed that the excavated coal was underlain by a floor coal of 100 m in thickness and overlain by a layer of 50 m thick partly mined clay roof. The inclined structure above the coal seam was simplified: in the roof layer between -300 to -330 m depth (above top coal), half the roof on the intake roadway side was assumed to be solid clay and the other half above the return roadway side was represented as failed clay goaf. Above this, a further 20 m thick layer was represented as solid clay (Figure 6.9 b).

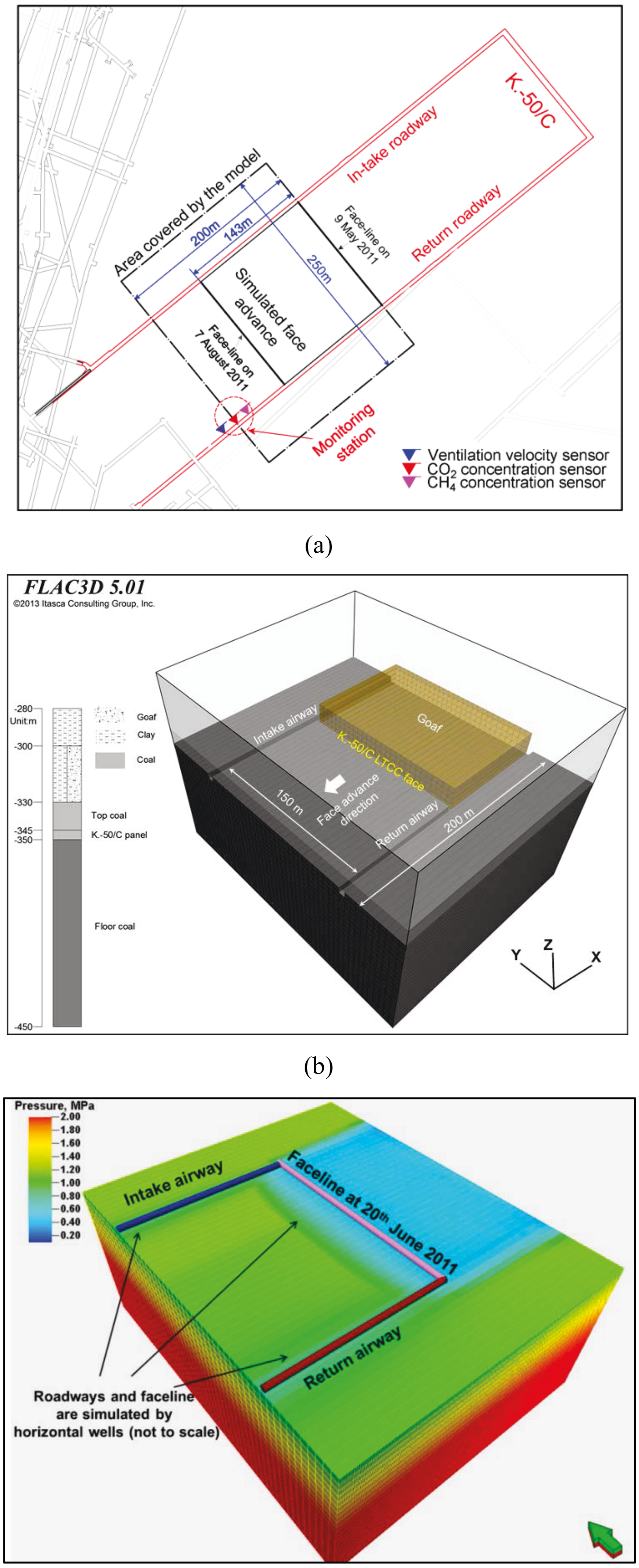

(a)

(b)

(c)

Figure 6.9: (a) Plan view of the simulated K. -50/C LTCC panel illustrating the modelled area and the ventilation/gas concentration monitoring sensors, (b) model geometry and the general stratigraphy used for coupled geomechanics and gas flow modelling, and (c) pressure distribution within the model domain in ECLIPSE, with the position of the face-line on 20th June 2011 and the horizontal wells representing the roadways and the face marked.

Due to the density difference between coal and clay, this simplification may have slightly overestimated the load on the solid side, however, its impact was marginal compared with the stress induced by the entire overburden.

There are 340,000 elements in the model grid, each measuring 1 m × 5 m × 5 m (length × width × height). For seamless two-way coupling, the corresponding flow model in ECLIPSE was also assigned exactly the same grid dimensions as the geomechanical model (see Figure 6.9 c).

The selection of grid size in the direction of face advance was based on the preliminary numerical experiments conducted in Section 6.3.1. Since the focus of the study is the coal seam and gas dynamic responses to face advance, a larger grid size was used in the other two directions to save computational resource.

The key geomechanical parameters used in this study are summarised in Table 6.3. Rock elastic and strength properties were obtained from laboratory tests on samples taken from exploration boreholes at Coal Mine Velenje. For the post-failure behaviour of clay and coal it was assumed that cohesion would be reduced by 83.3% when the inelastic strain exceeds 0.001. The Velenje Mining Method ensures a relatively high recovery of top coal and leaves a very small portion of coal under the clay roof. Therefore, roof goaf was assumed to be occupied mostly by failed clay and assigned the post-failure properties of clay.

Table 6.3: Rock mechanical and strength properties used in the K. -50/C LTCC panel model (after Zavšek, 1993).

Lithology	K (GPa)	G (GPa)	c (MPa)	θ (^{o})	T_0 (MPa)	c_r (MPa)	T_r (MPa)
Coal	0.90	0.19	2.10	23	0.92	0.35	0.52
Clay	1.10	0.24	1.90	30	0.92	0.63	0.52
Roof goaf	0.77	0.17	0.63	30	0.52	0.63	0.52

*K is the bulk modulus, G is the shear modulus, c is the cohesion, θ is the internal friction angle, T_0 is the tensile strength, c_r is the residual cohesion, and T_r is the residual tensile strength.

The pre-mining horizontal stresses were assumed to be equal and are a result of the rock Poisson's Ratio response to gravity loading, while the vertical stress was estimated by computing the overburden weight using an average rock density of 2,360 kg/m^3. The initial stress equilibrium was established in the model before any excavation was performed. The boundary conditions of the model were such that it was laterally confined and fixed at the base.

The reservoir properties used in the flow model were taken from laboratory experiments and field measurements carried out at Coal Mine Velenje, and are presented in Table 6.4. Both laboratory experiments and field observations have shown rapid gas desorption from Velenje lignite, therefore, a relatively high diffusion coefficient was assumed.

A dual porosity model was used to simulate the unique coal structure, whereby coal matrix was assumed to be saturated with gas while the gas saturation in the cleat was 90%. The relative permeability relationship measured by Durucan *et al.* (2014) for the Schwalbach coal with a similar volatile matter content was adopted. Reservoir temperature was set as 35 ˚C, which is also the temperature for the measured Langmuir parameters. The horizontal wells that are placed to simulate the intake gateroad, the longwall face, and the return gateroad were assumed to have a radius of 2 m and a bottomhole pressure of 90, 85, and 80 kPa, respectively.

Table 6.4: Reservoir properties used for the modelled LTCC panel K. -50/C.

Lithology	ϕ (%)	D_c (m^2/day)	P_L CO$_2$/CH$_4$ (MPa)	V_L CO$_2$/CH$_4$ (m^3/t)	k_0 (×10^{-15} m^2)	k_{f0} (×10^{-15} m^2)
Coal	10	200	4.7/7.5	50/25	0.2	0.1
Clay	5	-	-	-	0.2	0.1
Roof goaf	30	-	-	-	30	30

*ϕ is the porosity, D_c is the diffusion coefficient, P_L is the Langmuir pressure, V_L is the Langmuir volume, k_0 is the initial permeability for intact coal, k_{f0} is the initial permeability for fractured coal.

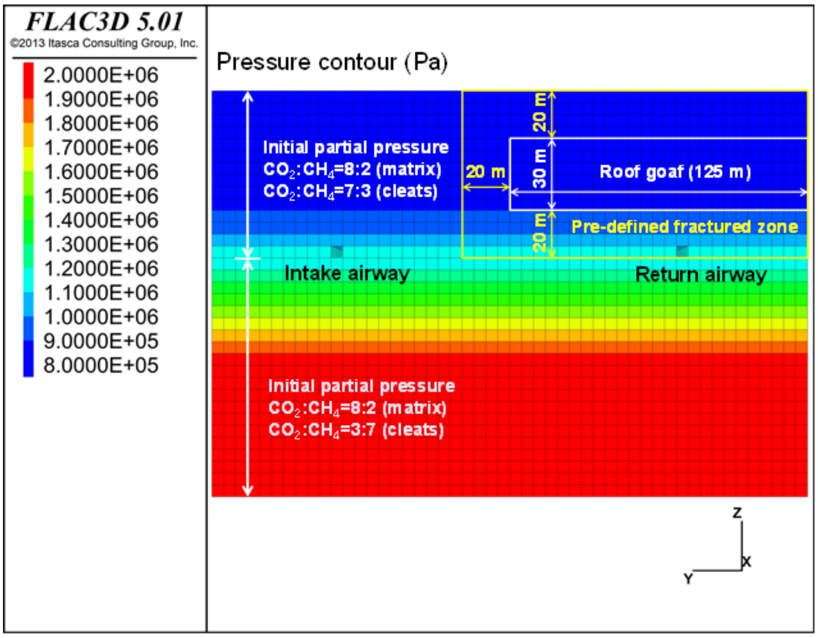

Figure 6.10: The initial pressure gradient and pre-defined fractured zone around the K. -50/C LTCC panel.

Field borehole gas pressure and composition measurements conducted at Coal Mine Velenje have shown that, for undisturbed coal seams, the in-situ pore pressure is around 2 MPa and the primary component of free gas is CH_4 (~70%), while CO_2 dominates (~80%) the adsorbed gas. The same measurements have also suggested that the LTCC panel K.-50/C is more likely to act like a second mining level panel due to its part mined out roof. Therefore, the seam gas pressures in the roof goaf, mined coal and undisturbed floor coal in the K.-50/C panel coupled model were assigned as 0.8, 1.0 and 2.0 MPa respectively. In addition, the predominant gas component in the free gas for the mined coal was assumed to be CO_2 due to overmining stress relief and pressure drawdown.

Table 6.5: Simulated face advances for K.-50/C LTCC panel from 9th May to 7th Aug 2011.

Date (dd/mm/yy)	Face advance (m)	Date (dd/mm/yy)	Face advance (m)	Date (dd/mm/yy)	Face advance (m)	Date (dd/mm/yy)	Face advance (m)	Date (dd/mm/yy)	Face advance (m)
09/05/11	2	28/05/11	0	15/06/11	3	03/07/11	0	21/07/11	0
10/05/11	5	29/05/11	0	16/06/11	2	04/07/11	2	22/07/11	0
11/05/11	3	30/05/11	3	17/06/11	2	05/07/11	3	23/07/11	0
12/05/11	4	31/05/11	2	18/06/11	0	06/07/11	2	24/07/11	0
13/05/11	5	01/06/11	2	19/06/11	0	07/07/11	3	25/07/11	0
14/05/11	0	02/06/11	3	20/06/11	3	08/07/11	3	26/07/11	0
15/05/11	0	03/06/11	2	21/06/11	2	09/07/11	0	27/07/11	0
16/05/11	3	04/06/11	0	22/06/11	3	10/07/11	0	28/07/11	0
17/05/11	3	05/06/11	0	23/06/11	3	11/07/11	2	29/07/11	0
18/05/11	3	06/06/11	3	24/06/11	3	12/07/11	3	30/07/11	0
19/05/11	2	07/06/11	2	25/06/11	0	13/07/11	3	31/07/11	0
20/05/11	2	08/06/11	2	26/06/11	0	14/07/11	3	01/08/11	2
21/05/11	0	09/06/11	3	27/06/11	2	15/07/11	2	02/08/11	3
22/05/11	0	10/06/11	2	28/06/11	3	16/07/11	0	03/08/11	2
23/05/11	2	11/06/11	0	29/06/11	2	17/07/11	0	04/08/11	2
24/05/11	3	12/06/11	0	30/06/11	4	18/07/11	0	05/08/11	2
25/05/11	2	13/06/11	2	01/07/11	0	19/07/11	0	06/08/11	0
26/05/11	3	14/06/11	4	02/07/11	0	20/07/11	0	07/08/11	0
27/05/11	2								

Moreover, a fractured zone with enhanced permeability around the LTCC panels also needs to be considered. Before running the coupled model, a geomechanical model simulating only the coal extraction at the assumed first mining level was run to determine the approximate size of the fractured zone. Geomechanical properties listed in Table 6.3 were used and the face advance rate was set as 3 m/day in that model. It was found that coal extraction at the first mining level would result in a fractured zone extending 20 m into the floor coal. Therefore, the initial pressure gradient and gas composition (in the cleat and matrix) in the fractured zone of the coupled model were assigned as illustrated in Figure 6.10.

The face was advancing from right to left at a depth of -350 m, leaving behind the face a layer of newly caved goaf (Figure 6.9 b). During geomechanical modelling of coal excavation, each excavation step represented the actual face advance achieved by the K.-50/C panel on the relevant date (please see Table 6.5). Note that there was no production during weekends and over a two-week holiday period which started on 16th July 2011.

6.5 Results and Discussion

The fractured coal elements around the LTCC face on 30th Jun 2011 are shown in Figure 6.11. As can be seen, the fractured zone extends 40 m ahead of the coal face and 10 to 30 m below the mining level depending on the face advance rate.

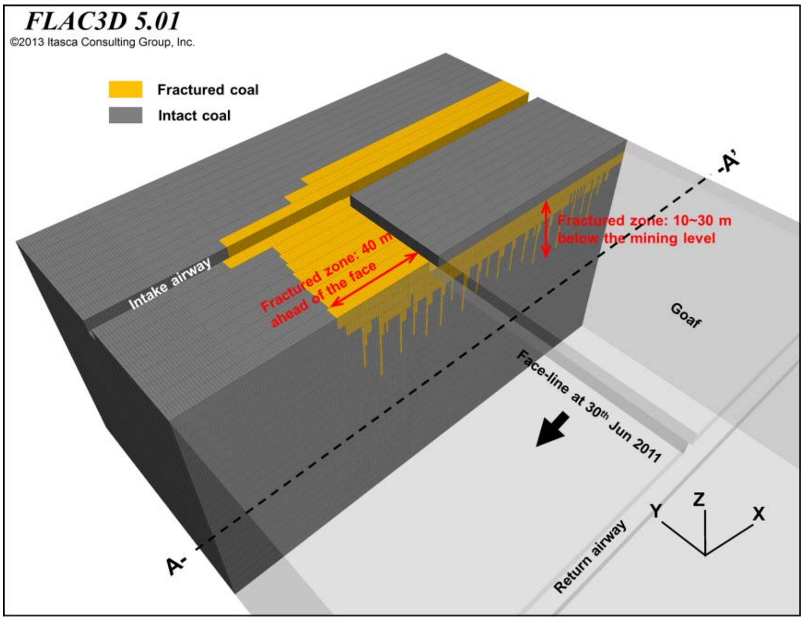

Figure 6.11: Fractured zone around the face-line position at 30th Jun 2011 ($k_{f0} = 10k_0$, $C_f = 0.65$).

Vertical stress and pore pressure profiles at different depths along A-A' (as shown in Figure 6.11) with respect to distance from the face-line on 9 May 2011, 16 May

2011, 30 May 2011 and 13 Jun 2011 are plotted in Figures 6.12 and 6.13. On these dates, face had advanced 2m, 22 m, 47 m, and 70 m, respectively, from the face starting position in the model. Note that these profiles are plotted along a vertical section below a mined out zone or previously caved goaf (Figure 4.8). The figures show that modelled stress and pore pressure profiles stabilise after 30 May 2011. The figures show that, at K.-50/C mining horizon, a notable stress relief and pore pressure drop induced by fracturing of the coal seam is observed within 40 m ahead of the face-line. Abutment stress at mining level and roof coal peaks at around 40 m ahead of the face-line but is not as notable in the floor coal except for the fractured zone within 20 m of the mining horizon. Pressure profiles at and above the K.-50/C mining level present the most dramatic pressure decline, which is believed to be the main source for gas emissions at the face. Pressure relief at floor coal also confirms its contribution to overall gas emissions, however, this effect becomes weakened with an increase in burial depth.

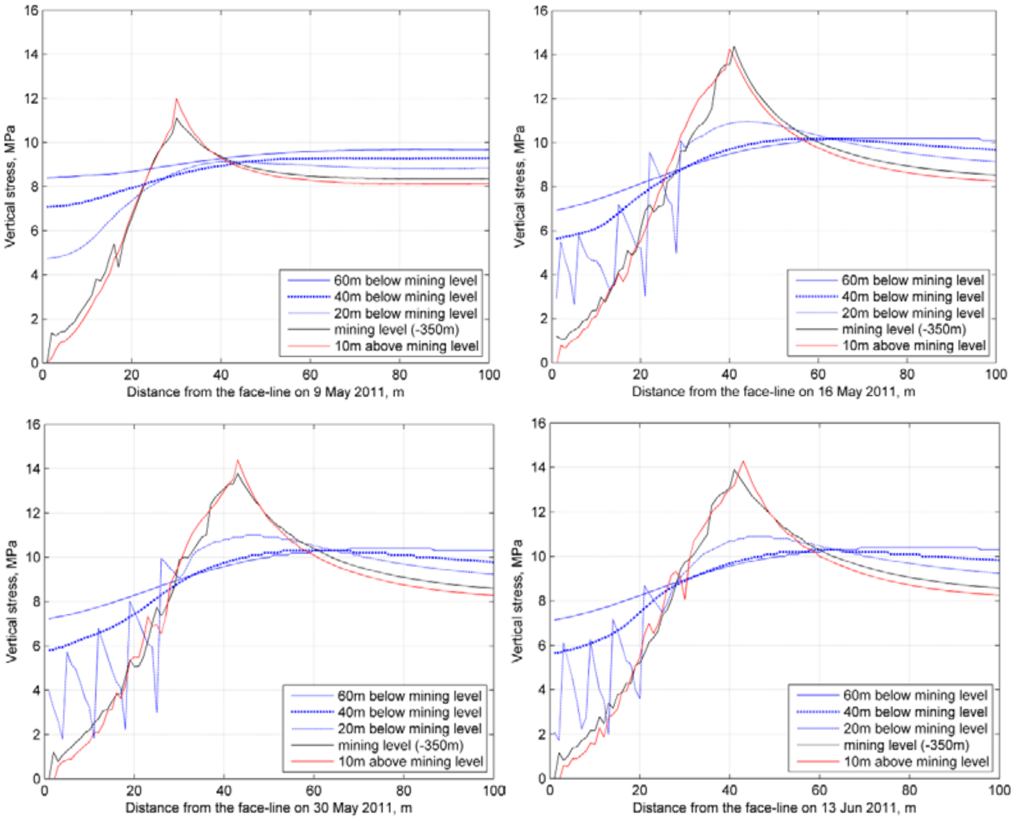

Figure 6.12: Evolution of stress profiles with respect to distance from the face-line (k_{f0} =10 k_0, C_f = 0.65).

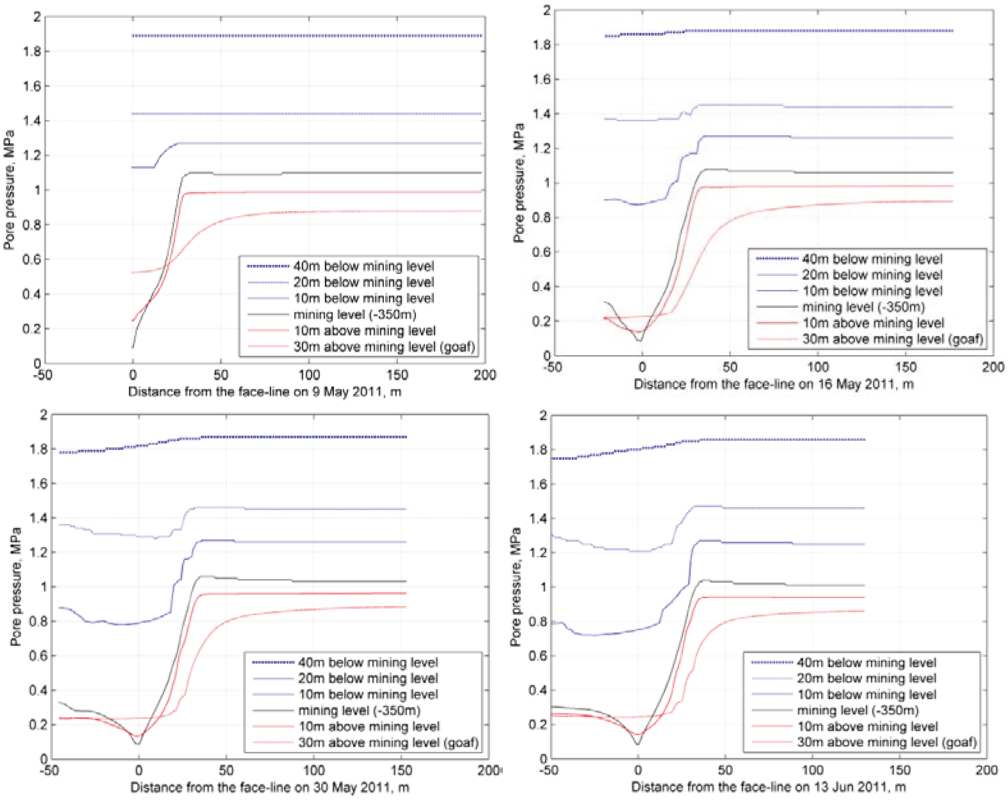

Figure 6.13: Evolution of gas pressure profiles with respect to distance from the face-line ($k_{f0} = 10k_0$, $C_f = 0.65$).

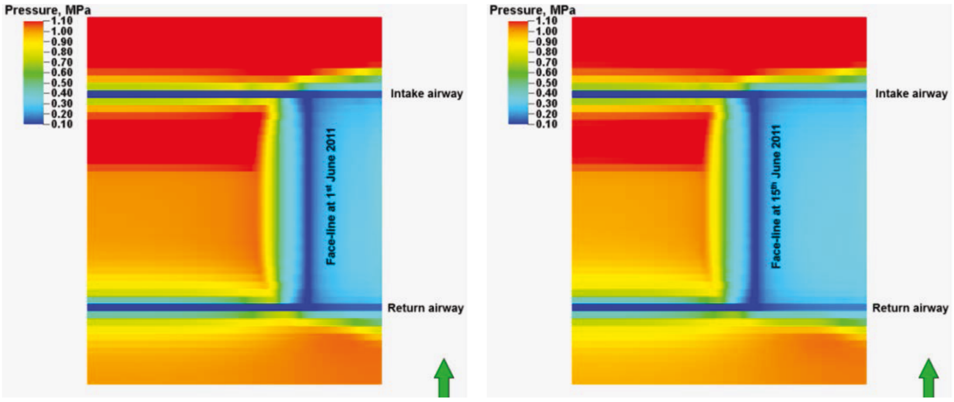

(a) 1 June 2011 (b) 15 June 2011

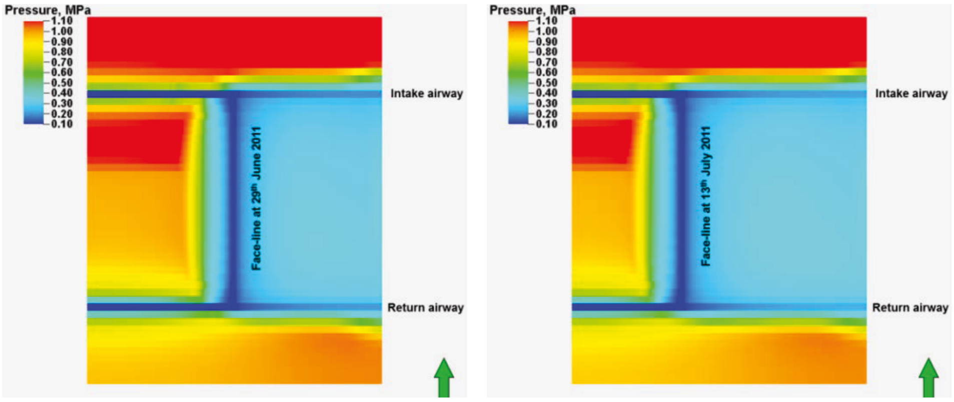

(c) 29 June 2011 (d) 13 July 2011

Figure 6.14: Evolution of gas pressure contours at different face-line locations: plan view at the mining level ($k_{f0} = 10k_0$, $C_f = 0.65$).

The evolution of pressure contours during face advances is shown in Figure 6.14. A 40 m pressure relief zone can be seen in front of the face-line, which moves along with the advance of the coal face. The simulated stress, pressure, and fractured zone distributions generally agree well with field observations at Coal Mine Velenje. The model findings also confirm the conceptual designs presented in Section 4.5.2.

6.5.1 The Effect of Coal Production on Permeability around Longwall Top Coal Caving Faces

Figure 6.15 illustrates vertical permeability distribution around the K.-50/C LTCC face with respect to distance from the face-line. In order to cover the wide range of permeability changes experienced, the ratio of new to initial permeability is plotted in log scale in these figures. Five cross-sections of permeability contours at different distances from the face-line on 30th Jun 2011 (when the face had advanced 106 metres from the face starting position in the model) are shown in this figure. The most significant permeability enhancement, which is about two orders of magnitude, is found to be above the K.-50/C mining level 10 metres ahead of the face-line (Figure 6.15 c). In all cases, permeability in the floor coal also shows an increasing trend, and note that the largest magnitude of increase can be found in an area 15~20 m below the current mining level. Permeability in the recompacted goaf elements declines as the face moves away as indicated in Figures 6.15 (e) and (f).

The horizontal permeability distribution around the LTCC face is illustrated in Figure 6.16. The abutment stresses create an arc of reduced permeability at a distance from the face-line Figures 6.16 (b) and (c). On the other hand, nearly three orders of permeability enhancement is observed in the near face fracturing zone. A notable increase in floor coal horizontal permeability can also be observed in an area directly below the face, and the degree of enhancement varies with burial depth.

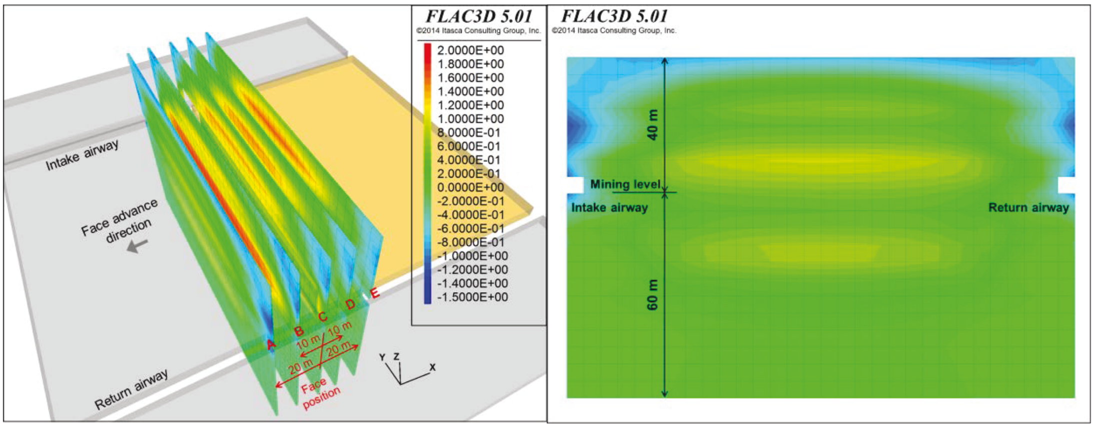

(a) Legend and crossectional plane positions (b) 20 m ahead of the face-line (Plane A)

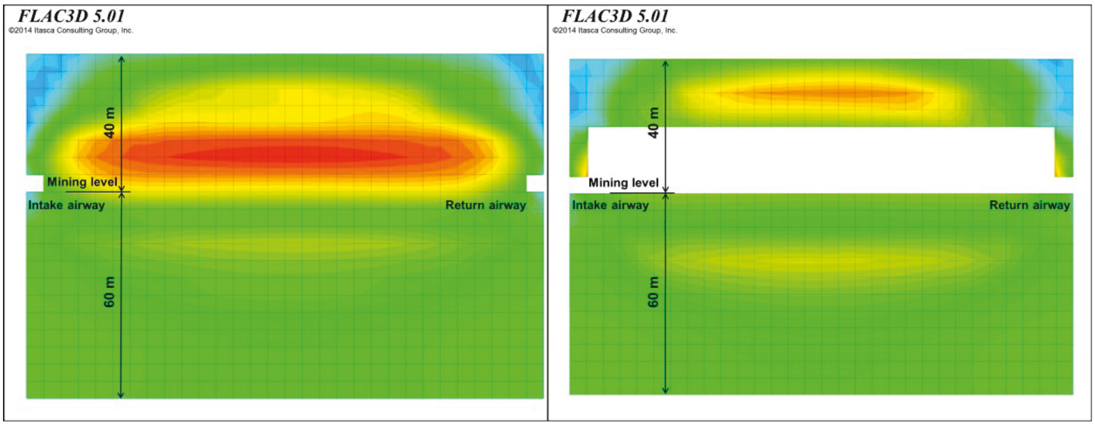

(c) 10 m ahead of the face-line (Plane B) (d) face-line position (Plane C)

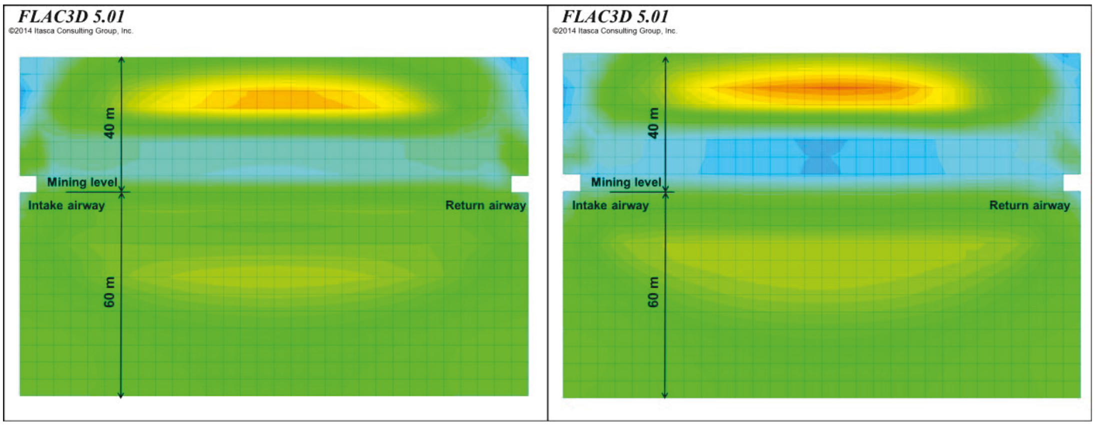

(e) 10 m behind the face-line (Plane D) (f) 20 m behind the face-line (Plane E)

Figure 6.15: Cross-sections illustrating the change in vertical permeability due to excavation at the face, $\log(k_z/k_{z0})$ ($k_{f0} = 10k_0$ and $C_f = 0.65$).

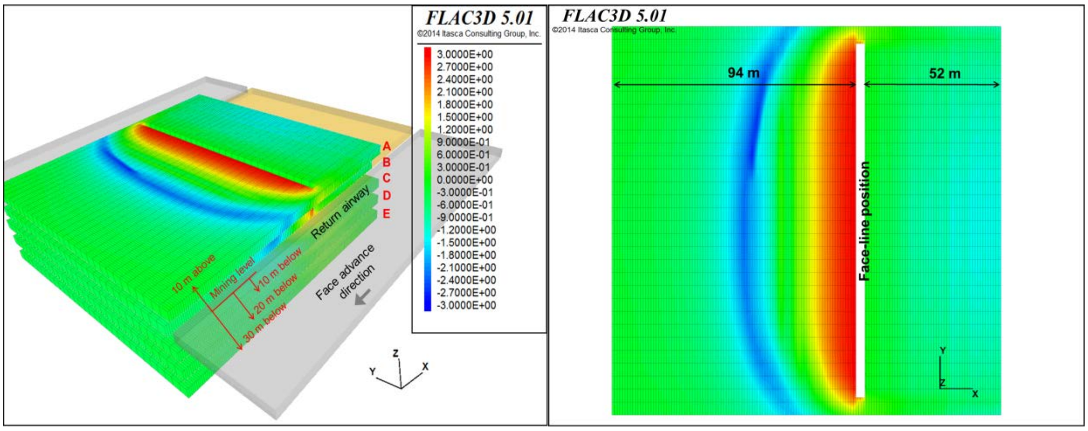

(a) Legend and crossectional plane positions (b) 10 m above the mining level (Plane A)

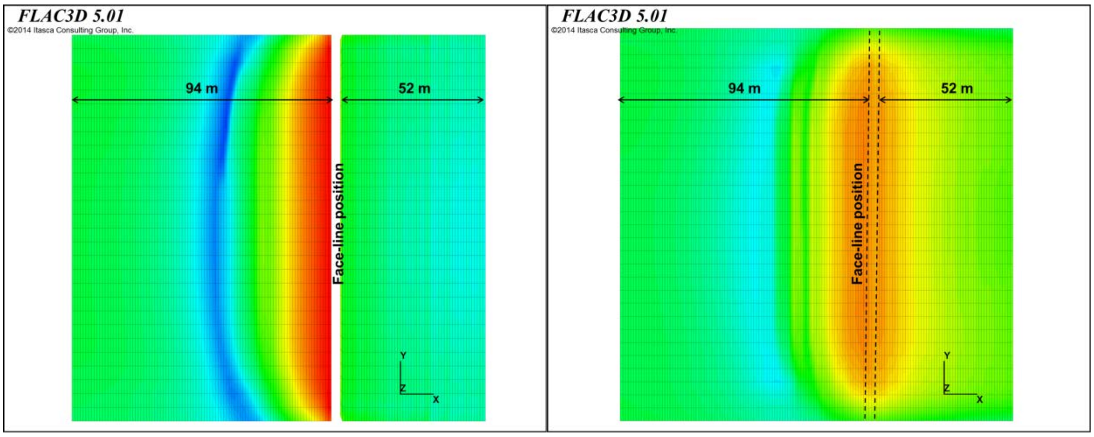

(c) the mining level (Plane B) (d) 10 m below the mining level (Plane C)

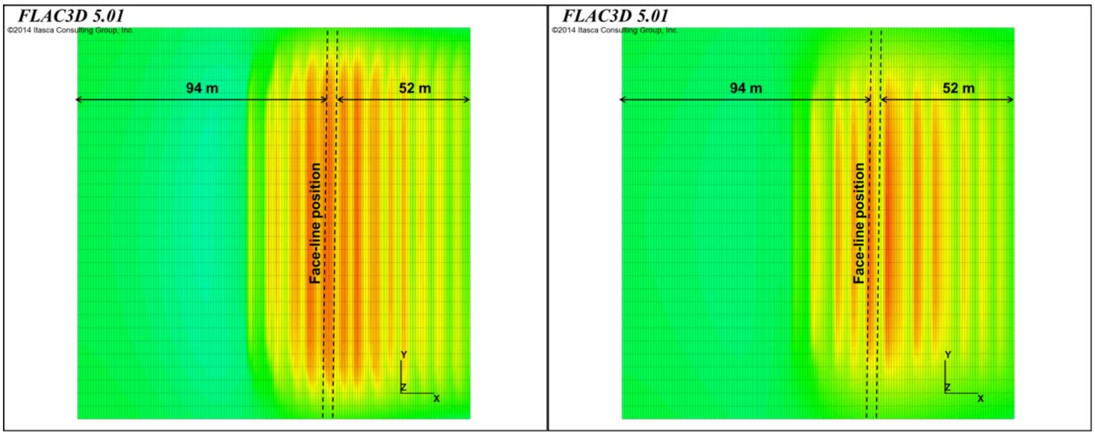

(e) 20 m below the mining level (Plane D) (f) 30 m below the mining level (Plane E)

Figure 6.16: Plan views illustrating the distribution of horizontal permeabilities around the LTCC face, log(k_x/k_{x0}) ($k_{f0} = 10k_0$ and $C_f = 0.65$).

6.5.2 Dynamic Effects of Face Advance on Stress, Pore Pressure and Permeability

One particular floor coal element at -350 m depth (or 10 metres below the working horizon) in the centre of the model has been selected as a monitoring element to record stress, pore pressure and permeability changes with respect to the face advance at K.-50/C LTCC panel. As shown in Figure 6.17, the changes in permeability can be divided into three stages, corresponding to the ‘abutment – fracturing – recovery’ zones in the stress profile depicted in Figure 6.2.

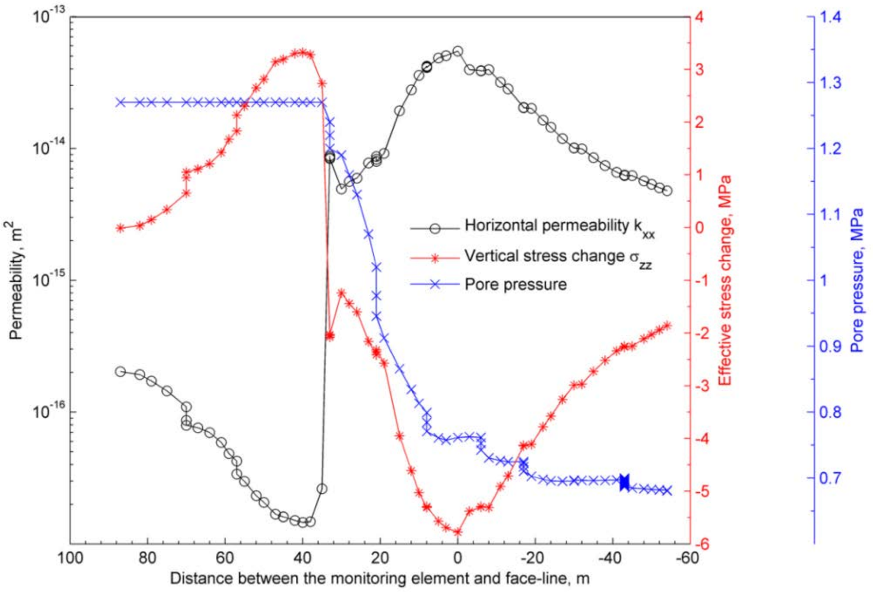

Figure 6.17: Stress, pressure, and permeability changes with respect to distance from the face-line (k_{f0} = $10k_0$, $C_f = 0.65$).

Coupled geomechanical and flow modelling has shown that, in the first stage, as the face advanced from 100 m to 40 m towards the monitoring element, the abutment stress on this element increased steadily, and was accompanied by a reduction in the horizontal permeability. The second stage saw a steady drop/rise in the stress/permeability levels as a result of coal failure and fracturing as the face advanced from 40 to 0 m towards the monitoring element. After that, when the coal face moved past the monitored element, the vertical stress started building up with time and recovered to the level of in-situ stress due to the recompaction of goaf above. In the third stage, although the permeability also experienced more than one order of magnitude reduction as a consequence of goaf recompaction its value was still much higher than the initial value of intact coal due to fracturing. As Figure 6.17 illustrates, the pore pressure at this monitoring element also responded to the changes in horizontal permeability and dropped from 1.27 MPa to 0.7 MPa in the fractured zone. The simulated residual pore pressure of 0.7 MPa is also consistent with measured field gas pressure at lower level panels which have experienced pressure relief.

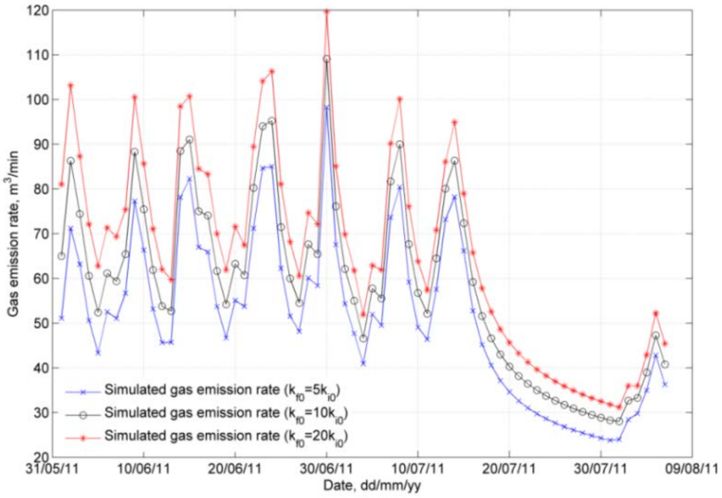

Figure 6.18: The effect of initial fractured coal permeability (k_{f0}) on total gas emission rate ($C_f = 0.65$).

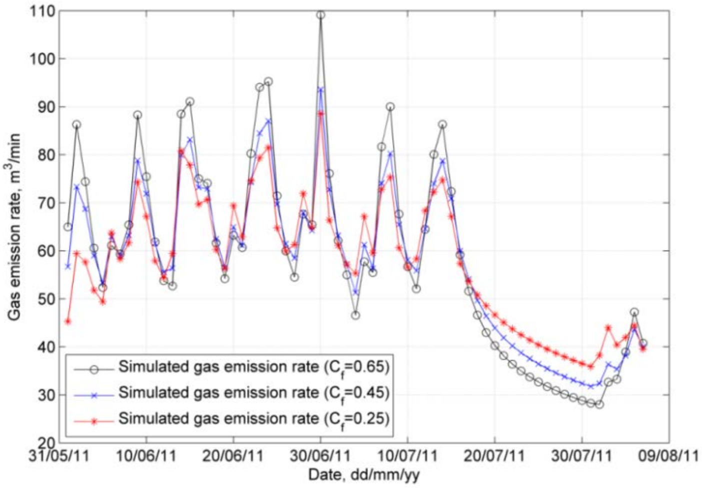

Figure 6.19: The effect of fractured coal compressibility coefficient (C_f) on total gas emission rate ($k_{f0} = 10\ k_0$).

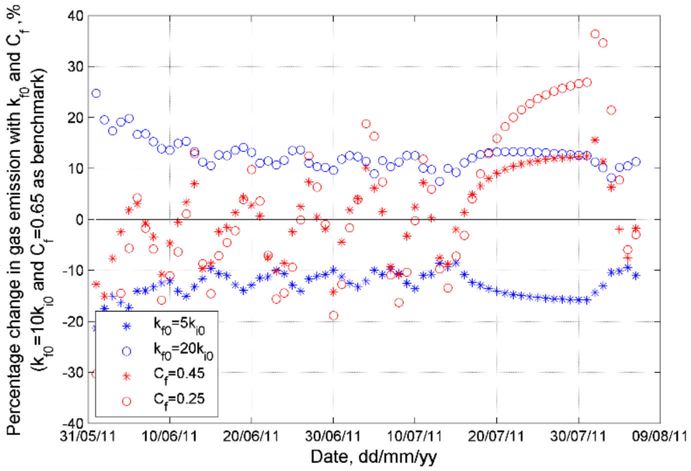

Figure 6.20: A sensitivity plot showing the impact of C_f and k_{f0} on overall gas emissions.

Figures 6.18 and 6.19 show the effect of initial fracture permeability (k_{f0}) and fractured coal compressibility coefficient (C_f) on overall gas emission rate, respectively. It is not surprising that increased initial fracture permeability shifts the entire gas emission curve upwards. On the other hand, the increased fractured coal compressibility coefficient mostly affects the peak gas emissions. The same observation is presented in the sensitivity plot shown in Figure 6.20, which uses the model results obtained with k_{f0} = 10 k_0 and C_f = 0.65 as the benchmark. These two parameters are considered as the two most uncertain inputs that can largely affect the gas emission modelling output. Further research should be prioritised to obtain more accurate estimation of these two values.

6.5.3 Comparison between the Simulated and Measured Gas Emission Data at Longwall Panel K.-50/C

The mine ventilation and gas monitoring data collected by the sensors illustrated in Figure 6.9 (a) were used to compare the predicted gas emission rates with the measured values. Here, the total flow rate of gas predicted by the compositional simulator represents the CO_2/CH_4 mixture presented in Figures 6.17 to 6.23. As illustrated in Figure 6.21, the best-match was obtained with k_{f0}=10k_0 and C_f=0.65. It is believed that the rounded face advance rate (from 3.6 m/day to 4 m/day) caused the significant overestimate on 30th June 2011.

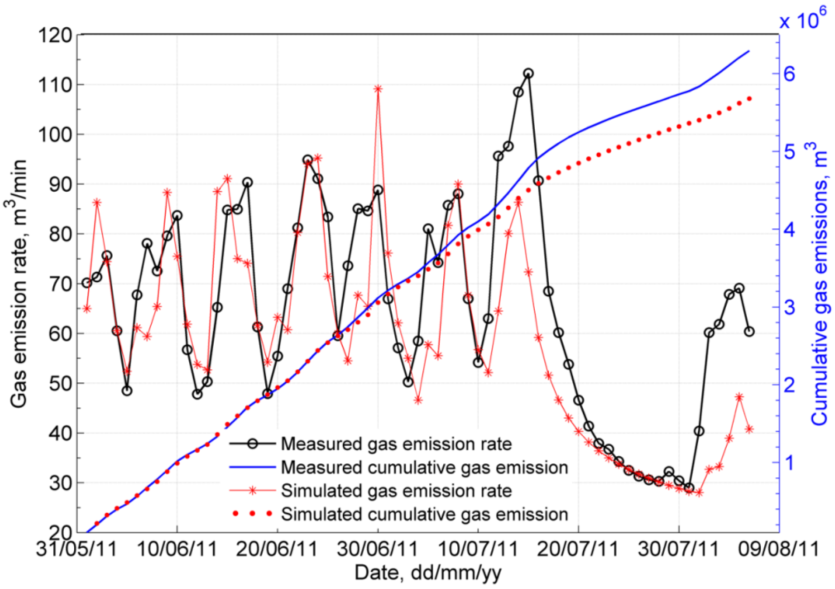

Figure 6.21: Comparison of predicted and monitored total gas emission rate and cumulative emission volume over the modelling period (k_{f0} = 10k_0, C_f = 0.65).

Figure 6.21 also shows that the cumulative gas emission predicted during the monitoring period is in good agreement with the monitored data until the week the mine experienced an unusually increased gas emission episode which affected production at the face.

As shown in Figure 6.21, the most notable mismatch between the simulated and measured gas emission rates is during the week with excessive gas emissions (11th July to 17th July, 2011). As discussed earlier in Section 5.4.5, a relatively high strength xylite-rich zone forming a barrier in front of a low strength high gas content detritic zone detected by both microseismic monitoring and seismic tomography may be responsible for the excessive gas emissions at Coal Mine Velenje. However, since the model assumed a homogeneous coal seam, the simulated gas emission rates were not able to capture the behaviour during this period.

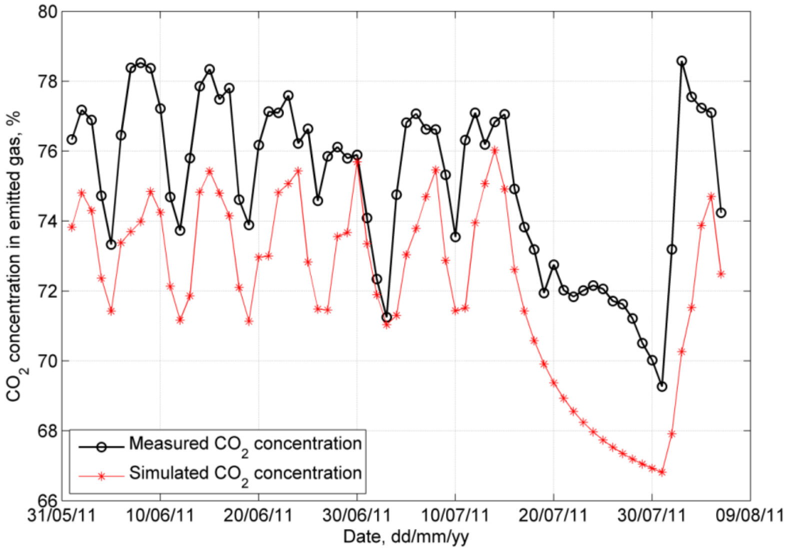

Figure 6.22: Comparison of field monitored and simulated CO_2 concentrations in the emitted gas ($k_{f0} = 10k_0$, $C_f = 0.65$).

Figure 6.22 compares the simulated CO_2 concentration in emitted gas with the measured concentrations, which generally captures its trend and matches the absolute values of the measured data reasonably well.

6.5.4 Sources of Gas Emission at Longwall Top Coal Caving Panels

In order to identify the sources of all gas emissions at LTCC panel K.-50/C, the origin of gas released in to each gateroad and the face was tracked over the simulation period. The flow rates of gas migrated from the mined, floor coal and roof goaf are plotted in Figure 6.23 (a). In addition, CO_2 concentration in the gas emitted from these sources is illustrated Figure 6.23 (b). As illustrated by this figure, the rate of gas emission from the mined coal is strongly affected by the coal face advance. In contrast, floor coal and roof goaf act as a constant and steady gas source accounting for a considerable part of the overall gas emissions, which is approximately 50% and consistent with the mass balance analysis reported in Table 4.3. This observation may also explain the difference between the baseline and dynamic gas emissions referred to earlier in Section 4.4. The dynamic gas emissions are closely related to coal extraction activities, while baseline gas is a mixture of emissions from all the above mentioned sources. It is also clear from Figure 6.23 (b) that intense fracturing of coal and a significant pressure drop experienced at the face results in the release of a large amount of CO_2, which is much strongly held in the coal matrix.

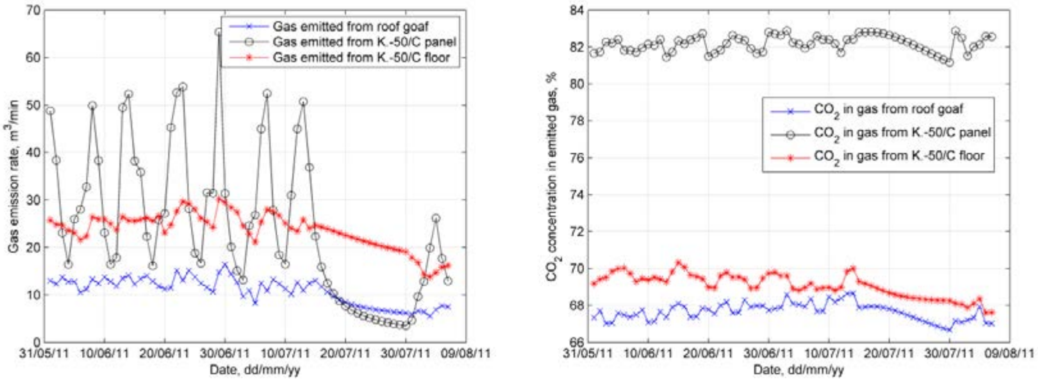

(a) (b)

Figure 6.23: Sources of gas emission at LTCC panel K.-50/C: (a) gas flow rates from different sources, and (b) CO_2 concentration in the emitted gas ($k_{f0} = 10k_0$, $C_f = 0.65$).

6.5.5 Comparison Between One-way Coupling and Two-way Coupling

In addition to the two-way coupling methodology implemented throughout the research described here, a one-way coupling simulation without considering the feedback of pore pressure from the gas flow modelling to the geomechanical modelling was also conducted to compare the two approaches. Model set-up and procedures used in the one-way coupling runs were exactly the same as the two-way coupling approach, except that the pore pressures were not considered in the geomechanical simulations. A comparison between the results of one-way coupling and two-way coupling runs, including stress, pressure, and permeability distributions, is presented in Figure 6.24.

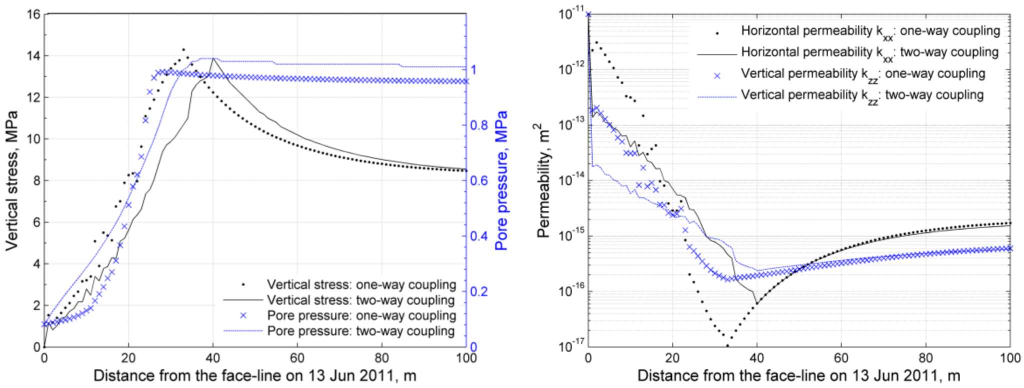

(a) (b)

Figure 6.24: Comparison between one-way coupling and two-way coupling results: (a) Stress and pressure regimes at K.-50/C mining level; (b) Permeabilities at K.-50/C mining level ($k_{f0} = 10k_0$ and $C_f = 0.65$).

The importance of developing a two-way coupling approach in modelling gas emissions can be clearly seen. Without considering the impact of pore pressure depletion during coal extraction, mining induced fractured zone ahead of the face, which is ~40 m as suggested by field observations, is underestimated by the one-way coupling approach (~30 m). Furthermore, one-way coupled model seems to predict a much stronger effect on coal permeability due to abutment stresses in the far-field or coal fracturing in the near face area.

6.6 Conclusions

A two-way sequential coupling approach between a geomechanical and a compositional reservoir simulator for the modelling of mixed gas emissions around a LTCC panel was developed and implemented at Coal Mine Velenje. Permeability and pore pressure are used as coupling parameters between the two simulators at each longwall excavation step, enabling the representation of interactive physics between geomechanics and gas flow. A stress-permeability relationship for intact and post-failure coal and rock was implemented.

The developed coupling approach has been successfully applied to the K.-50/C LTCC panel at Coal Mine Velenje, which also was the site of most comprehensive data monitoring campaign during the project. By constructing a geomechanical and a flow model for longwall panel K.-50/C, a total of 143 m coal face advance was simulated by following the mining schedule at the mine. Model findings have shown that the modelling method implemented can reproduce the dynamic changes of stresses and gas pressure around a LTCC face and predict the total gas emissions accurately.

Furthermore, model results have clearly shown the permeability enhancement and gas mobilisation zones around the panel, which can be the target zones for gas drainage boreholes. For example, as pre-drainage of the mined seam in the first and/or upper mining levels is not likely to be possible due to low permeability of the coal seam, floor drainage boreholes drilled at an angle towards the goaf area below the mining level could be effective in pre-draining the next LTCC level below the current mining horizon. The results have also shown that there is a zone of permeability enhancement ahead of the face, especially in the top coal section which can be targeted by the drainage boreholes. Based on these analyses, Coal Mine Velenje launched a pilot drainage trial in the first quarter of 2015 and started targeting these zones for gas drainage monitoring.

It is also worth noting that the developed approach is not limited to thick/ultra-thick mining and gas emissions around thinner seams with mechanised conventional longwall layouts can also be successfully modelled using this technique. In addition, with some advanced knowledge of the existence of geological and structural anomalies, risk assessment of mining hazards such as uncontrolled gas emissions or outbursts can also be performed.

Gas outbursts or uncontrolled gas emissions also involve the interactive physics between geomechanics and gas flow. The two-way sequential coupling approach developed in this research can be readily applied to the modelling of this violent mining hazard, which will be discussed in detail in the next chapter.

Chapter 7 Numerical Modelling of Coal and Gas Outbursts

7.1 Introduction

As discussed in previous Chapters, numerical modelling research into outburst conditions is relatively new and needs further work to improve the techniques employed. This Chapter presents the application of the two-way sequential coupling approach developed to simulate two types of well-recorded outbursts, more specifically, the gas pocket initiated outbursts and the dynamic outbursts. Note that the occurrence of outbursts is not limited to thick seams, and a significantly large number of field observations and outburst cases are reported in thin seam mining. Furthermore, development headings, which are common to both thick and thin seam mining, are reported to be the sites with most frequent outburst occurrences in underground coal mining (Beamish and Crosdale, 1998). Therefore, outburst modelling reported in this chapter aims at studying outbursts in development headings, and not restricted to thick seam mining only.

The first part of this chapter presents a general methodology developed to model outbursts, building upon the two-way sequential coupling approach described earlier in Chapter 6. An algorithm to characterise the ejection of outburst elements was developed and incorporated into the coupling approach. Next, the upgraded two-way coupling approach has been applied to simulate two types of outbursts experienced in an outburst-prone coal field in China. Simulation results are used as an aid to explain the field observations made before the occurrence of outbursts.

7.2 Development of an Outburst Modelling Methodology

7.2.1 Fundamental Concepts

The onset of an outburst is a result of the domino effect of catastrophic coal failure, and the whole outburst process can be characterised by the *initiation*, *development*, and *die-out stages*. During the initiation stage, the plastic deformation of yielded coal occurs in a quasi-static manner. Following this, a state transfer of the coal/rock/gas system from quasi-static to dynamic state suddenly takes place in the development stage. With the dissipation of the elastic strain energy stored in rock/coal and the energy contribution by compressed gas, the coal/rock/gas system returns into a static state.

In the *initiation stage*, the creation of mine openings causes stress redistribution, which may result in shear/tensile failure in the roof/floor, as well as the coal seam being mined. Furthermore, a pressure gradient is created between the mine opening at the atmospheric pressure and surrounding coal at a higher pressure (Figure 7.1). An outburst may occur if the strength of failed coal cannot withstand the pressure driven force.

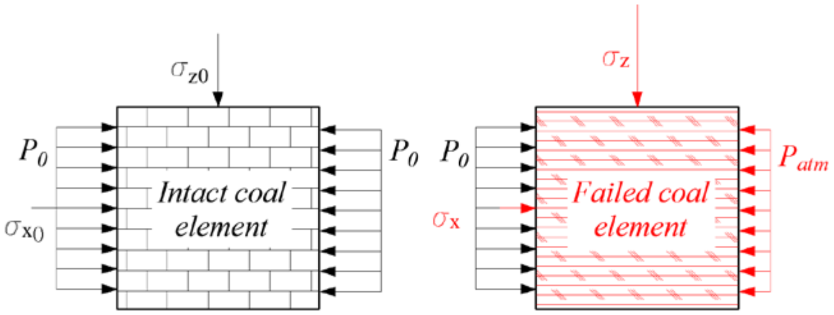

(a) The initial state (b) After creating a mine opening at its right hand side

Figure 7.1: Changes to a coal element after a mine opening has been created at its right hand side.

In the *development stage*, gas pressure and mining stresses jointly contribute to fracture initiation and propagation. Highly fragmented rock/coal adjacent to mine openings can be pushed into an open space by high velocity gas flow. This complex process involves a two-phase flow of particles and gas, as well as the interactions between these two media.

In the *die-out stage*, an outburst will cease as the pressure gradient can no longer break and eject solid coal. A new equilibrium of pressure and stress is established in both free space and the solid coal. The intensity of an outburst depends on the volume of gas and the amount of coal that can be released into the mine opening over the duration of an outburst.

Therefore, to simulate the *initiation stage* of an outburst, dynamic stress and pore pressure changes around a mine opening need to be simulated first. Permeability, which is stress depedent and determines the pressure distribution around a mine opening, also needs to be considered. Furthermore, strain softening behaviour of coal needs to be pre-defined as yield generally degrades the strength of coal, as well as its ability to resist a pressure driven force. It is believed that all these key physics can be captured by the two-way coupling methodology developed in Chapter 6.

However, modelling of the *development* and *die-out stages* of an outburst is not feasible in the current simulators since this requires the simulation of two-phase turbulent flow of gases and solid particles. Given that the main objective of this research was to establish an understanding of the gas outburst mechanism and their early detection, accurate modelling of the *initiation stage* of outbursts was the primary target. Furthermore, for the *post-initiation stages*, based on certain assumptions, the author attempted to calculate the volume of the cavity created by an outburst to estimate the intensity of an outburst.

7.2.2 Criterion and Model Development for Coal Ejection in Coal and Gas Outbursts

In order to model coal and/or gas outbursts, the first problem to be addressed is to define a criterion in order to detect the outburst onset. Since it is well-recognised that an outburst is induced by a combined effect of stress, pressure gradient, and coal strength, the outburst criterion proposed here attempts to cover all of these three factors.

In this research, an outburst element is defined as an element which has the potential to be detached from its original grid. More specifically, an outburst element which is adjacent to an open space is deemed to be ejected if the pore pressure gradient towards the opening (which is at atmospheric pressure) exceeds the coal cohesion. Coal cohesion can be pre-defined as a function of plastic strain, which is determined by the stress regime. As illustrated in Figure 7.2, the red element will be “ejected” from the grid if Equation 7.1 is satisfied and there is an empty space along the ejection direction:

$$\sqrt{(L_x \cdot \frac{\partial P}{\partial x})^2 + (L_y \cdot \frac{\partial P}{\partial y})^2 + (L_z \cdot \frac{\partial P}{\partial z} + \rho_c \cdot g)^2} + - c(\varepsilon^p) > 0 \qquad 7.1$$

where, L_x (m), L_y (m), and L_z (m) are the size of a coal element along the x-, y-, and z-axes respectively, P (Pa) is the gas pressure, ρ_c (kg/m^3) is the coal density, g (m/s^2) is the gravitational acceleration, and c (Pa) is the coal cohesion when its shear plastic strain is ε^p (dimensionless).

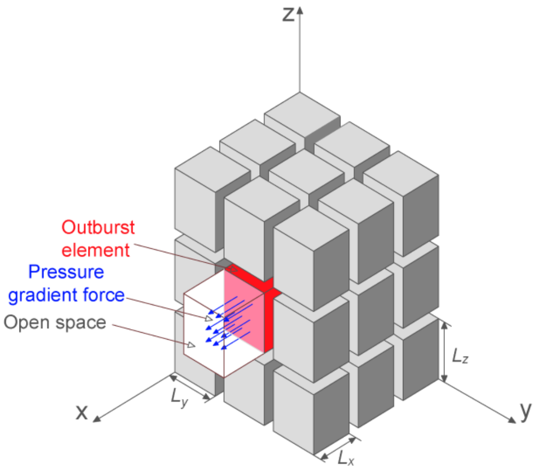

Figure 7.2: A schematic representation of the criterion for coal element ejection in outburst modelling.

7.2.3 Modelling of Outburst Development and Die-out Stages in a Development Heading

A period of roadway drivage is simulated to replicate the dynamic and progressive advance of a development heading. In FLAC^{3D}, the development of a roadway is modelled by removing coal elements that are to be excavated by a roadheader. Similar to the modelling of longwall face advance, the temporal nature of the drivage is represented by a series of excavation steps, and each excavation step represents a period of time that can be modelled in the fluid simulator.

In parallel with the geomechanical modelling in FLAC^{3D}, a reservoir model with the same mesh is developed in ECLIPSE to obtain the pore pressure distribution around the development heading. The modelling of the heading is achieved by assigning a horizontal well with ventilation pressure to the elements representing the heading. The length of the horizontal well is extended along with the development of the roadway after every excavation step.

The two-way sequential coupling procedure between FLAC^{3D} and ECLIPSE illustrated in Figure 6.1 is used in outburst modelling. A routine written in the built-in *fish* code in FLAC^{3D} to detect the outburst elements is added to the coupling script. After each coal excavation step, this routine is performed to check if the user-defined outburst criterion has been violated.

Once the outburst criterion has been triggered, the modelling of an outburst moves from the *initiation stage* to the *development stage*. In this stage, only geomechanical simulator is used. This is because gas release is mostly turbulent flow and the duration of an outburst is normally too short for the reservoir model to respond.

In FLAC^{3D}, the "ejected" elements are assigned with null properties and the simulation is re-run until a new equilibrium state is reached. Then the routine to detect outburst elements is performed again to check if there are any new elements qualified as outburst elements. This is an iterative process as the ejection of coal elements could create a larger cavity and thus more coal elements would be exposed to the cavity at a lower pressure. And this, in turn, may result in the ejection of more elements.

With the ejection of coal element(s) and the rapid release of the gas contained in the cavity, the cavity gas pressure is likely to experience dynamic changes depending on the volume of gas released and the volume of connected void space, including the roadways. For each ejected coal element(s) with mass m (kg), the volume of released gas (V_{gas}, m^3) can be calculated from the Langmuir isotherm:

$$V_{gas} = \left[m \cdot \frac{V_L \cdot P}{P_L + P} \right]_{P_{cavity}}^{P_{coal}} \tag{7.2}$$

where, P_{coal} (Pa) is the pore pressure of a solid coal element before being ejected. The cavity pressure P_{cavity} (Pa) is the mean gas pressure in the connected void space prior to the ejection of coal element(s). The post-ejection cavity pressure can be estimated from the Boyle's law (Equation 7.3) assuming that the equilibration of gas pressure is quickly established.

$$\frac{P_{cavity}}{P_{sc}}=\frac{V_{gas}}{V_{void}} \tag{7.3}$$

where, V_{void} (m^3) is assumed to be the cavity volume together with the volume of developed roadway, and P_{sc} (Pa) is the atmospheric pressure which is 101,325 Pa.

After the start of the outburst *development stage*, a distinct pressure difference is established between the solid coal face and the outburst cavity, and this pressure difference provides the driving force for the domino effect of an outburst. The pressure distribution in solid coal is assumed to be unchanged after the triggering of an outburst, since compared with the time required for fluid transport in porosity media, the duration of an instantaneous outburst is almost negligible. On the other hand, cavity pressure, which can affect the pressure gradient in outburst criterion, is updated after each time the coal is ejected.

In reality, the *die-out* of an outburst is normally decided by the size of geological structures and the amount of gas energy stored in, which are site-specific and difficult to be quantified. Therefore, here, it is assumed that a coal and gas outburst will cease when there are no more elements in the solid coal which satisfy the ejection criterion.

7.3 Coal and Gas Outbursts in the Pingdingshan Coalfield

7.3.1 A Brief Introduction to the Pingdingshan Coalfield

The Pingdingshan coalfield contains the largest coal deposit in the Henan Province, central China (Figures 7.3 and 7.4), and suffers the most from catastrophic outbursts. Most of the Pingdingshan coalfield is mined by Pingmei Shenma Energy and Chemical Group (PCG). PCG currently operates 36 coal mines, producing 50 million tonnes coal per year with over 70 % of the coal mined from outburst-prone coal seams. The first outburst in the coalfields was reported in 1984. Since then, a total of 156 outbursts have been recorded in PCG mines. The average amount of ejected coal and emitted gas in each outburst is 117.2 tonnes and 8633.6 m^3, respectively.

Figure 7.3: The Henan Province and the city of Pingdingshan in China.

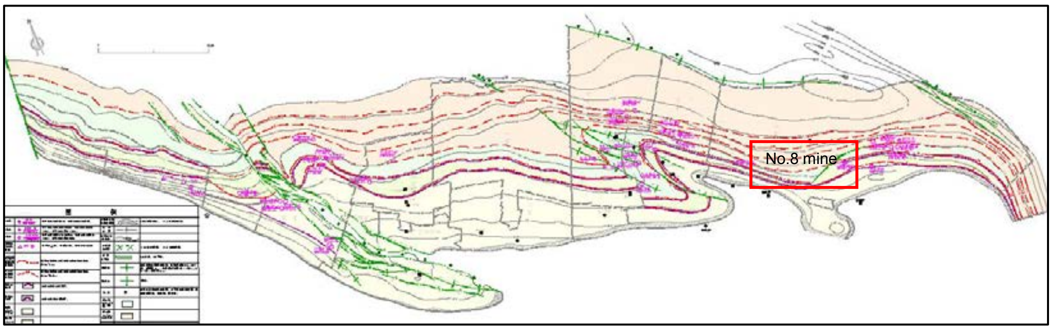

Figure 7.4: Pingdingshan coal field and the location of Mine No 8.

Amongst all the minable coal seams in PCG, coal seam groups B, C, and D are particularly outburst prone, accounting for approximately 87% of the recorded incidents. This is probably due to the fact that these coal seams are made up of soft coal with extremely low permeability (coal permeabilities as low as $1\times10^{-19} \sim 6.1\times10^{-18}$ m^2 have been reported in some regions). In addition, the existence of relatively strong roofs may also have contributed to the frequent occurrence of outbursts (Lama and Bodziony, 1998).

Table 7.1: Average gas contents of coal seams in No.8 coal mine, PCG.

Coal seam	$D_{5\text{-}6}$	C_8	$C_{9\text{-}10}$	B_{15}	$B_{16\text{-}17}$
Gas content (m^3/t)	5.2	6.16	17.4	22	20

Methane contributes to approximately 90% of overall gas emissions. Thus, it is no surprise that the emitted gas in outbursts is mainly methane. Coal seam gas pressure and gas content in PCG mines varies with depth of burial and is also affected to a different degree by previous mining. The maximum gas pressure is reported to be 6.6 MPa. Table 7.1 presents the average gas content of coal seams (from top to bottom) in mine No.8.

7.3.2 Coal and Gas Outbursts in PCG Mines

A fractured coal band, or structurally referred to as a bedding shear zone, has been considered as the most common geological structure that is associated with outbursts in group C coal seam (noted as Wu coal seam by Li (2001)). In this type of bedding shear zone, coal tends to be highly deformed and a rapid variation of thickness is normally observed. Field experience also suggests that areas with increased thickness of the bedding shear zone are susceptible to outbursts. Most intensive coal and gas outbursts in PCG are induced by the thickening of bedding shear zone, which is locally known as ‘the thickening of soft coal’. This may be attributed to the decrease of coal strength and the increase of gas storage capacity in the bedding shear zone. It has also been suggested by Li (2001) that compressive structures existing in the bedding shear zone are normally low permeability or even impermeable (see Figure 3.8). These compressive structures may act as a tectonic intrusion, which can block gas migration and yield a dramatic pressure gradient between the bedding shear zone and a mine opening.

Once initiated, catastrophic failure may occur in the bedding zone due to its very soft nature. Compressed high pressure gas can easily push the highly fractured and even powder-like coal in the bedding shear zone towards the mine opening, which can further destabilise the solid coal face. On the other hand, the ejected coal will soon lose its retained gas and contribute to overall gas emissions. Therefore, this type of outbursts, characterised by the gas pocket theory, always involve the emission of gas as well as the ejection of coal particles.

Outbursts originating from adjacent gassy seams, particularly floor coal seams, have also been observed in PCG mines. These can be better described by the dynamic theory since it is closely related to mining induced fracturing in the surrounding strata.

One of the techniques employed in PCG mines for outburst protection is so called “Protective Mining”, whereby an over-/under-lying less gassy seam is first mined so that a gassy seam can be pre-degassed to reduce the risk of outburst, as illustrated in Figure 3.10. However, driving longwall entries in protection seams in PCG mines occasionally encounters serious gas emission issues where the expected release of gas from the protected seam is sometimes hindered by spatial variations in coal strength and/or thickness and lead to floor gas accumulations. When the floor coal eventually fails, a rapid release of the accumulated gas may occur, leading to (predominantly) gas outburst (the amount of ejected rock/coal, if present, is less than 100 tonnes).

7.4 Modelling of Coal and Gas Outbursts Induced by a Bedding Shear Zone during Roadway Development

7.4.1 Model Set-up

The model developed for a large scale outburst, which involves the violent ejection of both coal and gas, aimed at simulating the behaviour of Seam C in Pingdingshan coalfield. As one of the C group coal seams, $C_{9\text{-}10}$ is considered as an outburst-prone coal seam since it is relatively thick, which ranges from 4.6 ~5.8 m, and contains widespread bedding shear zones (Li, 2001). Therefore, a roadway heading driven in $C_{9\text{-}10}$ coal seam has been selected as the site for this mode of outburst.

The immediate roof of the coal seam $C_{9\text{-}10}$ is sandy mudstone with a thickness of 8.0 ～13.0 m. The main roof rock is medium strength sandstone. The immediate floor is mudstone containing plant roots and fossils, and easily swells when in contact with water. Below the immediate floor is a layer of medium strength mudstone followed by sandstone. A schematic representation of the simplified stratigraphy used in the model is shown in Figure 7.5.

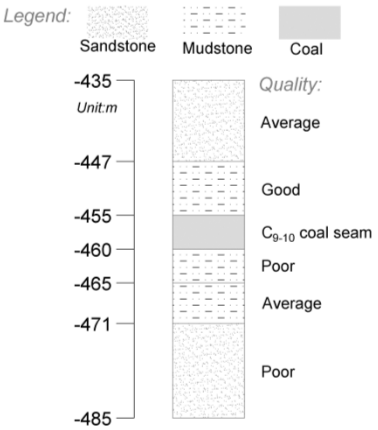

Figure 7.5: General stratigraphy used for the coal and gas outburst model.

As shown in Figure 7.6, the physical dimensions of the model are 50×30×50 m (length×width×height) and a uniform size of 1×1×1 m (length×width×height) is used for each element. The simulated $C_{9\text{-}10}$ coal seam has a thickness of 5 m and its floor depth is -460 m. The roadway has a cross-section of 9 m^2 (3 m wide × 3 m high). Roadway excavation starts from the left side boundary and advances along the floor of this coal seam towards the opposite side. Each excavation step represents 1 m advance of the development heading. The simulated drivage rate is set at 10 m/day, thus the required fluid simulation time in ECLIPSE is 0.1 day following the reaching of geomechanical equilibrium at each excavation step. Within each excavation step, four iterations of the coupling parameters are carried out between the two simulators to improve coupling tightness. The bottom-hole pressure for the horizontal well representing this roadway is assigned as the atmospheric pressure (0.1 MPa).

A 20×30×10 m (length×width×height) bedding shear zone was assigned to this model, which covers 20 m wide section of the coal seam along the x-axis as shown in Figure 7.6. The coal seam thickness in this zone was increased to 10 m (from -463 to -453m vertically) as suggested by Li (2001). A number of geomechanical and reservoir input parameters used here are also different from the other parts of $C_{9\text{-}10}$ coal seam (Tables 7.2 and 7.3). Within this bedding shear zone, a three-metre long low permeability area (from 20 to 23 m along the x-axis) corresponding to a tectonic intrusion is also defined.

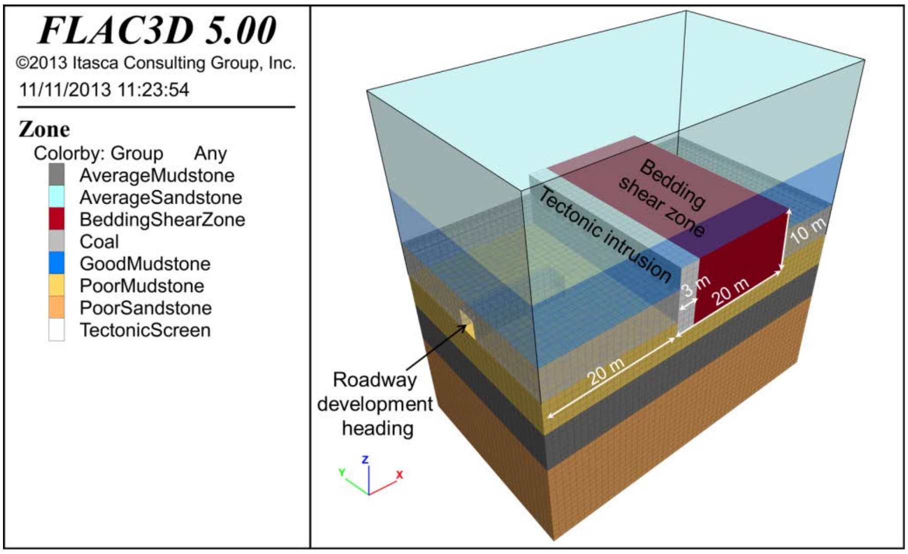

Figure 7.6: Model geometry for the coal and gas outburst induced by a bedding shear zone.

Table 7.2: Rock mechanical properties of coals and coal measure rocks at PCG.

Lithology	K (GPa)	G (GPa)	c (MPa)	θ (^{o})	T_0 (MPa)	c_r (MPa)
Coal $C_{9\text{-}10}$	0.86	0.40	1.5	22	0.03	0.50
Bedding Shear Zone	0.86	0.40	0.6	22	0.01	0.20
Coal B_{15}	1.25	0.60	2.0	25	0.50	0.60
Inter-bedding layer	2.00	0.92	2.0	23	0.20	0.20
Coal $B_{16\text{-}17}$	0.86	0.40	0.8	23	0.03	0.24
Poor Mudstone	2.00	0.92	4.0	26	2.00	0.40
Average Mudstone	2.90	1.35	5.0	32	2.50	0.50
Good Mudstone	4.00	1.83	7.0	35	3.00	0.70
Poor Sandstone	5.00	2.31	8.0	38	3.50	0.80
Average Sandstone	8.00	3.70	10.0	40	4.00	1.00
Good Sandstone	10.00	4.62	12.0	45	5.00	1.20

*K is bulk modulus, G is shear modulus, c is cohesion, θ is internal friction angle, T_0 is tensile strength, and c_r is residual cohesion.

The maximum principal stress in Pingdingshan coal field is mostly due to tectonic stresses and can range from 15 MPa at a depth of -420 m to 28.6 MPa at a depth of -657 m (Han *et al.*, 2012). Considering the origin of the modelled bedding shear zone, the maximum principal stress is assumed to be parallel to the x-axis. Based upon the in-situ stress measurement conducted by Han *et al* (2012), the initial stresses applied at the depth of $C_{9\text{-}10}$ coal seam were 16 MPa, 10 MPa, and 13 MPa in x-, y-, and z-axes, respectively. The boundary conditions of the model were such that it is laterally confined and the model base is fixed.

The constitutive model applied here is the strain-softening model in FLAC^{3D}. The post-failure behaviour of coal measure rocks is represented by the weakening of cohesion with respect to inelastic strain. It is assumed that the residual cohesion is 10% of that of intact rock once the inelastic strain has exceeded 1 millistrain.

Rock elastic and strength properties used in the model were obtained from the laboratory experiments on samples taken from exploration boreholes at PCG. Coal in the bedding shear zone has been pre-defined as fractured coal with a reduced cohesion of 0.6 MPa. To emphasise the strength contrast between the soft coal in the bedding shear zone and the rest of $C_{9\text{-}10}$ seam, a much higher residual cohesion (0.5 MPa) has been assigned to the rest of $C_{9\text{-}10}$ seam. Table 7.2 summaries the rock mechanical properties of the coals and coal measure rocks in PCG mines.

Table 7.3: Reservoir properties of coals and coal measure rocks in PCG.

Lithology	ϕ (%)	D_c (m^2/day)	P (MPa)	P_L (MPa)	V_L (m^3/kg)	k_0, horizontal/vertical ($\times 10^{-15}$ m^2)
Coal $C_{9\text{-}10}$	2.0	100	1.8	2.1	0.023	0.50/0.20
Bedding shear zone	2.0	100	1.8	2.0	0.055	0.010/0.007*
Coal B_{15}	1.8	100	1.0	2.9	0.022	0.10/0.05
Coal $B_{16\text{-}17}$	1.5	1000	2.5	2.6	0.020	0.10/0.07
Inter-bedding layer	1.0	--	--	--	--	0.010/0.005
Other coal measure rocks	1.0	--	--	--	--	1.0/0.6

*Permeability used for the tectonic intrusion is horizontally 1×10^{-18} m^2 and vertically 7×10^{-19} m^2. ϕ is porosity, D_c is diffusion coefficient, P is initial pressure, P_L is Langmuir pressure, V_L is Langmuir volume, k_0 is initial permeability for intact coal.

Reservoir properties used are collected and adopted from laboratory experiments and field measurements as summarised in Table 7.3. Since the primary gas emitted from the PCG coal is methane, a single component gas model was considered. A dual porosity model was applied to simulate the unique coal structure, whereby coal matrix was assumed to be saturated with gas while the gas saturation in coal cleats was 66.7%. The relative permeability relationship measured by Durucan *et al.* (2014) for the Tupton coal seam from Derbyshire UK, with a similar volatile matter content, was adopted. Reservoir temperature was set as 23 ˚C. Low permeability was assigned to the bedding shear zone and even lower for the tectonic intrusion. The initial permeability (k_{f0}) for fractured coal/rock was assumed to be ten times of that for intact coal (k_0). Compressibility factors for intact coal (C) and fractured coal (C_f) were selected as 0.5 and 0.3, respectively.

7.4.2 Model Results

Figure 7.7 presents a plan view of pressure distribution modelled around the development heading in Seam $C_{9\text{-}10}$ at -458 m level in PCG. The figure illustrates the evolution of pore pressure with respect to the advance of the development heading during the initiation stage of an outburst. It should be noted that in this figure, pressure contours indicate the pressure redistribution after the pervious excavation step, and the effects of the current excavation step on pressure changes have not yet been updated.

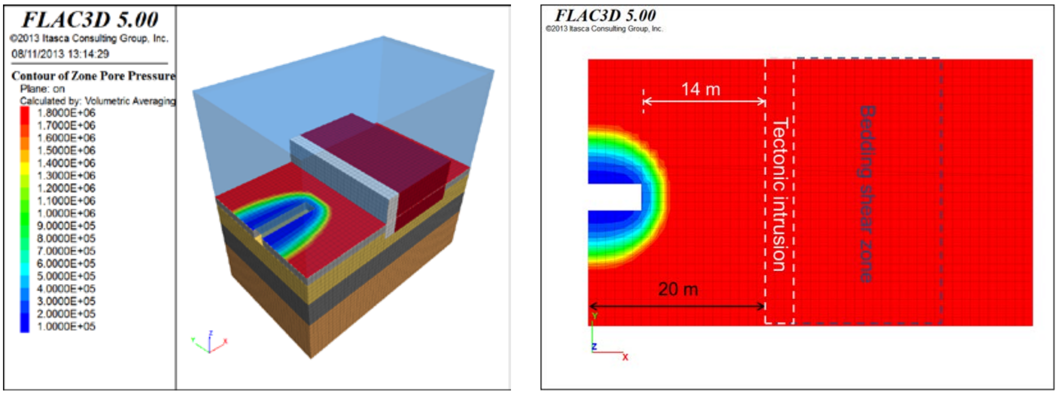

(a) Legend and the cutting plane position (b) Excavation step 6

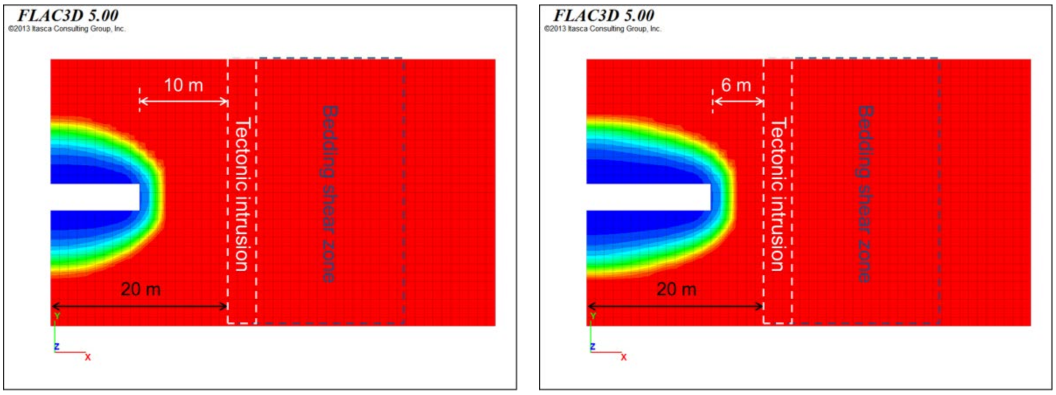

(c) Excavation step 10 (d) Excavation step 14

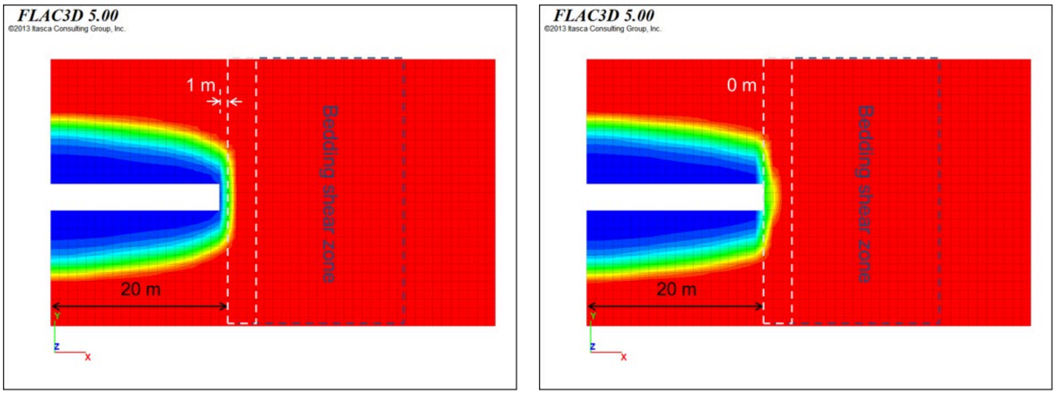

(e) Excavation step 19 (f) Excavation step 20

Figure 7.7: Pressure evolution as the development heading advances towards the bedding shear zone (gas pocket type) scenario (unit: Pa).

A relatively stable pressure change can be observed in the first 17 excavation steps. Pressure redistribution seems to follow a certain pattern, whereby the dramatic pressure drop occurs 3 m ahead of the heading. This is probably because the coal within 3 m of the heading is highly fractured and permeable. As the development heading approaches the bedding shear zone, the pressure gradient right ahead of the heading becomes increasingly high due to the existence of the low permeability tectonic intrusion. After the 20th excavation step, the heading starts to come into contact with the soft coal in the bedding shear zone, where an elevated pressure gradient acts on the low cohesion soft coal. An outburst would be triggered by the coal extraction in this excavation step since the pressure gradient driven force could easily break and eject the low strength solid coal ahead of the heading.

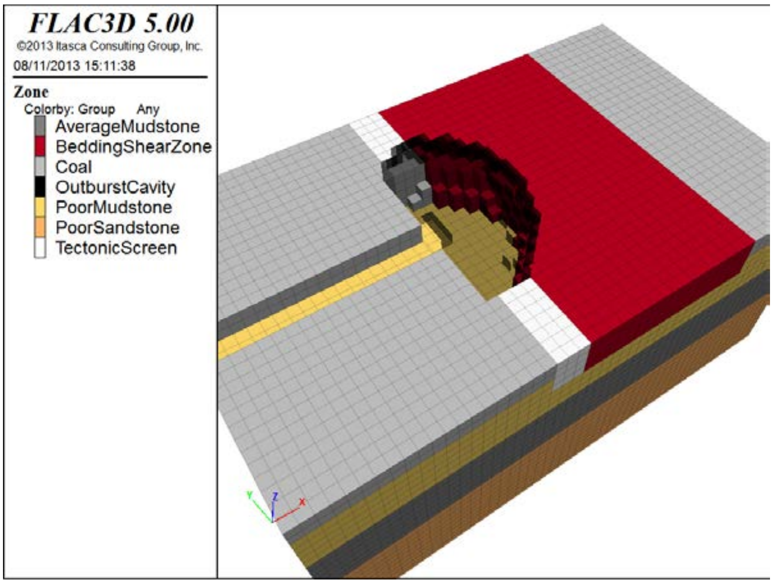

Figure 7.8: Cavity expansion in an outburst induced by a bedding shear zone.

Following the initiation stage, the post-initiation stage of this outburst was modelled following the methodology described in Section 7.2.3. A dome-shaped outburst cavity resulting from the modelled outburst is plotted in Figure 7.8. This is broadly consistent with previous studies that the cavity of an outburst is normally a dome or pear shaped (Shepherd *et al.*, 1981; Singh, 1984; Li, 2001). The predicted maximum length, width, and height of the outburst cavity are 15 m, 7 m, and 10 m, respectively. According to the model, 602.3 tonnes of coal and 9,436 m^3 methane in total would be released at this stage of the outburst. These numbers are reasonable when compared to the recorded outburst cases occurred in group C coal seams at PCG. It has been reported that abnormal gas emission rates (gas emissions dramatically increase or decrease) were occasionally observed prior to most of the intensive outbursts at PCG. Thus the significant changes in gas emissions in development headings may suggest the initiation of an outburst. To confirm this observation, the volume of gas emissions over 20 excavation steps is plotted in Figure 7.9. Note that gas emission volume at the 20th excavation step is not a simulation result from ECLIPSE, but calculated based on the algorithm described in Section 7.2.3.

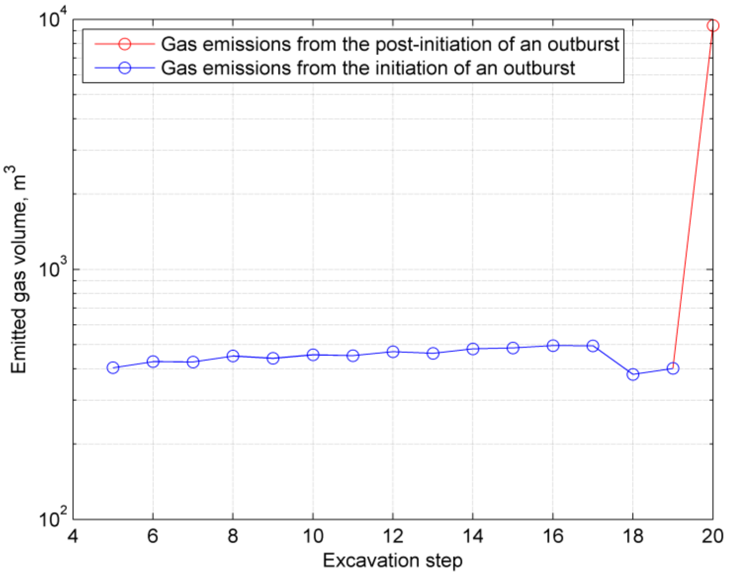

Figure 7.9: Average gas emission volumes during each excavation step as the development heading advances.

As can be seen in Figure 7.9, the predicted evolution of the emitted gas volume over 20 excavation steps shows a sharp increase following the onset of outburst after the 19th excavation step (9,500 m^3 vs. ~450 m^3 during the previous steps), which is consistent with the field observations. This is believed to be caused by the increase of exposed coal surface with roadway development. The sudden drop in gas emissions between the 17th and 19th excavation steps is due to the presence of low permeability tectonic intrusion and may also suggest the pre-initiation of an outburst. Following this, a sharp increase in gas emissions is observed as a result of the outburst onset.

7.5 Modelling of Gas Outbursts Induced by an underlying Gassy Seam during Roadway Development

7.5.1 Model Set-up

This model was developed to simulate floor outbursts (or known as ‘sudden emission’ in the UK) which involve sudden release of gas only. As mentioned earlier, protective mining is currently being employed in group B coal seams of PCG collieries, e.g., Seam B_{15} is first mined to improve the degassing of underlying seam $B_{16\text{-}17}$. Gas bubbling from the $B_{16\text{-}17}$ coal seam is often observed when mining in B_{15} coal seam. Therefore, a development heading driven in B_{15} coal seam has been selected as the model site for an outburst scenario induced by the underlying gassy seam $B_{16\text{-}17}$. The occurrence of this type of outburst is characterised by a dramatic increase in gas emissions, rather than the ejection of coal particles. Since there is no coal ejection takes place in this outburst type, only the methodology about outburst *initiation stage* modelling described in Section 7.2.3 is used to simulate this type of gas emission event.

Exploration data have suggested that B_{15} coal has a relatively high mechanical strength, whereas $B_{16\text{-}17}$ is described as brittle, loose, and can be broken into powder easily. The two coal seams are separated by a weak mudstone formation and sometimes intersected by mudstone with higher strength. This lithological heterogeneity may contribute to irregular fracturing and consequent floor gas outbursts. A schematic of the simplified stratigraphy used in the model is shown in Figure 7.10.

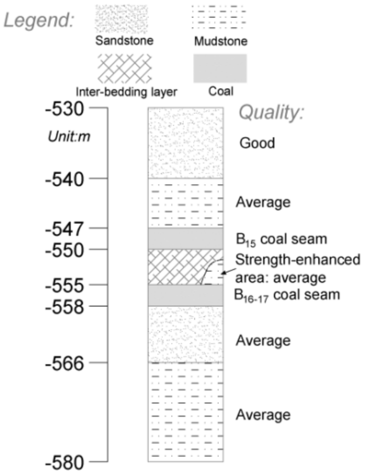

Figure 7.10: General stratigraphy for the gas outburst model.

Although the vertical distance between these two seams is only 8 m, pore pressures of these seams were reported to be quite different. The initial pressure in B_{16-17} is much higher than B_{15}, and this is probably due to the low permeability of the inter-bedding layer between them. The existence of this layer allows B_{16-17} to be less affected by the mining of above coal seams than B_{15} coal seam, and thus gas can be largely retained in it. Given this fact, the property of the inter-bedding layer was assigned as low strength and low permeability to maintain the in-situ high gas pressure in seam B_{16-17}.

The physical dimensions of this model was set as 50×30×50 m (length×width×height) and a uniform size of 1×1×1 m (length×width×height) was used for each element (Figure 7.11). Seam B_{15} has a thickness of 3 m, at -550 m depth. Seam B_{16-17}, which is also 3 m thick, is located 8 m below the B_{15} seam. The development heading modelled has a cross-section of 9 m^2 (3 m wide and 3 m high).

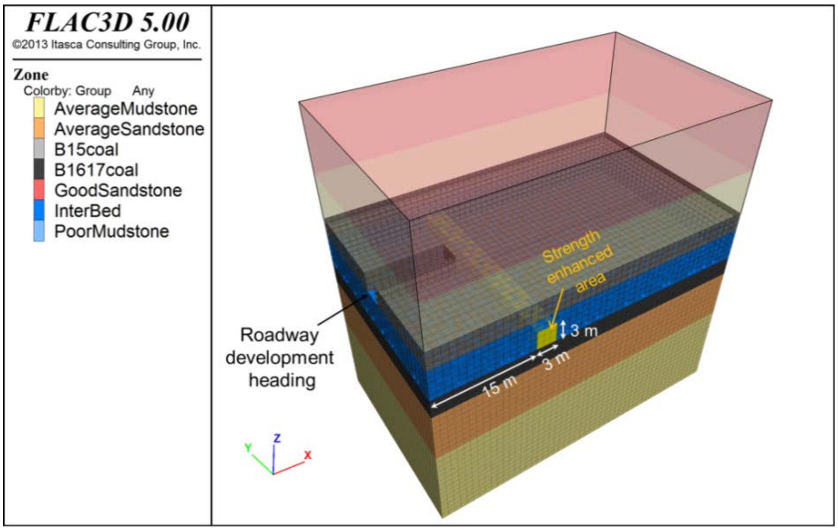

Figure 7.11: Model geometry used for the gas outburst induced by an underlying gassy seam.

As in Section 7.4.1, roadway excavation from the left-side-boundary at a rate of 10 m/day was simulated, with each excavation step representing 1 m advance. The bottom-hole pressure for the horizontal well, representing this roadway, was assigned as the atmospheric pressure 0.1 MPa. Given the depth of the modelled roadway and in-situ stress conditions in PCG (Han *et al*., 2012), the initial stresses applied at the depth of B_{16-17} seam were 21.3 MPa, 10.3 MPa, and 14.1 MPa along the x-, y- and z-axes, respectively. The boundary conditions of the model were such that it is laterally confined and the model base is fixed.

To reflect the heterogeneity in the inter-bedding layer, a region measuring 3×30×3 m and positioned at 15 to 18 m along the x-axis was assigned with the strength of average mudstone, as illustrated in Figure 7.11. The geomechanical and reservoir properties used in the model were the same as those used in the previous section (Tables 7.2 and 7.3). So were the other input parameters such as saturation, compressibility factor, constitutive model, and temperature.

7.5.2 Model Results

Vertical cross sections illustrating pressure distribution around the development heading are shown in Figure 7.12. As can be seen, the pressure distributions follow a similar pattern during the first 14 excavation steps, showing a notable gas release from the protected seam in the region underneath the B_{15} coal seam being-mined. As the development heading approaches the higher strength area in the inter-bedding layer, the gas pressure in that region starts to build up. It is noted that this high pressure cloud does not dissipate immediately after the passing of the development heading at the 18th excavation step, but rather at the 22nd excavation step.

Fracturing of floor strata plays a critical role for gas transportation from $B_{16\text{-}17}$ to the development heading in B_{15} coal seam. Figure 7.13 (continuous line) plots the cumulative number of failed elements in the floor strata (including both the inter-bedding layer and seam $B_{16\text{-}17}$) with the advance of development heading, showing almost a linear trend up to the 14th excavation step. This trend is temporarily disrupted as the higher strength area is approached, which leads to a sharp reduction in the number of new failed elements in seam $B_{16\text{-}17}$ (dotted line in Figure 7.13) suppressed the fracturing of the coal and rock elements in the floor strata.

As shown in Figure 7.14, the presence of the higher strength region in the floor strata leads to a significant reduction in gas emission over the period between the 14th and 20th excavation steps, compared to the base case with homogeneous strength properties in the floor strata, where gas emission is maintained at about 850 m^3 over the excavation period. During this period, approximately 2,000 m^3 of gas would be retained. This is followed by a sharp increase in gas emission with the passing of the development heading at the 22nd excavation step. The amount of gas emitted in this excavation step is as high as 2,206.4 m^3, which is made up by the retained gas and the newly released gas. The dip in the gas emission may be used as a precursor for a floor gas outburst.

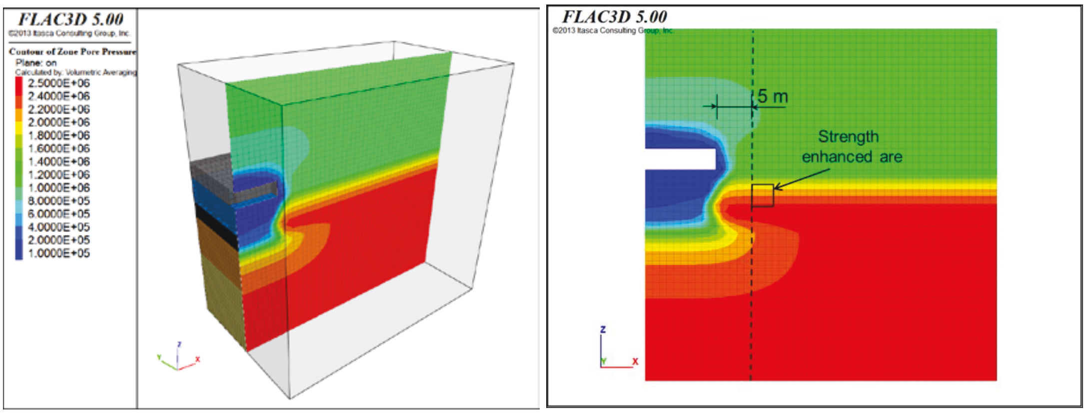

(a) Legend and the cutting plane position (b) Excavation step 10

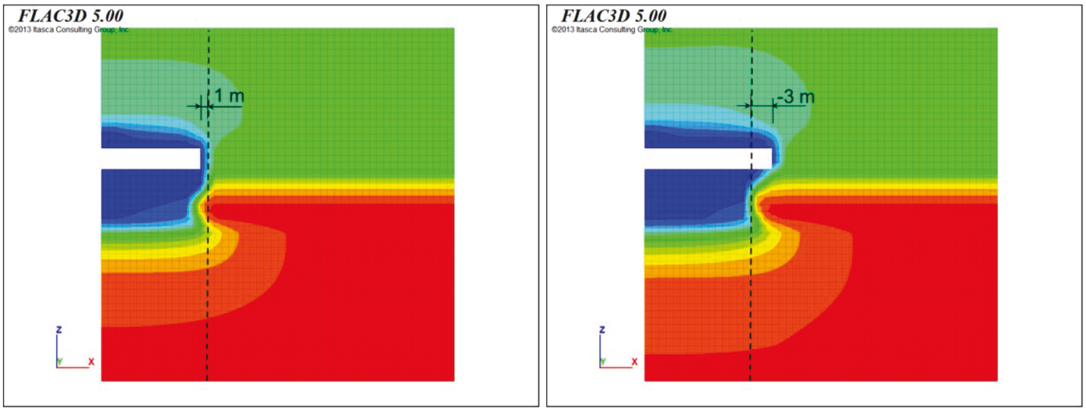

(c) Excavation step 14 (d) Excavation step 18

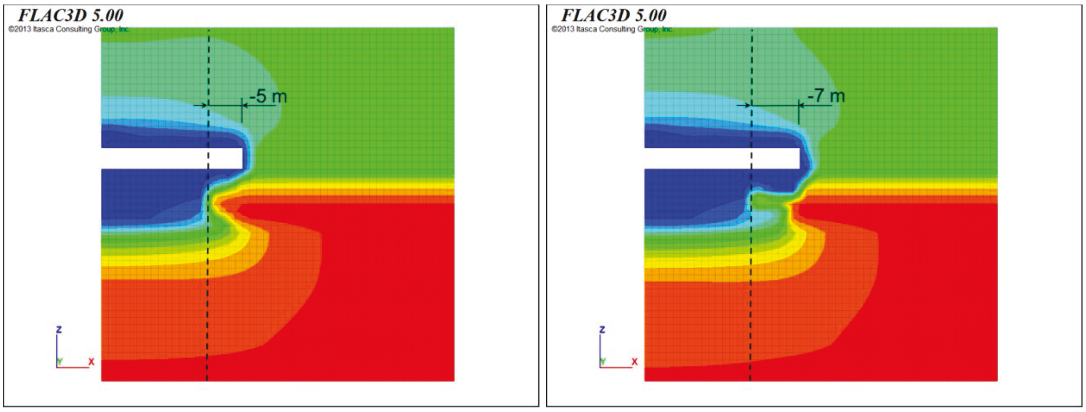

(e) Excavation step 20 (f) Excavation step 22

Figure 7.12: Pressure evolution as the development heading advances in the floor outburst scenario (unit: Pa).

It has been confirmed by the floor gas outburst model that gas emission rate is closely related to the fracturing of floor strata. Regular fracturing can result in a relatively constant gas emission rate. However, once this regular pattern is interrupted, for instance the failure of the floor strata is suppressed by a strong floor section (during the 15th to 18th excavation steps), a reduction in gas emission rate is expected to occur. The following resumption of floor strata failure gradually reconnect gas flow conduits from $B_{16\text{-}17}$ to B_{15}, from which the gas accumulated over previous excavation steps can suddenly rush into the development heading. Thus, a dramatic increase of gas emission volume, such as that experienced during the 22nd excavation step, is observed as soon as the conduits have been re-established.

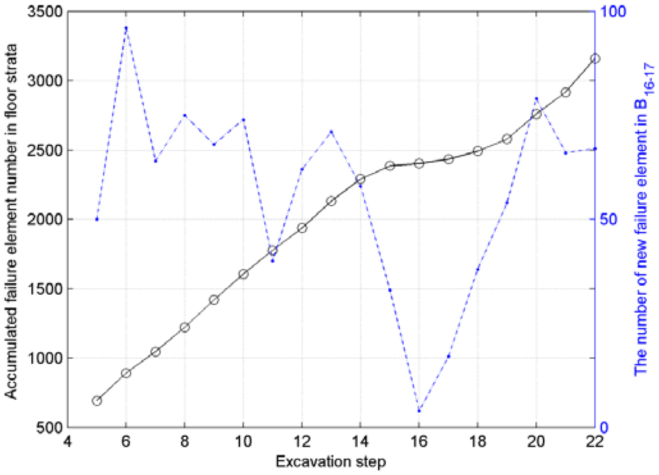

Figure 7.13: Number of failed elements in the floor strata as the development heading advances.

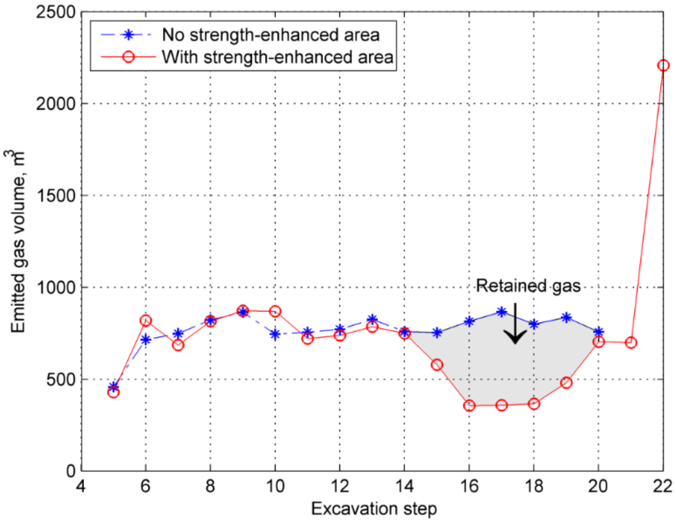

Figure 7.14: Gas emission as the development heading advances in a floor outburst scenario.

7.6 Discussions

7.6.1 Model Limitations

The intensity of the gas pocket outburst predicted using the PCG data set in Section 7.4 is somewhat limited by the conservative assumptions made in this research. For example, Equations 7.2 and 7.3 both assume fast equilibrium and the time-scale required in these two processes ideally should be much shorter than an outburst incident, however, this does not always hold. A better approach to estimate pressure and gas volume in the cavity needs to consider fluid dynamics, which could not be modelled by the simulators used.

In Equation 7.3, V_{void} is the sum of the volume of outburst cavity and a part of the development heading involved. However, it is rather difficult to estimate the latter accurately without knowing the mine’s roadway network and modelling the outburst gas flow rate in roadways. In the model, the latter was assumed to be the modelled roadway size ($20\times3\times3=180$ m^3). Compared with reality, in which the released high pressure gas can push gas front throughout the mine by the well-connected roadway network, the assumed low V_{void} may largely overestimate $V_{pressure}$ and result in the early die-out of an outburst. As a consequence, the volume of gas emissions may also be underestimated. The author acknowledges that the above assumptions limit the ability of model to mimic the development stage of an outburst in reality, however, since the main focus of this research was to model the outburst initiation stage, these assumptions were considered to be acceptable.

It may be debated that only cohesion was considered in the outburst criterion and the tensile strength should not be ignored, given that most previous investigations have stated the importance of tensile failure during an outburst (Gray, 1980; Paterson, 1986; Xu *et al.*, 2006). However, the author does believe that tensile strength is critical in the fragmentation of intact coal, while cohesion is critical for the ejection of broken and fractured coal. In terms of outburst modelling, the coal in the bedding shear zone has already been represented as highly fractured and powder-like. Thus, the cohesion of a coal element, which actually refers to the friction between small coal fragments inside the coal element, has been taken as the only factor affecting coal ejection. In the case of other outburst types involving a large bulk of coal to be fractured and fragmented by high pressure gas, the proposed criterion may need to be modified. In that case, parameters characterising the damaging of coal structure, fluid driven fractures, and the fragmentation of coal need to be considered. Defining these parameters will involve significant experimental work, which is out of the scope of this research.

7.6.2 Similarities with Thick Seam Outbursts at Coal Mine Velenje

The two outburst models developed based on the data from the PCG collieries in the Pingdingshan coalfield can also be used in modelling the outbursts experienced by thick seam mining at Coal Mine Velenje, which is suffering from both gas pocket type and dynamic outbursts.

In Coal Mine Velenje, there is a hypothesis that the different properties between xylite and detrite may be the main reason for the occurrence of gas gas outburst. It is believed that the conditions for a gas outburst is formed when mine workings suddenly pass from the “hard” xylite to “soft” detrite - especially when such contacts are sharp and connected to fault zones (Zavšek et al. 1997). The importance of this mechanical transitions was also pointed out by Jeremic (1985) who noted that existence of large pockets of weak porous coal (i.e. “soft” detrite-rich lignite) surrounded by strong heterogeneous coal (i.e. “hard” xylite-rich lignite) or vice versa can facilitate coal and gas outbursts after de-stressing of the coal seam. As discussed in detail in Chapter 5, the LTCC panel K.-50/C approaching one such structure lead to an episode of an excessive gas emission, which was clearly identified by microseismic monitoring and seismic tomography.

Gas emissions from the floor coal at Coal Mine Velenje may be more significant and serious than those experienced at PCG. The multi-level LTCC mining method implemented at Coal Mine Velenje develops a longwall panel or a heading directly above the gas source. In this case, the fracturing of floor coal, which may vary depending on lithological heterogeneity, determines the nature of gas emissions at the active mining level. As already mentioned in Section 4.5.2, coal extraction in an upper level may not completely fracture the coal in the lower level, and some intact areas with high strength xylite may exist. Therefore, it is likely that an abrupt transition from xylite to detrite in the floor coal may lead to a considerable increase in gas emissions.

7.7 Conclusions

The two-way sequential coupling methodology developed earlier has been successfully implemented in simulating two types of outbursts using field data from the outburst prone Pingdingshan coal field in China. Gas pocket type and dynamic outbursts experienced in development headings were simulated and studied separately in this Chapter.

A geological structure, referred to as the “bedding shear zone”, regularly seen at PCG is believed to be the cause of gas pocket type outbursts in this coalfield. The models implemented simulated not only the stress and pressure redistributions which evolve at the *initiation stage*, but also the cavity expansion that takes place during the *development stage* of coal and gas outbursts. Model findings were consistent with the field observations in terms of the quantity of ejected coal, the shape of outburst cavity, and the gas emission trends observed before an outburst.

The second outburst type, induced by gassy floor seam, is believed to be best-described by the dynamic theory. Although the violent ejection of coal experience in this type of outbursts was not captured in the simulations implemented, the retention/accumulation and sudden release of gas in an underlying coal seam were successfully reproduced.

The two outburst models presented have both demonstrated that an unusual gas emission trend may suggest an incoming outburst. In the case of outbursts induced by a bedding shear zone, a reduction in the volume of gas emission was noticed 2 m ahead of the outburst loci. A notable reduction in gas emissions was also observed 7 m ahead of the floor outburst loci. These observations emphasised the importance of continuous monitoring of gas emissions at development headings. Precautions such as reducing the drivage rate or employing gas drainage can be considered as the means to prevent these type of outbursts.

Underground gas drainage is no doubt the most effective technique that can be used to address excessive gas emissions and outbursts. Although gas drainage is widely applied in many coalfields, the design of drainage layouts used are mostly based on experience and without the guidance of the analysis of mining induced stresses and permeabilities. Chapter 8 in this thesis explores the effects of mining on gas drainage performance and how to optimise the design of drainage boreholes.

Chapter 8 Performance Analysis and Numerical Modelling of Field Gas Drainage Trials around Longwall Top Coal Caving Panels

8.1 Introduction

It has been well-recognised that gas drainage can significantly reduce gas content and improve coal mining safety. Although gas drainage from boreholes is not a new technique for gas emission control, its applications are mostly limited to high permeability or mining stimulated coal seams around relatively thin seam longwall operations. On the other hand, only very few examples of the use of gas drainage performance in mechanised LTCC panels can be found in the literature. Cheng et al. (2003) reported that, compared to the mechanised multi-slice longwall mining of thick seams, mechanised LTCC had largely increased gas emission rate at the Yangquan Coal Group in China, however, the specific emission was reduced by around 25% due to significant increase in coal production rate. Both Cheng et al. (2003) and Xu et al. (2007) report on gas drainage trials at LTCC districts in these mines, however, the drainage was implemented from roadways in rock above the production faces and were mostly targeting emission from the overlying seams and the rock strata.

Chapter 4 described the field monitoring and analysis of gas dynamics around LTCC faces at Coal Mine Velenje. The interpretation of the field data by the author led to the development of a conceptual model on gas release and emissions around LTCC panels in multi-level thick seam mining. This conceptual model was further validated through the analysis of seismic monitoring data as described in Chapter 5.

Based on the understanding established on gas dynamics around LTCC coal extractions in this research, this Chapter focuses on the analysis of the impact of mining activities on gas drainage performance at LTCC panels in multi-level thick seam mining. Guided by the findings of numerical modelling work presented in Chapter 6, a series of short-period drainage trials were designed and conducted at Coal Mine Velenje, and results obtained from these trials analysed by the author. Later, the gas emission model presented in Chapter 6 was modified to simulate the performance of horizontal, as well as inclined, boreholes used in the field trials. A parametric study was conducted to compare the effects of different borehole layouts (azimuth, inclination, length, and spacing) on gas drainage performance.

8.2 Gas Drainage Trials at Coal Mine Velenje

8.2.1 Background and General Description

Field measurements presented in Chapter 4 suggested that the initial permeability of Velenje lignite is relatively low (in the order of 10^{-16} m^2) and unfavourable for pre-drainage. On the other hand, it was noted that coal extraction at the LTCC face increases the permeability of coal 40 m into the seam from the face-line, and released a significant volume of roof and floor gas. Therefore, the main objective of gas drainage trials performed at Coal Mine Velenje was to investigate the technology required to achieve drainage to reduce gas content and pressure in the lignite before and during LTCC coal extraction. The associated borehole configuration, pipeline deployment, gas vacuum pump selection, and monitoring system set-up can be examined as well in these trials.

A first level LTCC panel (K.-65/F) at a depth of 455 m was selected as the test panel for drainage trials. The strata condition of this panel was relatively simple, which was under a clay roof and above more than 80 m thick virgin coal. Due to the initial high gas pressure and content, the ventilation system in this panel was not sufficient to maintain CO_2 and CH_4 concentration below the statutory levels.

A series of gas drainage trials were designed and conducted from the end of February 2013 to the beginning of April 2013 by the engineers at Coal Mine Velenje. Initially four pilot drainage boreholes (R1, R2, R3, and R4) were planned. However, as the longwall face advanced over boreholes R1 and R2 before the drainage trials could be started, additional (back-up) boreholes R5 and R6 were also drilled.

Since the mine had no previous experience in underground gas drainage, the trials were strictly performed under the mining regulations of Slovenia. The power supply, monitoring sensors, and other mechanical parts used for drainage trials were already tested and proven in coalmines worldwide, as well as at Coal Mine Velenje leading up to the trials. However, long-term automated/unattended performance of the drainage system was not possible due to concerns about potential risks. Instead, a number of trials with shorter drainage durations (up to 4 hours) were repeated under strict inspection.

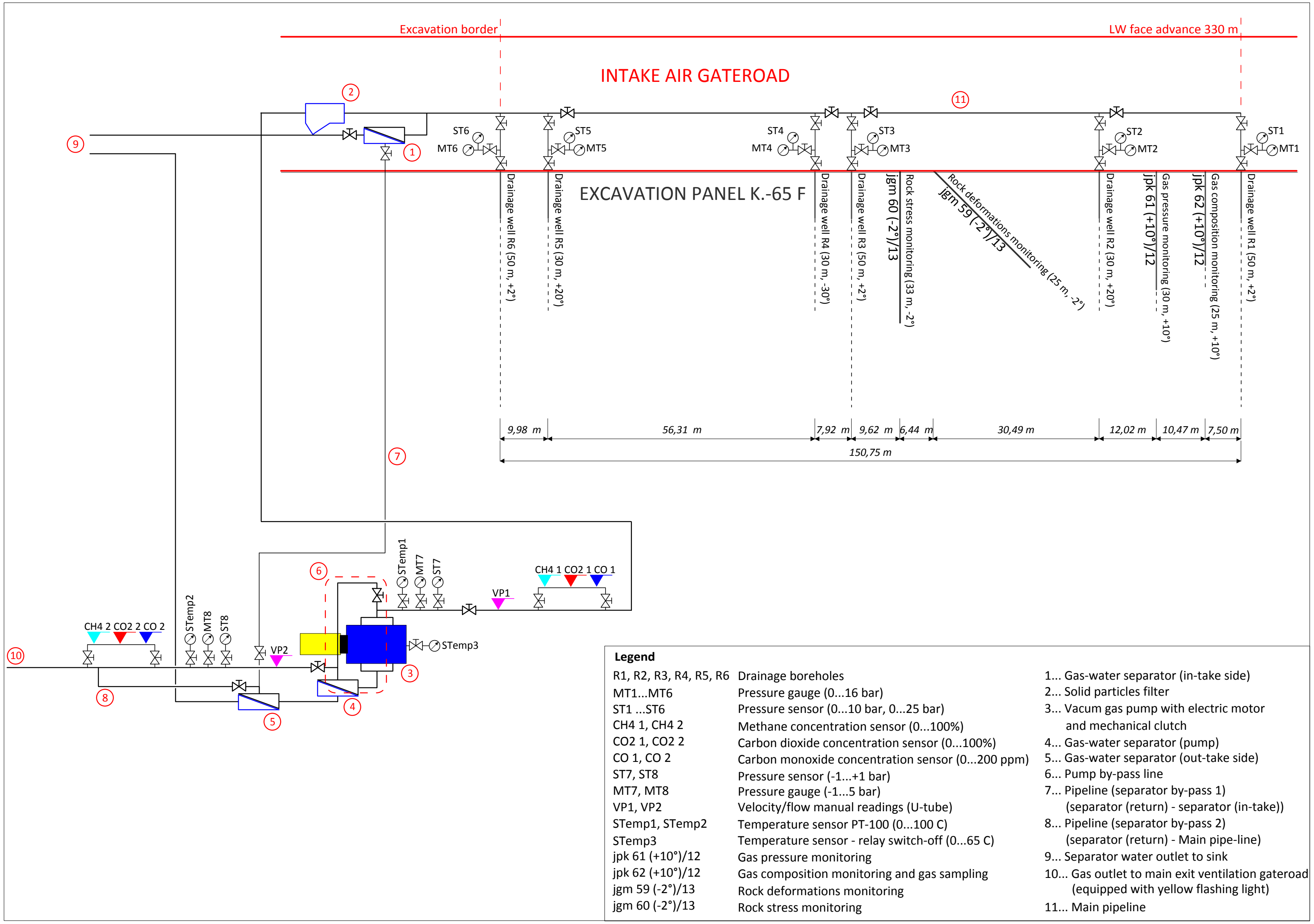

Figure 8.1: Schematic of the pilot gas drainage trials system (Courtesy of the Coal Mine Velenje Researchers)

8.2.2 Gas Drainage System and Monitoring Equipment

8.2.2.1 Drainage Boreholes

A schematic of the pilot gas drainage trial layout is presented in Figure 8.1. The pilot drainage boreholes were designed in different lengths and inclination in order to investigate the effects of borehole parameters on drainage performance. The drainage boreholes were all drilled in coal, in relative positions with respect to the retreating longwall panel K. -65/F (Figures 8.1 and 8.2) with a several other boreholes for stress, gas pressure and concentration monitoring. Previous experience has shown that drilling of horizontal or slightly inclined (-30 - +20°) boreholes was technically possible up to 50 metres, therefore, and in consideration of these limitations, all the boreholes were drilled to the planned depths shown in Table 8.1.

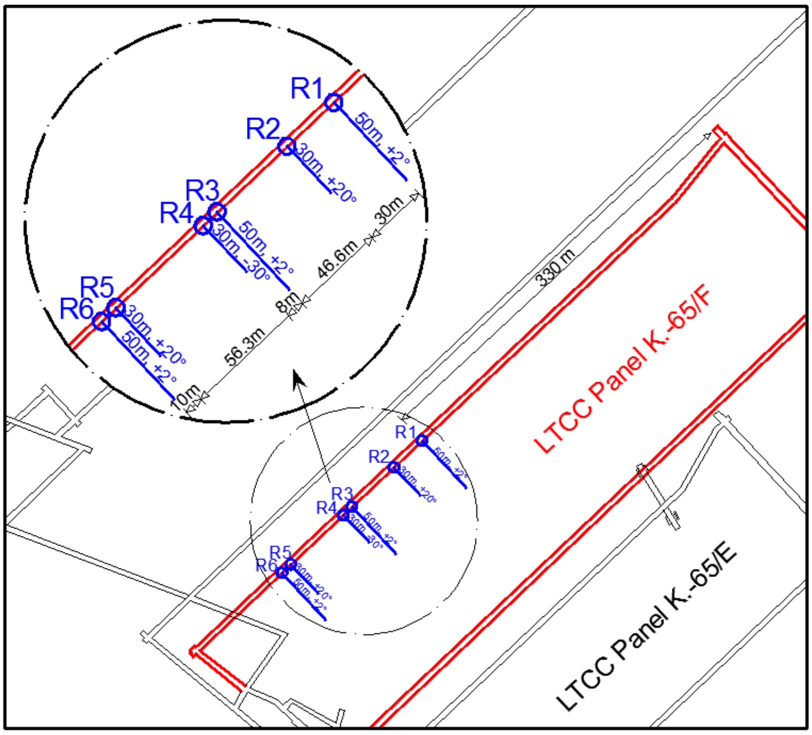

Figure 8.2: Locations of gas drainage and seam gas pressure-composition-rock stress and deformation monitoring boreholes (Courtesy of Coal Mine Velenje Researchers).

Table 8.1: Drainage borehole design parameters.

Borehole No.	Inclination (°)	Borehole length (m)	Borehole diameter (mm)	Standpipe length (m)
R1	+2	50	100	10
R2	+20	30	100	10
R3	+2	50	100	10
R4	-30	30	100	10
R5	+20	30	100	10
R6	+2	50	100	10

Each borehole was drilled parallel to the face-line in the intake gateroad with spacing around 10 m. Primary casing was applied to the first 10 m of the borehole length, and the rest of the borehole was equipped with a perforated antistatic plastic drainage tube. Borehole seal was completed by injecting cement between the standpipe and the surrounding coal. After the completion of a borehole, water was used to clean the borehole before the trails started.

8.2.2.2 Drainage Pipeline

Since there was no existing underground pipeline network for the transportation of captured gas, a new pipeline, which was around 400 m long, was built to transport the drained gas at the longwall panel to a return ventilation gateroad. Gas concentration sensors for both CH_4 and CO_2 were installed 20 m away from the outlet of the pipeline in the gateroad to continuously monitor the ventilation environment there. As shown in Figure 8.3, a rubber hose was used to connect the fixed plastic tube inside the borehole to the pipeline. In addition, at the outlet of each borehole, a pressure gauge was installed to test borehole seal and monitor seam gas pressure in the absence of drainage. After completion, the drainage pipeline was tested for leakages with compressed air to make sure the sealing was completed and no notable pressure drop was observed.

Figure 8.3: The connection between a drainage borehole and the pipeline at Coal Mine Velenje (Courtesy of Coal Mine Velenje Researchers).

8.2.2.3 Gas Vacuum Pump

For its capacity, reliability, and cost, Nash 2BE1 203, which is a fully mechanical water-cycle vacuum pump was selected as the vacuum pump for the gas drainage trials. To obtain a stable gas flow rate, suction pressure was maintained between -30 and -20 kPa during all trials.

In preparation for the underground trials, the pump was equipped with required sensors and other safety elements as shown in Figure 8.4. Gas vacuum pump required inflow of water as the working media when in operation. Consequently, part of the recycle water was continuously pumped into the compression section of the pipeline. As a preventative measure, a gas-water separator (element No. 4) was installed between the pump and the pipeline. The separated water was led to a sink nearby via an outflow hose (element No. 12).

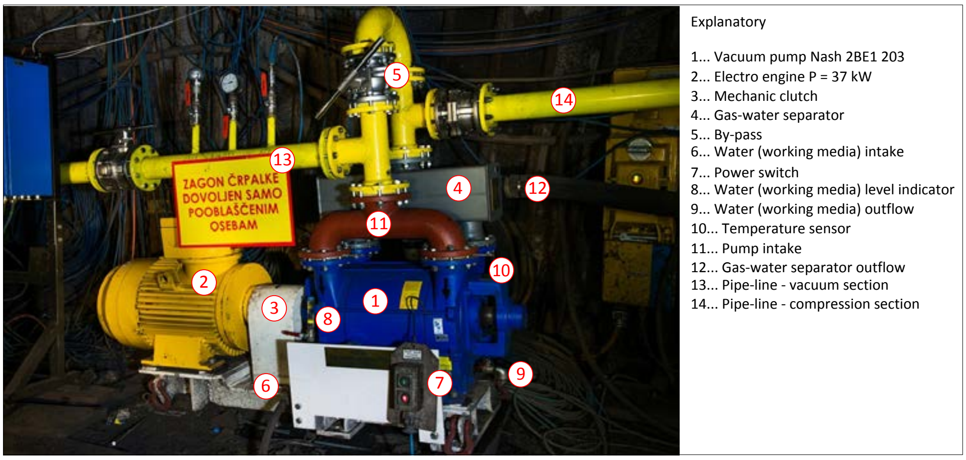

Figure 8.4: The gas vacuum pump used in gas drainage trials (Courtesy of Coal Mine Velenje Researchers).

(a) (b)

Figure 8.5: The gas drainage real-time monitoring equipment: (a) Gas concentration sensors (from left to right: CO_2 (0~100 %), CH_4 (0~100 %), and CO (0~200 ppm)); (b) Gas pressure and temperature monitoring (from left to right: pressure sensor (-1~1 bar), pressure gauge (-1~5 bar), and temperature sensor (0~100˚C)) (Courtesy of Coal Mine Velenje Researchers).

8.2.2.4 Real-time Monitoring Equipment

The concentration of captured gas was continuously monitored by a CO_2 sensor, a CH_4 sensor, and a CO sensor installed at the main pipeline (Figure 8.5 a). The ventilation environment (CO_2 concentration, CH_4 concentration, and ventilation flow rate) around the pump was also continuously monitored by nearby sensors. In addition, a pressure sensor, a temperature sensor, and a pressure gauge were installed at the pipeline near the pump to monitor gas drainage performance (Figure 8.5 b). Data acquisition was set at 10-second interval, and recorded data were sent to and stored on the surface information centre via underground cables.

The flow rate of captured gas was originally planned to be monitored by a real-time sensor. However, since this sensor was not available during the drainage trials, a mechanical U-tube was installed onto the pipeline as a substitute. The minimum flow rate that could be measured by this mechanical U-tube was approximately 12 l/s.

The ventilation air was monitored continuously in the area of drainage trials and along the pipeline with fixed mine sensors. During whole trials, technical staff in charge monitored methane concentration (to <0.5%) in ventilation air with portable sensors which were required during experiments and pilot trials.

8.2.3 Gas Drainage Data Analysis

In order to establish an understanding of the gas drainage performance of a single borehole as the face approached towards it, drainage trials were first performed with individual boreholes. As mentioned earlier, repeat drainage trials were conducted with respect to different face-line positions, but each trail only lasted from several minutes to several hours. Table 8.2 provides a detailed outline of the drainage cycles implemented and the performance achieved during the pilot trials using boreholes R3 and R4. Trials with Borehole R3 were performed in 13 separate time periods with respect to the longwall face advance (Table 8.2). The first three trials, when the longwall face was over 44.1 m from borehole R3, have recorded gas flow rates below the detection limit (~ 12 l/s) due to the low permeability of coal seam. The following trails have shown a dramatic increase in the average gas flow rate of up to 57.04 l/s. For the last trial when the face was 2.9 m from the borehole, the pump was switched off and gas flow was driven by the natural pressure difference between the gateroad and the coal seam.

Table 8.2: Details of the drainage cycles implemented and the performance achieved during the pilot trials using boreholes R3 and R4.

Date	Face position (m)	Face distance to borehole (m)	Time trial started (h/min/sec)	Time trial ended (h/min/sec)	Duration (h/min/sec)	*Suction pressure (kPa)	*Concentration (vol %)				*Total flow rate (l/s)	*CH_4 flow rate (l/s)	*CO_2 flow rate (l/s)	*Air flow rate (l/s)
							CH_4	CO_2	Air	CH_4 in air				
							Borehole R3							
27/02/2013	329	78.1					35.00	22.00	43.00	44.87	**	**	**	**
11/03/2013	354.5	52.6					37.00	24.00	39.00	48.68	**	**	**	**
15/03/2013	363	44.1					37.00	24.00	39.00	48.68	**	**	**	**
20/03/2013 10:35	369.5	37.6	10:35:50	10:36:30	00:00:40	-28.00	20.70	43.25	36.05	36.48	51.67	10.70	22.35	18.63
20/03/2013 10:42	369.5	37.6	10:42:10	10:53:00	00:10:50	-29.00	17.37	43.81	38.82	30.92	48.78	8.47	21.37	18.94
23/03/2013	377.2	29.9	11:10:10	11:20:00	00:09:50	-28.00	20.05	37.59	42.37	32.12	52.47	10.52	19.72	22.23
25/03/2013	380.3	26.8	09:54:40	10:35:10	00:40:30	-21.00	19.41	44.65	35.94	35.07	39.56	7.68	17.66	14.22
27/03/2013	386.9	20.2	09:09:10	09:39:50	00:30:40	-20.00	19.66	46.38	33.96	36.67	57.04	11.21	26.46	19.37
29/03/2013	391.1	16	10:27:00	10:46:40	00:19:40	-24.00	20.22	46.39	33.39	37.72	50.36	10.18	23.36	16.82
02/04/2013	393.7	13.4	08:40:50	10:29:40	01:48:50	-20.00	14.51	44.19	41.30	26.00	51.44	7.46	22.73	21.24
03/04/2013	396.6	10.5	08:50:00	09:20:20	00:30:20	-21.00	18.76	45.95	35.30	34.70	53.63	10.06	24.64	18.93
05/04/2013	400.2	6.9	08:41:50	12:20:40	03:38:50	-20.00	16.93	44.87	38.20	30.70	39.33	6.66	17.65	15.02
08/04/2013	404.2	2.9	09:36:00	09:39:00	00:03:00	-0.00	2.30	5.80	91.90	2.44	13.89	0.32	0.81	12.76
							Borehole R4							
20/03/2013	369.5	45.8	11:03:50	11:15:20	00:11:30	-31.85	19.16	42.20	38.64	49.58	36.49	6.99	15.40	14.10
27/03/2013	386.9	28.4	10:18:40	10:48:20	00:29:40	-22.77	20.21	41.70	38.09	53.07	42.58	8.61	17.76	16.22
29/03/2013	391.1	24.2	10:02:40	10:23:00	00:20:20	-20.34	21.94	44.56	33.50	65.49	41.39	9.08	18.44	13.87
02/04/2013 10:43	393.7	21.6	10:43:00	10:59:40	00:16:40	-23.67	20.03	37.03	42.94	46.64	46.62	9.34	17.26	20.02
02/04/2013 11:01	393.7	21.6	11:01:20	11:31:00	00:29:40	-18.58	17.25	36.98	45.77	37.68	45.82	7.90	16.94	20.97
03/04/2013	396.6	18.7	09:33:50	10:09:00	00:35:10	-21.72	18.61	36.86	44.53	41.79	48.05	8.94	17.71	21.40
05/04/2013	400.2	15.1	12:28:40	12:56:10	00:27:30	-22.84	18.33	37.74	43.93	41.72	42.94	7.87	16.21	18.86
08/04/2013	404.2	11.1	09:48:50	10:25:00	00:36:10	-17.13	20.16	41.45	38.39	52.51	38.84	7.83	16.10	14.91
10/04/2013	410.2	5.1	09:46:00	10:01:00	00:15:00	-0.29	14.79	41.42	43.80	33.76	16.76	2.48	6.94	7.34
							Borehole R3 and R4							
20/03/2013	369.5	45.8/37.6	11:24:20	11:34:30	00:10:10	-31.00	20.30	44.51	35.19	36.58	56.11	11.39	24.97	19.75

* The suction pressure and gas concentrations listed are mean values obtained from the continuous monitoring data during the pilot drainage trials.

** Flow rate was too low to be detected.

Trials with the drainage borehole R4 were performed in parallel with the trials with R3, with some delay after the initial tests on R3. A total of 9 separate drainage tests were carried out while recording the longwall movement towards R4. Similarly, the last trial with R4 also used the natural pressure difference rather than suction pressure by the pump. In addition to the trails with individual boreholes, R3 and R4 were operated together on 20th March 2013 to investigate the gas drainage interference between the two boreholes. Similar to the results obtained from borehole R3, total flow in borehole R4 pipeline consisted of methane, carbon dioxide and ventilation air.

In the following section, only part of the gas drainage data is plotted to assist the discussions. Gas drainage data for all the individual trials (duration ≥ 30 mins) are presented in Appendix 4.

8.2.3.1 The Impact of Suction Pressure on Gas Flow Rate

Drainage performance of the individual boreholes were analysed for the effect of suction pressure on performance, especially the CH_4 concentration in the system, were investigated. Figures 8.6 (a) and (b) present the flow rate response of different gasses to the changes in suction pressure in borehole R3 on two different dates and a distance from the longwall face. The total gas flow rate ranged from 30 l/s to 50 l/s throughout the period of pilot tests, which is believed to be affected by the change of suction pressure. The captured gas was primary a mixture of CO_2 and CH_4 from coal, as well as the air component from ventilation. It was clear that increased suction pressure increases the flow rate of air into the borehole, thus the total gas flow rate in the system.

8.2.3.2 The Impact of Suction Pressure on Gas Purity

Although increased suction pressure may favour total gas flow rate, higher suction pressures lead to a reduction in the drained CH_4 concentration which needs to be kept significantly above the explosive range for safety, as well as drainage efficiency. As shown in Figure 8.7, the concentration of air in total gas flow was very sensitive to the change of suction pressure. An increase of 5 kPa suction pressure could result in approximately 5% increase of air concentration in the total gas flow. Naturally, as the air in the total drained gas increases due to a change in drainage parameters (increased suction pressure, leakage of ventilation air in the crushed zone near the face etc.) methane concentration/flow rate would decrease to a great extent (Figure 8.8).

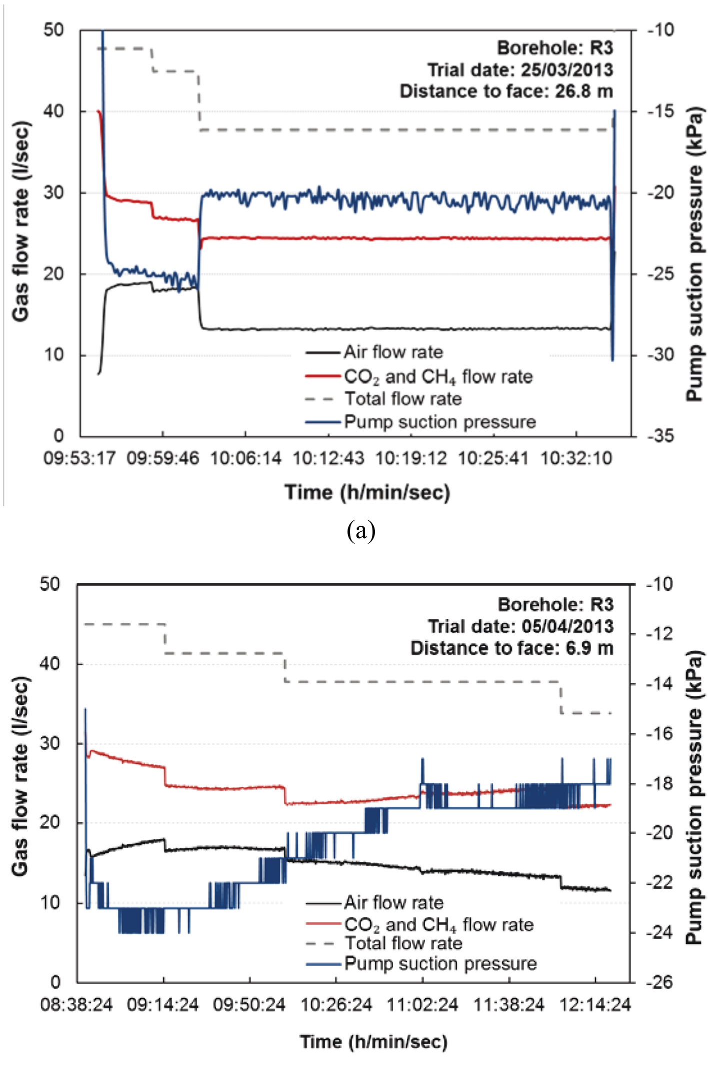

(a)

(b)

Figure 8.6: Gas flow rate response of different gas components to the change in the suction pressure in borehole R3 (a) trial on 25/03/13; (b) trial on 05/04/13.

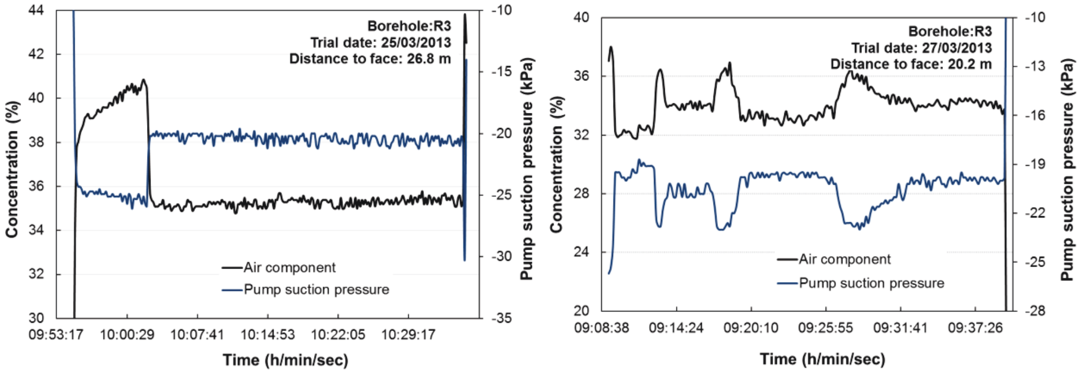

(a) (b)

Figure 8.7: Air concentration response to the change of suction pressure in borehole R3 (a) trial on 25/03/13; (b) trial on 27/03/13.

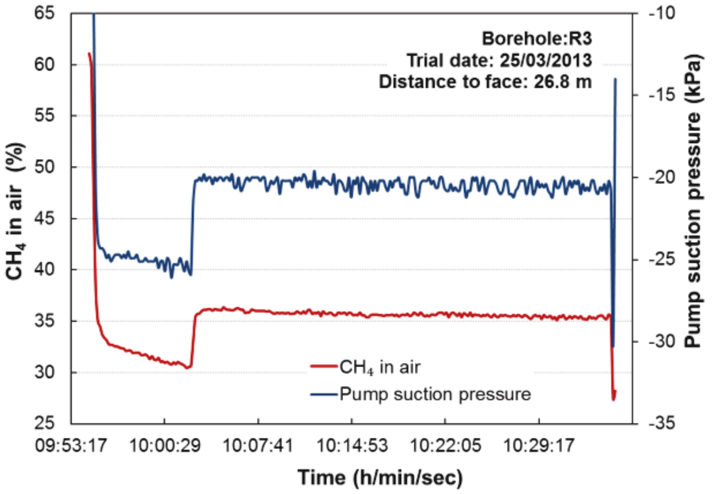

(a)

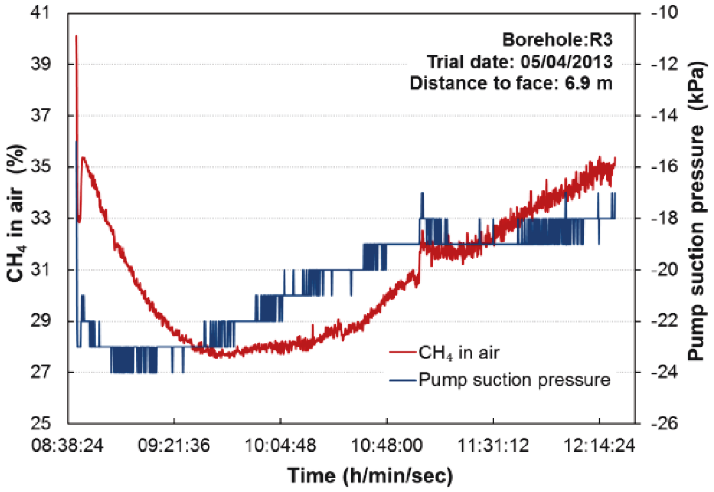

(b)

Figure 8.8: CH_4 concentration in air with respect to the change of suction pressure in borehole R3 (a) trial on 25/03/13; (b) trial on 05/04/13.

8.2.3.3 The Impact of Air Concentration on Captured Seam Gas Composition

Note that CH_4 concentration in captured seam gas mixture (CH_4 and CO_2) was not constant over each drainage trial. As illustrated in Figure 8.9, the concentration of CH_4 in captured seam gas appears to be related to the concentration of air in total gas flow. The increase in the air concentration in total gas flow leads to a reduction in the CH_4 component in the captured seam gas.

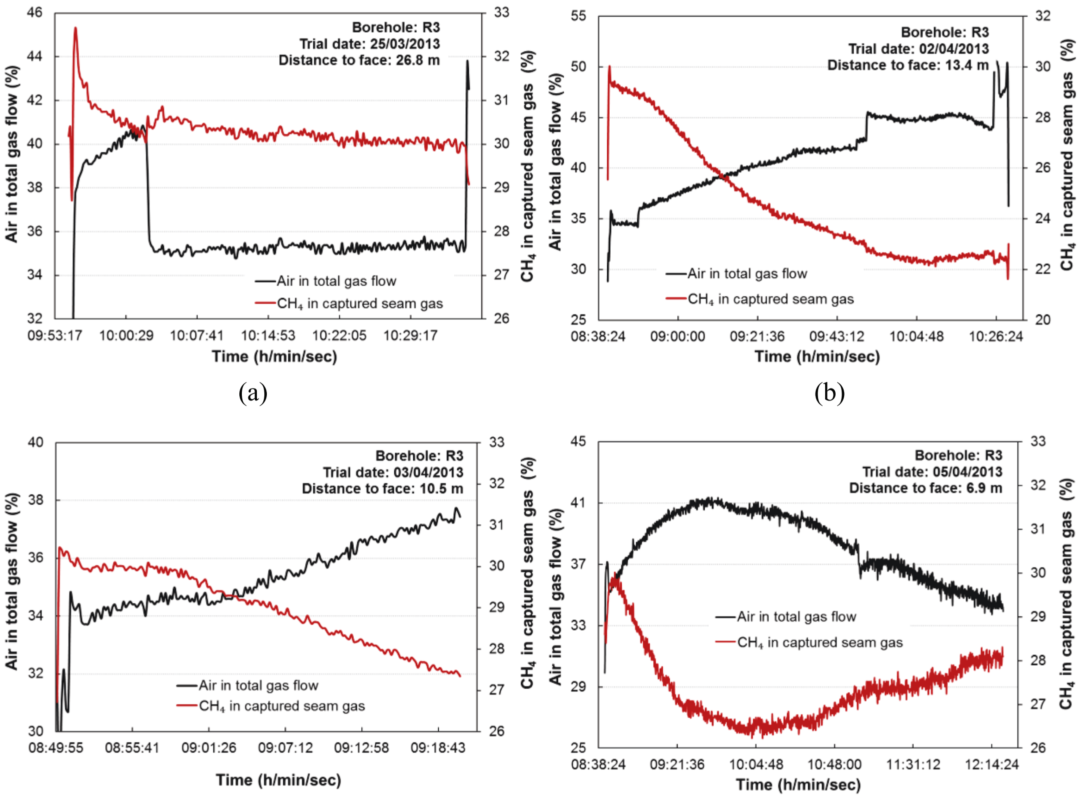

(a) (b)

(c) (d)

Figure 8.9: Concentration of air in total gas flow and CH_4 in drained seam gas mixture in Borehole R3 (a) trial on 25/03/13; (b) trial on 02/04/13; (c) trial on 03/04/13; (d) trial on 05/04/13.

8.2.3.4 Borehole Interference Tests

Borehole interference tests were conducted on 20th March 2013, when the longwall face was 45.8 m and 37.6 m away from boreholes R3 and R4, respectively. The first two trials were single borehole trials with one borehole open and the other shut. R3 was open at the first trial and R4 was open for the second. Both trials lasted around 11 minutes. The third trial was a combined borehole drainage trial with both R3 and R4 being open and operated for 10 minutes at the same suction pressure as the first two trials, which was -31 kPa.

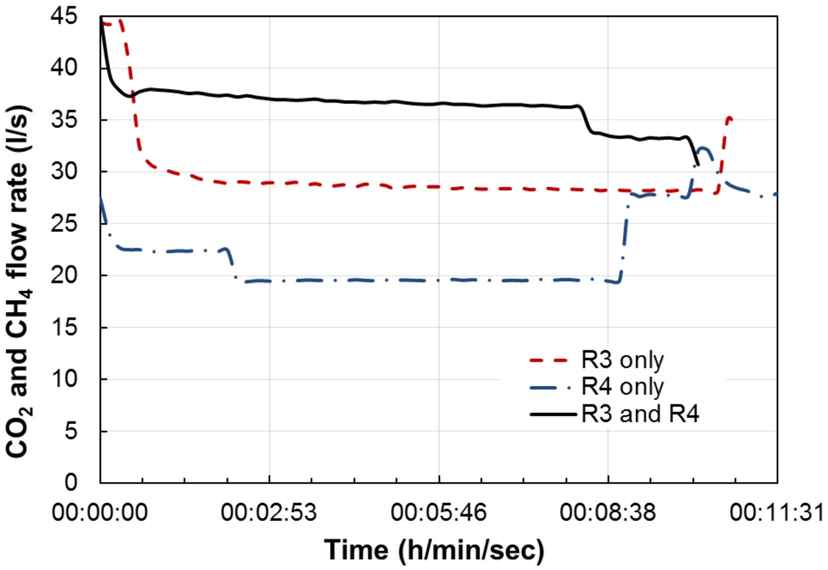

Figure 8.10: Flow rates of drained seam gas (the mixture of CO_2 and CH_4) during borehole interference tests.

Compared to the single borehole drainage trials, the third trial with multiple borehole drainage has shown a considerable increase in the drained gas flow rate, which was 23.3% higher than that of R3 alone, or 85% higher than that of R4 on its own (Figure 8.10). Since the spacing between these two boreholes was only 8 m, competition in capturing the seam gas was clearly observed during the third trial. This was indicated by the gas flow rate of the third trial being lower than the sum of flow rates for R3 and R4 alone, which would have been nearly 50 l/s. Note that the air flow rate in the total gas flow is much lower than the sum of two single boreholes. Furthermore, the concentration of the air component in total gas flow is slightly lower in the third trial compared with that in single borehole trials (Figure 8.11).

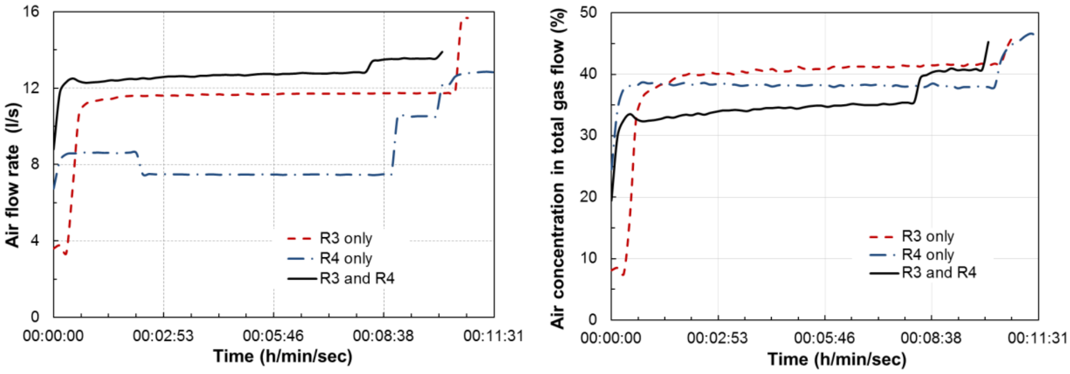

(a) (b)

Figure 8.11: Air contamination in total gas flow: (a) Air flow rate; (b) Air concentration.

8.2.3.5 Comparison Between Horizontal and Inclined Boreholes

Drainage borehole R3 was designed as a near-horizontal borehole to capture gas from the working level in the LTCC panel, while R4 was designed as an inclined borehole targeting gas in the floor coal. Previous figures suggest that the total flow rate of gasses in borehole R4 may have been lower, however, compared to the horizontal borehole R3, the length of R4 was limited to 30 metres (rather than 50 metres), which would have affected the area covered by the borehole, thus a lower gas drainage capacity as a whole.

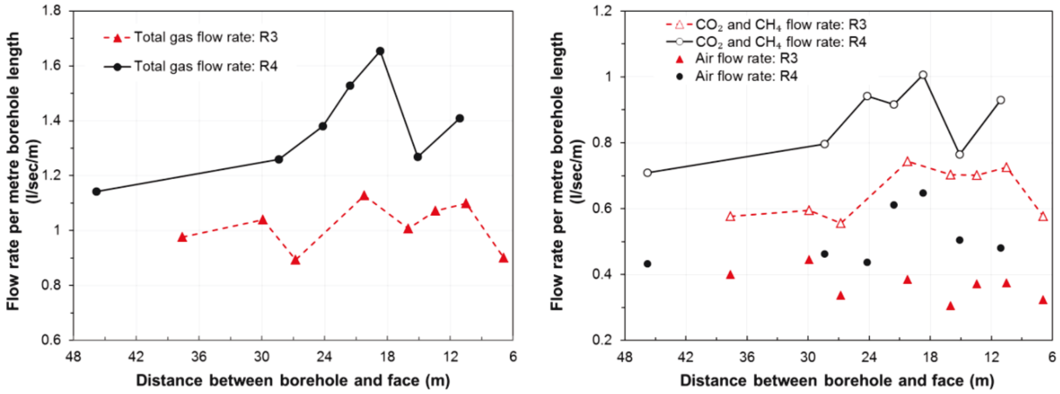

(a) (b)

Figure 8.12: Borehole performance comparison between R3 and R4: (a) Total gas flow rate per metre drilling; (b) Flow rate per metre borehole length for each gas component.

Figure 8.12 compares the performance of boreholes R3 and R4 (horizontal versus floor boreholes) per metre of borehole drilled. As Figure 8.12 illustrates, borehole R4 was stimulated slightly earlier than R3 by the approaching face. Furthermore, the floor borehole R4 appears to be more efficient than R3 in capturing the coal seam gas (CO_2 and CH_4 mixture). Given the same drilling length, the drained gas flow rates in borehole R4 were much higher than that in borehole R3. The higher performance of the floor borehole is most likely due to the higher permeability enhancement experienced by the floor coal, as suggested by the modelling result in Figure 6.15 (b). In addition, the higher gas pressure and content in floor coal of the first mining level may also contribute to the higher performance in the floor borehole.

8.2.3.6 Multiple Borehole Trials

Along with single borehole drainage and borehole interference trials, trials with multiple boreholes were also planned. Some of the technical specifications of the drainage system were modified after the first set of trials and 7 new multiple borehole trials were planned to extend the drainage area affected by the boreholes (Table 8.3). As detailed in Table 8.3, the flow rates, as well as gas purity, rose significantly. This is believed to be the result of enhanced drainage performance due to draining a larger fractured area in front of the longwall face (up to 40 metres from the boreholes). Total flow rate of gases varied between 56 – 76 l/s and again reached the highest values when boreholes R3+R4 were around 22 – 30 m from the longwall face. Flow rate and purity of the gas components increased as the longwall face approached the boreholes.

Table 8.3: Multiple borehole drainage trials.

	Bore-hole combination	LW distance to borehole (m)	CH_4 concentration (vol %)	CO_2 concentration (vol %)	Air concentration (vol %)	Pressure (kPa)	Total flow rate (l/s)	CH_4 flow rate (l/s)	CO_2 flow rate (l/s)	Air flow rate (l/s)
20.3.13	R3+R4	37.6 45.8	20.3	44.51	35.19	-31	56.1	11.4	25.0	19.7
25.3.13 10:42	R3+R4 + R5+R6	26.8 35.0 91.1 101.1	19.3	40.46	40.25	-27	63.2	12.2	25.5	25.6
25.3.13 11:29	R3+R4 + R5+R6	26.8 35.0 91.1 101.1	21.5	42.86	35.64	-24	65.6	14.1	28.1	23.4
27.3.13	R3+R4	20.2 28.4	22.7	47.63	29.71	-20	75.6	17.1	36.0	22.5
10.4.13*	R5+R6	61.2 71.2	8.7	7.70	83.60					
15.4.13*	R5+R6	56.4 66.4								
17.4.13*	R5+R6	50.6 60.6								

*Drainage trials were not performed.

Unfortunately, Coal Mine Velenje experienced a number of rock burst incidents within close proximity of longwall panel K.-65/F during 2013 which resulted in premature abandonment of the district for safety. This limited the number of drainage trials carried out at the mine. Nevertheless, one short trial was carried out with borehole R5, which was designed and drilled exactly same as borehole R2 as a roof drainage borehole. As presented in Table 8.4, this trial was performed when borehole R5 was 24 metres away from the longwall face. Unlike boreholes R3 and R4, drainage trials with R5 yielded a higher methane concentration compared to carbon dioxide. It was not possible to carry out further drainage trials with borehole R5 due to the rock burst incidents and the earlier than planned termination of production at longwall face K. -65/F.

Table 8.4: Gas drainage results for borehole R5.

	LW distance to borehole (m)	CH_4 concentration (vol %)	CO_2 concentration (vol %)	Air concentration (vol %)	Pressure (kPa)	Total flow rate (l/s)	CH_4 flow rate (l/s)	CO_2 flow rate (l/s)	Air flow rate (l/s)	Duration (h/min/sec)
8.5.13	20.9	38.64	22.20	39.16	-19	13.9	5.4	3.1	5.4	0:09:50

8.3 Numerical Modelling of Gas Drainage Trials at Coal Mine Velenje

The gas emission model developed for K.-50/C LTCC panel at Coal Mine Velenje was further developed to simulate the performance of horizontal and inclined gas drainage boreholes. The drainage boreholes were represented by wells in ECLIPSE, in the same way as the roadways and longwall faces were modelled earlier. As shown in Figure 8.13, the grids hosting a drainage borehole were locally refined in order to represent the trajectory of a drainage borehole accurately. The suction pressure of the drainage pump was modelled by assigning a bottomhole pressure with a value lower than the atmospheric pressure. Borehole performance data, such as gas production rate, total volume of gas production, and the volume of each gas component drained was continuously recorded throughout the gas drainage period. In addition, borehole parameters such as length, inclination, azimuth, and spacing were varied to assess gas drainage performance for different borehole layouts.

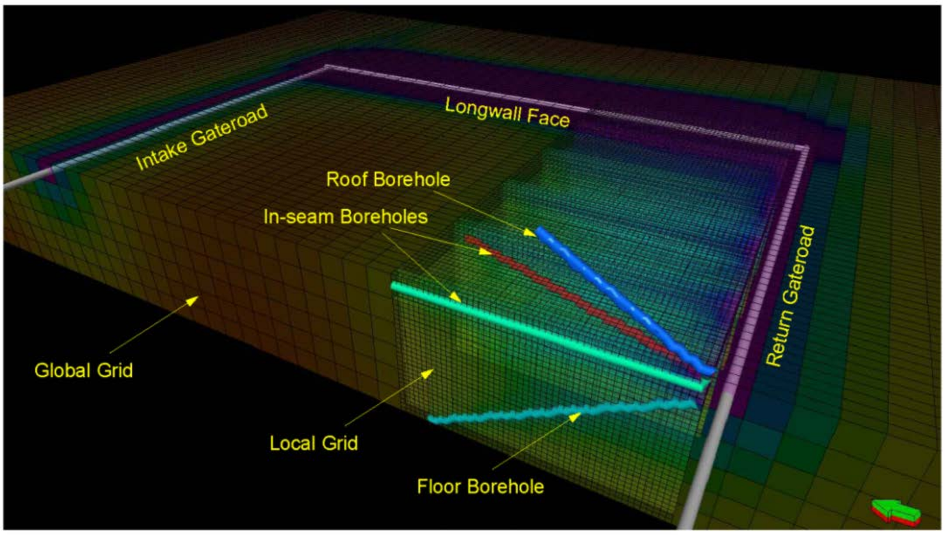

Figure 8.13: Schematic representation of horizontal, roof and floor drainage boreholes used in gas drainage modelling in ECLIPSE 300.

It is believed that, when compared to coal extraction and face advance, the impact of drilling a single borehole, or even a small group of boreholes, on the pressure and permeability distribution around longwall faces is fairly limited. Therefore, a simplified modelling approach, which uses the permeability distributions obtained from the coupled flow and geomechanics modelling of gas emissions for the K.-50/C LTCC panel in Chapter 6 was adopted to simulate and assess the drainage performance of different borehole layouts. While running the coupled model of K.-50/C LTCC panel, permeability distributions after each excavation step (every day from 9th May 2011 to 7th Aug 2011) were output and loaded into the reservoir simulator at the corresponding simulation time step, following the same modelling procedure and input parameters as those reported in Section 6.4.

Although the stability of inclined boreholes may be a concern since shear failure may damage the casing or cause borehole collapse (Whittles *et al*., 2007), this potential impact was ignored as borehole stability issues were out of the scope of this research. Instead, it was assumed that a drainage borehole would be ineffective once the face is within 2 m of the borehole.

8.3.1 Drainage Performance of Individual Boreholes

A total of 23 scenarios with different borehole layouts and operational parameters were conducted to assess the performance of single drainage boreholes as presented in Table 8.5. In order to emulate the field drainage trials (Figure 8.1 and Table 8.1), three base case scenarios configured same as the horizontal borehole (R1/R3), roof borehole (R2), and floor borehole (R4) used in the field trials, which were drilled from the intake gateroad of LTCC panel K.-50/C at 100 m distance to the face-line were modelled first. The performance of these boreholes was then compared to the performance of different borehole configured as those presented in Table 8.5. The selection of borehole parameters ensured that the complete trajectory of each borehole remained within the thick coal deposit.

Note that a zero azimuth denotes that a borehole is parallel to the face. A positive azimuth suggests a borehole rotating towards the face, and a negative azimuth suggests a borehole rotating away from the face. Naturally, coal extraction will, at some point in time, cut through the horizontal and roof boreholes and limit their lead time, and larger negative azimuths can cause an early intersection with the borehole. Assuming that the gateroads are maintained for some time behind the face-line, the floor boreholes were allowed to have a longer lead time compared to the roof or horizontal boreholes.

Table 8.5: Borehole layouts and operational parameters used in different gas drainage scenarios.

	Scenario No.	Inclination (˚)	Azimuth (˚)	Borehole length (m)	Lead time (day)	Suction pressure (kPa)	Diameter (m)	Standpipe length (m)
Base cases	1	0	0	50	50	-30	0.1	10
	2	+20	0	30	50			
	3	-30	0	30	--			
Azimuth change	4	0	+30	50	50			
	5	0	+60	50	50			
	6	0	-30	50	37			
	7	0	-60	50	18			
Inclination angle change	8	+5	0	30	50			
	9	+10	0	30	50			
	10	-5	0	30	--			
	11	-15	0	30	--			
	12	-45	0	30	--			
	13	-60	0	30	--			
Borehole length change	14	0	0	20	50			
	15	0	0	30	50			
	16	0	0	40	50			
	17	+10	0	20	50			
	18	+10	0	40	50			
	19	+10	0	50	50			
	20	-30	0	15	--			
	21	-30	0	20	--			
	22	-30	0	40	--			
	23	-30	0	50	--			

8.3.1.1 Horizontal Borehole Performance Analysis

Gas drainage performance indicators against distance from the face-line over the life-time of the base case horizontal borehole (Scenario 1) are presented in Figure 8.14. To have a clear vision of face approach and consequent mining effect, the distance between the borehole and the face is also plotted in this figure.

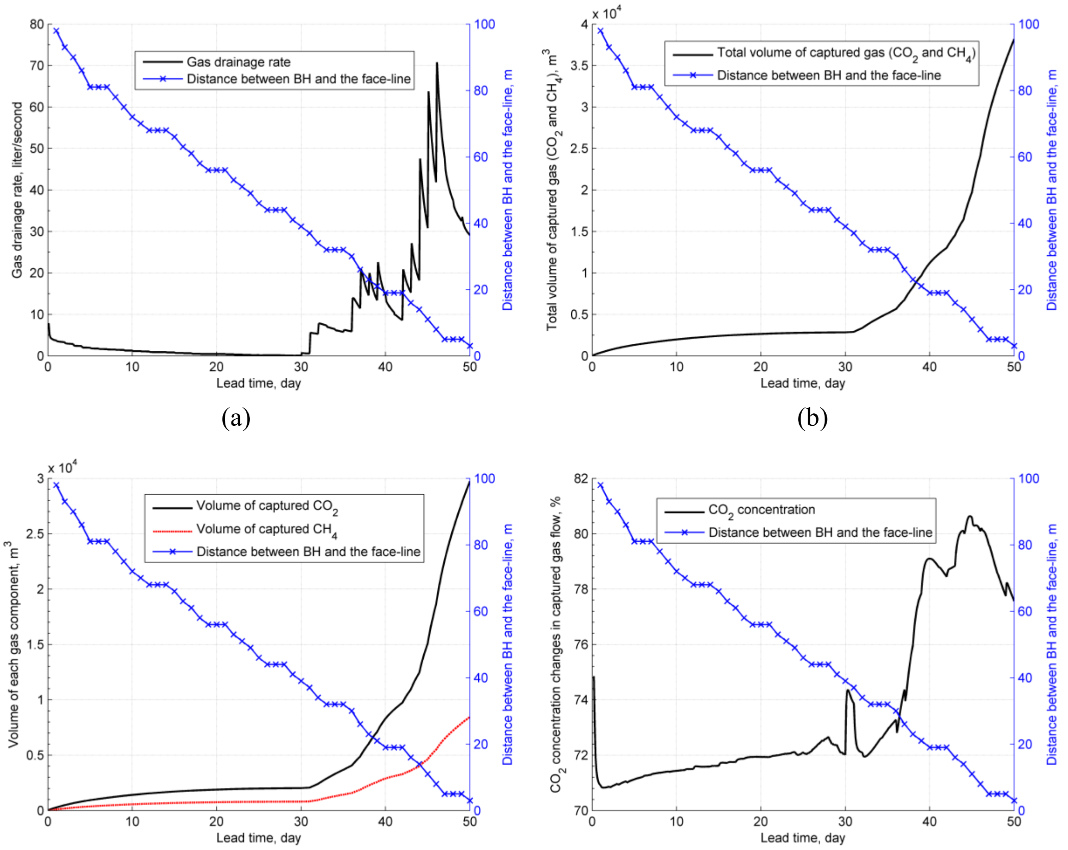

(a) (b)

(c) (d)

Figure 8.14: Gas drainage performance against distance from the face-line for a horizontal borehole: (a) Gas drainage rate; (b) Total volume of captured gas; (c) The volume of each gas component being captured; (d) CO_2 concentration in the captured gas (Scenario 1).

As shown in Figures 8.14 (a) and (b), due to initial low permeability and high front abutment stress, gas drainage rate is extremely low when the face is over 40 m away from the borehole. Mining induced fracturing and stress relief as the face advances from 40 m to 20 m from the borehole greatly increases the gas production. Following that, a further increase in gas production rate is observed as the face moves closer. At this point, almost 93% of total gas volume drained is produced as the borehole is stimulated by mining.

As previously observed from the gas pressure and concentration monitoring borehole data (Section 4.3), the composition of captured gas also changes as the face approaches the drainage borehole and fracturing and pressure drawdown stimulates CO_2 desorption. This is indicated by the enriched CO_2 concentration in drained gas (Figure 8.14 (d)).

8.3.1.2 Roof Borehole Performance Analysis

Similar observations apply to the gas drainage performance of a roof borehole (Figure 8.15). The first notable drainage increase occurs when the face-line is ~30 m from the borehole, followed by a shape increase as the face approaches further. A similar increase in CO_2 component in the captured gas is also observed in the roof borehole.

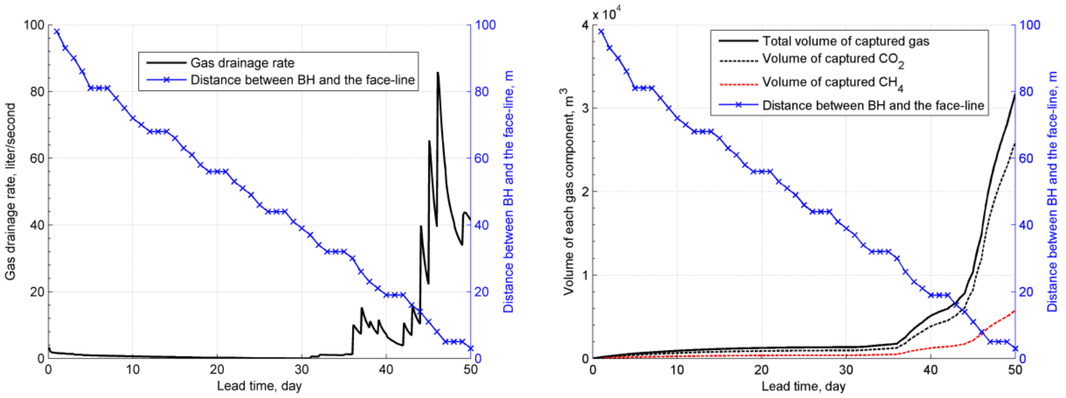

(a) (b)

Figure 8.15: Gas drainage performance against distance from the face-line for a roof borehole: (a) Gas drainage rate; (b) Cumulative volume of each gas component (Scenario 2).

8.3.1.3 Floor Borehole Performance Analysis

In addition to the period of face advance towards the borehole, another 40 days of gas production was simulated to cover the period after the face crossed the borehole position (Figure 8.16). Again, a sharp increase of gas drainage rate is observed when the face-line is ~30 m from the borehole. The gas drainage rate peaks around the time face-line overlaps with the borehole position. After that, gas drainage rate declines gradually due to gas content depletion and recompaction of the goaf area. It is noted that nearly two-thirds of the total gas volume is produced behind the face-line.

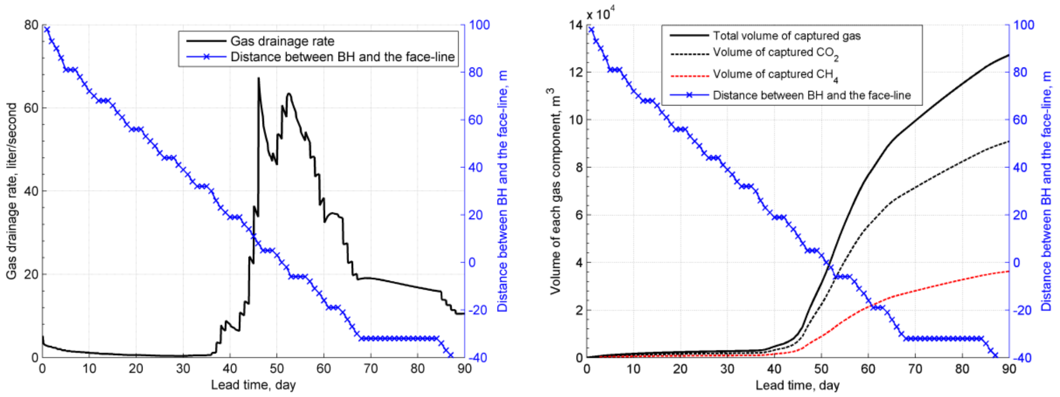

(a) (b)

Figure 8.16: Gas drainage performance against distance from the face-line for a floor borehole: (a) Gas drainage rate; (b) Cumulative volume of each gas component (Scenario 3).

8.3.1.4 The Effect of Azimuth Angle on Gas Drainage Performance

The results of scenarios with different azimuth angles are presented in Figure 8.17. For boreholes with negative azimuth angles the total volumes of gas production are rather limited due to early interaction with the production face. Furthermore, since the stress abutment and the fractured zone induced by mining are most likely to move as a strip together with the face advance (See Figure 6.11), face advance can maximise the total gas production from a borehole which is parallel to the face-line. It should be noted that, in this scenario, the horizontal permeability was assumed as isotropic. On the other hand, depending on the direction of face and butt cleats, and the orientation of the face advance direction with respect to these, the change in borehole azimuth may help improve gas drainage performance.

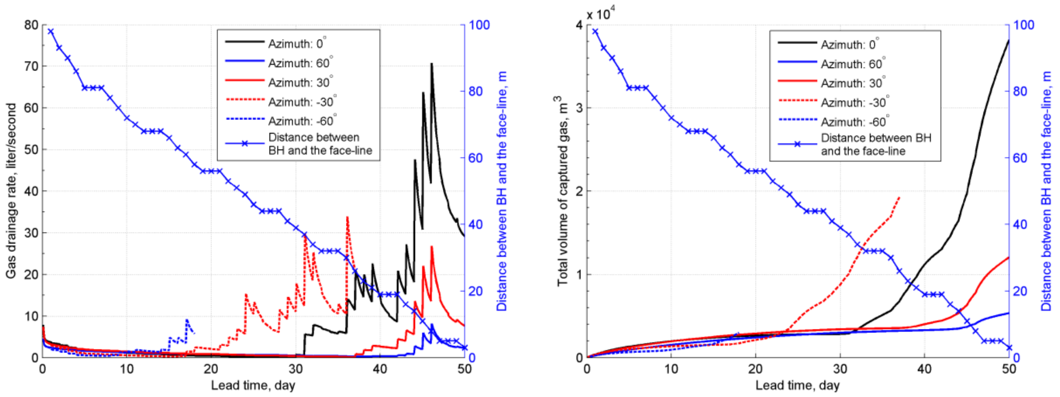

(a) (b)

Figure 8.17: The effect of azimuth on drainage performance: (a) Gas drainage rate; (b) Total volume of captured gas (Scenarios 1 and 4 to7).

8.3.1.5 The Effect of Borehole Inclination on Gas Drainage Performance

Figure 8.18 presents the gas drainage performance of roof holes at different angles of inclination from the horizontal. Roof boreholes at a higher angle can benefit gas drainage performance slightly, however, the angle of inclination available for roof boreholes is limited by the thickness of top coal left in LTCC panels.

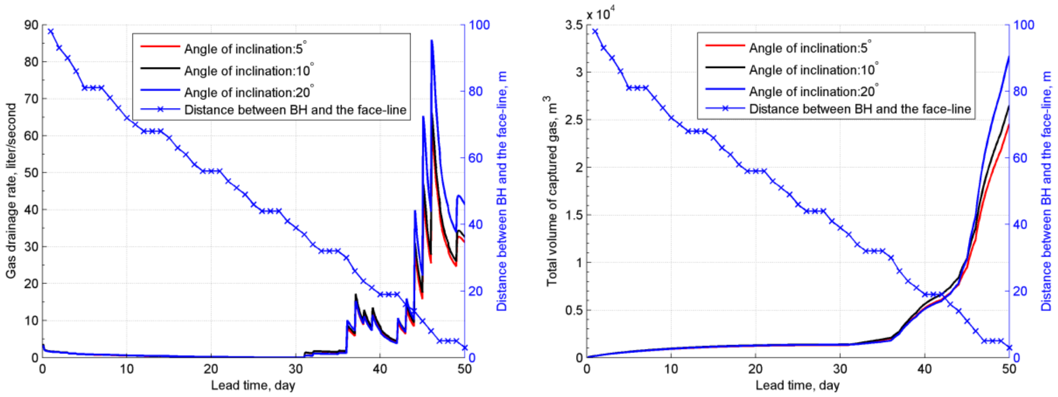

(a) (b)

Figure 8.18: The effect of roof borehole inclination on drainage performance of roof boreholes: (a) Gas drainage rate; (b) Total volume of captured gas (Scenarios 2, 8 and 9).

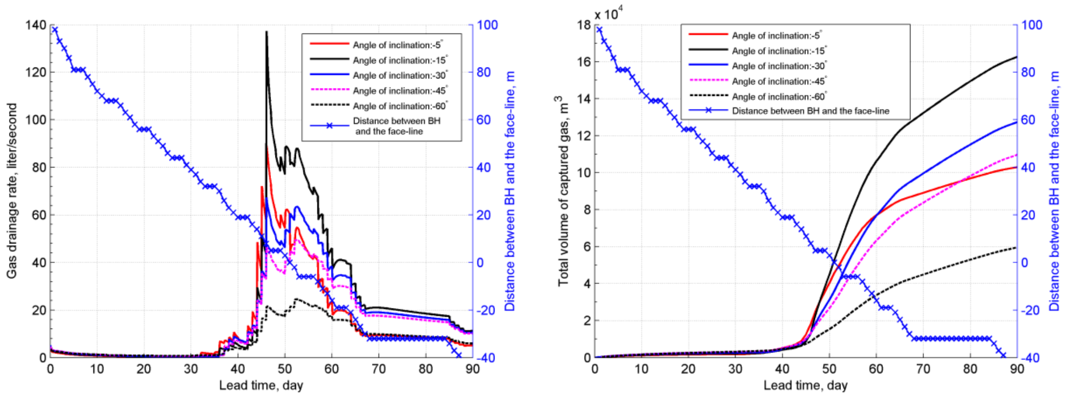

(a) (b)

Figure 8.19: The effect of floor borehole inclination on drainage performance of floor boreholes: (a) Gas drainage rate; (b) Total volume of captured gas (Scenarios 3 and 10 to 13).

Figure 8.19 presents the gas drainage performance of floor holes at different angles of inclination from the horizontal. Note that drainage with -15° floor borehole offers the highest gas drainage rate and the largest total volume of captured gas. Referring back to the numerical modelling results of permeability enhancement in Figure 6.15, this optimum drainage performance may be explained by the position of the largest permeability enhancement zone in the floor coal.

8.3.1.6 The Effect of Borehole Length on Gas Drainage Performance

Figures 8.20 and 8.21 compare the drainage performance of different borehole lengths for horizontal and roof boreholes respectively. It is clear that, in both cases, increasing the borehole length can improve drainage efficiency, and the boreholes being more productive once the face-line is around 30 metres from the drainage borehole.

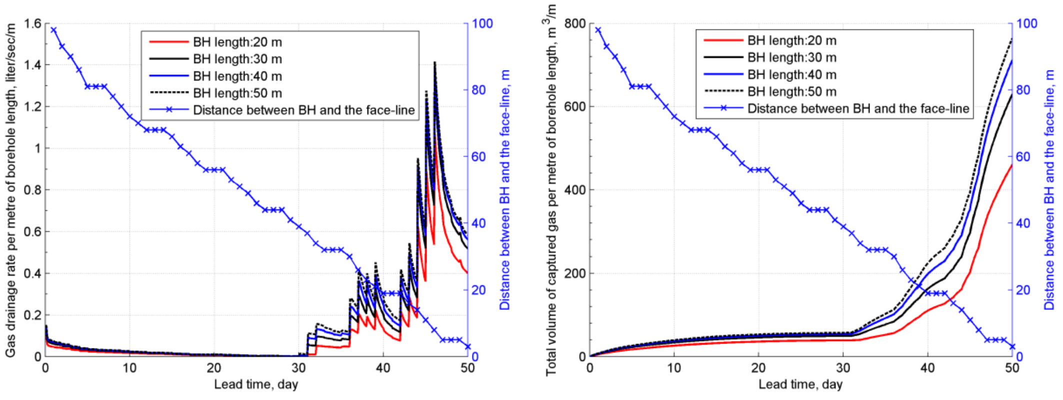

(a) (b)

Figure 8.20: The effect of horizontal borehole length on drainage performance: (a) Gas drainage rate; (b) Total volume of captured gas (Scenarios 1 and 14 to 16).

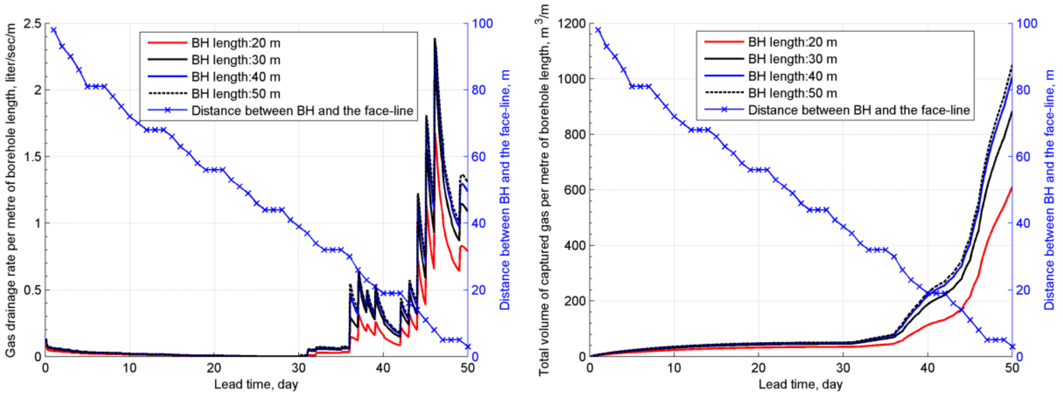

(a) (b)

Figure 8.21: The effect of roof borehole length on drainage performance: (a) Gas drainage rate; (b) Total volume of captured gas (Scenarios 9 and 17 to 19).

On the other hand, the optimum length for floor boreholes appear to be 20 metres, as further extension of a borehole is not very effective in the low permeability floor zone (Figure 8.22).

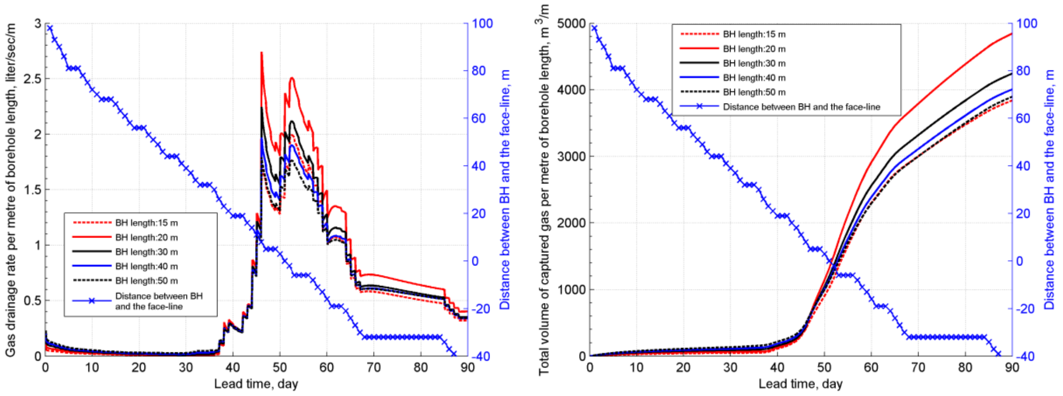

(a) (b)

Figure 8.22: The effect of floor borehole length on drainage performance: (a) Gas drainage rate; (b) Total volume of captured gas (Scenarios 3 and 20 to 23).

8.3.1.7 Horizontal Boreholes versus Inclined Boreholes

Using the three base case scenarios, Figure 8.23 compares the performance, in terms of gas drainage rate and captured gas volume, of roof, horizontal, and floor boreholes as the face approaches the boreholes, are plotted against distance between face and borehole.

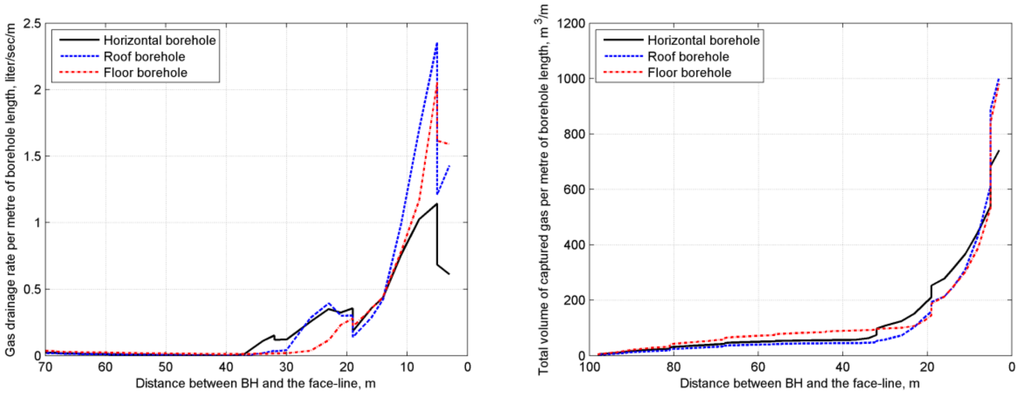

(a) (b)

Figure 8.23: Comparison of the performance of horizontal and inclined drainage boreholes: (a) Gas drainage rate; (b) Total volume of captured gas (Scenarios 1 to 3).

All three scenarios present a similar response to face advance: gas drainage rate and total drained volume are dramatically stimulated by the time the face-line reaches 30~40 m from the boreholes. The mining-induced stimulation of drainage performance is first observed in the horizontal borehole, and then followed by the roof and floor boreholes. In terms of captured gas flow rate and volume, roof and floor boreholes are shown to be more effective than the horizontal boreholes. This is consistent with the results of field trials as discussed in Section 8.2.3.5.

As suggested by the numerical model finding shown in Figure 6.15, at certain distance above or below the K.-50/C mining level, the coal seam tends to have a higher permeability response to mining activities. Higher drainage efficiency demonstrated by the roof and floor boreholes is due to the fact that these boreholes reach the areas with higher permeability responses. In addition, higher residual gas content in the floor coal may be another reason which contributes to the higher drainage efficiency of the floor boreholes.

8.3.2 Gas Drainage Performance of Multiple Boreholes

In addition to gas drainage from single boreholes, the performance of a group of boreholes drilled as roof, horizontal, and floor boreholes, were also modelled. Borehole spacing and the effect of the use of multiple borehole drainage system on reducing in-situ gas content were investigated.

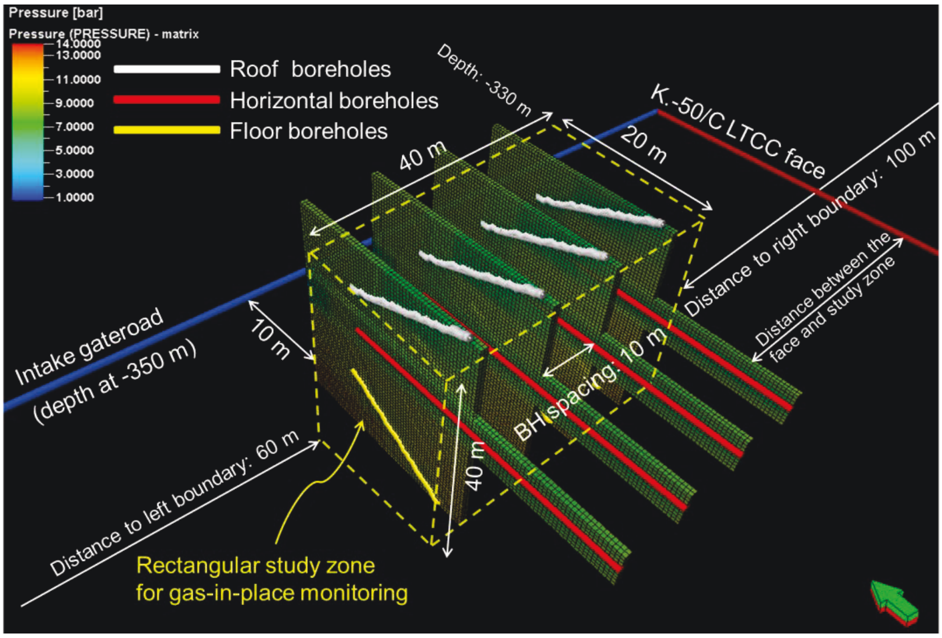

Figure 8.24: Multiple borehole layout used in the rectangular study area of K.-50/C LTCC panel (borehole spacing = 10 m).

As shown in Figure 8.24, a rectangular zone around the K.-50/C panel was selected as the study zone to apply different drainage schemes. A number of drainage slots were constructed around the panel, and each slot was equipped with a roof, a horizontal and a floor borehole vertically aligned with each other. In total, three scenarios with borehole (slot) spacings at 20 m, 10 m, and 4 m were conducted. Borehole parameters for roof, horizontal, and floor boreholes used here were assumed to be the same as the parameters of the three base cases reported in Table 8.5. As the face approached the boreholes, in-situ gas content in the study zone was continuously monitored. In order to represent borehole intersection with the highly fractured zone at the face, each roof and/or horizontal borehole was set as ‘SHUT’ when the face-line moved within 2 m of it.

Figure 8.25 illustrates gas drainage performance of multiple boreholes at different borehole spacing. Being stimulated by the approaching face, all three scenarios show a dramatic increase in gas drainage rate and captured gas volume. As expected, denser borehole layouts yield a much higher gas production rate and volume (Figures 8.25 a and b). However, too closely spaced borehole layouts may result in fierce competition between neighbouring boreholes and reduce the efficiency of each borehole, as indicated in Figures 8.25 (c) and (d).

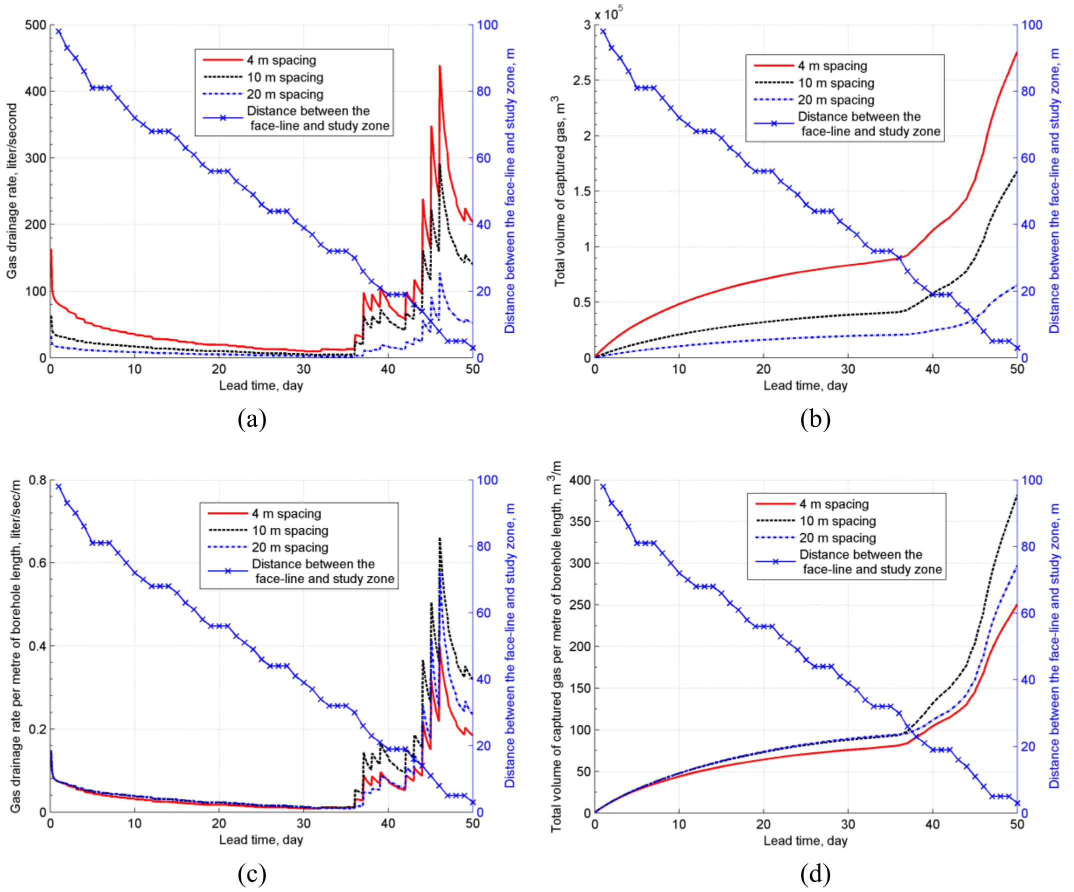

(a) (b)

(c) (d)

Figure 8.25: Gas drainage performance of multiple boreholes against distance from the face-line: (a) Gas drainage rate; (b) Total volume of captured gas; (c) Gas drainage rate per metre borehole length; (d) Total volume of captured gas per metre borehole length.

Figure 8.26 compares the residual gas in place within the study zone for the three borehole spacings simulated. The effect of gas drainage can be clearly observed, particularly during the period when the study zone gradually became the near face fracturing zone. As can be seen, the best scenario is provided by the 4 m borehole spacing, which can reduce the gas content by nearly 60%.

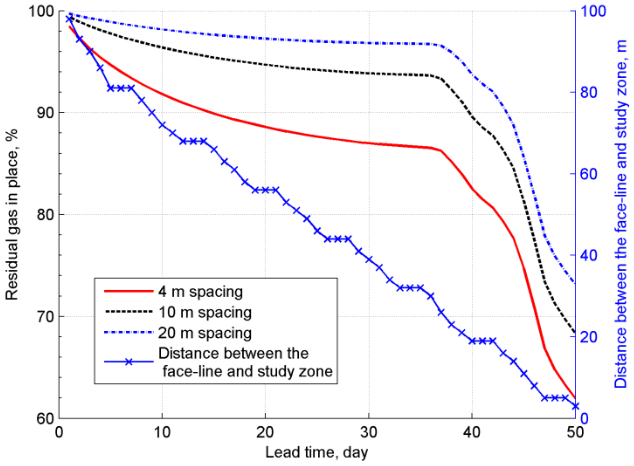

Figure 8.26: The residual gas content within the study zone.

8.4 Discussion and Conclusions

Through field trials and numerical experiments, this Chapter investigated the feasibility of utilising mining induced permeability enhancement zones to optimise gas drainage performance. A series of field trials at Coal Mine Velenje has demonstrated that gas drainage rate could increase from less than 12 l/s to around 50 l/s as a result of face approaching the drainage boreholes. Utilising mining-enhanced permeability to capture gas emissions at Coal Mine Velenje has been demonstrated as a promising approach for gas emission control in the thick and low permeability coal seam mined using LTCC method.

Numerical models for gas drainage were developed building upon the gas emission model of K.-50/C LTCC panel at Coal Mine Velenje. Although the LTCC panel used in numerical modelling was different from that used in the field drainage trials, the model results generally agree well with the results of the field gas drainage trials, as shown in Figure 8.27. The timing of dramatic gas production stimulation has been successfully modelled at ~40 m from the face-line. Results from both numerical experiments and field trials have suggested that gas drainage with a floor borehole is more efficient than that with a horizontal borehole in terms of gas drainage rate/volume per metre of borehole length. The numerical model findings further suggest that floor drainage can reduce the gas content at floor level significantly and improve the ventilation environment for the coal extraction in the next level. Meanwhile, horizontal and roof boreholes are also essential for gas emission control at the mining level, especially during the mining of first level panels.

The drainage rate increase recorded in numerical simulations falls within a reasonable range of the field observations. The relatively higher gas drainage rate obtained in field trials can be explained as:

- all field drainage trials were conducted at a first level panel (K.-65/F), which had a higher initial gas pressure than the modelled panel (K.-50/C).
- drainage period in field trials were much shorter than that used in the numerical models, and thus no gas pressure/content depletion caused by production had been experienced in the field.
- the suction pressure was simulated to be constant -30 kPa over the whole drainage period, however, the suction pressure in field trials varied and occasionally dropped to around -20 kPa.

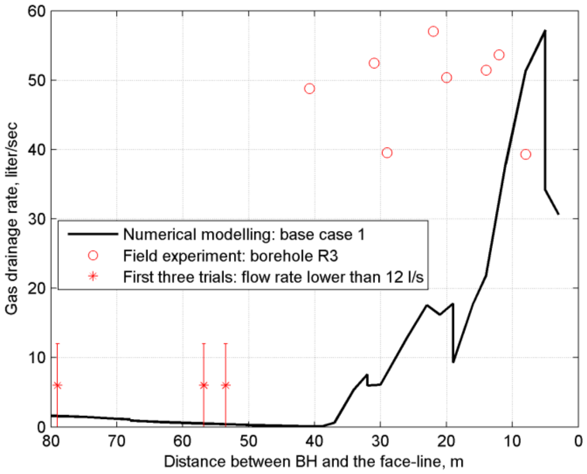

Figure 8.27: Comparison of gas drainage rates: numerical models (Scenario 1) *versus* field trials (borehole R3).

Borehole parameters including azimuth, inclination, borehole length, and borehole spacing were studied to optimise gas drainage performance. Main findings of the numerical modelling work are as follows:

- In general, inclined roof and floor boreholes are more efficient than the horizontal boreholes. Floor boreholes are the most effective since they have a longer lead time.

- For roof boreholes, increased inclination of the boreholes may slightly benefit gas drainage performance, however, the option to control the roof borehole inclination is rather limited. On the other hand, an optimal inclination angle may exist for floor boreholes, where gas drainage can be maximised by the knowledge of mining-enhanced permeability zones in the floor coal.

- Increased borehole length can improve drainage efficiency for horizontal and roof boreholes to some extent. However, for floor boreholes, increasing borehole length beyond 20 metres has a negative impact on gas drainage efficiency.

- The use of multiple drainage boreholes (roof, horizontal, and floor) can largely reduce in-situ gas content within the near face fracture zone. Increased borehole spacing can yield a much higher gas production rate and volume, however, this lowers the drainage efficiency of individual boreholes.

- The azimuth of the drainage boreholes should be controlled with the knowledge of permeability anisotropy in the seam.

Chapter 9 Conclusions and Recommendations for Future Research

9.1 Introduction

This thesis described research carried out to improve the understanding of gas emission patterns around Longwall Top Coal Caving faces used in thick seam coal mining. Knowledge gaps in terms of gas emission modelling and prediction, early detection of excessive gas emissions and outburst, and the development of gas drainage methods for thick and low permeability seams were investigated.

The first step in this research was to carry out field measurements and extensive analysis and interpretation of data obtained at Coal Mine Velenje. As a result of these analyses, a conceptual model describing stress, pressure, and gas emission patterns around LTCC faces was developed. The feasibility of using seismic monitoring techniques for the early detection of gas outbursts was also explored.

Next a two-way sequential coupling methodology for geomechanical and fluid flow simulators was developed. Using field data as input and matching parameters, this coupling methodology was applied to simulate face advance and associated gas emissions around LTCC faces. Later, the methodology was further modified to simulate common outburst types experience by the coal industry.

As the last step, this research investigated the impact of mining activities on the performance of gas drainage designs with different borehole layouts. Gas drainage data from field trials were analysed and different borehole layouts and settings were assessed using numerical models to optimise gas drainage performance.

9.2 Main Conclusions

Through integrated field measurements, data analysis, and numerical modelling, this research has largely advanced the understanding of gas emission patterns around Longwall Top Coal Caving faces used in thick seam coal mining. The main conclusions of this research are summarised as follows:

- A conceptual model describing the gas emission patterns and gas dynamics around multi-level LTCC mining in thick seams has been developed. Three gas pressure zones, namely the farfield abutment, peak abutment and near face fracturing zones, ahead of an advancing LTCC have been characterised in the conceptual model. The near face fracturing zone is defined as a highly fractured and stimulated zone with enhanced permeability, which contributes significant to the gas emissions around a LTCC face.
- At multi-level mining layouts, the first mining level is expected to experience the highest rate of gas emission, both from the mined coal and the floor level due to high in-situ gas pressures. On the other hand, in LTCC panels operating at lower mining levels, emission from the floor coal and the roof goaf are the main sources of overall gas emission.
- In order to identify and characterise the near face fracturing zone, various monitoring techniques, including gas pressure and composition monitoring, time-lapse seismic tomography, and microseismic monitoring have been tested and proved to be effective.
- Using microseismic monitoring in conjunction with time-lapse seismic tomography can identify geological anomalies, such as heterogeneous coal, which may lead to excessive gas emissions and gas outbursts. Compared to seismic tomography, real-time microseismic monitoring provides continuous remote monitoring data with significantly lower demand on staff time and no operational disturbance on production.
- Research has shown that excessive gas emissions are highly correlated with increased microseismicity. Fractal dimension, estimated from the spatial

density of mining-induced microseismic incidents, may provide a quantitative methodology to predict excessive gas emissions or gas/coal outbursts.

- Building upon comprehensive field data, this research developed a two-way sequential coupling methodology enabling accurate representation of interactive physics between geomechanics and gas flow. In particular, this modelling approach can reproduce the dynamic changes of stresses and gas pressure around LTCC faces and predict the total gas emissions accurately.
- Implementation of the two-way sequential coupling approach to simulate LTCC face advance have confirmed that the proposed conceptual gas emission model for thick seam LTCC mining is valid. Mining-enhanced permeability zones around LTCC faces can be identified accurately and used for gas drainage design. Note that the coupling approach is not limited to thick/ultra-thick mining, and that gas emissions around thinner seams with mechanised conventional longwall layouts can also be successfully modelled using this technique.
- The two-way sequential coupling approach was later implemented to simulate and explain common outburst types experience by the coal industry. Model findings were consistent with the field observations in terms of the quantity of ejected coal, the shape of outburst cavity, and the gas emission trends observed before an outburst. Outburst conditions in both thin and thick seam mining layouts can be evaluated via this approach and minimise the risk of outburst occurrences.
- Through field trials and numerical experiments, the feasibility of utilising mining induced permeability enhancement zones to optimise gas drainage performance in thick seam LTCC mining has been investigated. It was demonstrated that a significant increase in gas drainage can be achieved through boreholes within the near face fracturing zone.
- Gas drainage can be maximised by the knowledge of mining-enhanced permeability zones and the selection of drainage borehole parameters. In general, inclined roof and floor boreholes are more efficient than the horizontal boreholes in LTCC mining. Floor boreholes are the most effective since they have a longer lead time. The use of multiple drainage boreholes (roof, horizontal, and floor) can largely reduce in-situ gas content within the

near face fracturing zone, but borehole spacing needs to be determined carefully to avoid drainage interference between individual boreholes.

Strictly speaking, Coal Mine Velenje is a unique case among collieries exploiting thick seams, since the coal deposit there is unusually thick, which also provided the author with an opportunity to study the gas emission patterns in floor coal seam in six or seven mining levels. For more general cases in thick seam mining, where one or two levels are mined, the findings of this research would still be valid for emissions from the working and floor seam levels.

Although the only field scale gas emission model in this research was designed for the ultra-thick seam mining experience at Coal Mine Velenje, the two-way coupled modelling approach developed is generally applicable to both thin and thick seam mining. However, the author acknowledges that, in order to ensure that the models developed by this approach can accurately simulate gas flow patterns in other convention longwall or LTCC panels, a large amount of field data are necessary for model development, calibration, and validation. To achieve this, procedures presented in this research can be used as reference.

It is believed that this PhD research has a number of practical applications in the mining industry:

- To predict the amount of gas emissions induced by coal extraction;
- To design and optimise the ventilation and gas drainage systems;
- To assess the risk of outbursts and excessive gas emissions and provide early warnings;
- To understand other fluid flow behaviour around mine openings, such as the effect of coal extraction on surrounding aquifers and prevention of water inrushes.

9.3 Recommendation for Future Research

Building upon the main findings of this research, further research can help advance knowledge in the field of gas emissions and outburst control in underground coal mining. Several interesting subjects, which are worth investigating, are recommended as follows.

Improvement of stress-dependent permeability representation in numerical modelling

Since the modelling results are very sensitive to the selection of stress-dependent permeability relationship, the change in permeability parameters (k_{f0} and C_f) during the transition of rock from elastic to plastic needs more rigorous theoretical derivation and strong experimental data support.

Fractal dimension analysis of microseismic data

Using fractal dimension to further analyse microseismic data has been demonstrated to be a potential approach to detect an episode of increased gas emissions. However, the database of microseismic events used in this research is rather limited, which is only six-months of monitoring period. Further validation of this approach, using a longer monitoring period and a wider range of applications into various geological conditions and mining layouts, is needed.

Moreover, current microseismic data processing and fractal analysis involve several weeks, if not months, to finalise, which is too late as a predictive and preventative measure. It would be a significant improvement if coupled near-real time processing and further analysis of the microseismic data can be achieved to develop short-term prediction methods to prevent, risk assess and mitigate gas outburst hazards.

The heterogeneity of coal seams

Assuming homogenous coal properties in the numerical models work simplifies the modelling procedure, but also leads to the mismatch between simulation and measurement results. In addition, field observations suggest that the change of coal properties is a possible factor that contributes to the onset of outbursts. For more realistic simulations, it may be useful to establish probability functions (Wold *et al*, 2008), which can describe the heterogeneity and variability of the geological characteristics (e.g. geomechanical properties, reservoir properties etc.), based on core sample and borehole imaging data. Then these functions can be used to distribute coal properties and generate representative geostatistical realisations in numerical models. Critical parameters leading to uncontrolled gas emissions/outbursts can be assessed and evaluated by stochastically running various realisations.

An improved approach for coal and gas outbursts modelling

As stated in Chapter 7, due to the limitation of the geomechanical and fluid flow simulators, current outburst modelling approaches cannot simulate coal fragmentation and pressure-driven fracturing, which may be important in representing the nature of outburst initiation in a large bulk of intact coal. To solve this challenge, a geomechanical simulator which can consider discrete element behaviour needs to be integrated.

Borehole stability assessment and deviated boreholes

In this research, the borehole stability during face advance towards it was oversimplified. Since the life-span of a borehole significantly affects its gas drainage performance, it may be helpful to conduct a systematic study regarding the impact of mining geomechanics on borehole integrity. A smaller scale but much more detailed model needs to be developed to study standpipe strength, borehole deformation, and near-borehole stress distribution etc. The dynamic behaviour of these parameters as the face approaches also need to be considered.

In addition, only straight-line boreholes were studied in this research. With the advancement of drilling techniques, long distance deviated boreholes are becoming normal practice in the US and Australia to reduce gas content in thin seams. It would be interesting to explore the possibility of applying long distance deviated boreholes into thick seams and explore how these boreholes would perform during coal extraction and face advance.

References

Ahsan, M., 2006. Gas flow and retention characteristics of coal seams for enhanced coalbed methane recovery and carbon dioxide storage, Department of Earth Science and Engineering. Imperial College London, p. 225.

Airey, E.M., 1968. Gas emission from broken coal: An experimental and theoretical investigation. International Journal of Rock Mechanics and Mining Sciences 5, 475-494.

Airey, E.M., 1971. A theory of gas emission in coalmining operations, Proc. 14th Int. Conf. Directors of Safety in Mines Research. Donezk, USSR.

Alehossein, H., Poulsen, B.A., 2010. Stress analysis of longwall top coal caving. International Journal of Rock Mechanics and Mining Sciences 47, 30-41.

Archibald, J., Calder, P., Bullock, K., Madsen, D., 1990. Development of in-situ rockburst precursor warning systems. Mining Science and Technology 11, 129-152.

Balankin, A.S., 1997. Physics of fracture and mechanics of self-affine cracks. Engineering Fracture Mechanics 57, 135-203.

Barker Read, G.R., Radchenko, S.A., 1989. Methane emission from coal and associated strata samples. International Journal of Mining and Geological Engineering 7, 101-126.

Barton, C.C., Larsen, E., 1985. Fractal geometry of two-dimensional fracture networks at Yucca Mountain, southwestern Nevada, Proc. of the International Symposium on Fundamentals of Rock Joints, Bjökliden, Sweden, pp. 77-84.

Beamish, B.B., Crosdale, P.J., 1998. Instantaneous outbursts in underground coal mines: An overview and association with coal type. International Journal of Coal Geology 35, 27-55.

Beattie, C.I., Boberg, T.C., McNab, G.S., 1991. Reservoir simulation of cyclic steam stimulation in the cold lake oil sands. SPE Reservoir Engineering 6, 200-206.

Berry, D.S., Sales, T.W., 1967. An elastic treatment of ground movement due to mining, Part 2, Transversely isotropic ground movement. J. Mech. Phys. Solids. 9.

Brady, B., Leighton, F., 1977. Seismicity anomaly prior to a moderate rock burst: a case study, International Journal of Rock Mechanics and Mining Sciences & Geomechanics Abstracts. Elsevier, pp. 127-132.

Brezigar, A., 1985/86. Premogova plast Rudnika lignita Velenje (Coal seam of the Velenje coal mine). Geologija – Razprave in poročila 28/29, 323.

Broek, D., 1986. Elementary engineering fracture mechanics. Springer.

Brune, J.N., 1970. Tectonic stress and the spectra of seismic shear waves from Earthquake. J Geophys Res, Wiley, 75:4997–5009.

Brune, J.N., 1971. Correction. J Geophys Res, Wiley, 76:5002.

Bumb, A., McKee, C., 1988. Gas-well testing in the presence of desorption for coalbed methane and devonian shale. SPE formation evaluation 3, 179-185.

Cai, M., Kaiser, P.K., Martin, C.D., 1998. A tensile model for the interpretation of microseismic events near underground openings, Seismicity Caused by Mines, Fluid Injections, Reservoirs, and Oil Extraction. Springer, pp. 67-92.

Cai, W., Dou, L., Cao, A., Gong, S., Li, Z., 2014. Application of seismic velocity tomography in underground coal mines: A case study of Yima mining area, Henan, China. Journal of Applied Geophysics.

Cao, Y.X., He, D.D., Glick, D.C., 2001. Coal and gas outbursts in footwalls of reverse faults. International Journal of Coal Geology 48, 47-63.

Chaudhry, A.U., 2003. Gas well testing handbook. Gulf professional publishing.

Cheng, G., Huang, K., Yan, F., Li, W., Wang, S., 2003. Methane control for mechanised longwall top-coal caving faces in high gas content mines. Mining Technology 112, 141-148.

Chin, L.Y., Raghavan, R., Thomas, L.K., 2000. Fully coupled geomechanics and fluid-flow analysis of wells with stress-dependent permeability. SPE Journal 5, 32-45.

Choi, S.K., Wold, M.B., 2001. A mechanistic study of coal and gas outbursts, DC Rocks 2001, The 38th U.S. Symposium on Rock Mechanics (USRMS), . 2001. Swets & Zeitlinger Lisse,, Washington D.C., pp. 343-350.

Choi, S.K., Wold, M.B., 2004a. A Coupled geomechanical-reservoir model for the modelling of coal and gas outbursts, in: Ove, S. (Ed.), Elsevier Geo-Engineering Book Series. Elsevier, pp. 629-634.

Choi, S.K., Wold, M.B., 2004b. Study of the mechanisms of coal and gas outbursts using a new numerical modeling approach, 5th Coal Operators' Conference, University of Wollongong & the Australasian Institute of Mining and Metallurgy, Wollongong, pp. 181-194.

Clarkson, C.R., Bustin, R.M., 2000. Binary gas adsorption/desorption isotherms: effect of moisture and coal composition upon carbon dioxide selectivity over methane. International Journal of Coal Geology 42, 241-271.

Connell, L.D., 2009. Coupled flow and geomechanical processes during gas production from coal seams. International Journal of Coal Geology 79, 18-28.

Cook, N., 1964. The application of seismic techniques to problems in rock mechanics, International Journal of Rock Mechanics and Mining Sciences & Geomechanics Abstracts. Elsevier, pp. 169-179.

Cook, N., 1976. Seismicity associated with mining. Engineering Geology 10, 99-122.

Curl, S. J., 1978. Methane prediction in coal mines. Rep. ICI'IS/TR 04. London: IEA Coal Research, 80 pp.

Crank, J., 1975. The Mathematics of diffusion. Oxford University Press, London.

Das, B., Nikols, D.J., Das, Z., Hucka, V.J., 1991. Factors affecting rate and total volume of methane desorption from coalbeds. Guidebook for the Rocky Mountain Association of Geologists Fall Conference and Field Trip, Glenwood Springs, Colorado, 69-76.

Dougherty, H.N., Karacan, C.Ö., 2011. A new methane control and prediction software suite for longwall mines. Computers & Geosciences 37, 1490-1500.

Durucan, S., 1981. An investigation into the stress-permeability relationship of coals and flow patterns. University of Nottingham p. 301.

Durucan, S., Daltaban, T., Shi, J., Foley, L., 1993. Permeability characterisation for modelling methane flow in coal seams, Proc. of the 1993 Internat. Coalbed Methane Symp, pp. 453-460.

Durucan, S., Ahsan, M., Shi, J-Q., Syed A., Korre, A., 2014. Two phase relative permeabilities for gas and water in selected European coals. Fuel 134, 226–236.

Ediz, I.G., 1991. An application of numerical methods to the prediction of strata methane flow in mining. University of Nottingham, p. 160.

Ertekin, T., Sung, W., Schwerer, F., 1988. Production performance analysis of horizontal drainage wells for the degasification of coal seams. Journal of Petroleum Technology 40, 625-632.

Esterhuizen, G.S., Karacan, C.Ö., 2005. Development of numerical models to investigate permeability changes and gas emission around longwall mining panel, The 40th U.S. Symposium on Rock Mechanics (USRMS). American Rock Mechanics Association, Anchorage, Alaska p. 13.

Ettinger, I.L., Radchenko, S.A., Shul'man, N.V., Kovaleva, I.B., 1986. Specification of gas dynamics in coal seams with the application of methane diffusion in pieces. Urgent Problems of Mine Aerogas Dynamics Izd-vo IPKON AN SSSR, Moscow, 88-93.

Farmer, I., Pooley, F., 1967. A hypothesis to explain the occurrence of outbursts in coal, based on a study of West Wales outburst coal, International Journal of Rock Mechanics and Mining Sciences & Geomechanics Abstracts. Elsevier, pp. 189-193.

Flores, R.M., 1998. Coalbed methane: from hazard to resource. International Journal of Coal Geology 35, 3-26.

Friedel, M.J., Jackson, M.J., Williams, E.M., Olson, M.S., Westman, E., 1996. Tomographic imaging of coal pillar conditions: Observations and implications. International Journal of Rock Mechanics and Mining Sciences & Geomechanics Abstracts 33, 279-290.

Friedel, M.J., Tweeton, D.R., Jackson, M., Jessop, J., Billington, S., 1992. Mining applications of seismic tomography, 1992 SEG Annual Meeting.

Fujii, Y., Ishijima, Y., 1991. Numerical simulation of microseismicity induced by deep longwall coal mining. Mining Science and Technology 12, 265-285.

Fujii, Y., Ishijima, Y., Deguchi, G., 1997. Prediction of coal face rockbursts and microseismicity in deep longwall coal mining. International Journal of Rock Mechanics and Mining Sciences 34, 85-96.

Gale, W., Heasley, K., Iannacchione, A., Swanson, P., Hatherly, P., King, A., 2001. Rock damage characterization from microseismic monitoring, Proceedings of the 38th US Rock Mechanics Symposium, Washington, DC, 7–10 July, pp. 1313-1320.

Gash, B.W., 1991. Measurement of "Rock Properties" in Coal for Coalbed Methane Production, SPE Annual Technical Conference and Exhibition.

Ghose, A.K., 1984. Underground methods of extraction of thick coal seams—a global survey. Mining Science and Technology 2, 17-32.

Gibowicz, S.J., Kijko, A., 1994. An introduction to mining seismology. Academic Press: London, 397p.

Gray, I., 1980. The mechanism of and energy release associated with outbursts, Symposium on the Occurrence, Prediction, and Control of Outbursts in Coal Mines, Australasian Inst. of Mining and Metallurgy, Melbourne,Austrilia pp. 111-125.

Gray, I., 1987. Reservoir engineering in coal seams: Part 1-the physical process of gas storage and movement in coal seams. SPE Reservoir Engineering 2, 28-34.

Griffith, A.A., 1921. The phenomena of rupture and flow in solids. Philosophical transactions of the royal society of london. Series A, containing papers of a mathematical or physical character, 163-198.

Gringarten, A.C., 2008. From straight lines to deconvolution: The evolution of the state of the art in well test analysis. SPE Reservoir Evaluation & Engineering 11, 41-62.

Gu, F., Chalaturnyk, R.J., 2010. Permeability and porosity models considering anisotropy and discontinuity of coalbeds and application in coupled simulation. Journal of Petroleum Science and Engineering 74, 113-131.

Guan, P., Wang, H., Zhang, Y., 2009. Mechanism of instantaneous coal outbursts. Geology 37, 915-918.

Guo, H., Yuan, L., Shen, B., Qu, Q., Xue, J., 2012. Mining-induced strata stress changes, fractures and gas flow dynamics in multi-seam longwall mining. International Journal of Rock Mechanics and Mining Sciences 54, 129-139.

Gutenberg, B., Richter, C.F., 1956. Magnitude and energy of earthquakes. Annals of Geophysics 9, 1-15.

Han, J., Zhang, H., Li, S., Song, W., 2012. The characteristic of in situ stress in outburst area of China. Safety Science 50, 878-884.

Hanson D.R., Vandergrift T.L., DeMarco M.J. and Hanna K, 2002: Advanced techniques in site characterization and mining hazard detection for the underground coal industry, International Journal of Coal Geology, V.50, Issues 1-4, pp. 275-301.

Hargraves, A.J., Upfold, R.W., 1985. Aspects of laboratory simulations of instantaneous outbursts. In: Green, A.R. (Ed.), Safety in Mines Research. A.A. Balkema, Rotterdam, pp. 129– 137.

Hargraves, A.J., 1993. Update on instantaneous outbursts of coal and gas. Proc. Australas. Inst. Min. Metall. 298 (2), 3 – 17.

Harpalani, S., Pariti, U., 1993. Study of coal sorption isotherms using a multicomponent gas mixture, Proceedings of the International Coalbed Methane Symposium, Birmingham, Alabama, May, pp. 17-21.

Harpalani, S., Chen, G.L., 1995. Estimation of changes in fracture porosity of coal with gas emission. Fuel 74, 1491-1498.

Harpalani, S., Chen, G.L., 1997. Influence of gas production induced volumetric strain on permeability of coal. Geotechnical and Geological Engineering 15, 303-325.

Harrison, J.P., Hudson, J.A., 2000. Engineering rock mechanics-an introduction to the principles. Elsevier.

Hasenfus, G.J., Johnson, K.L., Su, D.W.H., 1988. A hydrogeomechanical study of overburden aquifer response to longwall mining, Proceedings of 7th Conf Ground Control in Mining, Morgantown,West Virginia pp. 144-152.

Hebblewhite, B., 2005. Status and prospects of underground thick coal seam mining methods, Proceedings of the 19th International Mining Congress and Fair of Turkey.

Hedberg, H.D., 1980. Methane generation and petroleum migration. In:W.H.Roberts and R.J Cordell (Editors), Problems of Petroleum Migration. (Studies in Geology, 10.) AAPG, pp. 179-206.

Iannacchione, A.T., Esterhuizen, G., Swanson, P., Chapman, M., Bajpayee, T., 2005. Characteristics of mining-induced seismicity associated with roof falls and roof caving events, Alaska Rocks 2005, The 40th US Symposium on Rock Mechanics (USRMS), pp. 1-10.

IEA, 2009. Coal Mine Methane in China: A Budding Asset with the Potential to Bloom, IEA Information Paper. International Energy Agency, Paris.

ITASCA, 2012. FLAC^{3D} Version 5.0-user manual, Minneapolis, pp. 42-44.

Jaeger, J.C., Cook, N.G.W., Zimmerman, R.W., 2007. Fundamentals of Rock Mechanics (4th Edition).

Jeromel, G., Medved, M., Likar, J., 2010. An analysis of the geomechanical processes in coal mining using the Velenje mining method, Acta Geotechnica Slovenica, vol. 7, no. 1, pp.31-45.

Jones, A.H., Bell, G.J., Schraufnagel, R.A., 1988. A review of the physical and mechanical properties of coal with implications for coal-bed methane well completion and production. Geology and coal-bed Methane Resources of the Northern San Juan Basin, Colorado and New Mexico, J.E. Fassett (ed.), Rocky Mountain Association of Geologists, Denver, Colorado, 169-181.

Kabiesz, J., Makówka, J., 2009. Selected elements of rock burst state assessment in case studies from the Silesian hard coal mines. Mining Science and Technology (China) 19, 660-667.

Karacan, C.Ö., 2008. Modeling and prediction of ventilation methane emissions of U.S. longwall mines using supervised artificial neural networks. International Journal of Coal Geology 73, 371-387.

Karacan, C.Ö., 2009a. Degasification system selection for US longwall mines using an expert classification system. Computers & Geosciences 35, 515-526.

Karacan, C.Ö., 2009b. Elastic and shear moduli of coal measure rocks derived from basic well logs using fractal statistics and radial basis functions. International Journal of Rock Mechanics and Mining Sciences 46, 1281-1295.

Karacan, C.Ö., 2009c. Forecasting gob gas venthole production performances using intelligent computing methods for optimum methane control in longwall coal mines. International Journal of Coal Geology 79, 131-144.

Karacan, C.Ö., Diamond, W.P., Schatzel, S.J., 2007a. Numerical analysis of the influence of in-seam horizontal methane drainage boreholes on longwall face emission rates. International Journal of Coal Geology 72, 15-32.

Karacan, C.Ö., Esterhuizen, G.S., Schatzel, S.J., Diamond, W.P., 2007b. Reservoir simulation-based modeling for characterizing longwall methane emissions and gob gas venthole production. International Journal of Coal Geology 71, 225-245.

Karacan, C.Ö., 2010. Prediction of porosity and permeability of caved zone in longwall gobs. Transport in porous media 82, 413-439.

Karacan, C.Ö., Goodman, G.V., 2011. Probabilistic modeling using bivariate normal distributions for identification of flow and displacement intervals in longwall overburden. International Journal of Rock Mechanics and Mining Sciences 48, 27-41.

Keen, T.F., 1977. The simulation of methane flow in carboniferous strata. University of Nottingham.

Kelly, M., Luo, X., Craig S., 2002. Integrating tools for longwall geomechanics assessment. International Journal of Rock Mechanics and Mining Sciences 39, 661-676.

Khan, A.S., 1995. Continuum theory of plasticity. John Wiley & Sons.

Kidybinski A., 1980: Significance of in situ strength measurements for prediction of outburst hazard in coal mines of Lower Silesia. Proc. Symp. on the occurrence, prediction and control of outbursts in coal mines. Aust Inst Min Metall, Melbourne pp193–201.

Kim, A.G., 1977. Estimating methane content of bituminous coalbeds from adsorption data. Department of the Interior, Bureau of Mines.

King, G., Ertekin, T., Schwerer, F., 1986. Numerical simulation of the transient behavior of coal-seam degasification wells. SPE Formation Evaluation 1, 165-183.

King, J., Wilkins, E., 1944. The internal structure of coal, Proceedings of a Conference on the Ultrafine Structure of Coals and Cokes, pp. 46-57.

Kormendi, A., Bodoky, L. and Hermann, L., 1986. Measurements for safety in mines. Geophysical Prospecting 34, No. 7, pp.1022-1037.

Kowalczuk, J. and Szwejkowski, J., 1975. Relation between anomaly of seismic velocity and state of stress around geological structures. Scientific Bulletins Academy of Mining and Metallurgy, No 467, Geology, p.2 (in Polish).

Kvapil, R., 1992. Sublevel caving, SME mining engineering handbook, pp. 1789-1814.

Lama, R.D., Bodziony, J., 1998. Management of outburst in underground coal mines. International Journal of Coal Geology 35, 83-115.

Langmuir, I., 1918. The adsorption of gases on plane surfaces of glass, mica and platinum. Journal of the American Chemical Society 40, 1361.

Lazar, J., Kanduč, T., Jamnikar, S., Grassa, F., Zavšek, S., 2014. Distribution, composition and origin of coalbed gasses in excavation fields from the Preloge and Pesje mining areas, Velenje Basin, Slovenia. International Journal of Coal Geology 131, pp.363-377.

Lee, J., 1982. Well testing. New York: Society of Petroleum Engineers.

Leighton, F., 1984. Microseismic activity associated with outbursts in coal mines, Proc. 3rd Conf. on Acoustic emission/microseismic activity in geologic structures and materials, University Park, PA, USA, pp. 467-477.

Li, H., 2001. Major and minor structural features of a bedding shear zone along a coal seam and related gas outburst, Pingdingshan coalfield, northern China. International Journal of Coal Geology 47, 101-113.

Li, T., Cai, M.F., Cai, M., 2007. Earthquake-induced unusual gas emission in coalmines — A km-scale in-situ experimental investigation at Laohutai mine. International Journal of Coal Geology 71, 209-224.

Likar, J., 1995. Analiza mehanizmov nenadnih izbruhov premoga in plina v premogovnikih.– Oddelek za montanistiko – University of Ljubljana, PhD Thesis, 216 pp (in Slovene).

Likar, J., Dervarič, E., Medved, M., Čadež, J., Jeromel, G., 2006. Some methods of analysing caving processes in sublevel coal mining. RMZ - Materials and Geoenvironment, vol. 53, no. 2, pp. 203-220.

Likar, J., Medved, M., Lenart, M., Mayer, J., Malenković, V., Jeromel, G., Dervarič, E., 2012. Analysis of geomechanical changes in hanging wall caused by longwall multi top caving in coal mining. Journal of Mining Science 48, 135-145.

Longuemare, P., Mainguy, M., Lemonnier, P., Onaisi, A., Gerard, C., Koutsabeloulis, N., 2002. Geomechanics in reservoir simulation: overview of coupling methods and field case study. Revue de l'Institut français du pétrole 57, 471.

Lu, C.-P., Dou, L.-M., Liu, H., Liu, H.-S., Liu, B., Du, B.-B., 2012. Case study on microseismic effect of coal and gas outburst process. International Journal of Rock Mechanics and Mining Sciences 53, 101-110.

Lu, C.-P., Dou, L.-M., Zhang, N., Xue, J.-H., Wang, X.-N., Liu, H., Zhang, J.-W., 2013. Microseismic frequency-spectrum evolutionary rule of rockburst triggered by roof fall. International Journal of Rock Mechanics and Mining Sciences 64, 6-16.

Lu, C.-P., Dou, L.-M., Zhang, N., Xue, J.-H., Liu, G.-J., 2014. Microseismic and acoustic emission effect on gas outburst hazard triggered by shock wave: a case study. Nat. Hazards 73, 1715–1731.

Lu, C., Mai, Y.-W., Xie, H., 2005. A sudden drop of fractal dimension: a likely precursor of catastrophic failure in disordered media. Philosophical magazine letters 85, 33-40.

Lu, T., Zhao, Z., Hu, H., 2011. Improving the gate road development rate and reducing outburst occurrences using the waterjet technique in high gas content outburst-prone soft coal seam. International Journal of Rock Mechanics and Mining Sciences 48, 1271-1282.

Lunarzewski, 1998. Gas emission prediction and recovery in underground coal mines. International Journal of Coal Geology 35, 117-145.

Markič, M., Sachsenhofer, R.F., 2010. The Velenje lignite-its petrology and genesis. Geological Survey of Slovenia, Ljubljana, Slovenia.

Majewska Z. and Marcak H., 1989: The relationship between acoustic emission and permeability of rock under stress. Mining Science and Technology, 9.

Mavor, M.J., Owen, L.B., Pratt, T.J., 1990. Measurement and evaluation of coal sorption isotherm data, SPE Annual Technical Conference and Exhibition, New Orleans, Louisiana, pp. 158-170.

Maxwell, S.C. and Young, R.P., 1996. Seismic imaging of rock mass responses to excavation. Int. J. Rock Mech. Min. Sci. Geomech. Abstracts 33, No.7, pp. 713-724.

McKavanagh, B., Enever, J., 1978. Developing a microseismic outburst warning system, Proceedings of the 2rd conference on acoustic emission/microseismic activity in geological structures and materials. Pennsylvania, pp. 211-225.

McKee, C.R., Bumb, A.C., Koenig, R.A., 1988. Stress-dependent permeability and porosity of coal and other geologic formations. SPE Formation Evaluation 3, 81-91.

McPherson, M.J., 1975. The occurrence of methane in mine workings. Journal of Mine Ventilation Society of South Africa 28, 118-128.

Mendecki, A.J., 1997. Seismic monitoring in mines, Chapman & Hall, 262 p.

Miller, C., Dyes, A., Hutchinson Jr, C., 1950. The estimation of permeability and reservoir pressure from bottom hole pressure build-up characteristics. Journal of Petroleum Technology 2, 91-104.

MINING.com, 2014. Caterpillar to supply two complete longwall top coal caving systems to mine in Turkey. Retrieved Dec 3, 2014 from http://www.mining.com/web/caterpillar-to-supply-two-complete-longwall-top-coal-caving-systems-to-mine-in-turkey/.

Mining accident, n.d. *In Wikipedia*. Retrieved August 10, 2015, from http://en.wikipedia.org/wiki/Mining_accident.

Minkoff, S.E., Stone, C.M., Arguello, J.G., Bryant, S., Eaton, J., Peszynska, M., Wheeler, M., 1999. Staggered in time coupling of reservoir flow simulation and geomechanical deformation: Step 1 - one-way coupling, SPE Reservoir Simulation Symposium, Houston, Texas.

Mordecai, M., 1971. An investigation into the effect of stress on permeability of rock taken from carboniferous strata. University of Nottingham.

MRDE, 1980. Prediction of firedamp emission. Final report on ECSC research project 7220-AC/801. Burton-on-Trent: Mining Research and Development Establishment, National Coal Board, 102p.

Mutke, G., 2013. Registration of seismic foci under mining coal seam – The experience of polish mines. Acta Geodyn. Geomater 10(2) , 147–153.

Odling, N.E., 1997. Scaling and connectivity of joint systems in sandstones from western Norway. Journal of Structural Geology 19, 1257-1271.

O'Shaughnessy, S.M., 1980. The computer simulation of methane flow through strata adjacent to a working longwall coalface. University of Nottingham.

Osorio, J.G., Chen, H.Y., Teufel, L.W., Schaffer, S., 1998. A two-domain, 3D, fully coupled fluid-flow/geomechanical simulation model for reservoirs with stress-sensitive mechanical and fluid-flow properties, SPE/ISRM Eurock 98, Trondheim,Norway pp. 455-464.

Palchik, V., 2002. Influence of physical characteristics of weak rock mass on height of caved zone over abandoned subsurface coal mines. Environmental Geology 42, 92-101.

Palchik, V., 2003. Formation of fractured zones in overburden due to longwall mining. Environmental Geology 44, 28-38.

Pappas, D.M., Mark, C., 1993. Behavior of simulaterd longwall gob material, in: United States Department of the Interior, B.o.M. (Ed.). Bureau of Mines, p. 39.

Patching, T.H., 1965. Variation in permeability of coal, Proceedings of the Rock Mechanics Symposium, Uinversity of Toronto.

Patching, T., 1970. Retention and release of gas in coal-a review. Canadian mining and metallurgical bulletin 63, 1302-1308.Paterson, L., 1986. A model for outburst in coal. Int. J. Rock Mech. Min. Sci. Geomech. Abstr. 23, 327-332.

Peng, S.S., Chiang, H.S., 1984. Longwall Mining Wiley, New York.

Poliakov, A.N., Herrmann, H.J., Podladchikov, Y.Y., Roux, S., 1994. Fractal plastic shear bands. Fractals 2, 567-581.

Remner, D., Ertekin, T., Sung, W., King, G., 1986. A parametric study of the effects of coal seam properties on gas drainage efficiency. SPE Reservoir Engineering 1, 633-646.

Ren, T.X., Edwards, J.S., 2000. Three-dimensional computational fluid dynamics modelling of methane flow through permeable strata around a longwall face. Mining Technology 109, 41-48.

Ren, T.X., Edwards, J.S., 2002. Goaf gas modelling techniques to maximise methane capture from surface gob wells, in: De, S.E. (Ed.), Mine Ventilation, The North American/Ninth US Mine Ventilation Symposium Swets & Zeitlinger B.V., Lisse, The Netherlands, Kingston,Ontario,Canada, p. 8.

Reznik, A., Dabbous, M., Fulton, P., Taber, J., 1974. Air-water relative permeability studies of Pittsburgh and Pocahontas coals. Society of Petroleum Engineers Journal 14, 556-562.

Rodrigues, C.F., Lemos de Sousa, M.J., 2002. The measurement of coal porosity with different gases. International Journal of Coal Geology 48, 245-251.

Rogers, R., Ramurthy, K., Rodvelt, G., Mullen, M., 2007. Coalbed Methane: Principles and Practices. Oktibbeha Publishing Co. LLC.

Rutqvist, J., Tsang, C.-F., 2003. TOUGH-FLAC: a numerical simulator for analysis of coupled thermal-hydrologic-mechanical processes in fractured and porous geological media under multi-phase flow conditions, Proceedings of the TOUGH Symposium, pp. 12-14.

Sang, S., Xu, H., Fang, L., Li, G., Huang, H., 2010. Stress relief coalbed methane drainage by surface vertical wells in China. International Journal of Coal Geology 82, 196-203.

Sato, K., Fujii, Y., 1988. Induced seismicity associated with longwall coal mining, International Journal of Rock Mechanics and Mining Sciences & Geomechanics Abstracts. Elsevier, pp. 253-262.

Saulsberry, J.L., Schafer, P.S., Schraufnagel, R.A., 1996. A guide to coalbed methane reservoir engineering. Gas Research Institute.

Schlumberger, 2010. ECLIPSE reservoir simulator, Manual and technical description, Houston, TX.

Schweinfurth, S.P., Finkelman, R.B., 2003. Coal--a complex natural resource: an overview of factors affecting coal quality and use in the United States. US Dept. of the Interior, US Geological Survey.

Scott, F., Jordan, J., Tesarik, D., Williams, T., Denton, D., 1999. Validation of seismic tomography to detect stress in an underground mine. NIOSH report.

Scott, T.E., Ma, Q., Roegiers, J.C., 1993. Acoustic velocity changes during shear enhanced compaction of sandstone. International Journal of Rock Mechanics and Mining Sciences & Geomechanics Abstracts 30, 763-769.

Scott, F. and Williams, T., 2004. Geophysical methods to detect stress in underground mines, Spokane Research Laboratory, NIOSH.

Seidle, J.P., Jeansonne, M.W., Erickson, D.J., 1992. Application of matchstick geometry to stress dependent permeability in coals, SPE Rocky Mountain Regional Meeting Casper, Wyoming, pp. 433-444.

Shearer, P.M., 2009. Introduction to seismology. Cambridge University Press.

Shepherd, J., Rixon, L., Griffiths, L., 1981. Outbursts and geological structures in coal mines: a review, International Journal of Rock Mechanics and Mining Sciences & Geomechanics Abstracts. Elsevier, pp. 267-283.

Shi, J.-Q., Durucan, S., 2005. A model for changes in coalbed permeability during primary and enhanced methane recovery. SPE Reservoir Evaluation & Engineering 8, 291-299.

Si, G., Jamnikar, S., Lazar, J., Shi, J. Q., Durucan, S., Korre, A., Zavšek, S., 2015a, Monitoring and modelling of gas dynamics in multi-level longwall top coal caving of ultra-thick coal seams, part I: Borehole measurements and a conceptual model for gas emission zones. International Journal of Coal Geology, 144, 98-110.

Si, G., Durucan, S., Jamnikar, S., Lazar, J., Abraham, K., Korre, A., Shi, J. Q., Zavšek, S., Mutke, G., Lurka, A., 2015b, Seismic monitoring and analysis of excessive gas emissions in heterogeneous coal seams. International Journal of Coal Geology, 149, 41-54.

Singh, J., 1984. A mechanism of outbursts of coal and gas. Mining Science and Technology 1, 269-273.

Singh, S.K., 2011. Extraction of thick coal seam. National Insitute of Technology Rourkela, p. 56.

Smith, D.M., Williams, F.L., 1984. Diffusion models for gas production from coal: Determination of diffusion parameters. Fuel 63, 256-261.

Snow, D.T., 1968. Rock fracture spacings, openings, and porosities. Journal of Soil Mechanics & Foundations Div.

Somerton, W.H., Söylemezoḡlu, I.M., Dudley, R.C., 1975. Effect of stress on permeability of coal. International Journal of Rock Mechanics and Mining Sciences 12, 129-145.

Spencer, S., Somers, M., Pinczewski, W., Doig, I., 1987. Numerical simulation of gas drainage from coal seams, SPE Annual Technical Conference and Exhibition.

Styles, P., Emsley, S., Jowitt, T., 1988. Microseismic monitoring for the prediction of outbursts at Cynheidre Colliery, Dyfed, S. Wales. Geological Society, London, Engineering Geology Special Publications 5, 423-433.

Talebi, S., Mottahed, P., Corbett, G., 1995. Outburst monitoring using microseismic techniques in the Phalen colliery, Sydney, Nova Scotia, Canada, in: Lama, R.D. (Ed.), Management and Control of High Gas Outbursts In Underground Coal Mines, Westonprint, Kiama, NSW, Australia, pp. 153–160.

Tang, C., 1997. Numerical simulation of progressive rock failure and associated seismicity. International Journal of Rock Mechanics and Mining Sciences 34, 249-261.

Thimons, E.D., Kissell, F.N., 1973. Diffusion of methane through coal. Fuel 52, 274-280.

Tran, D., Nghiem, L., Buchanan, L., 2005. Improved iterative coupling of geomechanics with reservoir simulation, SPE Reservoir Simulation Symposium, The Woodlands, Texas.

Unver, B., Yasitli, N., 2006. Modelling of strata movement with a special reference to caving mechanism in thick seam coal mining. International Journal of Coal Geology 66, 227-252.

U.S. Energy Information and Administration, retrived December 2, 2014 from http://www.eia.gov/todayinenergy/detail.cfm?id=18951.

Vakili, A., Hebblewhite, B.K., 2010. A new cavability assessment criterion for Longwall Top Coal Caving. International Journal of Rock Mechanics and Mining Sciences 47, 1317-1329.

Wang, J., Yang, S., Li, Y., Wei, L., Liu, H., 2014. Caving mechanisms of loose top-coal in longwall top-coal caving mining method. International Journal of Rock Mechanics and Mining Sciences 71, 160-170.

Warren, J.E., Root, P.J., 1963. The behavior of naturally fractured reservoirs. SPE Journal 3, 245-255.

Watanabe, T. and Sassa, K., 1996. Seismic tomography and its application to rock mass evaluation. Int. J. Rock Mech. Min. Sci. Geomech. Abstracts 33, No.5, pp.467-477.

Westman, E., Haramy, K., Rock, A., 1996. Seismic tomography for longwall stress analysis. Rock Mechanics Tools and Techniques, 397-403.

Westman, E.C., 2001. A correlation between seismic tomography, seismic events and support pressure, Rockmechanics in the National Interest, Tinucci & Heasley, p.p.319-326, Swets& Zeitlinger.

Westman, E.C., 2004. Use of tomography for inference of stress redistribution in rock. Industry Applications, IEEE Transactions on 40, 1413-1417.

Whittaker, B.N., 1974. An appraisal of strata control practice. Trans. Inst. Mining and Metallurgy 134, 9-24.

Whittaker, B.N., Reddish, D.J., 1989. Subsidence: occurrence,prediction and control. Elsevier Science Amsterdam.

Whittles, D.N., Lowndes, I.S., Kingman, S.W., Yates, C., Jobling, S., 2006. Influence of geotechnical factors on gas flow experienced in a UK longwall coal mine panel. International Journal of Rock Mechanics and Mining Sciences 43, 369-387.

Whittles, D.N., Lowndes, I.S., Kingman, S.W., Yates, C., Jobling, S., 2007. The stability of methane capture boreholes around a long wall coal panel. International Journal of Coal Geology 71, 313-328.

Williams, R.J., Weissman, J.J., 1995. Gas and emission and outburst assessment in mixed CO_2 and CH_4 environments, Pro. ACIRL Underground Mining Seminar, North Ryde, pp. 1-12.

Wold, M.B., Connell, L.D., Choi, S.K., 2008. The role of spatial variability in coal seam parameters on gas outburst behaviour during coal mining. International Journal of Coal Geology 75, 1-14.

World Coal Association, 2015. Coal Statistics. Retrieved August 27, 2015 from http://www.worldcoal.org/resources/coal-statistics/.

Xie, G.-X., Yang, K., Liu, Q.-M., 2006. Study on distribution laws of stress in inclined coal pillar for fully-mechanized top-coal caving face. Yanshilixue Yu Gongcheng Xuebao/Chinese Journal of Rock Mechanics and Engineering 25, 545-549.

Xie, H.-P., Zhou, H.-W., Liu, J.-F., Xue, D.-J., 2011. Mining-induced mechanical behavior in coal seams under different mining layouts. Journal of China Coal Society 36, 1067-1074.

Xie, Y.-S., Zhao, Y.-S., 2009. Numerical simulation of the top coal caving process using the discrete element method. International Journal of Rock Mechanics and Mining Sciences 46, 983-991.

Xu, J., Yu, B., Lou, J., Wang, D., 2007. Characteristics of gas emission at super-length fully-mechanized top coal caving face. Journal of China University of Mining and Technology 17, 447-452.

Xu, T., Tang, C.A., Yang, T.H., Zhu, W.C., Liu, J., 2006. Numerical investigation of coal and gas outbursts in underground collieries. International Journal of Rock Mechanics and Mining Sciences 43, 905-919.

Xue, S., Wang, Y., Xie, J., Wang, G., 2011. A coupled approach to simulate initiation of outbursts of coal and gas — Model development. International Journal of Coal Geology 86, 222-230.

Yasitli, N.E., Unver, B., 2005. 3D numerical modeling of longwall mining with top-coal caving. International Journal of Rock Mechanics and Mining Sciences 42, 219-235.

Yavuz, H., 2004. An estimation method for cover pressure re-establishment distance and pressure distribution in the goaf of longwall coal mines. International Journal of Rock Mechanics and Mining Sciences 41, 193-205.

Young, R., Maxwell, S., 1992. Seismic characterization of a highly stressed rock mass using tomographic imaging and induced seismicity. Journal of Geophysical Research: Solid Earth (1978–2012) 97, 12361-12373.

Zapušek, A. and Hoćevar, S., 1998. Adsorption and desorption properties of lignite. - In: Meunier, F. (ed.), 1998: Fundamentals of adsorption 6 – Proceedings of the 6th International Conference of fundamentals of adsorption, Presqu'ile de Giens, 24-28 May; Elsevier; 653-658.

Zhao, Y., Huang, J., Wang, R., 1993. Fractal characteristics of mesofractures in compressed rock specimens, International Journal of Rock Mechanics and Mining Sciences & Geomechanics Abstracts. Elsevier, pp. 877-882.

Appendices

Appendix 1: Borehole Configurations Used at Coal Mine Velenje

1.1 Borehole Design for Gas Pressure Measurement

Figure A1.1 shows a schematic of the borehole design used for seam gas pressure measurements. A 25 m long borehole is first cored at a diameter of 101 mm. The first 20 m of the borehole is then re-drilled to a larger diameter of 160 mm. Next, a steel casing of 128 mm diameter and 20 m long is inserted into the borehole and the annulus between the steel casing and the borehole is filled with cement. A 25 m long Alcaten tube (ϕ = 25.4 mm) perforated in the bottom 5 m is then inserted into the steel casing, with the annulus sealed by a sealant foam. Finally, a flange with a fixed digital pressure transducer (Pemex-LC type calibrated to $0 - 10$ or $0 - 20$ bar, supplied by Kirchgaesser), with an accuracy of ±1 % of its maximum range, is connected to the steel casing. Pressure recorded by the transducers is sent to the surface information centre of the mine via underground cables. Acquisition of gas pressure readings is set at 30 minutes interval and recorded in real time. A pressure gauge (rated at 0 - 10; 0 - 16 or 0 - 20 bar) is also connected to the borehole, which is read manually to confirm the measurements taken by the digital transducer (Figure A1.2).

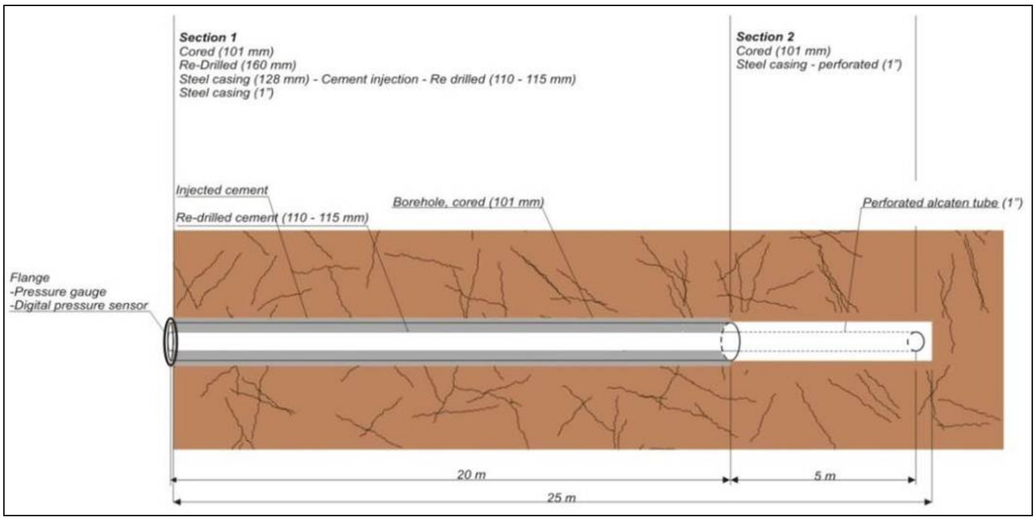

Figure A1.1: Schematic of 25 m borehole for in-seam gas pressure monitoring (after Si *et al*., 2015a).

Figure A1.2: A completed pressure monitoring borehole on-site (Courtesy of Coal Mine Velenje researchers).

1.2 Borehole Design for Gas Composition Measurement

Two different borehole configurations have been used for monitoring gas composition and its response to face advance. The first design involved the drilling of a series of so called short boreholes (3 m in length), at 50 m spacing, into the panel under preparation. A schematic of the short borehole is shown in Figure A1.3. After drilling the 43 mm diameter borehole a partly perforated Alcaten tube ($\phi = 25.4$ mm) is installed into the borehole. Sealing foam is used to fill the gap between the solid part of the Alcaten tube and the borehole and a plug is mounted at the borehole mouth to prevent leakage of mine air into the Alcaten tube. Gas samples are manually taken using a capillary sampling tube (ϕ = 0.5 mm) inside the Alcaten tube for analysis by a portable gas composition sensor.

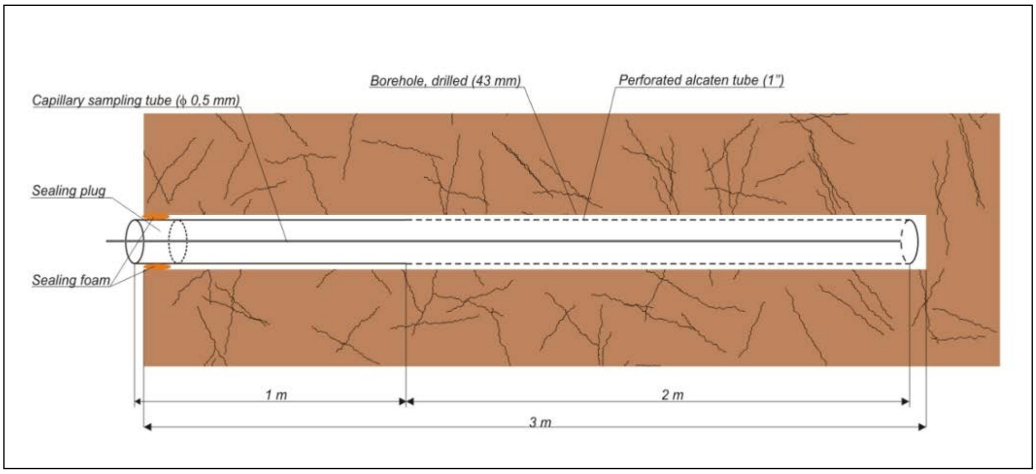

Figure A1.3: Schematic of a short borehole for gas composition monitoring (Courtesy of Coal Mine Velenje researchers).

The second borehole configuration was introduced to improve the accuracy of gas composition measurements whereby gas samples are taken from 20 m long boreholes and analysed in the laboratory. The long boreholes are drilled into the coal panels during the development of gateroads for the longwall faces. To improve the stability of the borehole, a steel casing and a backup sampling tube are installed (Figure A1.4).

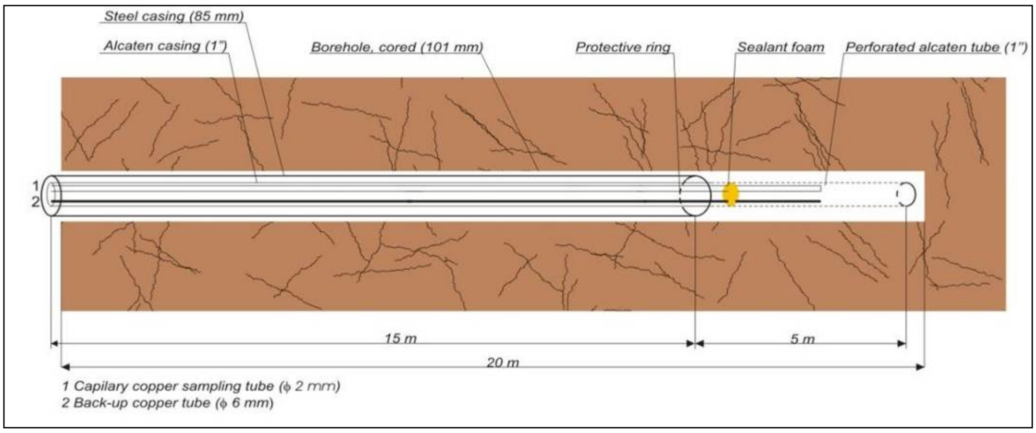

Figure A1.4: Schematic of 20 m long borehole for gas composition monitoring (after Si *et al*., 2015a).

Appendix 2: Histograms of Microseismic Energy

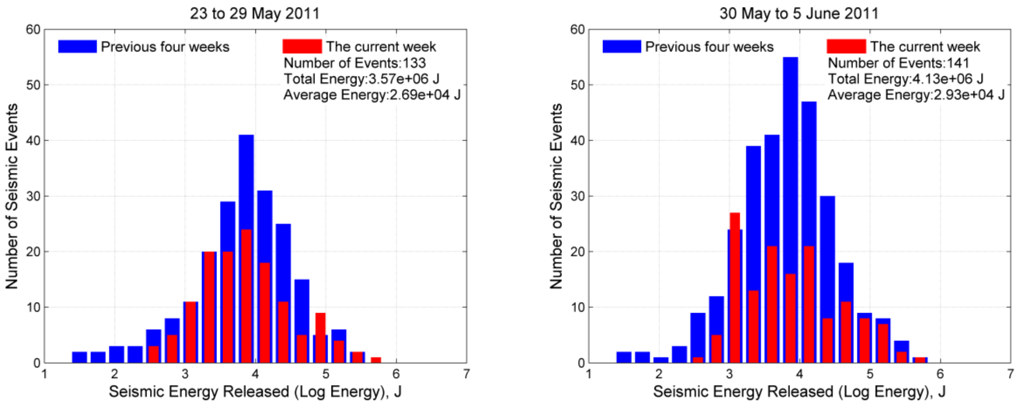

(a) Week 23 to 29 May 2011 (b) Week 30 May to 5 June 2011

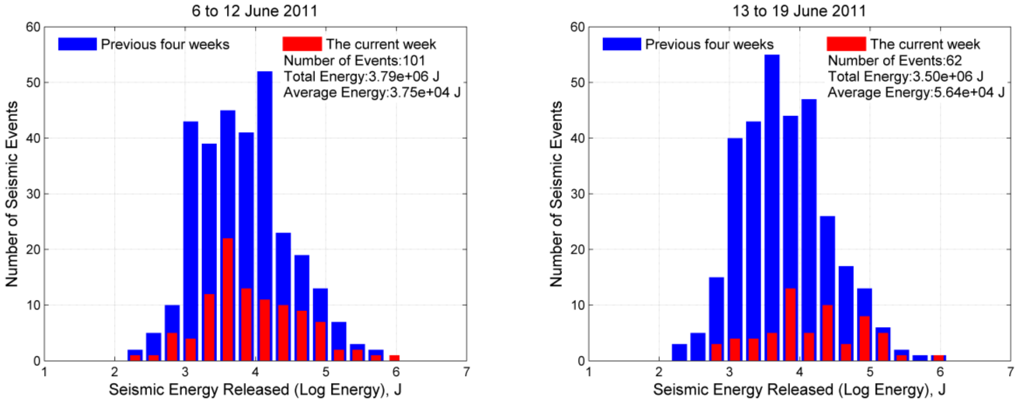

(c) Week 6 to 12 June 2011 (d) Week 13 to 19 June 2011

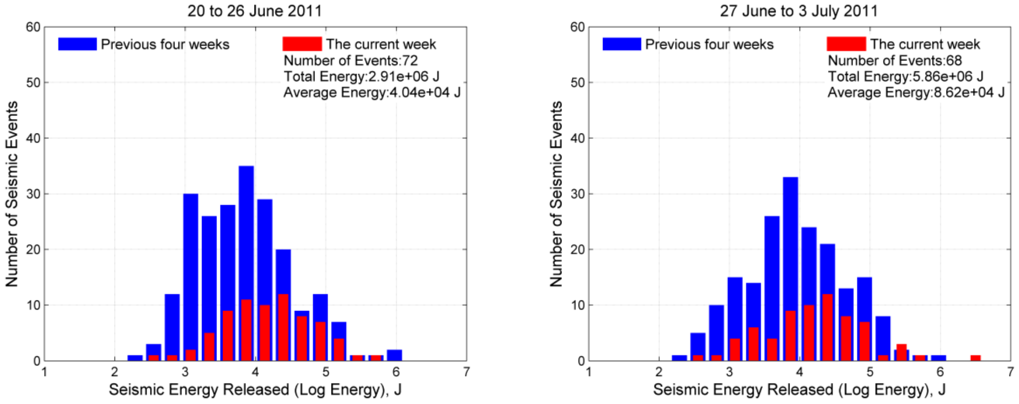

(e) Week 20 to 26 June 2011 (f) Week 27 June to 3 July 2011

Figure A2.1: Histograms of seismic energy released in each production week and the previous weeks.

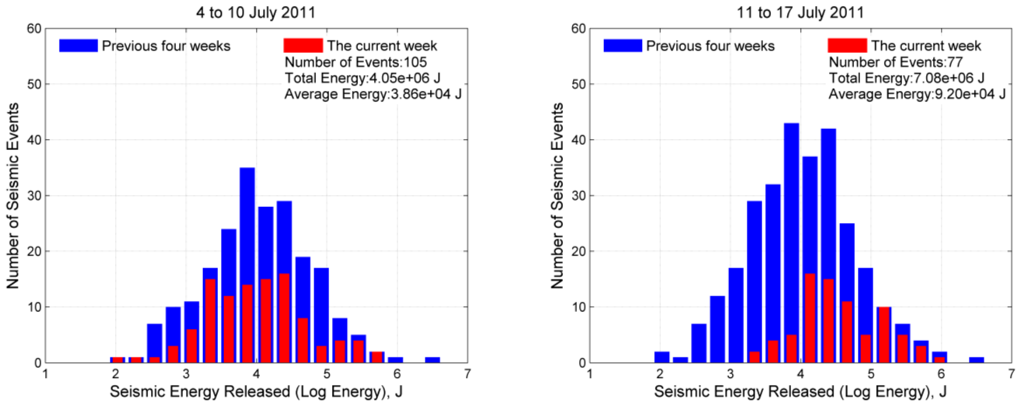

(g) Week 4 to 10 July 2011 (h) Week 11 to 17 July 2011

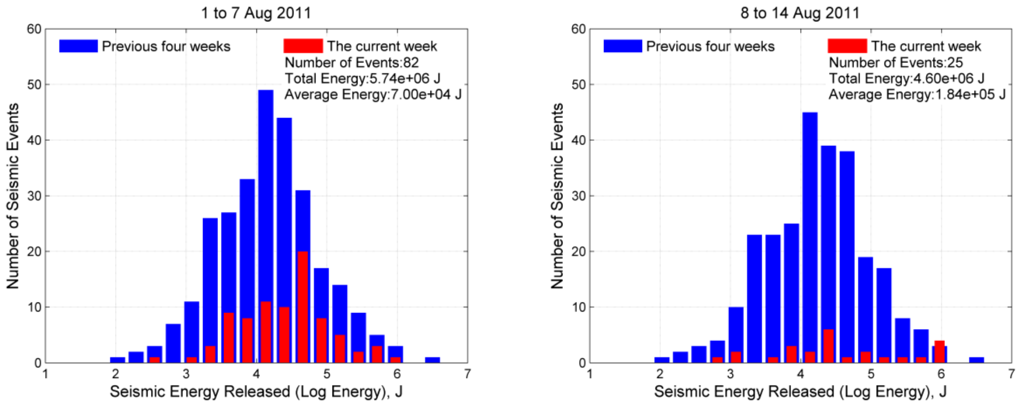

(i) Week 1 to 7 August 2011 (j) Week 8 to 14 August 2011

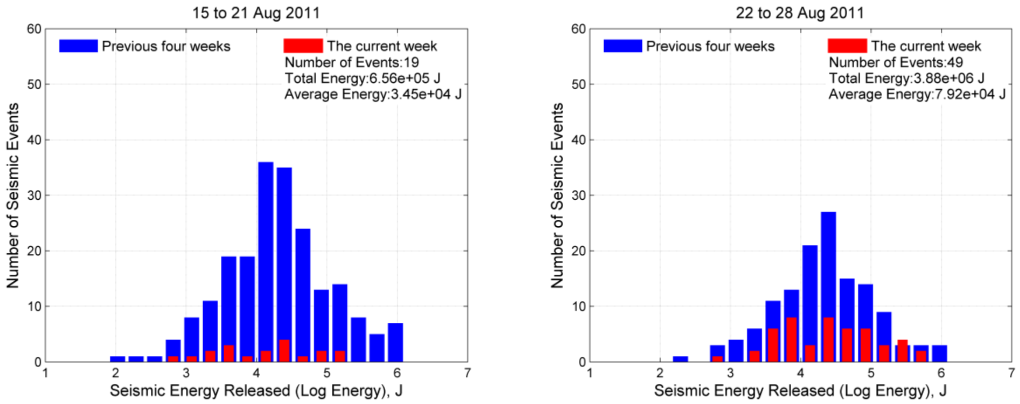

(k) Week 15 to 21 August 2011 (l) Week 22 to 28 August 2011

Figure A2.1: Histograms of seismic energy released in each production week and the previous weeks (continued).

Appendix 3: Calculation of Fractal Dimensions

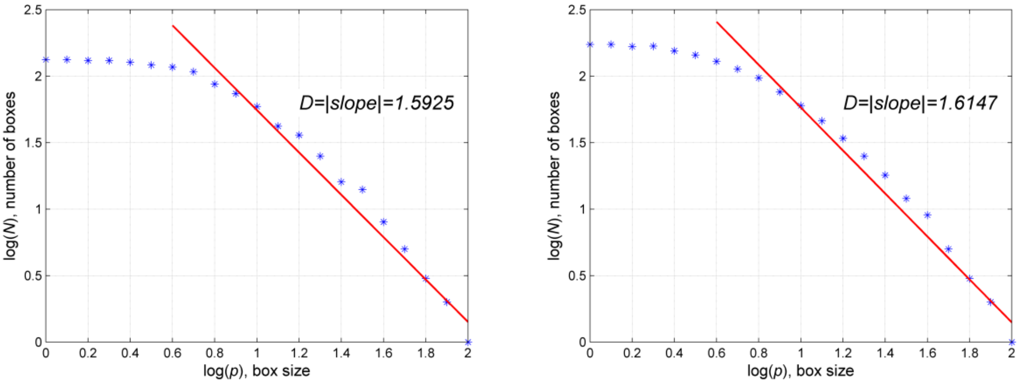

(a) Week 23 to 29 May 2011 (b) Week 30 May to 5 June 2011

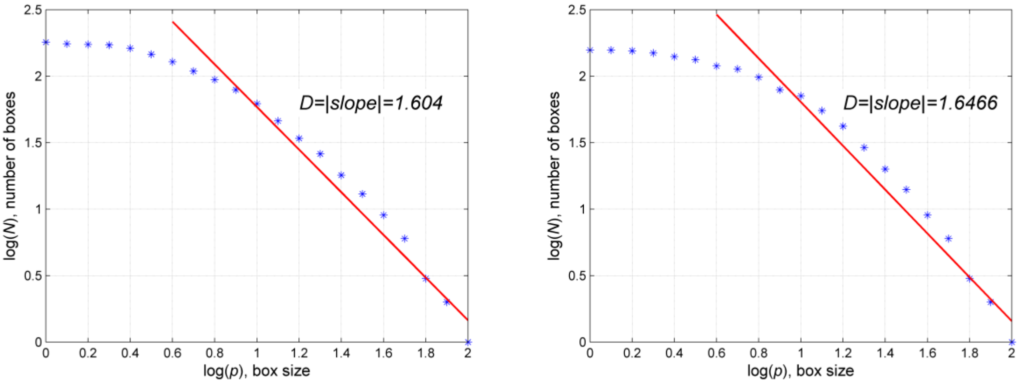

(c) Week 6 to 12 June 2011 (d) Week 13 to 19 June 2011

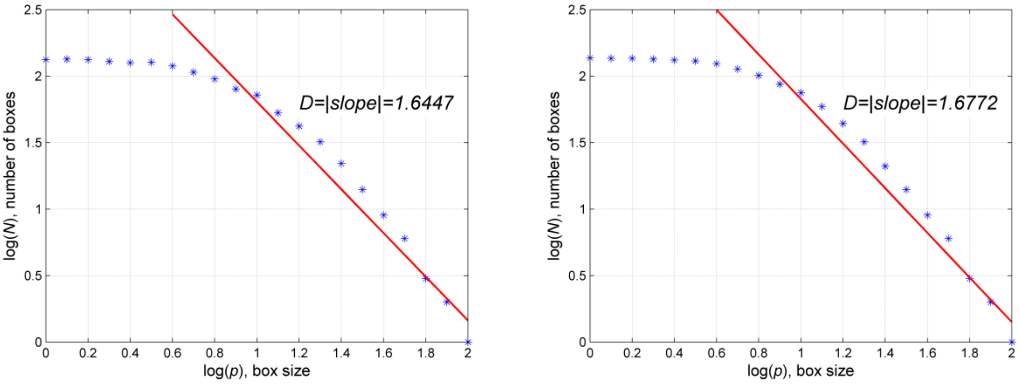

(e) Week 20 to 26 June 2011 (f) Week 27 June to 3 July 2011

Figure A3.1: Calculation of fractal dimension using the box counting method from 23rd May 2011 to 28th Aug 2011.

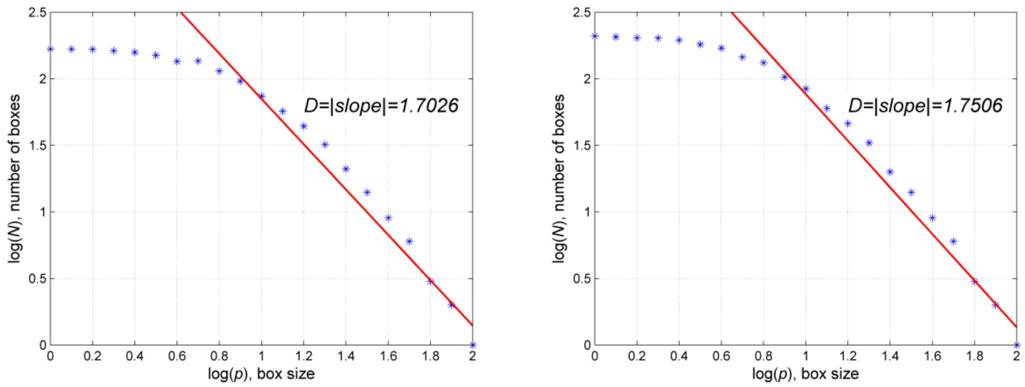

(g) Week 4 to 10 July 2011 (h) Week 11 to 17 July 2011

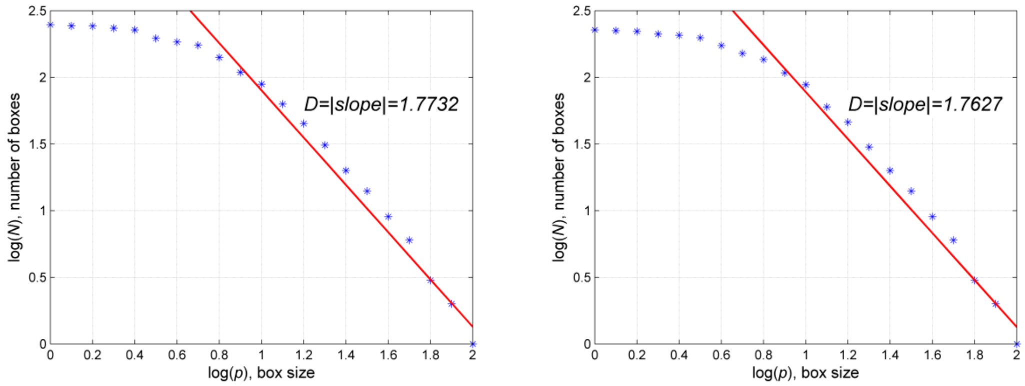

(i) Week 1 to 7 August 2011 (j) Week 8 to 14 August 2011

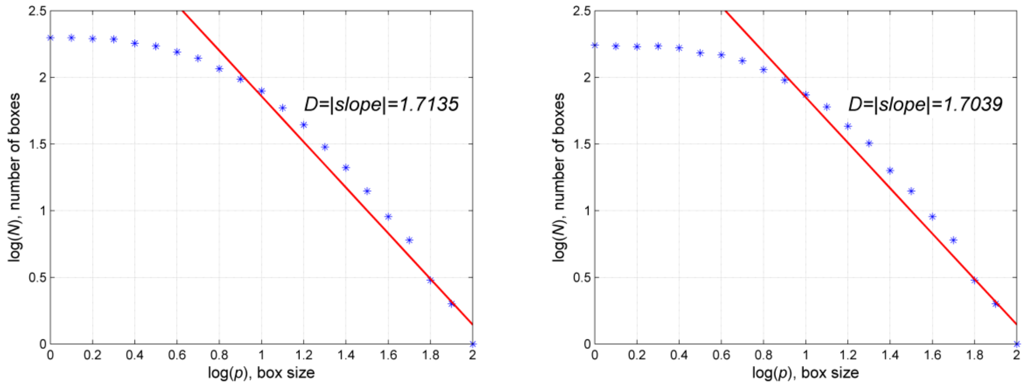

(k) Week 15 to 21 August 2011 (l) Week 22 to 28 August 2011

Figure A3.1: Calculation of fractal dimension using the box counting method from 23rd May 2011 to 28th Aug 2011 (continued).

Appendix 4: Results of Gas Drainage Trials

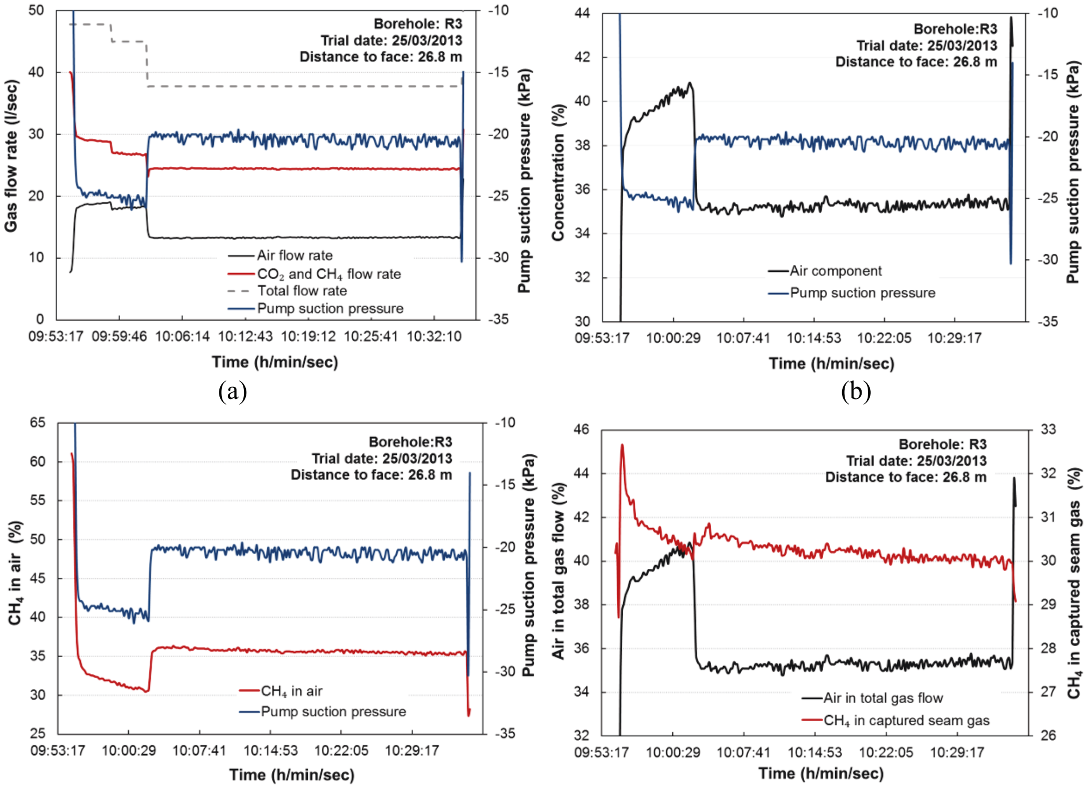

(a) (b)

(c) (d)

Figure A4.1: Results of **R3** gas drainage trial on **25/03/2013**: (a) Gas flow rate *vs* suction pressure; (b) Air concentration *vs* suction pressure; (c) CH_4 concentration in air *vs* suction pressure; (d) Concentration of air in total gas flow *vs* CH_4 in captured seam gas.

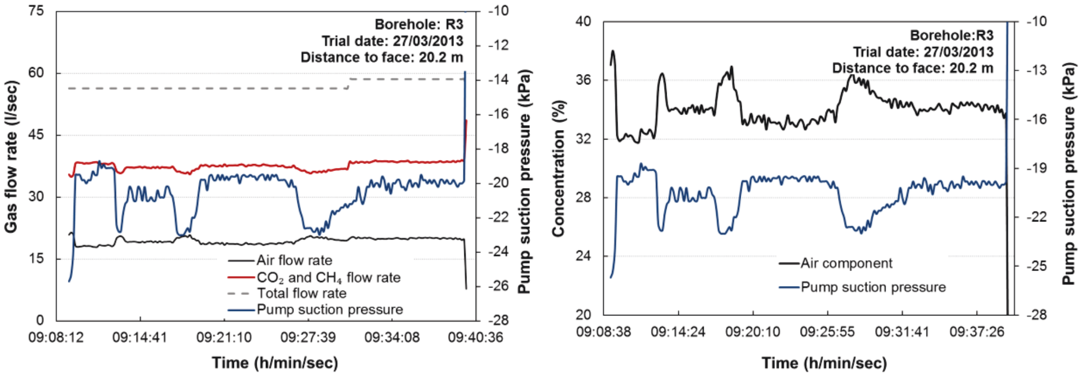

(a) (b)

Figure A4.2: Results of **R3** gas drainage trial on **27/03/2013**: (a) Gas flow rate *vs* suction pressure; (b) Air concentration *vs* suction pressure; (c) CH_4 concentration in air *vs* suction pressure; (d) Concentration of air in total gas flow *vs* CH_4 in captured seam gas.

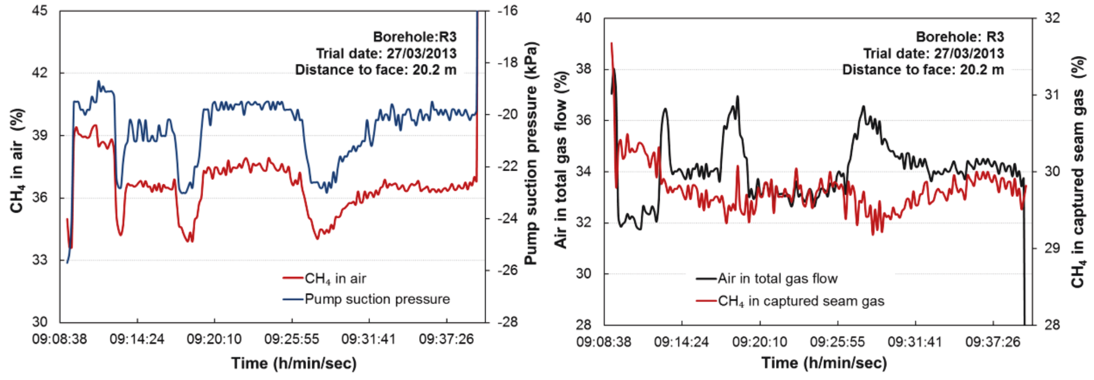

(c) (d)

Figure A4.2: Results of **R3** gas drainage trial on **27/03/2013**: (a) Gas flow rate *vs* suction pressure; (b) Air concentration *vs* suction pressure; (c) CH_4 concentration in air *vs* suction pressure; (d) Concentration of air in total gas flow *vs* CH_4 in captured seam gas (continued).

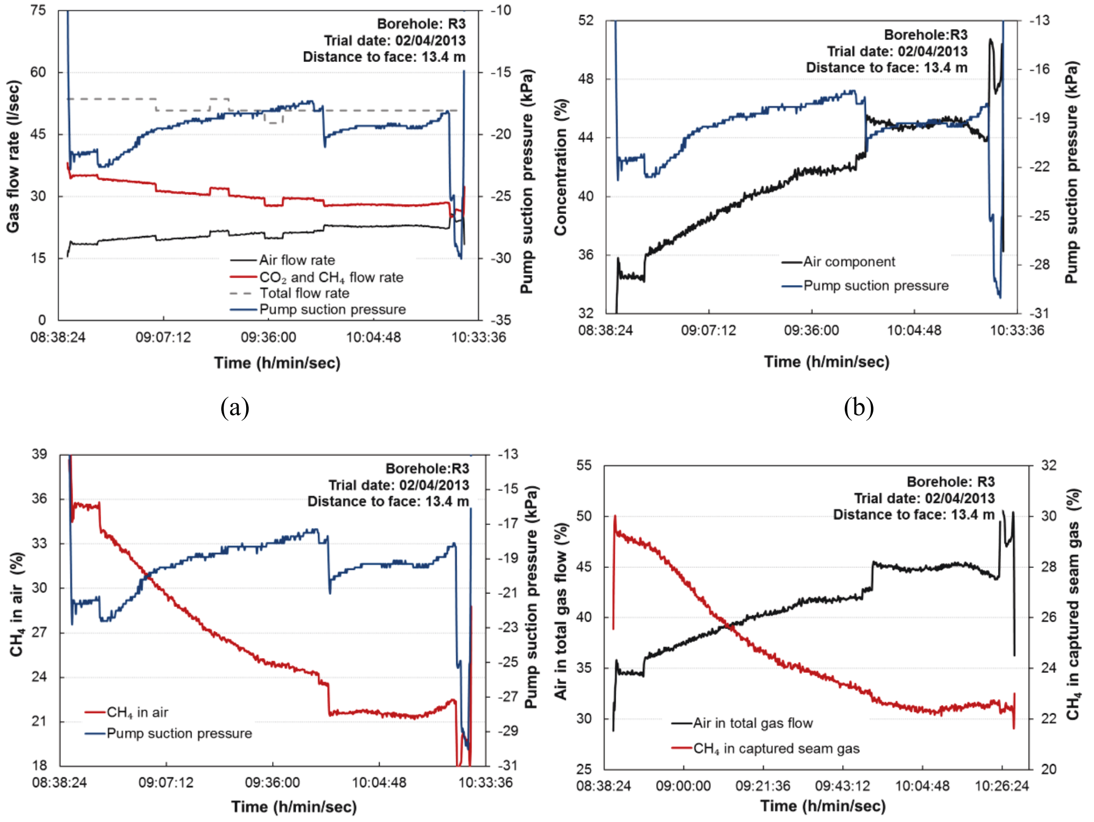

(a) (b)

(c) (d)

Figure A4.3: Results of **R3** gas drainage trial on **02/04/2013**: (a) Gas flow rate *vs* suction pressure; (b) Air concentration *vs* suction pressure; (c) CH_4 concentration in air *vs* suction pressure; (d) Concentration of air in total gas flow *vs* CH_4 in captured seam gas.

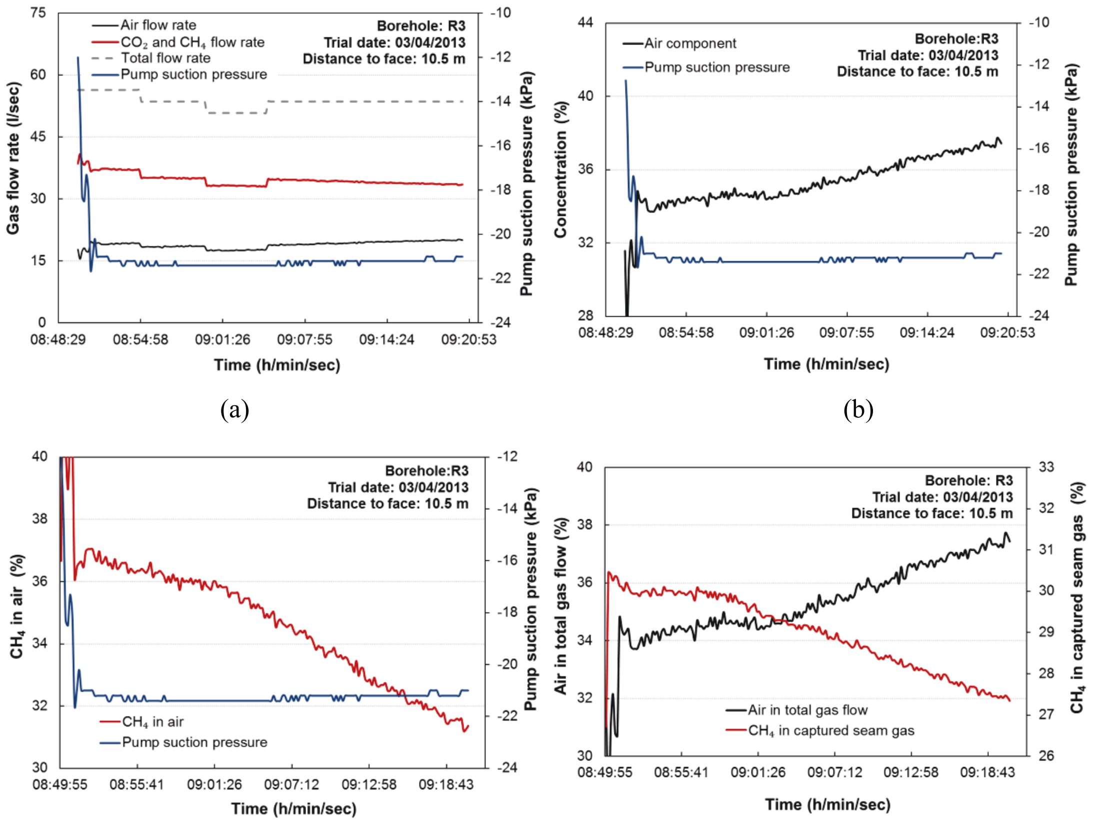

(a) (b)

(c) (d)

Figure A4.4: Results of **R3** gas drainage trial on **03/04/2013**: (a) Gas flow rate *vs* suction pressure; (b) Air concentration *vs* suction pressure; (c) CH_4 concentration in air *vs* suction pressure; (d) Concentration of air in total gas flow *vs* CH_4 in captured seam gas.

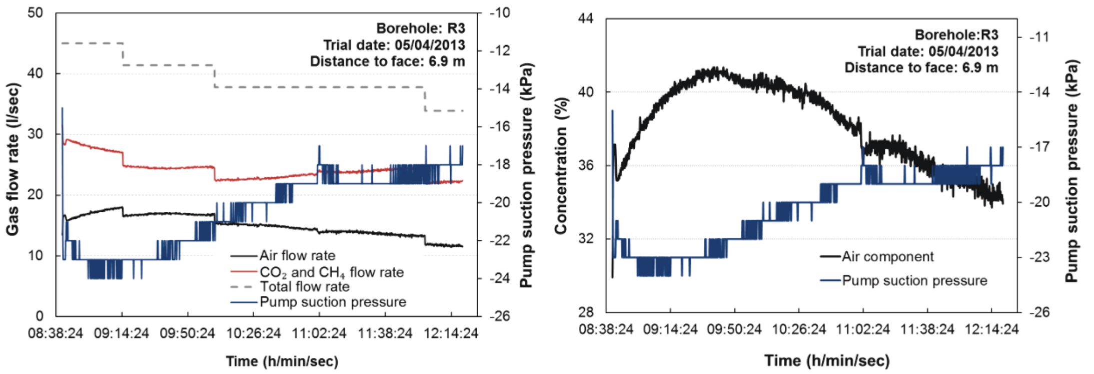

(a) (b)

Figure A4.5: Results of **R3** gas drainage trial on **05/04/2013**: (a) Gas flow rate *vs* suction pressure; (b) Air concentration *vs* suction pressure; (c) CH_4 concentration in air *vs* suction pressure; (d) Concentration of air in total gas flow *vs* CH_4 in captured seam gas.

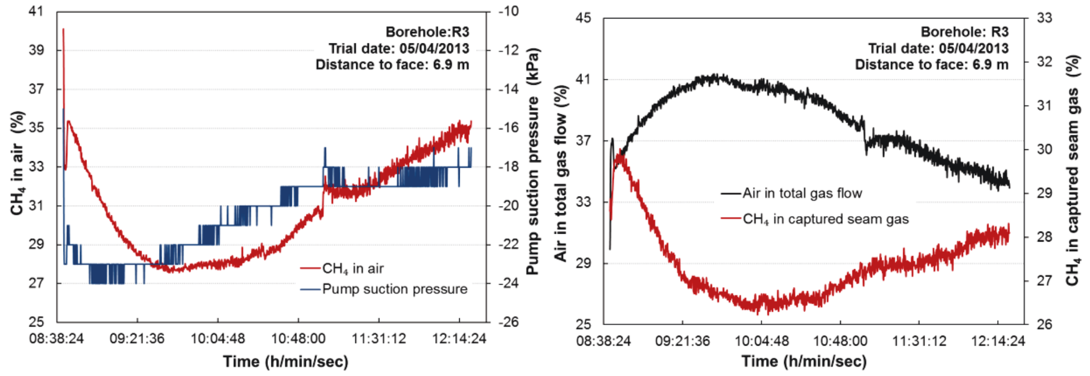

(c) (d)

Figure A4.5: Results of **R3** gas drainage trial on **05/04/2013**: (a) Gas flow rate *vs* suction pressure; (b) Air concentration *vs* suction pressure; (c) CH$_4$ concentration in air *vs* suction pressure; (d) Concentration of air in total gas flow *vs* CH$_4$ in captured seam gas (continued).

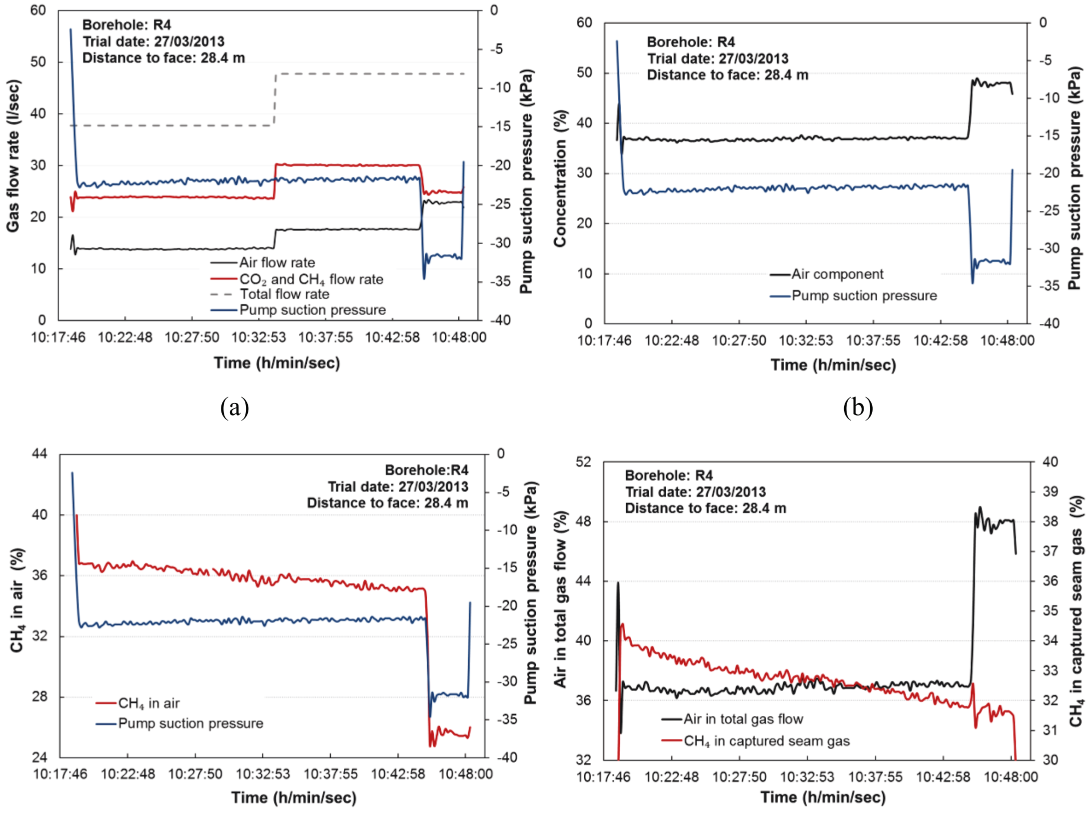

(a) (b)

(c) (d)

Figure A4.6: Results of **R4** gas drainage trial on **27/03/2013**: (a) Gas flow rate *vs* suction pressure; (b) Air concentration *vs* suction pressure; (c) CH$_4$ concentration in air *vs* suction pressure; (d) Concentration of air in total gas flow *vs* CH$_4$ in captured seam gas.

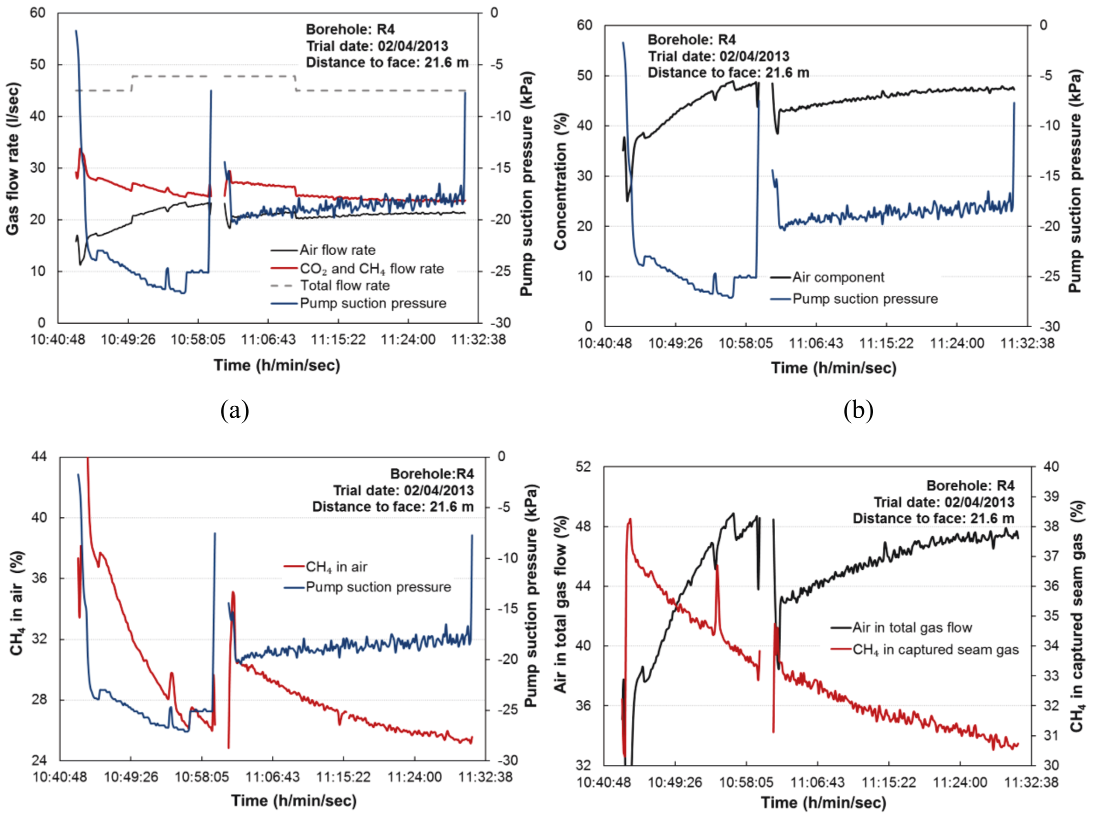

(a) (b)

(c) (d)

Figure A4.7: Results of **R4** gas drainage trial on **02/04/2013**: (a) Gas flow rate *vs* suction pressure; (b) Air concentration *vs* suction pressure; (c) CH$_4$ concentration in air *vs* suction pressure; (d) Concentration of air in total gas flow *vs* CH$_4$ in captured seam gas.

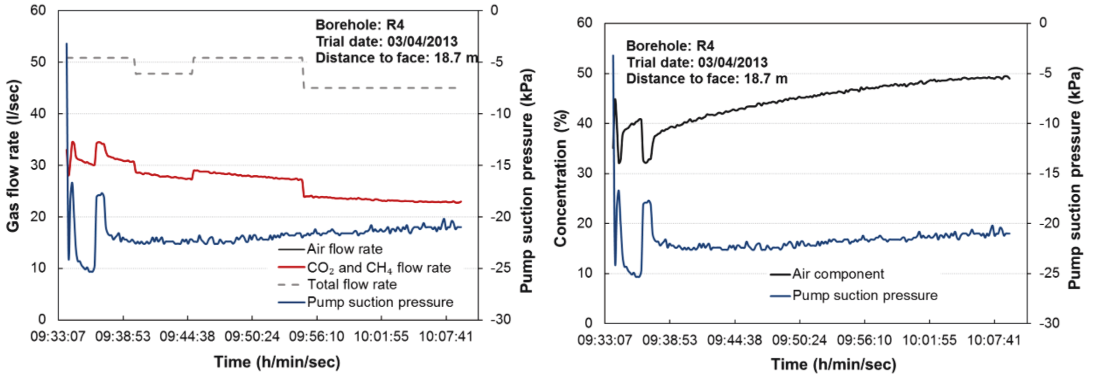

(a) (b)

Figure A4.8: Results of **R4** gas drainage trial on **03/04/2013**: (a) Gas flow rate *vs* suction pressure; (b) Air concentration *vs* suction pressure; (c) CH$_4$ concentration in air *vs* suction pressure; (d) Concentration of air in total gas flow *vs* CH$_4$ in captured seam gas.

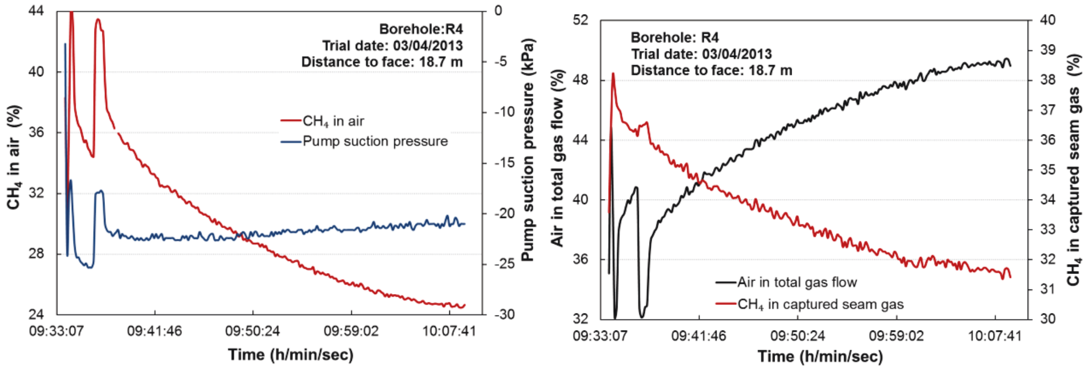

(c) (d)

Figure A4.8: Results of **R4** gas drainage trial on **03/04/2013**: (a) Gas flow rate *vs* suction pressure; (b) Air concentration *vs* suction pressure; (c) CH$_4$ concentration in air *vs* suction pressure; (d) Concentration of air in total gas flow *vs* CH$_4$ in captured seam gas (continued).

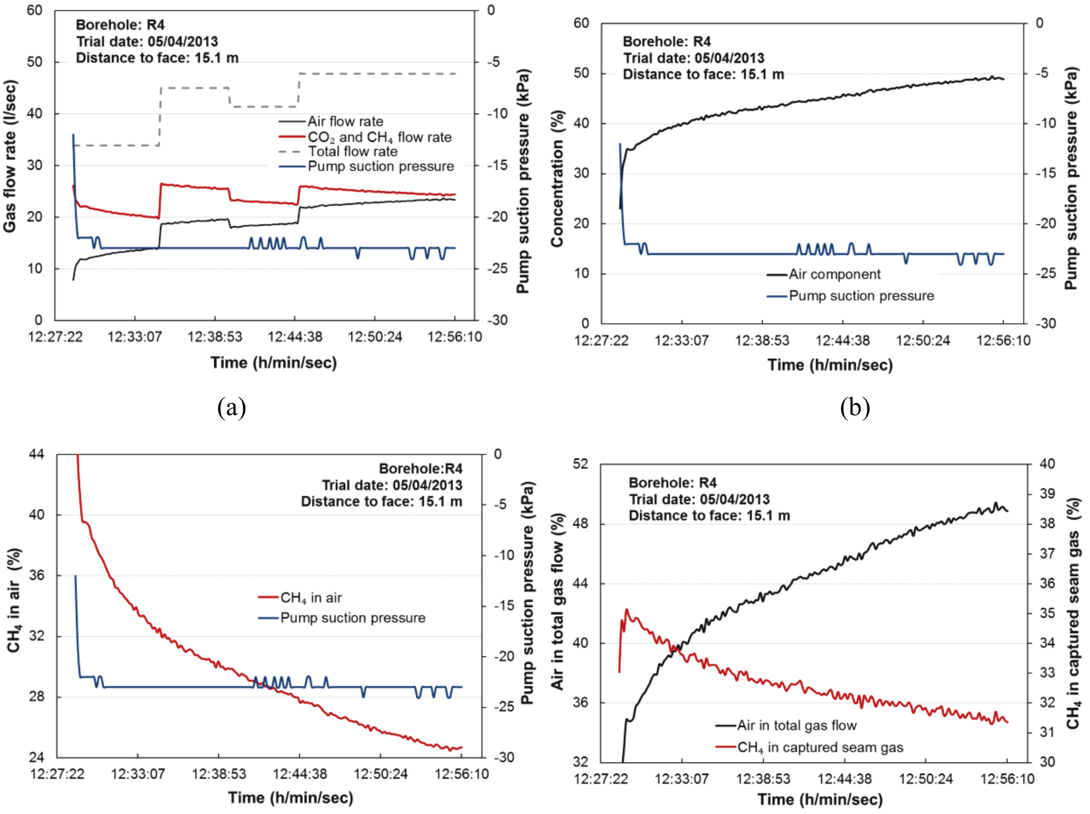

(a) (b)

(c) (d)

Figure A4.9: Results of **R4** gas drainage trial on **05/04/2013**: (a) Gas flow rate *vs* suction pressure; (b) Air concentration *vs* suction pressure; (c) CH$_4$ concentration in air *vs* suction pressure; (d) Concentration of air in total gas flow *vs* CH$_4$ in captured seam gas.

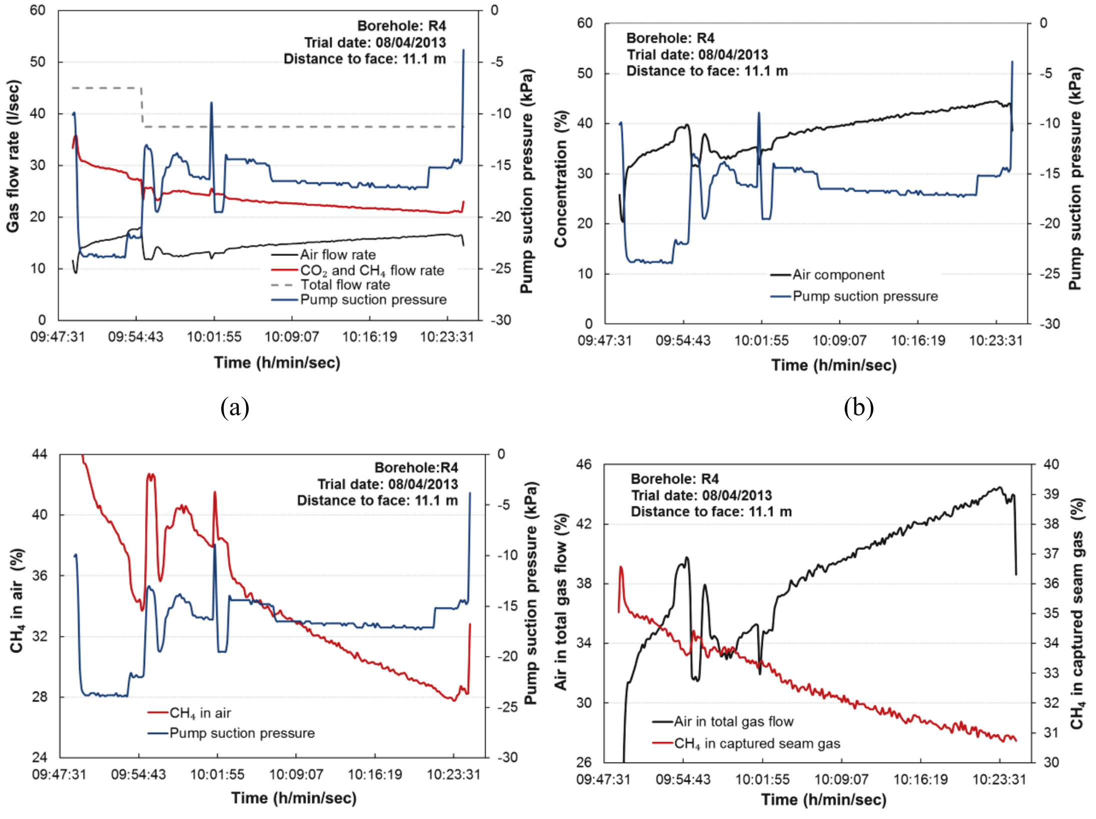

(a) (b)

(c) (d)

Figure A4.10: Results of **R4** gas drainage trial on **08/04/2013**: (a) Gas flow rate *vs* suction pressure; (b) Air concentration *vs* suction pressure; (c) CH_4 concentration in air *vs* suction pressure; (d) Concentration of air in total gas flow *vs* CH_4 in captured seam gas.